Development of Thermochromic Lateral Flow Assay for Sensitive Detection

Thithawat Trakoolwilaiwan

Supervisors

Professor Nguyễn Thi Kim Thanh

Dr Lena Ciric

A dissertation submitted to University College London in partial fulfilment of the requirements for the degree of Doctor of Philosophy in the Faculty of Mathematical and Physical Sciences, Department of Physics and Astronomy, University College London

January 30, 2023

Declaration

I, Thithawat Trakoolwilaiwan, confirm that the work presented in my thesis is my own. Where information has been derived from other sources, I confirm that this has been indicated in the thesis.

Abstract

Lateral flow assay (LFA) is a cost-effective and simple detection method providing a prompt colourimetric result to users. However, the low sensitivity of detection is one of the main disadvantages of the LFA. This project aims to develop a new technique based on thermal sensing strategy to enhance the sensitivity of LFA detection.

Thermochromic sheet, along with photothermal nanoparticles and a light-emitting diode (LED), was utilised in the LFA. In the thermal sensing LFA, photothermal nanoparticles were optically stimulated to generate heat energy whereas the temperature change was monitored and converted into a visual signal by a thermo-responsive material. The novel thermal sensing platforms were developed to separately detect two antigens: *Salmonella typhimurium* and dengue virus serotype 2 NS1 (DENV2-NS1). Various types and shapes of photothermal nanoparticles were fabricated, of which the photothermal response was investigated. At the same mass, gold nanospheres (AuNSPs) with a diameter of 12 nm could raise to a relatively higher temperature than other materials. Hence, they were chosen to be utilised in the thermal sensing platform.

The analytical performances of the typical and the thermochromic LFA were compared in the thesis. The colour intensities of the typical visual signal and the thermochromic signal was quantified using MATLAB. The power and duration of LED illumination were optimised to maximise the performance of the thermochromic assay. The thermochromic LFA was deployed to identify *Salmonella typhimurium*. The result showed that the typical visual measurement had a detection limit of 0.25 x 10^7 colonies forming unit (CFU) per mL, while using the thermochromic technique reduced the detection limit to 0.5x10^6 CFU/mL. For the detection of DENV2-NS1, the typical LFA yielded the detection limit of 6.125 ng/mL, while the thermochromic LFA provided the limit of detection (LOD) of 1.5 ng/mL.

The linear relationship between the colour intensity ratio and the concentration of the analytes was found in both detection platforms. Furthermore, the

thermochromic assay offered a semi-quantificative analysis to estimate the range of analyte concentration without the requirement of additional equipment.

In conclusion, various types and shapes of nanoparticles were prepared and examined for their photothermal response. AuNSPs were chosen to be the visual signal provider in the conventional LFA and the heat generator in the thermochromic LFA. Two analytes were tested in this thesis to assess the performance of the thermochromic LFA. It was found that the analytical performance was significantly improved. Therefore, the thermochromic-based method is an effective colourimetric detection method for sensitive detection and early diagnosis.

Statement of impact

Rapid detection techniques have recently received interest from worldwide research. They are extremely beneficial as a result can be obtained in a short time of analysis. To date, there are several detection methods such as polymerase chain reaction (PCR), enzyme-linked immunosorbent assay (ELISA), biosensors, and immunoassay, each with its own advantages and disadvantages. For example, PCR is highly accurate and sensitive, but it requires advanced equipment, operation in laboratories, expensive reagents, and specialists. Compared to other conventional detection methods, LFA has some advantages such as portability, user-friendly, low cost, rapidness, and simplicity making it one of the most popular detection methods. However, the low sensitivity of LFA is the main issue compared to other analytical assays.

Numerous studies have demonstrated the powerful LFA signal enhancement technique based on thermal measurement, by exploiting the photothermal properties of LFA labels. A laser was reported to be used as a light source to optically stimulate photothermal nanoparticles. It is, however, noted that the use of laser needs extra care and caution whilst operating, as its exposure may cause permanent eye and skin damage. Most of the lasers used in the previous studies of the thermal sensing LFAs are beyond the Class 3 laser. The operator potentially experiences the damage caused by laser irradiation. Hence, previous thermal sensing LFA configurations have a limitation of accessibility as it strongly requires specialists to manipulate.

The thermal sensing platform in this study replaces a laser light source by an LED. It is identified to be under Risk Group 1 (standard IEC 62471:2006), being a low-risk optical item as it does not cause photobiological hazards under normal behaviour. To monitor temperature production, the thermosensitive material was used in this study. The thermochromic sheet is sensitive to external heat and changes its colour corresponding to the temperature. The liquid crystal thermochromic sheet used to

monitor temperature generation eliminates the need for an infrared (IR) camera, which typically cost over £500. The thermochromic LFA converts heat into a visible colour change, therefore a standard smartphone camera can be used as a reader. A 300 x 450 mm thermochromic sheet costs only £34 and can produce approximately 6750 pieces of strips (~£0.005 per strip), significantly reducing production and handling costs.

Salmonella typhimurium is a major contributor to food-borne disease, causing economic losses and adverse public health impacts. Standard detection approaches for pathogenic contamination in food is time-consuming and not suitable for on-site analysis. The thermochromic based assay developed in this thesis can contribute positively to to the survillence of bacterial contamination to effectively prevent outbreaks. The thermochromic LFA can be used as a rapid screening method for a large number of samples. Suspected samples can then be further examined using standard detection methods.

In addition to its potential to detect *Salmonella typhimurium*, the thermochromic LFA developed in this thesis can also be used to determine DENV2-NS1, a critical biomarker of dengue fever. Dengue disease is endemic in remote areas where access to advanced equipment and facilities for diagnosis is limited. The thermochromic LFA is cost-effective, sensitive and simple-to-use. It can be used without specilised training, making it an ideal tool for early daignois of dengue fever in these settings.

The thesis presents a rapid detection using thermochromic-based technique for colourimetric signal generation in LFA detection. The thermochromic LFA was successfully fabricated to detect two different analytes, demonstrating its adaptability to a variety of targets. The developed platform is simpler and more affordable than previously reported thermal detection LFAs, expanding the utility of LFAs to more applications requiring high sensitivity and quantitative analysis. Moreover, not only LFA, the thermochromic-based technique is transferable to other biosensing platforms, such as microfluidic paper-based chips, to provide visual signal with affordability and analytic effectiveness.

Table of contents

Declaration 2

Abstract 3

Statement of impact 5

Table of contents 7

Publications and presentations 13

1. Publications 13

2. Presentations 14

2.1 Oral presentation 14

2.2 Poster presentations 14

Acknowledgements 15

List of figures 17

List of tables 27

List of equations 29

Abbreviations 31

Chapter 1 : Background knowledge 34

1.1 Nanotechnology 34

1.1.1 Classifications of nanomaterials 34

1.1.2 Fabrication of nanomaterials 36

1.1.3 Properties of nanomaterials 37

1.1.4 Nanotechnology applications 41

1.2 Dengue disease.....43

1.2.1 General information 43

1.2.2 Dengue biomarkers.....44

1.2.3 Determination of dengue virus.....45

1.3 *Salmonella typhimurium* 47

1.3.1 General information 47

1.3.2 Impact of *Salmonella* spp. outbreak.....48

1.3.3 Detection of *Salmonella* spp. 49

1.4 Lateral flow assays.....53

1.4.1 General information 53

1.4.2 Nanoparticle conjugation 57

1.4.3 Sensitivity enhancement techniques.....61

1.4.4 Commercial lateral flow assays 67

1.5 Photothermal effect of noble nanoparticles.....69

1.5.1 Localised surface plasmon resonance 69

1.5.2 Heat production.....74

1.6 Research aim and objectives.....75

1.6.1 Research aim.....75

1.6.2 Research obejctives 75

Chapter 2 : Fabrication of magnetic nanoparticles and gold nanoparticles.....77

2.1 Introduction 77

2.2 Synthesis and characterisation 78

2.2.1 Materials 78

2.2.2 Synthesis of nanoparticles 79

2.2.2.3 Gold nanorods 81

2.2.3 Characterisation of nanoparticles 83

2.3 Statistical analysis 86

2.4 Results and discussion 86

2.4.1 Synthesis and Characterisation of magnetic nanoparticles 86

2.4.2 The synthesis and characterisation of gold nanospheres 100

2.4.3 The synthesis and characterisation of gold nanorods 104

2.4.4 The synthesis and characterisation of gold nanostars 109

2.5 Conclusion 110

Chapter 3 : Light-to-heat conversion capability of photothermal nanoparticles 114

3.1 Introduction 114

3.2 Materials and methods 115

3.2.1 Materials 115

3.2.2 Determination of nanoparticle concentration 116

3.2.3 Nanoparticle alignment on nitrocellulose membranes 118

3.2.4 Visual signal measurement 118

3.2.5 Thermal signal measurement 119

3.2.6 Thermochromic signal measurement....120
3.2.7 Comparison between different types of signals....122
3.2.8 Statistical analysis....123
3.3 Results and discussion....124
3.3.1 Determination of nanoparticle concentration....124
3.3.2 Nanoparticle alignment on nitrocellulose membranes....125
3.3.3 Visual signal measurement....127
3.3.4 Thermal signal measurement....130
3.3.5 Thermochromic signal measurement....137
3.3.6 Comparison between different types of signals....140
3.4 Conclusion....144
Chapter 4 : Bioconjugation of nanoparticles and lateral flow assay detection....146
4.1 Introduction....146
4.2 Materials and methods....147
4.2.1 Materials....147
4.2.2 *Salmonella typhimurium* growth curve....148
4.2.3 Aptamer-immobilised zinc ferrite nanoparticles....149
4.2.4 Antibody-conjugated gold nanospheres....152
4.3 Results and discussion....157
4.3.1 *Salmonella typhimurium* growth curve....157
4.3.2 Aptamer-immobilised zinc ferrite nanoparticles....159

4.3.3 Antibody-conjugated gold nanospheres 169

4.4 Conclusion 181

Chapter 5 : Development of thermochromic lateral flow assay.....184

5.1 Introduction.....184

5.2 Materials and methods 185

5.2.1 Materials.....185

5.2.2 Fabrication of thermochromic lateral flow strips.....186

5.2.3 The operation of lateral flow assay 187

5.2.4 Conjugate pad preparation and optimisation 188

5.2.5 Optimisation of the thermochromic signal 188

5.2.6 Comparison between typical signal and thermochromic signal 189

5.3 Results and discussion.....190

5.3.1 Development of the thermochromic lateral flow assay for *Salmonella typhimurium* detection.....190

5.3.2 Development of the thermochromic lateral flow assay for DENV2-NS1 detection.....197

5.3.3 Discussion 204

5.4 Conclusion 208

Chapter 6 : Conclusions and future works.....210

6.1 Conclusions.....210

6.2 Future works.....213

Bibliography 219

Appendices 239

Appendix A 239

Appendix B 240

Appendix C 242

Appendix D 243

Appendix E 244

Appendix F 245

Appendix G 246

Appendix H 247

Publications and presentations

1. Publications

1.1 Hildebrand, S., Löwa, N., Paysen, H., Fratila R.M., Salisa, L. R., **Trakoolwilaiwan, T.**, Niu, Z., Kasparis, G., Preuss, S F., Kosch, O., de la Fuente, J. M., Thanh, N. T. K., Wiekhorst, F., and Pfeifer, A. (2021) Quantification of lipoprotein uptake in vivo using magnetic particle imaging and spectroscopy. *ACS Nano.*15: 434-446.

1.2 Arshad M. I., Rehman U., Hasan M. S., Akhtar, M., Tung L. D., Amin N., Mahmood K., **Trakoolwilaiwan, T.** and Thanh, N. K. T. (2022) Structural, Optical, Electrical, Dielectric, Molecular Vibrational and Magnetic Properties of La^{3+} doped Mg-Cd-Cu Ferrites Prepared by Co-precipitation Technique. *Ceramics International.* **48***:* 14309-14323.

1.3 Stati, G., Rossi, F., **Trakoolwilaiwan, T.**, Tung, L. D., Mourdikoudis, S**.,** Thanh, N. T. K. and Di Pietro, R. (2022) Development and Characterization of Curcumin-Silver Nanoparticles as a Promising Formulation to Test on Human Pterygium-Derived Keratinocytes. *Molecules.* 27: 282.

1.4 **Trakoolwilaiwan, T.**, Takeuchi, Y., Leung, T.S., Sebek, M., Storozhuk, L., Nguyen, L., Tung, L.D., Thanh, N.T.K. (2023) Development of Thermochromic Lateral Flow Assay to Improve Sensitivity for Dengue Virus Serotype 2 NS1 Detection. *Nanoscale.* To be submitted in March 2023.

2. Presentations

2.1 Oral presentation

2.1.1 *Development of the Colourimetric Thermal Sensing Lateral Flow Assay for Dengue Serotype 2 Detection*. Presented at BME9 (The 9th International Conference in Vietnam on the Development of Biomedical Engineering), 26-29th December 2022, International University – Vietnam National University, Ho Chi Minh, Vietnam.

2.2 Poster presentations

2.2.1 *Development of Metallic Nanoparticle-Based Sensor for Bacteria Detection in Food*. Presented at Physical Approaches to Understanding Microbial Life (PALM) Summer School, 28th August – 06th September 2018, centre CGT Benoît Frachon, Paris, France.*Enhancement of thermochromic signal from photothermal nanoparticles*. Presented at American Chemical Society Spring 2021, 5-30th April 2021 [online participation].

Acknowledgements

First of all, I would like to express my deepest gratitude to my supervisor, Prof. Nguyen T.K. Thanh, for welcoming me into her research group and providing guidance and support throughout my PhD journey. Her dedication to her students has been an inspiration to me, and I am truly grateful for her tireless efforts.

I would also like to extend my sincere appreciation to all the members of the "Healthcare Biomagnetics Laboratories" for their invaluable assistance, both academically and personally. Their willingness to sheir knowledge have been instrumental in my growth and development as a researcher. In particular, I would like to thank Dr. Stephen Nesbitt for his patience and guidance during my general lab training and orientation to lab safety procedures. I am also grateful to Dr. Le Tung for his constructive comments and feedback on my writing. Thanks to Dr. Paul Southern for generously lending me a thermal imager, which has proven to be an invaluable tool in my research. His willingness to share his resources has significantly enhanced my research capabilities.

Thanks to Dr Lena Ciric to accept the request to be my secondary supervisor. I would like to express my gratitude for her support either inside or outside the university as well as her professional advice. I would like to thank the "Healthy Infrastructure Research Group", especially Dr Melisa Canales and Dr Rupy Matharu to babysit me since I was in MSc. programme and to be patient while I was messing up the lab.

I would like to acknowledge the Royal Thai Government scholarship to fund the tuition fee and all living expenses for the whole of my MSc and PhD courses. Without their offer, I could not even imagine continuing my further degree abroad.

Apart from academic life, I have to mention these people from the North Mews house, namely Professor Adrian Paul Rabe, Wayne Cheung, and Justin Yu Yan Lok. I, to be honest, will not be able to achieve the degree without their continued invaluable support. I would express my distinctive gratitude to, particularly, Professor Adrian who always support me when I was in trouble, such as being homeless. Thanks

for the warm couch next to a Mahjong table. It is such a nice and warm vibe of the North Mews house. I would give a huge thanks to Wayne for the high-performance laptop he sponsored me. I also would like to thank Justin for being annoyed but always besides me. He and Dr Zhi Lin have always pushed and challenged me to complete my PhD, even after they left the UK.

Moreover, I would like to thank Patara Thai fine restaurant to nourish me with the best Thai food, preventing me from starving. It saves me lots of money. Thank you, Mr Junior, my brother from another mother too for these precious years we spent together.

Thanks to London badminton communities. Special thanks are given to my favourite clubs: ISO, White hart, and Broken strings badminton club. They are my favourite places to go to handle and release the pressure from lab failure and reset my brain. I would thank the ISO badminton club to recruit me into their team after the UCL badminton team rejected my request. I would like to thank the White hart badminton club. The games I played there were so intense and high quality but fun. I love the Broken strings badminton club as lovely and friendly people are around.

Lastly, I sincerely express gratitude to my parents and family for growing me up and directing me to be who I am today. Thanks for their patients and for having faith in me that I will finally get through my PhD course. I would like to thank you for the unlimited and unconditional support they have provided me until now. I wholeheartedly show appreciation to everyone who is behind the success of this thesis. They truly deserve my gratitude.

List of figures

Figure 1.1 Classifications of nanomaterials by nanoscale dimensions: 0D, 1D, 2D, and 3D. 35

Figure 1.2 Concepts of nanomaterial production: top-down and bottom-up approaches. 36

Figure 1.3 Schematic illustration of the quantum confinement of quantum dots. The variation of energy bands corresponds to the size of quantum dots. 38

Figure 1.4 Development of dengue biomarkers at different stages in primary and secondary infections. 44

Figure 1.5 Classification of *Salmonella* genus 48

Figure 1.6 The general structure of LFA comprising a sample pad, conjugate release pad, detection pad, and adsorbent pad (wicking pad). Test and control lines are printed on the detection pad. All components are adhered to a backing card.55

Figure 1.7 Diagram of a functional aptamer to bind a biological target. A short single-strand oligonucleotide (aptamer sequence) is folded into a three-dimensional structure, fitting to the binding site of the cancer biomarker. IOP is the abbreviation of initial oligonucleotide pool. 58

Figure 1.8 Diagram showing the SELEX process to produce high-affinity aptamers. SELEX stands for systematic evolution of ligands by exponential enrichment. 59

Figure 1.9 The scheme of antibody functionalisation on AuNSP using EDC coupling reaction with the addition of NHS. 60

Figure 1.10 Scattering and absorption of incident light by the nitrocellulose and AuNSPs. 61

Figure 1.11 Illustrations of A) SPR in a bulk material and B) LSPR in a nanoparticle. 70

Figure 1.12 The schematic of the interaction of a nanoparticle and electromagnetic radiation of A) nanosphere and B) nanorod. 71

Figure 1.13 The absorption spectrums of AuNSPs, AuNRs, gold nanoflowers, gold nanoprisms, and AuNSTs. 73

Figure 2.1 TEM images at 50000X magnification and size distribution of the IONPs@TREG and the ZFNPs@TREG yielded from the polyol synthesis. They represent the structural detail of IONPs@TREG that were incubated in an autoclave for A) 8 h, B) 24 h, and C) 48 h, and ZFNPs@TREG that were incubated for D) 8 h, E) 24 h, and F) 48 h (n = 500). d = mean diameter, δd = standard deviation, PDI = polydispersity index. 88

Figure 2.2 The XRD patterns of IONPs (red) and ZFNPs (blue). The bottom panel (black) represents the diffraction patterns of magnetite according to PDF No. 01-089-0691. 89

Figure 2.3 Percentage of metallic contents of IONPs and ZFNPs determined by ICP-AES measurement. Data are presented as the mean ± standard deviation (n = 3). P-values were obtained using a two-tailed paired-samples t-test. *p < 0.05, **p < 0.01, ***p < 0.001, and ****p < 0.0001. 90

Figure 2.4 Hydrodynamic sizes of IONPs@citrate and ZFNPs@citrate after ligand exchange reaction performed at 70 °C for 2 h under mechanic stirring. The citrate concentration was varied from 25 mM to 1000 mM and 0 mM of trisodium citrate coating was used as a negative control (IONPs@TREG and ZFNPs@TREG). Data represented as the mean ± standard deviation of three independent samples (n = 3). P-values obtained by one-way ANOVA, followed by Dunnett's T3 t-test (unequal variances t-test). *p < 0.05, **p < 0.01, ***p < 0.001, and ****p < 0.0001. 92

Figure 2.5 Hydrodynamic sizes of IONPs@citrate and ZFNPs@citrate after ligand exchange reaction performed at different reaction temperatures under

mechanic stirring. The citrate concentration was 1000 mM. Data represented as the mean ± standard deviation of three independent samples (n = 3). P-values obtained by one-way ANOVA, followed by Bonferroni t-test (equal variances t-test). *p < 0.05, **p < 0.01, ***p < 0.001, and ****p < 0.0001.....94

Figure 2.6 Hydrodynamic sizes of IONPs@citrate and ZFNPs@citrate after ligand exchange reaction performed at RT under gentle rotation. The citrate concentration was varied from 25 mM to 1000 mM and 0 mM of trisodium citrate coating was used as a negative control (IONPs@TREG and ZFNPs@TREG). Data represented as the mean ± standard deviation of three independent samples (n = 3). P-values obtained by one-way ANOVA, followed by Dunnett's T3 t-test (unequal variances t-test). *p < 0.05, **p < 0.01, ***p < 0.001, and ****p < 0.0001.....95

Figure 2.7 Hydrodynamic sizes of IONPs@citrate and ZFNPs@citrate after ligand exchange reaction performed under gentle rotation with different reaction times: 24 h, 48 h, and 72 h, at a citrate concentration of 1000 mM. Data are represented as the mean ± standard deviation of three independent samples (n = 3). P-value obtained by one-way ANOVA indicates no significant differences between samples. 96

Figure 2.8 The IR spectrums of IONPs@TREG, ZFNPs@TREG, trisodium citrate, IONPs@citrate, and ZFNPs@citrate.....98

Figure 2.9 Zeta potential of IONPs@citrate and ZFNPs@citrate in water with pH ranging from 3 to 9. 99

Figure 2.10 TEM images (on the left) and size distributions (on the right) of AuNSPs produced with A) 0.01 wt% $HAuCL_4$ and B) 0.03 wt% $HAuCL_4$ (n = 500). d = mean diameter, δd = standard deviation, σ = polydispersity index. 100

Figure 2.11 TEM images (on the left) and size distributions (on the right) of AuNSPs produced with different volumes of 1 wt% trisodium citrate: A) 1.25 mL, B) 2.5

mL, and C) 5 mL (n = 400). d = mean diameter, δd = standard deviation, σ = polydispersity index. 101

Figure 2.12 Absorption spectra of AuNSPs produced by the addition of different volumes of trisodium citrate, in the wavelength range of 400-700 nm. 102

Figure 2.13 A) TEM image and B) optical absorption of AuNSPs with 0.4 mL trisodium citrate added. 103

Figure 2.14 TEM images and aspect ratios of the NaBr-assissted AuNRs synthesized with different amounts of 10 mM $AgNO_3$: A) 75, B) 100, and C) 125 µL (n = 500). L = average length of AuNRs, W = average width of AuNRs. 105

Figure 2.15 TEM image and aspect ratio of the $NaNO_3$-assissted AuNRs (n = 500). L = average length of AuNRs and W = average width of AuNRs. 106

Figure 2.16 Absorption spectra of AuNRs produced with the A) NaBr additive with the diversity of the added amount of $AgNO_3$ and B) $NaNO_3$ additive.....107

Figure 2.17 TEM images of AuNSTs produced with A) 12 nm and B) 20 nm AuNSPs. 110

Figure 3.1 The principle of image recording and determination of the colour intensity ratio. A .RAW image of the strip containing the region of nanoparticle alignment is taken and then analysed in MATLAB to find the average RGB intensities of printed nanoparticles and the background of the membrane. 119

Figure 3.2 Principle of thermal signal measurement. The nanoparticles on the nitrocellulose membrane are illuminated by the LED and the thermal recording is performed by an IR camera. 120

Figure 3.3 The ZFNP-deposited nitrocellulose membrane. A piece of a thermochromic sheet is attached underneath the area of ZFNPs. 121

Figure 3.4 Diagram of the thermochromic signal measurement. The LED generates light to illuminate a membrane sample. A mobile phone camera records the

colour change of the thermochromic sheet, which is then analysed in MATLAB. 122

Figure 3.5 The thickness of the IONP line created from various dispensing rates (0.1, 0.2, and 0.3 µL/mm) and head speeds (32.5 and 50 mm/sec). Data are presented as the mean ± standard deviation (n = 50). P-values were obtained using a two-tailed paired-samples t-test. *p < 0.05, **p < 0.01, ***p < 0.001, and ****p < 0.0001.....127

Figure 3.6 Appearance of the membranes deposited with various concentrations of IONPs (0.5, 1, 1.5, and 2 mg/mL) and dispensing rates (0.1 and 0.2 µL/mm). The coffee ring effect is highlighted in red. 128

Figure 3.7 Correlation between the colour intensity ratios and the concentrations of IONPs on nitrocellulose membranes. The colour intensity ratios are shown in red, green, and blue channels. The dash lines represent the linear trend lines. The linear equations and the R^2 values are labelled alongside the graph. Data are presented as the mean ± standard deviation (n = 3). 129

Figure 3.8 Absorption spectrum of IONPs in water 130

Figure 3.9 Temperature gradients of IONPs and ZFNPs after 3 min of light irradiation. The concentrations of IONPs and ZFNPs ranged from 0.5 to 2 mg/mL and the dispensing rates were adjusted to 0.1 and 0.2 µL/mm. Data are presented as the mean ± standard deviation (n = 3). * indicates the LOD and S_{LOD} indicates the signal of detection limit determined by IUPAC.....131

Figure 3.10 Temperature gradients of 12-nm and 18-nm AuNSPs after 3 min of light irradiation. The concentrations ranged from 0.5 to 2 mg/mL and the dispensing rates were adjusted to 0.1 and 0.2 µL/mm. Data are presented as the mean ± standard deviation (n = 3). * indicates the LOD and S_{LOD} indicates the signal of detection limit determined by IUPAC. 132

Figure 3.11 Temperature gradients of AuNRs with LSPRs of 560, 600, and 625 nm after 3 min of light irradiation. The concentrations ranged from 0.5 to 2 mg/mL

and the dispensing rates were adjusted to 0.1 and 0.2 µL/mm. Data are presented as the mean ± standard deviation (n = 3). * indicates the LOD and S_{LOD} indicates the signal of detection limit determined by IUPAC. 133

Figure 3.12 Absorption spectra of nanoparticles (0.05 mg/mL) in the wavelength range of 400 to 800 nm.....134

Figure 3.13 Particle number of nanoparticles in 1 mL of water, calculated based a the mass of 0.5 mg. 137

Figure 3.14 Display of the thermochromic sheets at different concentrations of ZFNPs (0.0625 to 2 mg/mL) and a bare nitrocellulose membrane (negative control). The images of the thermochromic sheets were taken after LED illumination. 138

Figure 3.15 Colour intensity signal ratios of RGB of the thermochromic sheet. The ZFNP concentrations ranged from 0 and 2 mg/mL. Data are presented as the mean ± standard deviation (n = 3). 139

Figure 3.16 Appereances of the signals of A) typical membrane strips B) thermal images and C) thermochromic sheets with various concentrations of ZFNPs.141

Figure 3.17 Correlations between ZFNP concentration and the intensities of various types of signals: A) typical visual signal ratio, B) thermal gradient signal, and C) thermochromic signal ratio. The red lines in each panel represent the linear trendlines. Data are presented as the mean ± standard deviation (n = 3). * indicates the LOD and S_{LOD} indicates the signal of detection limit determined by IUPAC.....142

Figure 4.1 Schematic showing covalent immobilisation between amine-containing aptamers and ZFNPs@citrate using EDC and sulfo-NHS. ZFNPs@citrate are activated by EDC and sulfo-NHS in MES buffer. Amine-tagged aptamers are then added to mix wih the particles.....151

Figure 4.2 Diagram of the immunoseparation technique. The aptamer-conjugated ZFNPs were incubated with bacteria to allow for antigen-aptamer interaction. A

permanent magnet was held aside the mixture to attract the ZFNP-bound bacteria cells. Unbound bacteria were transferred to an LB agar plate for colony counting. 152

Figure 4.3 Diagram of a half-strip LFA for *Salmonella typhimurium* detection. Capture antibody is coated on the membrane.The strip is dipped into the mixture of gold conjugates and the bacteria in running buffer. 155

Figure 4.4 Diagram of a half-strip LFA for DENV2-NS1 detection. Capture antibody is coated on the membrane.The strip is dipped into the mixture of gold conjugates and DENV2-NS1 in running buffer. 156

Figure 4.5 Optical characteristic of *Salmonella typhimurium*. A) Calibration growth curve of *Salmonella typhimurium*, showing OD_{600} as a function of incubation time. B) The concentration of *Salmonella typhimurium* versus OD_{600} identified by the colony counting method. Insets display bacteria culture plates. Data are presented as the mean ± standard deviation (n = 3).....157

Figure 4.6 Results of DLS and zeta potential measurements of ZFNPs@citrate after adding various concentrations of EDC: 3.5, 7, 14, 28, and 56 mM.....160

Figure 4.7 Hydrodynamic sizes and electrical surface properties of ZFNPs before and after conjugation. A) The hydrodynamic diameter of ZFNPs before and after aptamer immobilisation with various concentrations of EDC and sulfo-NHS. P-values were obtained using a two-tailed paired-samples t-test. *$p < 0.05$, **$p < 0.01$, ***$p < 0.001$, and ****$p < 0.0001$. B) The hydrodynamic diameter and zeta potential of the aptamer immobilised ZFNPs with various concentrations of EDC and sulfo-NHS ($p > 0.05$). P-values obtained by one-way ANOVA. Data are represented as the mean ± standard deviation of three independent samples (n = 3).....161

Figure 4.8 FTIR spectra of ZFNPs@citrate and ZFNPs@aptamer. 163

Figure 4.9 Visualisation of the stained aptamers under UV illumination: lane 1) free aptamer; lane 2) ZFNPs@citrate; lane 3) – lane 7) ZFNPs@aptamer with the

addition of 10 to 50 µL of 100 mM aptamers; lane 8) blank; lane 9) – lane 13) supernatant collected after centrifuged of after conjugation of ZFNPs@aptamer with the addition of 10 to 50 µL of 100 mM aptamers. 164

Figure 4.10 Fluorescene intensities of aptamers on an agarose gel. A) The fluorescence intensities of ZFNPs@aptamer (top bands) and the aptamers that eluted from ZFNPs@aptamer (bottom bands) from lanes 2 to 7. B) The intensities of the supernatant after conjugation from lanes 9 to 13. 165

Figure 4.11 Capture efficiencies of ZFNPs@citrate and ZFNPs@aptamer with and without BSA blocking. Data are presented as the mean ± standard deviation (n = 3). P-values were obtained using a two-tailed paired-samples t-test. *p < 0.05, **p < 0.01, ***p < 0.001, and ****p < 0.0001. 167

Figure 4.12 Results of the flocculation tests to identify optimal conjugation conditions of anti-*Salmonella typhimurium* mAb. A) UV spectrum absorption of the conjugation at different pH values. B) The stability index at different pH values while keeping the number of antibodies. C) The spectral absorption of the conjugate at various antibody concentrations. D) The stability index at different antibody concentrations while keeping the pH constant. 172

Figure 4.13 The membranes strips after interaction with blank sample and Salmonella Typhimurium at the concentrations between 10^1 and 10^8 CFU/mL. 173

Figure 4.14 Appearance of the strips after migration of A) bare AuNSPs and B) AuNSPs@anti-*Salmonella typhimurium* mAb, with and without BSA blocking. Theses strips were incubated with *Salmonella typhimurium* (10^6 – 10^8 CFU/mL) and blank samples (negative controls). 174

Figure 4.15 Diagram of the sample loading strategy. The strips were incubated with different concentrations of *Salmonella typhimurium* (10^8 and 10^7 CFU/mL), followed by the addition of conjugates. The displays of the strips after the assays were completed are shown on the right. 175

Figure 4.16 Images of the stips after incubating with *Salmonella typhimurium* and AuNSPs@anti-*Salmonella typhimurium* mAb with various concentrations of antibody coating. 176

Figure 4.17 Diagram illustrating the interaction between various concentrations of *Salmonella typhimurium* and AuNSPs@anti-*Salmonella typhimurium* mAb. .177

Figure 4.18 Images of the strips after incubating with the diluted conjugates and *Salmonella typhimurium* (10^3 – 10^8 CFU/mL).....178

Figure 4.19 Results of the flocculation tests to identify optimal conjugation conditions of anti-DENV-NS1 DA034 mAb. A) UV spectrum absorption of the conjugation at different pH values. B) The stability index at different pH values while keeping the number of antibodies. C) The spectral absorption of the conjugate at various antibody concentrations. D) The stability index at different antibody concentrations while keeping the pH constant. 179

Figure 4.20 Colour intensity ratios derived from the green channel representing the visualisation of the signal. Each antibody was used as the detection antibody and capture antibody. Data are presented as the mean ± standard deviation (n = 3). * indicates the LOD and S_{LOD} indicates the signal of detection limit determined by IUPAC. 181

Figure 5.1 Illustration of the thermochromic LFA architecture comprising of a sample pad for loading an aqueous sample containing biological analytes of interest, a conjugate pad to release conjugated nanoparticles and maintain optimal conditions for the reaction, a nitrocellulose membrane containing test line and control line antibodies, and a wicking pad at the terminal end. All components are attached on a backing card. A piece of a thermochromic sheet is attached to the backside of the nitrocellulose membrane. 186

Figure 5.2 Impact of the gold conjugate concentration (OD 2.0 and OD 4.0) on visaulisation of test and control lines. A) The intensity ratio of the test line. Data are presented as the mean ± standard deviation (n = 3). P-values were obtained

using a two-tailed paired-samples t-test ($p > 0.05$). B) Images of the LFA results. C) Images of the LFA strips showing the aggregation of the particles. 191

Figure 5.3 Displays of A) typical LFA strips and B) thermochromic sheets upon illumination with the incident light. They were tested with *Salmonella typhimurium* with concentrations scaling from 10^5 to 10^8 CFU/mL and the blank sample. 194

Figure 5.4 Relationships between the colour intensity ratios (red, green, blue) and *Salmonella typhimurium* concentration (0-10^8 CFU/mL). A-C) Typical LFA; D-F) thermochromic LFA. Data are presented as the mean ± standard deviation (n = 3). * indicates the LOD and S_{LOD} indicates the signal of detection limit determined by IUPAC. 195

Figure 5.5 Results of the LFA strips testing with DENV2-NS1 concentration ranges from 0 to 400 ng/mL. A) Correlation between visual intensity ratio and the concentration of DENV2-NS1. B) Displays of LFA strips assembled with the conjugate pads immersed with an OD of 2.0 and C) OD 5.0. * indicates the detection limit. 198

Figure 5.6 Displays of A) typical LFA strips and B) thermochromic sheets upon illumination with the incident light. They were tested with DENV2-NS1 with concentrations ranging from 0 to 400 ng/mL and the blank sample. 200

Figure 5.7 Relationships between the colour intensity ratios (red, green, blue) and DENV2-NS1 concentration (0-400 ng/mL). A-C) Typical LFA; D-F) thermochromic LFA. Data are presented as the mean ± standard deviation (n = 3). * indicates the LOD and S_{LOD} indicates the signal of detection limit determined by IUPAC. 202

Figure 6.1 Semi-quantificative analysis of the thermochromic LFA. Thermochromic sheets were exposed to DENV2-NS1 concentrations ranging from 0 to 400 ng/mL following LED illumination. 216

List of tables

Table 1.1 Comparion of different rapid detection methods of DENV. 47

Table 1.2 Advantages and disadvantages of optical-based enhancement techniques for LFA. 65

Table 1.3 Commercial LFAs in the market 68

Table 2.1 Impact of various parameters tested on MNPs using modified-polyol method. [201] Top panel shows the influence of reaction time and precursor mass on MNP size. Bottom panel shows the effect of solvents on MNP size and polydispersity. 87

Table 3.1 Appearance of the IONPs absorbed on the nitrocellulose membranes. The dispensing rates ranged from 0.1 to 0.3 µL/mm and the head speed was varied to 32.5 and 50 mm/sec. 126

Table 3.2 Analytical performances of typical visual, thermal contrast, and thermochromic measurements, determined by IUPAC. 142

Table 5.1 Response of the 30-35 °C thermochromic sheet under different conditions of illumination. The power intensities are 3.69, 5.2, and 6.5 W/cm^2 and the lengths of exposure are 20, 30, and 40 s. The concentrations of *Salmonella typhimurium* range from 0 to 10^8 CFU/mL. 193

Table 5.2 Colour measurement of the typical and thermochromic LFA. The results are shown in red, green, and blue channels. The analytical performances of both assays are determined by IUPAC. 196

Table 5.3 Response of the 30-35 °C thermochromic sheet under different conditions of illumination. The power intensities are 5.2, 6.5, and 8.16 W/cm^2 and the lengths of exposure are 10, 20, 30, and 60 s. The concentrations of DENV2-NS1 ranged from 0 to 100 ng/mL. 199

Table 5.4 Colour measurement of the typical and thermochromic LFA. The results are shown in red, green, and blue channels. The analytical performances of both assays are determined by IUPAC. 203

List of equations

(Equation 1.1).....71

(Equation 1.2).....72

(Equation 1.3).....72

(Equation 1.4)..... 72

(Equation 1.5) 72

(Equation 1.6) 73

(Equation 1.7) 73

(Equation 1.8) 73

(Equation 1.9) 73

(Equation 1.10) 73

(Equation 1.11).....74

(Equation 2.1) 85

(Equation 3.1) 117

(Equation 3.2).....118

(Equation 3.3) 119

(Equation 3.4) 120

(Equation 3.5) 121

(Equation 3.6) 123

(Equation 3.7) 135

(Equation 4.1).....152

Abbreviations

AuNSP	Gold nanosphere
AuNR	Gold nanorod
AuNST	Gold nanostar
BSA	Bovine serum albumin
CFU	Colony forming unit
DENV	Dengue virus
DENV2	Dengue serotype 2
DHF	Dengue fever with haemorrhage
DI	Deionised
DLS	Dynamic light scattering
DSS	Dengue shock syndrome
EDC	1-ethyl-3-(3-dimethylaminopropyl) carbodiimide hydrochloride
ELISA	Enzyme-linked immunosorbent assay
FTIR	Fourier transform infrared
ICP-AES	Inductive coupled plasma atomic emission
IgG	Immunoglobulin G
IgM	Immunoglobulin M

IONP	Iron oxide nanoparticle
IR	Infrared
LED	Light emitting diode
LOD	Limit of detection
LFA	Lateral flow assay
LSPR	Localised surface plasmon resonance
MNP	Magnetic nanoparticle
mAb	Monoclonal antibody
NHS	N-hydroxysuccinimide
NIR	Near-infrared
NS1	Nonstructural protein 1
OD	Optical density
pAb	Polyclonal antibody
PCR	Polymerase chain reaction
RGB	Red, green, and blue
ROS	Reactive oxygen species
RT	Room temperature
RT-PCR	Reverse transcription polymerase chain reaction
SPR	Surface plasmon resonance
Sulfo-NHS	N-hydroxysulfosuccinimide sodium salt

UV-Vis	Ultraviolet-visible
ZFNP	Zinc ferrite nanoparticle

Chapter 1 : Background knowledge

1.1 Nanotechnology

Nanotechnoloy is the manipulation of the matter at atomic, molecular, and macromolecular scale to exploit their size- and composite-dependent properties as well as unique phenomenon that only manifest in nanomaterials. In terminology, the prefix “nano” originates from Greek which means one billionth, hence one nanometer is equal to 10^{-9} of a meter. [1-4] Nanotechnology refers to the innovative technologies that harness new and unique properties of materials that emerge at the nanoscale, which are not observed in bulk materials. Importantly, a nanomaterial is structurically characterised as an object with at least one dimension in the scale of 1 to 100 nm. This is due to the quantum effect, which becomes dominant at the nanoscale and confines electrons in certain dimensions. Further explanation will be given later in this chapter.

1.1.1 Classifications of nanomaterials

Nanomaterials can be generally classified based on either their dimensionality or compositions. Based on the dimension, nanomaterials can be catagorised into 0D, 1D, 2D, and 3D, where the numeric letter represents the number of dimensions in the range between 1 and 100 nm (Figure 1.1). [1-5]

Zero-dimensional nanostructures (0D) have none of their dimensions beyond 100 nm, such as nanoparticles, nanospheres, nanoclusters, and nanodots. All electrons are confined in all directions and cannot move freely along any axis. One-dimensional nanomaterials (1D) have two dimensions in the nanoscale and the remaining dimension is significantly larger. Therefore, electrons can travel only along the length of the nanomaterial. Commonly, 1D nanostructures have a large aspect ratio, such as nanorods, nanotubes, and nanowires. Two-dimensional nanomaterials (2D) are in

the form of sheet- and film-like materials with a thickness less than 100 nm but width and length are considerably larger. Electrons can move throughout the surface of corresponding dimensions but are confined within one dimension. When all dimensions are not confined in the nanoscale, it forms a bulk nanomaterial, called a three-dimensional nanomaterial (3D). This type of nanomaterial typically composes of the building block of 0D, 1D, or 2D nanomaterials. At least one of the internal dimensions is align within the range of the nanoscale, making it maintains uqnique properties of nanomaterials. Electrons are allowed to move freely in all directions. Graphite and metal organic framework are examples of 3D nanomaterials.

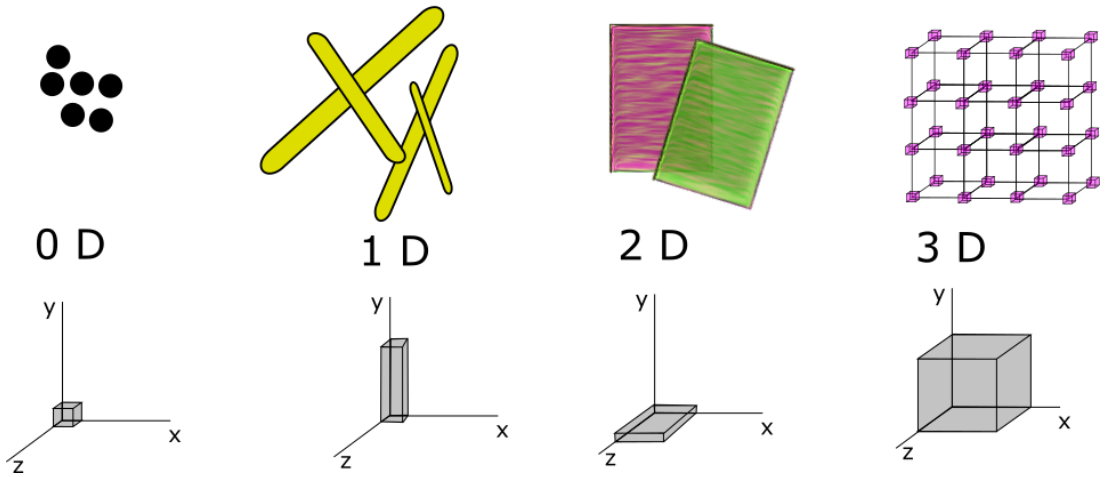

Figure 1.1 Classifications of nanomaterials by nanoscale dimensions: 0D, 1D, 2D, and 3D.

Nanomaterials can be catagorised by their elemental components. [2, 4, 5] Carbon-based nanomaterials include fullerenes, carbon nanotubes, graphenes, carbon nanofibers, carbon quantum dots, and nanodiamonds. Organic nanomaterials are mainly composed of organic compounds such as lipids, carbohydrates, or polymeric nanoparticles. Inorganic nanomaterials include metal, metal oxide , and ceramic-based nanomaterials. The inorganic nanomaterials can exhibit intriguing optical, electronic, and magnetic properties as their size approaches to the nanoscale. Semiconductor nanostructures have features of both metals and non-metals. They possess quantum confinement effects and express unique and tunable optical properties. Composite-based nanomaterials contain multiple phases, of which at least one has nanoscale dimensions, or a nanoscale repeat distance between the different phases of the material. Composite-based nanomaterials are the

combination of two or more different materials that are mixed to exploite the best properties of each material.

1.1.2 Fabrication of nanomaterials

In fabrication, there are numerous methods available nowadays which are based on either breaking down the bulk materials (top-down) or builing up from atoms (bottom-up), as shown in Figure 1.2. [2, 4] The top-down technique is a simple way, assisted by mechanical force (milling process), heat, laser ablation (therma vaporisaton), sputtering (high-energy plasma ions). The transformation begins with the bulk material followed by breaking down toward nanosize. However, it is difficult to fabricate irregular-shaped and ultra-tiny nanomaterials using the top-down technique. In contrast, the bottom-up approach is the construction of nanomaterials from small atoms and molecules. This technique offers well-defined size, shape, and chemical composition. The bottom-up based approaches include chemical vapor deposition, hydrothermal, co-precipitation, sol-gel method.

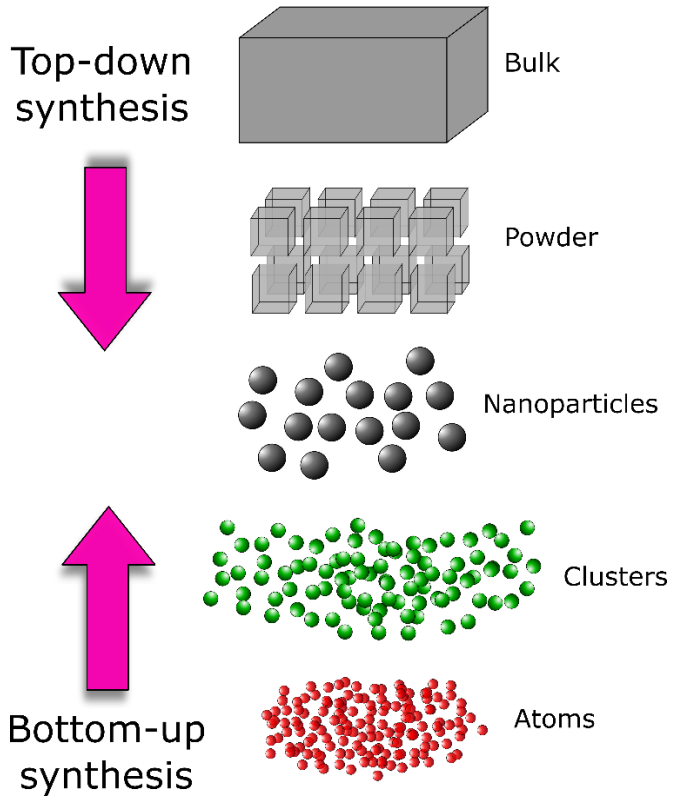

Figure 1.2 Concepts of nanomaterial production: top-down and bottom-up approaches.

1.1.3 Properties of nanomaterials

A key advantage of using nanomaterials is their large surface-to-volume ratio. When the dimensions are enough small, the chemical and physical properties are transformed compared to their corresponding bulk materials, due to the large fraction of surface atoms, high surface energy, special confinement, and reduction of imperfections. Physical and chemical reactivities are size- and compostite-dependent and are highly enhanced in nanomaterials.

1.1.3.1 Physical properties

For physical properties, the melting point of nanomaterials is typically lower than that of their bulk counterparts. [3, 6] The increase in surface reactivity promotes the oxidation of the surface layer, altering the surface composition and decreasing the phase transition temperature. Moreover, the reduction of impurities or defects and the increased crystal perfection at the facets contribute to the enhancement of mechanical properties in nanostructured materials. [3, 6] Nanomaterials contains smaller grains, which restrict the movement at grain boundaries and thereby increase the strength, hardness and abrasion resistance. Scaling down the size of magnetic materials to the nanoscale renders superparamagnetic behavoior. [3, 6] In general, large ferromagnetic materials have multiple domains that respond to the external magnetic field with size-dependent coercivity. Below a critical size, MNPs contain a single domain growth mechanism and exhibit superparamagnetism, providing a rapid response to the external magnetic field to fully magnetise with the least coercivity.

Peculiar optical properties are manifested in nanomaterials when their dimensions reach the nanoscale, resulting in a variation in colour expression that is size-dependent. At this point, conventional physics are no longer applicable. This well-known optical property is explained by the phenomena of quantum confinement and plasmonic effects. [3, 4] Approching the nanoscale leads to the occurrence of quantum confinement, which renders the energy levels discrete (Figure 1.3). Further size

decrease can widen the energy band gap, which subsequently changes the optical appearance and electrical properties of nanomaterials. In noble metal nanoparticles, they possess exceptional optical extinciton which is absent in bulk materials. Their size-dependent colour-changing ascribes to the intriguing optical phenomenon of the localised surface plasmon resonance (LSPR). The interaction with the light causes the confinement of electrons and subsequent oscillation at the resonance frequency, producing LSPR. It is considered the key fundamental in this thesis and will be explained later in section 1.4.

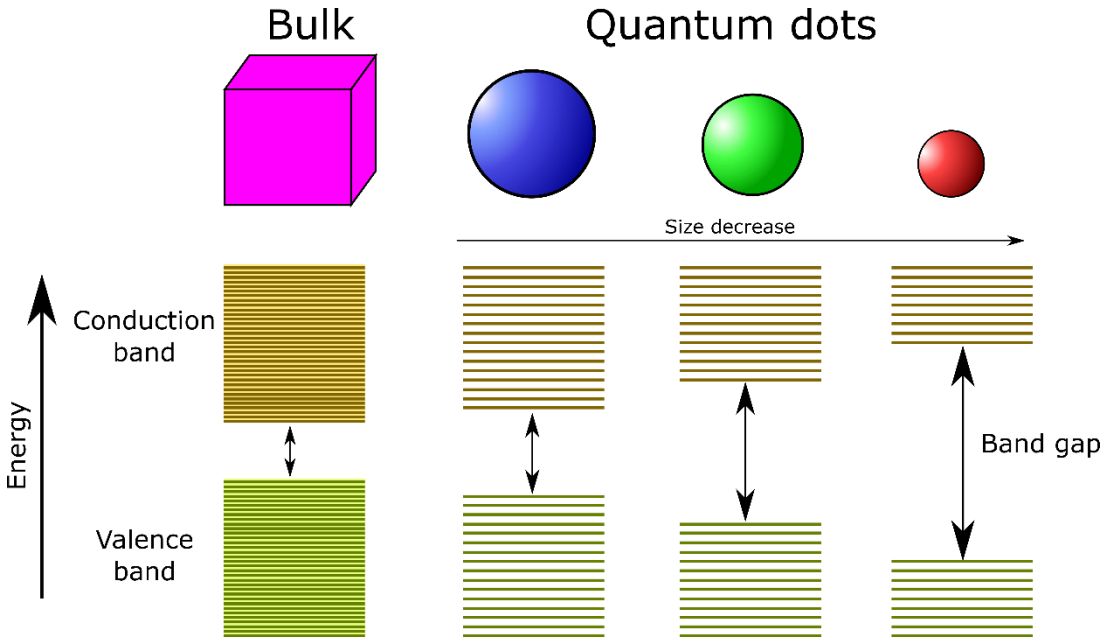

Figure 1.3 Schematic illustration of the quantum confinement of quantum dots. The variation of energy bands corresponds to the size of quantum dots.

1.1.3.2 Chemical properties

Speaking of the chemical properties, nanomaterials are more chemically reactive than their bulk form. [3] Decreasing the size exposes more surface area to the environment, which increases chemical interaction. The rate of chemical reaction exponentially increases with the size reduction due to the higher surface area of nanomaterials.

A number of chemical properties uniquely exist in nanomaterials. The surface energy of nanomaterials is size-dependent. [3, 6] Hence, smaller particles have better

solubility than larger ones. Reducing the size of a material breaks the surface bonds of atoms, which increases surface energy. This imbalance is mitigated by surface recontrution, chemisorption, phyiosorption, or agglomeration. Nanoparticles with small radii have high chemical reactivity, which promotes catalytical activity. Noble metal nanomaterials are excellent catalysts, while their bulk forms are inert and considered poor catalysers.

1.1.3.3 Toxicological properties

Despite numerous advantageous characteristics of nanomaterials, several studies have reported significant harm to humans and environment. Exposure to nanomaterials through skin absorption, medical injection, inhalation, and consumption, may result in toxicological effects, including cell growth inhibition and alteration. [7] Hence, understanding the toxicological mechanism of nanomaterials is essential for designing biocompatible materials.

Oxidative stress is a key determinant of the toxicity of nanomaterials when they interact with biological cells. Overproduction of reactive oxygen species (ROS) and resulting oxidative stress are the main causes of toxicity. [7-9] The dissolution of metal-based nanomaterials can induce oxidative stress by catalysing ROS production and the formation of radicals ($OOH^{\bullet}$ and $OH^{\bullet}$) from hydrogen peroxide.

To cause toxic effects, nanomaterials must invade the body and then the cell. Toxicity depends on the physicochemical factors of nanomaterials, such as dissolubility, chemical composition, size, shape, aggregation state, crystallinity, surface area, surface charge, and surface coating. [4, 7, 10-13] These factors influence the ability of nanomaterials to enter cells, transport through the body, and interact with biological components in living organisms. Because nanomaterials are relatively small size, they can penetrate biological barriers to accumulate inside cells, generate chemically harmful reaction of oxidative stress, induce apoptosis and inflammatory response, and cause cell and DNA damage, and permanent cell death.

Physical properties are important for promoting or discouraging interaction with biological cells. Their size, surface area, surface charge, and zeta potential affect

toxicity, as they determine how well nanomaterials can be taken up by and interact with biological components. [7, 8] Nanomaterials must cross the phospholipid membrane barrier, and the extent of nanomaterial interaction determines the intensity of toxicity. The electrical charage of the cellular membrane components can interact electrostatically with the countercharged nanomaterials. The longer the intereaction, the more likely nanomaterials are to internalize to the cell. With the proper size and surface charge, nanomaterials can enhance permeability to enter the cell and subsequently damage organelles. [11, 14] Cell uptake is dominated by electrostatic interactions, therefore, increasing surface charge results in higher toxicity of nanomaterials.

Morphology is also critical in determining toxicity of nanomaterials. Amorphous nanomateriasls are more toxic because their surface defects provide active sites that are capable of causing ROS. [14] Also, the toxicity is found to be shape-dependent. Li et al. investigated the toxicity of alumina nanoparticles and revealed that nanorods are significantly more toxic than nanoflakes and induced higher ROS accumulation, inflammation, and apoptosis. [15] Similarly, rod-shaped IONPs showed a higher degree of toxicity to mouse macrophages than spherical IONPs as they damaged membranes and induced ROS production to a greater extent. [16]

Particle size, concentration, and surface charge are among the most dominant factors that significantly influence the stability of nanomaterials. [8, 17] The molecules coated on the surface of nanomaterials are responsible for the degree of hydrophilicity, lipophilicity, or catalytical activity, which plays a crucial role in stability and interaction with membranes. It is also contradictorily reported that the shape-dependent toxicity is not always the case, but surface coating can be harmful to biological cell. For example, spherical gold nanoparticles are not toxic to human dermal cells, whereas gold nanorods (AuNRs) are extremely toxic because of the CTAB coating and aggregation.

Following internalisation into the cell, metal-based nanomaterials can dissolute and release metal ions, which can induce and accelerate cellular oxidative stress. [7, 9, 18, 19] This interrupts cell physiological processes, leading to DNA damage and cell

apoptosis. The presence of ROS at high concentrations causes oxidative stress to damage cells and alter protein modification and gene expression. The higher surface area of nanomaterials increases the reactive sites for chemical activity, thereby increasing and accelerating ROS production. [11, 16] Additionally, metal nanomaterials can indirecty provoke the generation of ROS. Metal ions are released into intracellular space and damage mitochondria and impair the electron transport chain, leading to cellular injuries and death. Intert nanomaterials, on the other hand, do not directly catalyze the production of ROS, but they can still induce ROS production under biological conditions.

Green synthesis has been developed to produce them in an eco-friendly way. Green synthesis is the production of nanomaterials from a broad range of biological products, such as chocolate, [20] bread, [21] honey, [22] and plant extracts. [23-26] These materials are abundant in nature and rich in organic compounds. Various types of nanoparticles have been produced by the green synthesis approach, including gold nanoparticles, [24, 27] silver nanoparticles, [25] carbon dots, [20, 21] and copper oxide nanoparticles. [26] This approach offers many advantages, such as cost-effectiveness, environmental friendliness, safe reagents, and non-toxicity, and has received great attention from reasearchers in recent years.

1.1.4 Nanotechnology applications

To date, due to versatility and tailorable properties, nanotechnology has been utilised in a broad range of applications, including but not limited to medical treatment, [28-30] biosensors, [31-33] food and agriculture, [34-37] energy storage, [38, 39] and sustainable environmental applications. [40, 41]

The opical properties of nanoparticles have been explored in cancer treatment by harnessing their photothermal effect. [28, 42, 43] Following accumulation at cancer cells in the body, heating with a laser can destroy the cancer cells. Furthermore, MNPs have also been utilised to kill cancer cells. MNPs are directed to the tumor and then an external magnetic field is applied to cause oscillation, which generates heat to

attack cancer cells, known as magnetic hyperthermia technique. [44, 45] The magnetic properties of MNPs also enable applications based on the magnetic separation technique which can be useful to purify and concentrate analytes in complex matrices. [46, 47] Nanomaterials with excellent catalytical activities and high active surface areas are of interest for the use in surface modification of electrodes to improve electrochemical analytical performance. [33, 48-51] Plasmonic nanomaterials are also used to develop simple colourimetric assays in many industries [52-55] and to replace traditional antimicrobial treatment. [56, 57]

Additionally, nanotechnoly plays a significant role in drug delivery for effective clinical treatment. [58, 59] Engineered delivery systems have also been applied in agriculture to improve fertilization and pesticide applications. [34, 60] Nano-based wearable devices for human use have recently been developed to monitor plants for early determination of volatile compounds associated with plant stress. [61] In the past decade, many studies have demonstrated the use of in vivo nanosensors for plant health monitoring. [62-65] Single-walled carbon nanotubes have intricsic fluorescent properties that can be tuned to the NIR region of the electromagnetic wavelength (850-1700 nm). Thus makes them ideal for embedding in living plants to monitor plant stress development. [62, 63, 66-68] The fluorescent signal of sigle-walled carbon nanotubes is highly beneficial because it provides strong signal intensity, high spatiotemporal resolution, ultra-low background signal, and it is not interfered by the autofluorescence of chlorophyl. [69, 70] Multiplex detection of plant stress hormones has recently been achieved using silver nanoshells to express surface-enhanced Raman scattering according to plant-released hormones. [71] These studies show advance of nanotechnology in plant health monitoring which could accelerate the development of precison farming technology.

Nanotechnology has been developed significantly but continues to evolve. Nanoscale robots, known as nanobots, are an emerging advanced technology that uses smart autonomuous robots with specific functions. Nanobots havepotential for many applications, such as heavy metal removal, [59] beverage processing, [72] and smart drug delivery. [73] However, nanobot are still in the early stages of development, and their toxicity is a significant concern. [74]

1.2 Dengue disease

1.2.1 General information

Dengue disease is a mosquito-borne viral illness caused by the infection of the dengue virus (DENV). It is transmitted by *Aedes aegypti* and *Aedes albopictus* mosquitoes, which live in warm and humid areas. [75, 76] Dengue fever is an endemic disease that is widespeard across tropical regions. [76-78] The number of DENV infections has increased significantly over the past two decades, with approximately 390 million cases of infection reported annually in the world, of which 75% are asymptomatic. [79] There are over 500,000 hospitalizations and 25,000 deaths associated with dengue infection every year. Recently, a dengue disease outbreak was found in the northern province of Thailand, Mae Hong Sorn, between 2019 and 2020, with 131,157 cases reported in 2019 and 70,000 cases reported in 2020. [80, 81] An effective early on-site diagnostic tool is essential for surveillance and containment of the disease in remote areas with limited resources and facilities.

DENV is in the *Flavivirus* genus which can be subdivided by antigenic structures into four serotypes: DENV1, DENV2, DENV3, and DENV4. [82] Of which, DENV2 is the most common and deadly serotype. [83] DENV infection can cause a range of symptoms, from mild dengue fever to life-threatening conditions inclduing dengue hemorrhagic fever (DHF) and dengue shock syndrome (DSS). [77, 84, 85]

In the early phase of infection, patients commonly experience acute flu-like symptoms in the first 4 -10 days after being bitten by a mosquito. Then, patients usually have clinical dynamic dengue-related symptoms with high temperature (up to 40 °C), fever, headache, malaise, joint and muscle pain, and vomiting. A rash typically appears 3-4 days after the onset of fever. Approximately 70%-80% of patients who earn positive clinical test results are asymptomatic. [79] However, the early phase of infection can be difficult to diagnose because the symptoms are similar to those of other flaviviruses, such as influenza, measles, Zika, chikungunya, yellow

fever, and malaria. [84] Therefore, an effective diagnostic tool is essential to provide fast, sensitive, and accurate result.

1.2.2 Dengue biomarkers

In primary dengue infection, there are only nonstructural protein 1 (NS1) and the virus itself which circulate in the body and increase over time (Figure 1.4). In this case, only two biomarkers are detectable after the fever onset. Immunoglobulin M (IgM) appears in the body 3-5 days after the fever onset and remains for several months at a high level. Immunoglobulin G (IgG) appears after day 6 of the fever onset. All biomarkers circulate in the sera until the end of the acute phase.

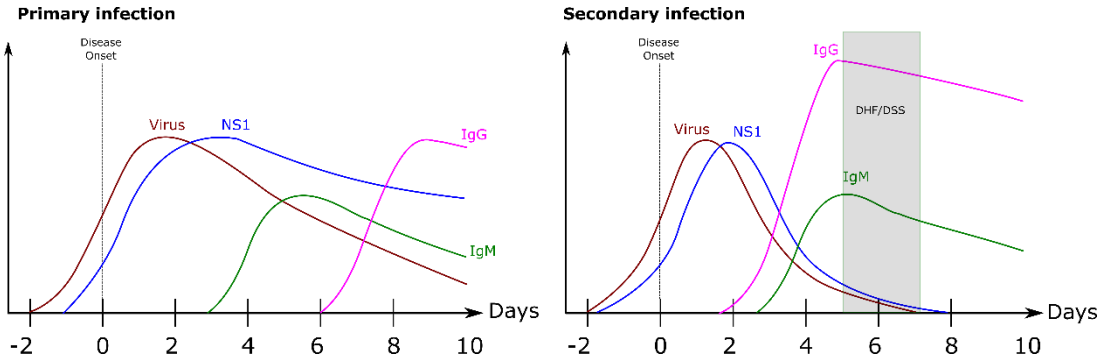

Figure 1.4 Development of dengue biomarkers at different stages in primary and secondary infections.

In the secondary dengue infection, the virus and NS1 are present for a shorter period of time than in primary infection due to a quicker immunological reaction responding to viral invasion. [84] Once IgG and IgM are present, the levels of virus and NS1 fall sharply. Most DHF and DSS patients have secondary infections, which occur when the number of viruses and NS1 decreases. Therefore, secondary infection tends to experience more severe symptoms than the primary infection.

After day 3, IgM level surges, followed by IgG level on day 6, due to the immunological response. However, in secondary infection, IgG appears at a very high level from day 3, showing a rapid anamnestic response to the NS1 protein. The level of NS1 is associated with viremia level in plasma and correlates with the severity of

the disease. [77, 84, 85] Patients with high levels of NS1 and viremia are more likely to develop severe DHF. NS1 level above 600 ng/mL in secondary infections within the first three days is an indicator of the progression to severe symptoms. [85] Secondary infections usually result in the development of antibodies that protect themselves from that particular serotype. [84] Hence, NS1 is only detectable in the first few days of infection, in contrast to primary infection. Overall, NS1 is the most suitble surrogate marker for the early detection of dengue disease.

1.2.3 Determination of dengue virus

Currently, clinicians identify DENV infection using virological and serological assays to detect the presence of viral components or viral proteins (secreted NS1 proteins) and immunogenic substances that are built against viral infection. [78, 84, 86, 87] Several types of biomarkers circulate in dengue patients, such as the virus itself, NS1 proteins, and IgM and IgG antibodies. However, each biomarker reaches its peak level at a different stage of disease development in primary and secondary infection, as shown in Figure 1.4.

Like other flaviviruses, DENV contains three encoded single-stranded RNA structures and seven nonstructural proteins. [84] Traditionally, DENV is isolated from patient serum and cultured in cell lines, which provides highly accurate results. However, this method is less effective and more difficult in secondary infection because the prompt reaction of anamnestic antibodies quickly eliminates the viruses. Additionally, it is time-consuming, requiring up to two weeks to obtain results. [84] Hence, the virus isolation method is recently replaced by other rapid tests.

The PCR-based method has substituted the conventional virus isolation method due to its efficiency, sensitivity, and lower cost, with results available within a day. The genomic nucleic acid of DENV is sought from human serum using reverse transcription polymerase chain reaction (RT-PCR). [77] Although the method is highly specific, selective, and sensitive DENV detection, it requires laboratory facilities,

specialized training, and expensive chemical reagents, making it impractical for the use in remote areas.

Due to deficiency in sensitivity of early NS1 detection in patients with secondary infection, other biological products, such as IgM and IgG antibodies produced against DENV, can be detected using ELISA kits. [77, 86] However, ELISA kits may suffer from cross-reactivity with antibodies to other flaviviruses, such as the Zika virus and yellow fever, due to their similar antigenic structure. [84] Hence, the detection of IgM and IgG antibodies should be confirmed by NS1 detection assays.

NS1 protein is an ideal dengue biomarker. It is released from infected cells and circulates in infected patients at high level ranging from ng/mL to µg/mL, and is detectable after fever onset. [84] In primary infection, it can be detected at the same time as viral RNA. Dipstick-based assays and ELISA are deployed clinically to determine NS1 proteins. [86, 88] LFA is a highly specific and sensitive tool for determining NS1, with no-cross reactivity with other flavivirus NS1 proteins. Nonetheless, the sensitivity of LFA is a drawback, especially in secondary dengue infections, as pre-existing antibodies can interfere with the binding of NS1 antigens to the test strip. Therefore, the NS1 test kit may not be sufficient for the use in countries where multiple DENV serotypes are prevalent. NS1 test results are often confirmed with RT-PCR or virus isolation. [88] It is important to determine the number of biomarkers in patients to assess the severity of the disease and predict its progression. Therefore, there is a need to quantify NS1 levels to predict the current state of the disease and its possible progression. However, all commercial NS1 test kits currently only provide qualitative results. The examples of various rapid tests for detecting DENV are shown in Table 1.1.

Table 1.1 Comparion of different rapid detection methods of DENV.

Methods	Targets	Matrix	LOD	Non-cross-reactivity	Ref.
RT-PCR	RNAs of DENV1-DENV4	Plasma	10 virals copies/mL for DENV1 100 virals copies/mL for DENV2 and DENV3 1000 virals copies/mL for DENV4	West Nile virus and yellowfever virus	[89]
Electrochemical sensor	DENV2-NS1	Serum	0.33 ng/mL	-	[90]
Molecular imprinted polymer-based impedimetric sensor	DENV-NS1	Serum	0.3 ng/mL	-	[91]
Microfluidic chip assisted by magnetic beads	DENV2	Serum	10^2 pfu/mL	-	[92]
Microfluidic dielectrophoresis chip	DENV2	-	10^4 pfu/mL	-	[93]
Microfluidic paper-based analytical device	DENV-NS1	Serum	74.8 ng/mL	Japanese encephalitis virus, and Zika virus.	[94]
LFA	RNA of DENV1	Serum	1.2 * 10^4 plaque forming units per mL	Chikungunya and zika viruses	[95]
LFA	DENV1-NS1, DENV2-NS1	Serum	4.9 ng/mL	DENV2-NS1, dengue IgG, Malaria parasite plasmodium vivax	[96]
LFA	DENV-NS1	Serum	DENV1-NS1 and DENV3-NS1 for 0.25 ng/mL, 0.1 ng/mL for DENV2-NS1, 1 ng/mL for DENV4-NS1	Zika NS1, Hepatitis B virus, Hepatitis C virus, and Japanese encephalitis virus	[97]

1.3 *Salmonella typhimurium*

1.3.1 General information

Salmonella spp. are gram-negative bacteria in the group of *Enterobacteriaceae*. [98] There are more than 2500 serotypes that can cause salmonellosis diseases in humans and animals. [98, 99] In terms of morphology, they are rod-shaped microbes with a length of 2-5 µm and a width of 0.5-1.5 µm. [100] In serology, motile H (peritrichous flagellar) and O (somatic) antigens are the identities of *Salmonella* spp. [100, 101]

Figure 1.5 shows the classification diagram of the *Salmonella* genus, which is divided into two species: *Salmonella Enterica* and *Salmonella Bongori*, of which *Salmonella Enterica* is clinically relevant to human disease. [99, 102] *Salmonella Enterica* consists

of 6 subspecies, based on their biochemical and genomic characteristics: *enterica, salamae, arizonae, diarizonae, houtenae,* and *indica*. [100, 101] *Salmonella Enterica* subsp.I is the major cause of food poisoning contributing to approximately 99% of salmonellosis cases in humans and warm-blooded animals. Other subspecies are rarely found in humans, but prevalent in the environment and cold-blood creatures. [101]

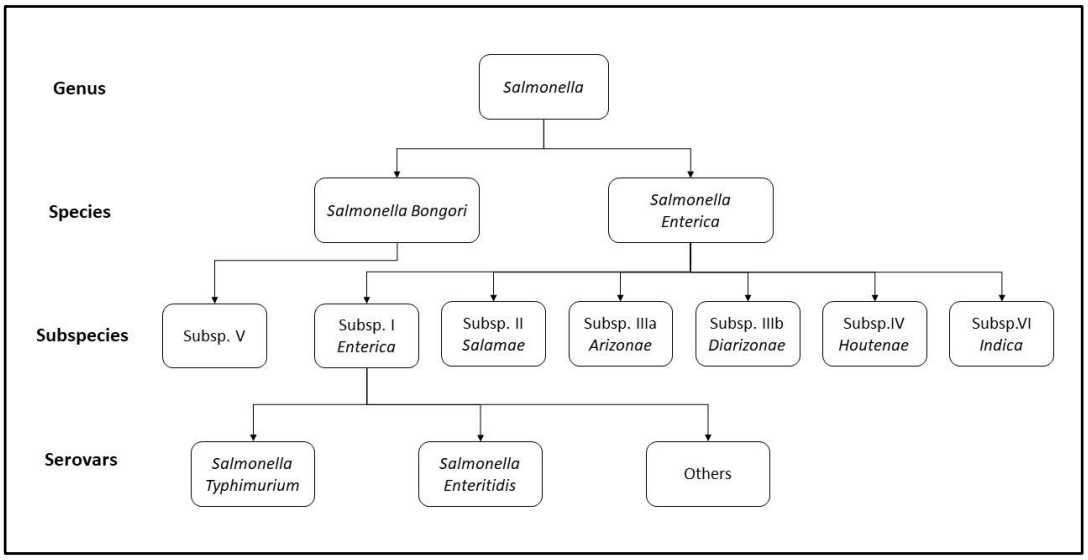

Figure 1.5 Classification of *Salmonella* genus

1.3.2 Impact of *Salmonella* spp. outbreak

The outbreak of foodborne pathogens is a major public health concern. Contamination can occur at any stage of food production, and failing prevention can lead to huge economic losses and negative impacts on public health. *Salmonella* spp. also causes the largest number of deaths and hospitalizations led by foodborne disease in the US. [103, 104] An estimated 9.4 million cases of foodborne illness in the US annually, of which 55,961 patients are hospitalized and 1,351 patients die, respectively.

Food poisoning contributes to the economic burden by increasing government spending. Outbreaks lead both direct and indirect costs associated with halting the spread of foodborne bacteria and mitigating health-related costs, such as

hospitalization, medication, and transportation. [105] Foodborne pathogens can contaminate food and agricultural products, such as plants, [106, 107] animal products [100, 108], and fodder [109] There were 8,914 cases of food incidents and recalls worldwide from 2008 to 2018. [110] In Canada, there were 19 outbreaks and 635 cases of *Salmonella*-contaminated frozen chicken between 2015 and 2019. [108] Products were recalled 13 times out of 19 outbreaks. The highest levels of contamination are reportedly found in meat and poultry products. Annually, $90 billion is spent to handle the outbreaks of foodborne pathogens, of which $20.3 billion is lost to meat and poultry products. [111] The costs of prevention are relatively cheaper than the costs associated with dealing with foodborne pathogen outbreaks. Therefore, regular monitoring of pathogen contamination is essential to avoid the economic burden.

1.3.3 Detection of *Salmonella* spp.

Food contamination has negative impacts on the economy and public health. *Salmonella typhimurium*, one of the main causes of food poisoning in humans and animals, can start colonizing in the gastrointestinal tract and causing infection with as low as 10 cells. [98, 99] Early identification of contamination is essential to prevent the outbreak of *Salmonella typhimurium*. The sensitivity of detection is critically important, but can be more challenging in the complex food matrix. [98] Ideally, *Salmonella* detection methods should be capable of detecting a single CFU in a sample, but the analytical process may need to be adjusted depending on the length of cell enrichment to reach the minimal bacterial concentration required for a particular assay. [112]

Food safety has been standardized to establish international and domestic rules for controlling and monitoring food and agricultural products for foodborne pathogens. Food industries must comply with these standards to ensure the safety of consumers. ISO 6579:2002 and Regulation (EC) No 2160/2003 are international standards providing guidelines and necessary information for detecting *Salmonella* contamination in food. [112, 113] They describe the criteria and details for characterizing food samples for *Salmonella* detection, such as sampling, equipment,

procedures, and sample storage, to assure consistent results and comparisons between laboratories. To be shelved in the market, a 25 g of food product must be free of *Salmonella*. [114]

Many emerging advanced technologies are applied to the field of food safety to accelerate, simplify, and improve the sensitivity, throughput, compact storage, and cost-effectiveness of *Salmonella* spp. detection in food and beverage products. In general, rapid detection approaches can detect 10^4 CFU/mL of bacteria in samples within an hour to a day. [112]

1.3.3.1 Bacteria culture

Traditional bacterial culture is currently the gold standard for confirming the presence of *Salmonella spp.* in the food matrix. [112, 115] This method involves the specific amplification of *Salmonella* spp. from food samples. First, 25 g of solid samples or 25 mL for liquid samples are processed in non-selective pre-enrichment to increase the number of bacteria. Then, selective enrichment is used to specifically grow the bacteria of interest, *Salmonella* spp., while inhibiting the growth of other bacteria in the samples. [115] If suspected *Salmonella* colonies are observed on the plate, they are screened and confirmed by biochemical and serological identification. [112] This is a powerful assay that can detect *Salmonella* spp. as low as 1 CFU per sample. [98] Despite that, it is time-consuming and requires specialists and laboratories to operate. The entire process may take up to 5 days, due to the length of the cell enrichment step. In some cases, such as vegetables with a short shelf life, bacteria culture assay is not suitable.

1.3.3.2 Immunoassays

Immunoassays use bioreceptors, such as antibodies and aptamers, to detect antigenic structures of *Salmonella*. ELISA is the most common immunoassay for identifying *Salmonella* antigens. [116, 117] In principle, two antibodies are involved in the detection. One of the antibodies is coated on a solid plate, while the other one is tagged with enzymes and binds to *Salmonella*. They form an antigen-antibody complex in a sandwich-like format. The concentration of *Salmonella* can be optically

measured after enzymatic cleavage by a substrate. Additionally, ELISA can also detect the antibody produced in response to *Salmonella* by using antigens coupled to a solid surface. ELISA can detect as low as 1.25 x 10^6 CFU/mL of *Salmonella typhimurium* from spiked milk, but cross-reactivity with *Salmonella paratyphi* B was observed. [116]. Another study demonstrated the identification of 5 x 10^4 CFU/mL of *Salmonella typhimurium* from artificially spiked meat after 24 h of pre-enrichmen. [117]

In addition to ELISA, an agglutination technique using latex beads and an immunoassay using gold nanoparticles have been deployed to detect *Salmonella*. [118, 119] For the agglutination technique, bioreceptors are immobilised on the surface of latex beads and interact with *Salmonella* to form aggregation and precipitation, which can be observed by the naked eye. For the immunoassay, gold nanoparticles are used as a detector. The binding between the gold nanoparticles and *Salmonella typhimurium* leads to the aggregation of the particles, which induces a colour change on the gold solution due to its unique plasmonic property. The study acheived a detection limit of 10 CFU/mL of *Salmonella typhimurium* in spiked milk and shrimp. Moreover, quantification can be achieved with the assistance of an optical reader such as an ultraviolet-visible (UV-Vis) spectrometer, making these techniques more suitable for sensitive detection.

Paper-based dipstick assays are a user-friendly, commercially available, and low-cost methods that provide rapid results. They are sued to screen multiple samples for *Salmonella* detection due to their high throughput. [112] In this assay, *Salmonella* are captured by immobilised bioreceptors on the dipstick, providing colourimetric results to users. However, a selective enrichment step is required to provide a sufficient level of bacteria to reach the detection level. Immunomagnetic separation can be used to concentrate *Salmonella* in the sample. This is an immune-based detection that purifies and concentrates the analytes of interest, leading to a shorter cell enrichment step and improvement in the sensitivity of detection. [112] Fang *et al*. showed that the combination of magnetic immunoseparation, DNA amplification, and LFA could detect *Salmonella* as low as 10^1 CFU/mL from a sample. [120] Another study demonstrated that magnetic separation technique can enhance the analytical

performance of the LFA. [121] Their method can dectec *Salmonella enteritidis* at 10^2-10^3 CFU/mL in spiked pork, milk, and watermelon juice.

Although the immunoassays are versatile, sensitive and specific, they have the drawbacks of cross-reacting with closely related antigenic structures and reduced sensitivity in complex sample matrices.

1.3.3.3 Nucleic acid-based assays

The determination of the nucleic acid of the pathogen is another preferred method for food analysis due to its sensitivity, specificity, and reliability. [112] Nucleic-based approaches has advantages over immunoassays, including higher sensitivity and specificity. [112] Moreover, nucleic-based methods can detect *Salmonella* contamination without cross-reaction.

PCR is a DNA amplification process that can detect very low number of DNA molecules by exponentially reproducing DNA from a single molecule to millions within a few hours. [112, 122] An enrichment step may be necessary to increase the number to pathogens to reach a critical amount of analytes for a reliable result, but PCR can shorten the length of the enrichment step. [122] Nonetheless, PCR accessibility is limited by its high cost of reagents and the requirement for specialists and a laboratory.

In addition to PCR, DNA probes can be utilised to form hybridization with complementary DNA sequences of the target pathogen. [112] The target organism is lysed to release DNA fragments, which are then purified in the preparation step. This is followed by hybridization and elution of unbound nucleic acids. The remaining DNAs are bound strongly and form hybrids with labeled DNAs to express detectable signals. However, DNA probe hybridization assays may require a pre-enrichment step or nucleic acid amplification to achieve sufficient *Salmonella* concentration.

1.3.3.4 Miniaturized biochemical assay

This approach is a mini-version of a biochemical assay requiring small volumes of reagents to rapidly identify *Salmonella*. [112] Each sample is inoculated into bacteria

culture and added to a microtiter plate containing a variety of media. The presence of *Salmonella* is indicated by a colour change. Smaller volume requires lees reagets to proceed the reaction. It has a shorter diffusion time which improves the rate of mass transfer between reagents and analytes. Due to higher surface-to-volume ration, the miniaturized biochemical assays increase the rate of binding between ragents and analytes. Therefore, this method allows quicker characterization of bacteria contamination than conventional biochemical assays. The test has high accuracy, an unsophisticated procedure, and is amenable to automation. This colourimetry assay also offers a high throughput, making it ideal for screening a massive number of samples, especially during food emergencies.

1.3.3.5 Biosensors

Biosensors utilise biological elements, such as antibodies, aptamers, nucleic acids, and enzymes, as transducers to monitor physiochemical changes. [112] When the biosensor detects the biomarker of *Salmonella*, it generates a measurable signal, such as an optical, thermal, chemical, and electrical signal. The physiological change in the presence of *Salmonella* induces a catalytic reaction of the enzyme in the biosensor system, which releases by-products that can be detected. Oh *et al.* demonstrated an LSPR chip using aptamers and AuNSPs to detect *Salmonella typhimurium*. [123] This optical biosensing method can detect *Salmonella typhimurium* at 10^4 CFU/mL.

1.4 Lateral flow assays

1.4.1 General information

The LFA is a dipstick-based method that is an attractive technology for users to receive rapid detection results. LFA is a simple-to-use detection assay for identifying the target of interest in a sample matrix. Nanoparticles are generally used as a label in LFA because they own many outstanding characteristics over common dyes. [124]

For example, gold nanoparticles offer strong visualisation because of their high extinction coefficient, and their colour does not degrade over time.

The analysis of LFA previously provided only a qualitative outcome: a positive or negative result. However, since the paper-based technique has gained attention and been widely adopted, many techniques have been developed to quantify the LFA signal and expand the utilities of LFA. Nowadays, in addition to a qualitative result, the LFA can present the result in the form of semi-quantification (without the need for an additional device to interprete the result) [125, 126] and a quantitative result (with an extra reader). [127-129]

Conventionally, the LFA strip comprises four major components: a sample pad, a conjugate pad, a detection pad (nitrocellulose membrane), and a wicking pad (Figure 1.6). [130] In principle, the operation is based on the automated migration of the liquid sample by capillary force. An aqueous sample is dropped onto the sample pad, where the flow begins. Analytical substances are dragged to the conjugate release pad, where they interact with bioreceptors to form antigen-nanoparticle complexes. These complexes then moved further to the detection pad and react with immobilised receptors on the nitrocellulose membrane, generating a single or double visible line, indicating a negative or positive result, respectively. In the detection zone, a control line represents the validation of the test result. It indicates whether the strip is kept in proper condition, implying the conjugates and capture antibodies on the membrane are in good condition. The complexes of analytes and conjugates are captured by the antibodies on the test line. If the test line appears, it indicates the presence of the targeted analytes in the sample. Eventually, the rest of the substances that are not captured by those bioreceptors on the membrane terminate at the wicking pad.

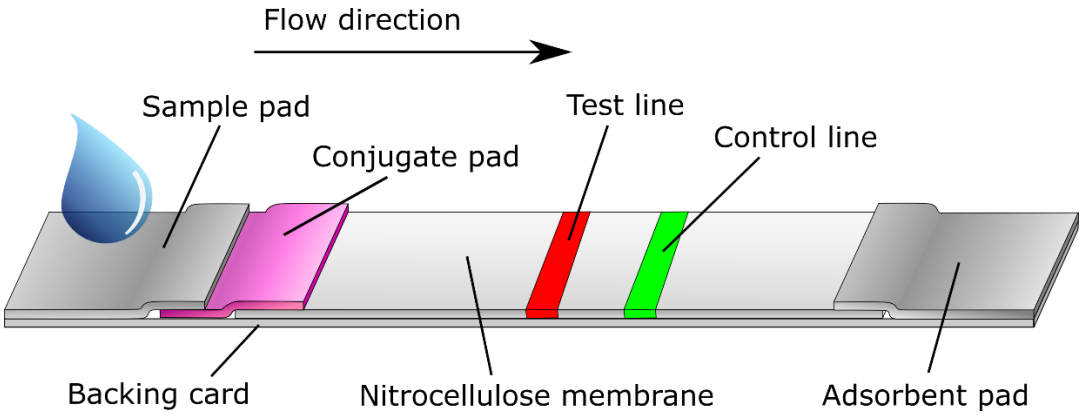

Figure 1.6 The general structure of LFA comprising a sample pad, conjugate release pad, detection pad, and adsorbent pad (wicking pad). Test and control lines are printed on the detection pad. All components are adhered to a backing card.

1.4.1.1 Sample pad

In the LFA strip, the sample pad is mounted at one end of the strip as the entry point to direct the sample to the conjugate pad. This is a crucial component of the strip to ensure homogenous fluid flow and reproducibility of the test. The sample pad can be pre-treated with a variety of reagents, such as buffer salts, surfactants, blocking agents, and other substances, to modify the condition for biological interaction to maximise the test result. [124, 130] The addition of such reagents provides the appropriate pH, ionic strength, and reduces non-specific binding. Pre-treatment of a sample pad can be simply carried out by immersing the sample pad into the treatment buffer and then leaving it to dry. Detergents, such as SDS, Tween 20, and Triton, are generally involved in LFA operation to reduce a non-specific binding event by eliminating weak ionic and hydrophobic bonds. They also promote the flow of conjugate particles and analytes. The sample pad can also be used as a filter to remove impurities from the sample.

1.4.1.2 Conjugate release pad

After introducing the liquid sample to the sample pad, it continues the capillary migration to the conjugate pad where the detection labels locate. The conjugate pad takes a role to maintain the stability and functionality of the conjugate particles until use. In general, a protein preservative, *i.e.* sucrose, is added to keep the function of

bioreceptors and facilitate re-solubility of the detection labels. [124, 130] Sugar molecules protect dry proteins by replacing the water around the proteins with their hydroxyl groups to form a sugar layer. This phenomenon can stabilise the biological structure in a dry condition. The sugar layer is dissolved quickly upon re-wetting and leads the detection particles into the flow to completely release them from the pad. It is essential to ensure minimal non-specific binding in the conjugate pad to minimise the retention of the detection particles and analytes of interest in the conjugate pad.

1.4.1.3 Detection pad

The detection pad is the location on the strip where bioreceptors are non-covalently immobilized. [124, 130] It is generally made of a nitrocellulose membrane, which is designed to promote the absorption and immobilisation of proteins through electrostatic and hydrophobic interactions. This ensures that the proteins are fixed and do not migrate with the fluid stream after striping.

The membrane is a crucial component of the assay, as its properties correspond to the sensitivity of the detection. It is a porous substrate that controls the capillary flow rate, which is defined by the time it takes for the fluid to completely fills the pores. The pore size can be varied from 0.05 to 12 µm, which affects the flow rate. The nitrocellulose membrane is typically represented in terms of capillary flow time, which us the period of time (sec) that the fluid travels for 4 cm. [124] The capillary flow time is indeed inversely proportional to the flow rate (cm/sec). A larger the pore size results in a faster fluid flow, which reduces sensitivity by shortening the interaction time. Conversely, a smaller pore size results in a slower fluid flow, which increases sensitivity but also increases the chance of non-specific binding. Alcohol, such as methanol, ethanol, and isopropanol, may be included in the immobilisation buffer to increase the evaporation rate during membrane striping, which improves the immobilisation of the proteins.

1.4.1.4 Wicking pad

The destination of the fluid flow is the wicking pad, also known as an absorbent pad. It can be considered as a wasting area where any unreacted substances terminate.

The dimension of the wicking pad contributes to the total volume of the sample that can participate in the test. [124, 130] This part of the strip draws the fluid along the strip and is relevant to the sensitivity of detection. Without the wicking pad, only a partial number of detection particles approach the end of the strip, accumulating on the strip and thereby generating background noise. Hence, this pad is essential to ensure that all substances flow through the entire strip.

1.4.2 Nanoparticle conjugation

In LFA application, nanoparticles are often used as transducers to generate detectable signals. Because nanoparticles are versatile and easily modified, their utilities can be expanded. Recognition biomolecules, such as antibodies [131-135] and aptamers, [123, 136-139] can be immobilised on the surface of nanoparticles to provide binding sites for targeted molecules. This enables the capture of specific substances.

Antibodies are prevalent in nature and have been widely integrated with nanoparticles for biosensing applications because they are biocompatible and have high capture affinity. [131, 140-142] Antibodies are generally assembled from four subunits to form an asymmetric Y-shape fragment. The body fragment of the antibody is called the Fc region and the other parts are called the Fab regions. The binding sites of the antibody are found in the Fab fragments and possess binding capability toward specific biological targets. [131, 140-142]. However, antibodies are expensive to produce and vary from batch-to-batch.

Reserachers have explored an aptamer which is a synthetic version of the antibody. It is composed of a short single-stranded DNA or RNA oligonucleotide that folds into a three-dimensional structure to firmly attach to the recognition site of a specific target (Figure 1.7). [143, 144] Aptamers have gained great attention from scientists because of their superior characteristics, such as excellent binding affinity, tolerance in harsh environments, inexpensive cost of production, mass production, and low batch-to-batch variation. [144]

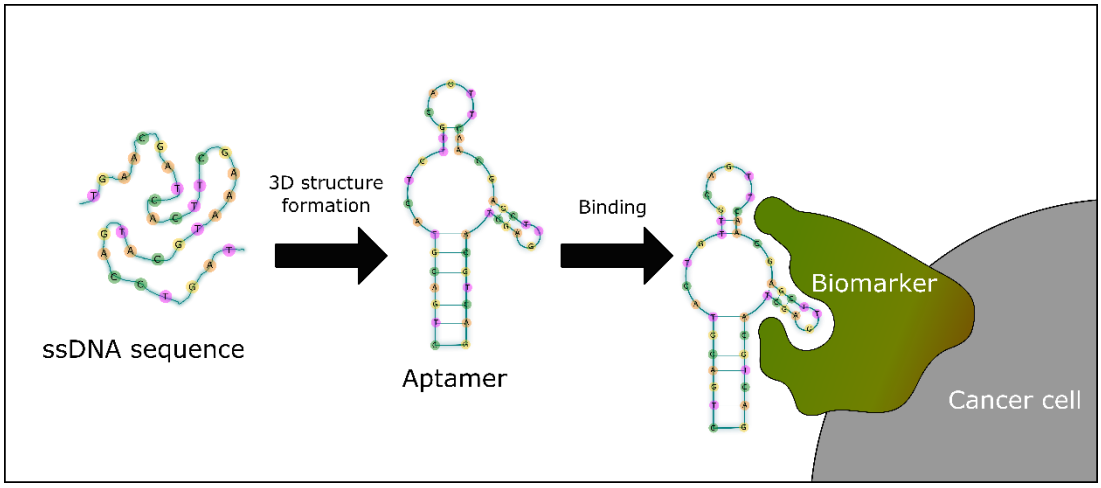

Figure 1.7 Diagram of a functional aptamer to bind a biological target. A short single-strand oligonucleotide (aptamer sequence) is folded into a three-dimensional structure, fitting to the binding site of the cancer biomarker. IOP is the abbreviation of initial oligonucleotide pool.

The aptamer is fabricated by the engineering loop process called "systematic evolution of ligands by exponential enrichment or SELEX" (Figure 1.8). [143] In SELEX, the antigens of interest are loaded into an "initial oligonucleotide pool", which contains random sequences of oligonucleotides. The antigens are then incubated with the library of oligonucleotides. The conditions of the incubation, such as pH and buffer, can be adjusted to meet the requirements of a particular application. Then, unbound oligonucleotides are removed from the pool and the bound ones are eluted from the targeted molecules. The remaining oligonucleotides being specific to the targets are amplified in the enrichment process and subsequently re-incubated with the antigens. The selection loop is repeated for 5-15 rounds to find the sequence of the oligonucleotide that provides the highest binding affinity to the target. Eventually, the selected sequence of nucleic acid is amplified and known as the aptamer.

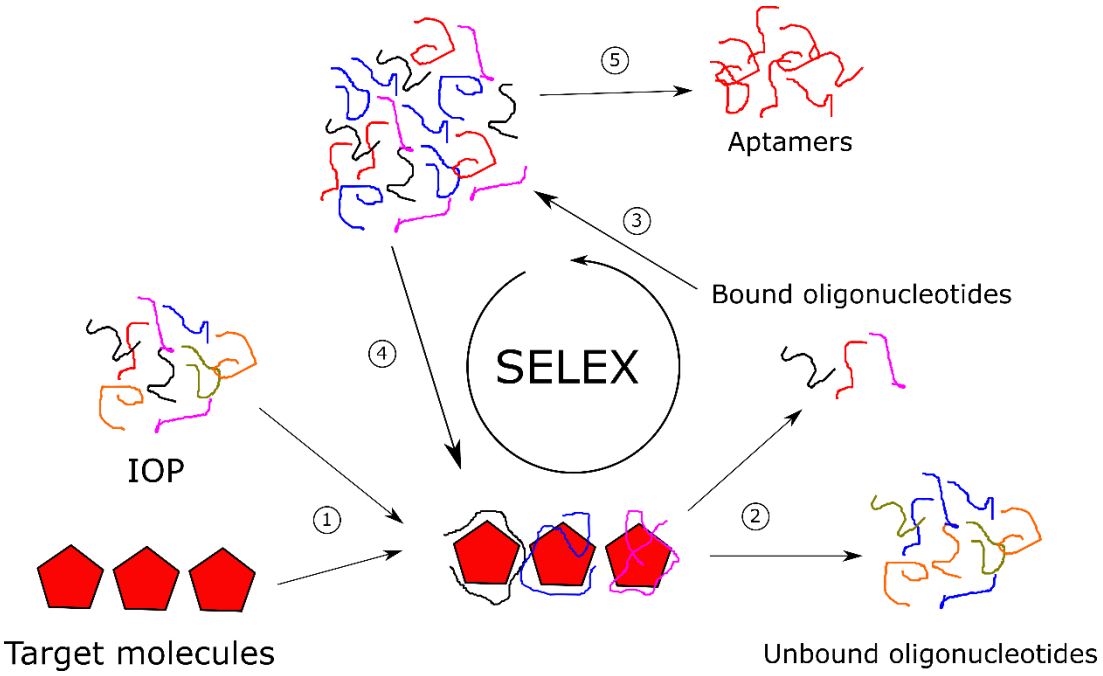

Figure 1.8 Diagram showing the SELEX process to produce high-affinity aptamers. SELEX stands for systematic evolution of ligands by exponential enrichment.

The anchoring of biorecognition molucules to nanoparticles can be achieved by many methods. Physical absorption is the most simple and widely used technique in immunoassays. [135, 145, 146] In physical absorption, the biomolecuels are absorbed on the surface of nanoparticles through electrostatic and hydrophobic interactions. However, physical absorption is susceptible to harsh environment such as high ionic strength solutions or the pH changes. Additionally, the orientation of the biomolecules is difficult to control, and some of the Fab fragments may face toward the nanoparticles surface, then the reduction of the capture efficiency.

Covalent bonding is one of the most common and preferred techniques for immobilising biomolecules to nanoparticles due to its robustness and reproducibility. [132, 135, 141, 147, 148] Covalent linkage is tremendously strong, allowing the conjugated molecules to withstand high-electrolyte environments. Carbodiimide, 1-ethyl-3-(3-dimethylaminopropyl) carbodiimide hydrochloride (EDC) is a zero-crosslinker commonly used in a covalent coupling assay, often in conjunction with *N*-hydroxysuccinimide (NHS) or sulfo-N-hydroxysuccinimide (sulfo-NHS). [134, 135, 140, 147] This coupling technique is known as the “EDC/NHS” or “EDC/sulfo-NHS” method. The schematic of the carbodiimide reaction is displayed in Figure 1.9. EDC activates the

carboxylic group, converting it into a reactive O-acylisourea intermediate ester. However, the active ester is not stable and degrades over time. The succinimide ester may be added to stabilise the active intermediate ester. A molecule containing a primary amine then interactas and replaces the intermediate ester, forming an amide bond.

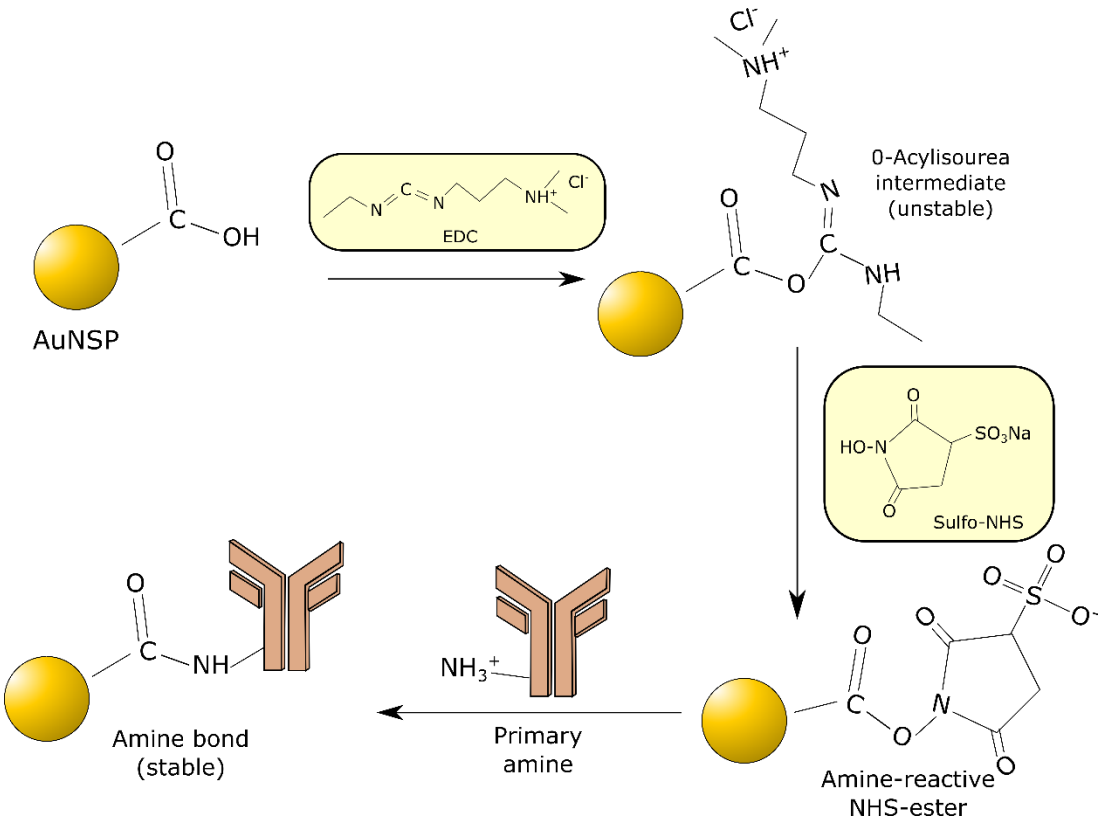

Figure 1.9 The scheme of antibody functionalisation on AuNSP using EDC coupling reaction with the addition of NHS.

Nonetheless, inapproporiated conjugation conditions can lead to decrease binding efficiency because of the random and non-uniform orientation of the biorecognition molecules. [140, 141, 146, 147] Many techniques have been demonstrated in the literature to direct antibodies to the surface of nanoparticles to form a uniform alignment. Intermediate proteins, *i.e.* biotin and avidin, protein A, and protein G, can be combined with the conjugation assay to induce the Fc fragments to attach to the nanoparticles while preserving the binding activity of the antibody. [46, 133, 147] Other methods have also been presented in previous studies to keep the Fab fragments of

the antibody exposed to the environment, such as pH adjustment, [142] deploying carbohydrate moiety of the antibody, [131, 134] and thiolation via disulfide bond. [149]

1.4.3 Sensitivity enhancement techniques

Despite its numerous advantages, *e.g.* simplicity, fast response, low cost, and ease of use, the utility of the LFA is often limited by its sensitivity of detection. Naked-eye readout is the most common interpretation method for colourimetric LFAs, but it is often restricted by the sensitivity of detection because the particles are buried under the surface of the membrane, hinderring light scattering (Figure 1.10). [150-153] In this regime, the incident light interacts with the nitrocellulose membrane and the embedded AuNSPs. Light passes through the pores and is scattered by the nitrocellulose membrane and AuNSPs, with some of the light transmitting through the membrane.

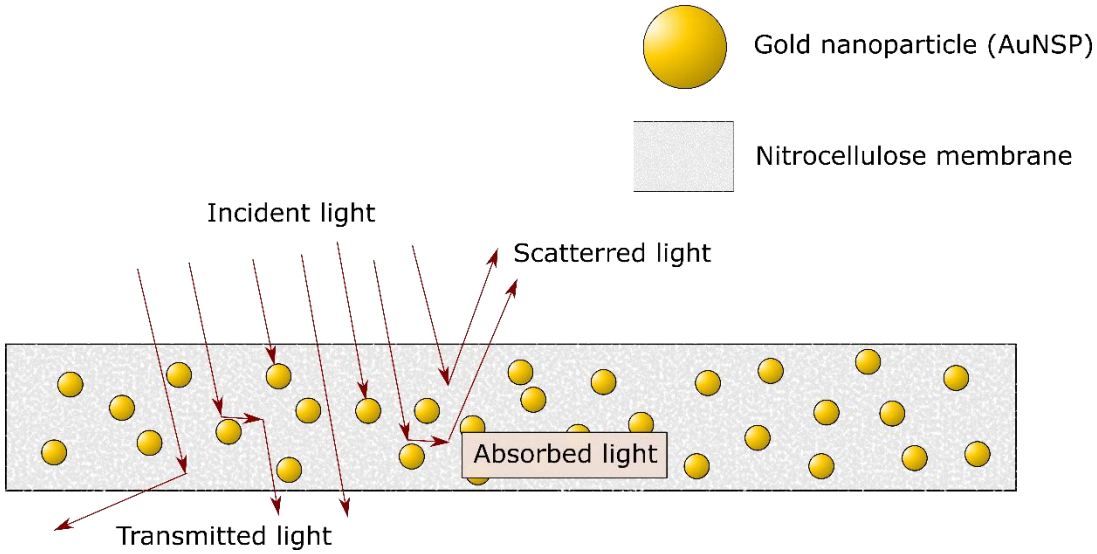

Figure 1.10 Scattering and absorption of incident light by the nitrocellulose and AuNSPs.

The colour of the result bands on the LFA strip is contributed by the AuNSPs that are embedded within 10 µm of the surface. [152] In physics, an object scatters the incident light to an eye or an optical detector, allowing the image to be recognized. Similarly, in the LFA, light is scattered by the particles and reflected to the eye, resulting in the observation of a colour band. However, light interacting with particles embedded

deeper than 10 µm is unlikely to reflect to the detector and thus cannot be observed. This results in a partial loss of the LFA singal, reducing sensitivity. Optical and non-optical techniques have emerged to enhance the analytical performance of the LFA in response to this limitation.

1.4.3.1 Optical measurement

Optical-based techniques provide colourimetric or fluorescent signals. These methods improve the optical extinction of the labels, generate fluorescence, or deploy additional reader devices to retrieve the hidden visual signal of the embedded labels.

Xu *et al*. demonstrated the use of large optical extinction nanomaterials as LFA labels. They fabricated long silica nanorods (3.4-7.0 µm in length) and decorated them with small AuNSPs. [154] This colourimetric assay improved the LOD by 50-fold. Several studies have shown that increasing the optical extinction of the labels by inducing aggregation on the LFA strip can improve sensitivity. Choi *et al.* developed the dual-gold conjugate technique using two different sizes of AuNSPs in their assay. [155] Primary gold conjugates captured the antigens of interest to form gold-antigen complexes. Subsequently, the secondary gold conjugates bond to the complex to form aggregation, which enahnced the optical extinction. As a result, the visualization of the colour bands on the strip was augmented. They found that the sensitivity was increase by 100-fold compared to the conventional method. Another study demonstrated the development of the dual-gold LFA for the detection of bacteria and achieved 100-fold sensitivity enhancement. [156] The other studies have shown that blocking the pores of the membrane due to aggregation can also improve optical extinction. [126, 157-160] Cluster formation between the nanoparticles and the targets leads to size enlargement, which traps them in the membrane pores during the capillary migration. This causes the accumulation of the nanoparticles on the membrane, which considerably magnifies the observal signal.

Moreover, the visibility of the LFA result can be enhanced by chemical catalytic activity, which creates an extra layer on the surface of the original labels. Recent

research has fabricated a catalyst-based LFA by inducing the catalysis of platinum core-shell nanoparticles to amplify the signal. [161] This platform shows high sensitivity towards HIV in the sample, allowing detection at the pico-scale. Many studies have demonstrated the deposition of silver on the surface of AuNSPs by either adding silver salt or immersing the strip into silver solution. [162-164] The gold surface catalyses the reduction of silver salt to activate the generation of a silver coating layer. In agriculture, the silver staining technique is applied to LFAs to determine the contamination of crop products. [162, 163] The silver enhancement solution was added to the strip after the completion of conjugate migration. The formation of a silver layer caused a significant improvement in sensitivity of detection. It can be assumed that the sensitivity enhancement is contributed by the the higher colour contrast between the black of the LFA bands and the white background of the nitrocellulose membrane. Rodriguez *et al*. conducted a comparison study of dual gold and silver staining enhancement. [164] They found that the immersing the strip into silver solution provided the most sensitive LFA results. However, it is noted that the immersion technique is a two-step assay that requires an additional step of strip immersion.

In addition to AuNSPs, magnetic nanoparticles (MNPs) are also powerful materials to be utilised in LFAs. In certain cases, a pre-enrichment process is highly required to ensure that the sample contains a sufficient amount of analytes for analysis. Detecting analytes of interest in complex matrices using LFAs is very challenging and usually results in poor sensitivity, as other substances may interfere with capture activity. MNPs possess intrinctic magnetic properties that respond to external magnetic fields. This allows the use of MNPs in sample preparation by purification and concentration, which can maximise the analytical performance of the LFA. [157, 160] Moreover, MNPs are yellow-brown in colour, which is highly contrasted with the colour of the nitrocellulose membrane, thus great visualization of the result.

Optical enehancement techniques can increase the intensity of test results to aid human recognition, but they lack quantitative information, which is essential in some applications, such as clinical diagnosis. Image processing technology has been merged with LFA analysis to enable quantitative measurement. A camera is typically

used to take images of the test results, and their colour intensities are transformed into digital values [152, 165, 166] using a Bayer filter, [152] ImageJ, [124, 164], or other methods. [128, 153, 162] Image analysis provides not only quantitative detail, but also reproducibility and higher sensitivity.

Colourimetric LFAs are limited in sensitivity. So, many researchers have included fluorescent labels into LFAs to produce fluorescent signals, which offers higher sensitivity and lower background noise. Carbon dots have intrinsic fluorescent properties and have been used as LFA labels to detect carcinoembryonic antigen in serum for cancer diagnosis. [167] Under irradiation with 365 nm light, the test line emitted fluoresncene at 453 nm, of which the intensity corresponded to the analyte concentration. Singh *et al.* showed the use of nitrogen-doped carbon quantum dots for LFA detection of aflatoxin M1 in milk sample. [168] Due to strong fluorescent signal of the nitrogen-doped carbon quantum dots, their LFA exhibited high sensitivity of detection. Furthermore, another study exploited the plasmonic properties of AuNRs to enhance the fluorescent signal of fluorophores. [169] This method resulted in ultrabright florescence. This plasmon-enhanced fluorescent LFA is very senstivie and specific for the detection of coronaviruses. In general, flouresncene-based LFAs provide more sensitive detection performance than conventional colourimetric assays due to their strong fluoresncence and low background noise. However, this method requires an optical reader tool and a UV lamp to excite the fluorescence emission.

Table 1.2 shows examples of optical sensitivity enhancement methods for LFA. Each method has its own advantages and disadvantages, and the most suitable methods should be selected based on the the cost, ease-of-use, sensitivity, portibility requirement of the final application. For example, incorporating magnetic separation techniques into LFA detection using AuNSPs and MNPs offers high sensitivity and allows the determination of analytes in complex matrices. However, the method is not portable, so it may not be suitable for being used onsite, such as remote areas and agricultural farms, but it may be applicable for medical diagnosis of body fluid samples in hospitals or laboratories.

Table 1.2 Advantages and disadvantages of optical-based enhancement techniques for LFA.

Label	Strategy	Pros	Cons	Ref.
Gold decorated silica nanorods	Increasing optical extinction	-Ease of use	-Potentially blocking a membrane -Limited stability	[154]
AuNSPs	Dual gold conjugates	-Ease of use	-Increasing the cost of production	[155, 170]
Platinum core-shell gold nanoparticles	Catalytic reaction	-Ease of use -High sensitivity	-Require many steps and reagents to operate	[161]
AuNSPs	Silver enhancement	-High sensitivity	-Require an additional step to operate -High background noise	[162, 163]
AuNSPs and MNPs	Magnetic separation	-Sample purification and concentration	-Require additional steps -Increasing cost of production -Not portable	[157]
Fluorophore@AuNRs	Plasmon-enhanced fluorescence	-High sensitivity	-Need a fluorescence reader -Photobleaching	[169]
Carbon-based nanoparticles	Fluorescence	-High sensitivity -Low cost of production	-Need a fluorescence reader	[167, 168, 171-173]

1.4.3.2 Non-optical measurement

Instead of the colourimetric and fluorescent signals, other signals can also be measured in LFA, depending on the types of label used. In the LFA platforms that deploy MNPs as labels, their magnetization can be detected by a magnetic reader. [127, 160] Magnetic LFA allows the detection of the magnetic signal throughout the entire thickness of the nitrocellulose membrane, which allows the retrieval of lost signal that cannot be seen by naked the eye. Hence, it is more sensitive than conventional LFA. In addition to magnetisation, the MNP-based LFA can also be measured by electrical impedance. [174]

A decade ago, scientists explored the possibility of exploiting the photothermal properties of nanoparticles to increase the sensitivity of the LFA, which led to the advent of thermal-contrast LFA. [175] In their study, AuNSPs concentrated at the test line were irradiated by a 532 nm laser at 0.5 W. The thermal gradient was then determined by an IR camera. This method enhances the sensitivity of the detection up to 100-fold compared to the colourimetric signal. This discovery opened a new pathway to increase the boundary of LFA performance by photothermalisation. Since then, the thermal-based LFAs have received great attention from researchers worldwide and have been continuously developed until today.

The performance of thermal-based LFAs relies on many factors, inclduing assay buffers, morphology of nanoparticles, and intensity and duration of irradiation. Plasmonic nanoparticles are the most common materiasl to be used in thermal contrast LFA systems becasue they have unique optical properties that can be tuned by altering their size and shape. [176] Therefore, various types of plasmonic noble nanoparticles have been utilised as phothermal agents in LFAs, such as AuNSPs, [175, 177] AuNRs, [175] gold nanoprisms, [178] and gold nanocages. [179] Moreover, the wavelength of light source needs to be carefully selected to align with the absorption of the nanoparticles to maximise the efficiency of detection. Hu *et al.* demonstrated a thermal contrast LFA platform using gold nanocages because of their high photothermal efficiency. [179] They found that gold nanocages yielded a considerably greater thermal signal than AuNSPs. Besides gold-based nanoaprticles, there is a study demonstrating the utilization of reduced graphene oxides in thermal-based LFA to determine pathogenic contamination, which showed a 10-time sensitivity enhancement. [180]

In general, thermal contrast LFA requires an expensive IR camera and a bulky laser source for thermal detection. To make the thermal detection system of LFA more portable and cost-effective, a laser pen was utilised to irradiate the AuNSPs in the LFA for the detection of *Salmonella typhimurium*, and a low-cost temperature sensor was used instead of the IR camera. [181] However, the use of a laser pen may suffer from its instability of the power intensity. Then, Cheng *et al.* developed a portable thermal reader using an application on a smartphone to determine the temperature

change. [182] Popcorn-like gold-palladium nanoparticles were used as labels and were irradiated by a near-infrared (NIR) laser, resulting in 71-fold sensitivity improvement.

Most studies on thermal LFA development show the measurement of the temperature gradient by measuring heat irradiation (irradiation mode). The temperature can also be detected by measuring heat dissipation (conduction mode) by attaching a thermal sensor to the LFA strip. [178] The cost of thermal sensors used in the heat conduction mode is cheaper than the IR cameras used in the irradiation mode, but their sensitivity was lower. Nonetheless, both irradiation and conduction modes offer greater sensitivity of detection than the typical visual signal. The temperature change in the conduction mode was first monitored by thermo-sensitive material in an electronic device. [183] A few years later, thermochromic material was introduced into the area of biosensing technology. [184] Gold nanoprisms were used as photothermal labels to maximise the photothermal response, whereas the thermos-sensitive paper acted as a sensor and changed its colour up on heat recognition. This assay achieved a significant improvement in the sensitivity of detection. Nonetheless, they used a high-power bulky fibre-coupled NIR, which is expensive and inconvenient.

1.4.4 Commercial lateral flow assays

LFA is a popular detection method that has gained widespread attention from many companies. It is very user-friendly and easily accessible to everyone, regardless of skill level. Table 1.3 shows examples of LFA test kits that are currently available in the market. As can be seen, most commercial LFAs provide colourimetric results to users, which maintains simplicity in operation as no additional reader is needed. Current commercial LFAs are highly encouraging for home testing.

The pregnancy test has been used widely for many decades as it provides a specific and accurate results. The “Check your drink” supplied by Abingdon Health provides a rapid test to detect drugs in drinks at a night club. During the COVID-19 pandemic, for example, the demand for FlowFlex COVID-19 Rapid Test Kits increased

dramatically, as LFAs can screen a larger number of samples and people with suspected symptoms of infection can perform the test themselves at home. Nonetheless, the LFA method is not sufficiently sensitive to detect the corona virus in body fluids in the first few days after infection, causing a false negative result.

Table 1.3 Commercial LFAs in the market

Label	Supplier	Product name	Signal	Target	Pros	Cons	Ref.
Gold nanoparticles	Meizheng Bio-Tech	*Salmonella* Rapid Test Cassette for Food and Environment	Colourimetric	*Salmonella*	-Simple to use	-For lab use -Require microbiological skills	[185]
n.p.	Merk	Singlepath® *Salmonella*	Colourimetric	*Salmonella*	-Simple to use	-Pre-enrichment step may be required -Require microbiological skills	[186]
n.p.	Romer Labs	RapidChek® SELECT™ *Salmonella* Test Kit	Colourimetric	*Salmonella*	-Simple to use	-For lab use -Pre-enrichment step may be required -Require microbiological skills	[187]
Gold nanoparticles	BioAssay Works	*Salmonella* Rapid Detection Kit	Colourimetric	*Salmonella*	-Simple to use	-Pre-enrichment step is required	[188]
n.p.	Attogene	Fluorescent Universal Lateral Flow Assay Kit	Fluorescent	DNA and RNA products	-Highly sensitive -Cost-effective	-Require fluorescent reader or black light -Require skill workers	[189]
n.p.	FlowFlex	FlowFlex COVID-19 Rapid Test Kits	Colourimetric	COVID-19 virus	-Simple to use	-Low sensitivity	[190]
n.p.	Abingdon Health	OraQuick® HIV Self-Test	Colourimetric	Antibodies produced in response to HIV-1 and HIV-2	-Simple to use -Applicable for home test -High specificity	-False positive obtained if users have received a HIV vaccine	[191]
n.p.	Abingdon Health	Check Your Drink	Colourimetric	Ketamine and Gamma Hydroxybutyrate	-Simple to use -Applicable for home test -Fast response	-	[192]

Some LFAs are more suitable for laboratory use rather than being a hometest. For example, *Salmonella* strip tests are designed to identify contamination in food and provide the colourimetric results. They can accelerate the identification of bacteria contamination by screening a large number of samples, and only suspected samples are further confirmed for contamination using other more sensitive methods. Pre-enrichment steps may be required to obtain reliable results from *Salmonella* strip tests. Furthermore, fluorescent LFAs are typically used in laboratories becasue a fluorescence reader is needed. They provide a strong signal, resulting in ultra-sensitive detection, but fluoresecents are not commonly found at home. Therefore, fluorescence-based LFAs are more suitable for use in specific settings, such as hosipotals, plants, and companies, where the tests are regularly performed on a daily basis.

1.5 Photothermal effect of noble nanoparticles

1.5.1 Localised surface plasmon resonance

Since Michael Faraday's discovery of the unusual optical effect of colloid nano-gold, scientists have intensively studied the fundamental mechanisms behind it. [193] The outstanding characteristics of gold nanoparticles are attributed to an optical effect called "surface plasmon resonance (SPR)". This phenomenon causes a variety of colour expressions of colloidal gold nanoparticles, which is size-dependent.

The size of materials extremely matters from the view of physics. Bulk materials undergo different optical mechanisms with nanoscaled particles. In bulk noble metals, SPR is induced when the surface is impinged by electromagnetic radiation at an angle nearly parallel to the surface. [193-195] The electromagnetic wave then propagates along the metal-dielectric interface, covering the visible and NIR region of the light spectrum. Free electrons are oscillated, resulting in a strong enhancement of the electric field at the interface, which decays exponentially from the surface (Figure 1.11A).

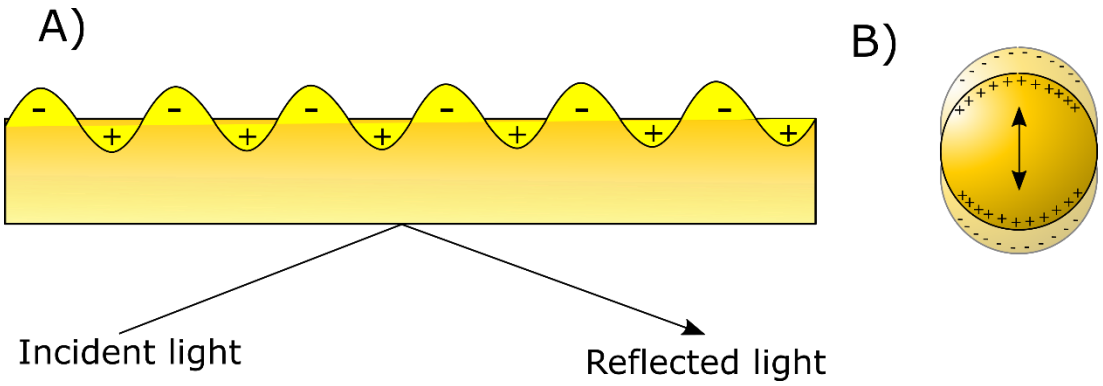

Figure 1.11 Illustrations of A) SPR in a bulk material and B) LSPR in a nanoparticle.

On the other hand, if SPR occurs in a confined space, such as a noble nanoparticle, the continuous conduction bands become discrete. The electromagnetic wave cannot travel freely as it does in the bulk material. [193-195] When the incident electromagnetic wave is comparable to or longer than the size of a nanoparticle ($\frac{R}{\lambda}$ < 0.1, where R is the radius of the nanoparticle and λ is the radiative wavelength), the corresponding plasmon resonance is termed LSPR, and the nanoparticle is generally known as a plasmonic nanoparticle.

The particle can be considered as a conducting medium containing an equivalent number of positive ions and electron clouds. Immediately upon external irradiation by electromagnetic radiation, the equilibrium of these charged clouds is disrupted, causing a displacement and dipole in the nanoparticle. In this case, the electromagnetic radiation deeply penetrates through the nanostructure, of which all electrons experience oscillation but they are not allowed to move freely on the surface due to limited space. Within a nanoparticle, the electron cloud is displaced in parallel to the direction of the electrical field of the electromagnetic wave. Nonetheless, the distance of displacement is very small from the nuclei, so the displaced electrons are reversed to their original positions by Columbic attraction due to the positive charge of the nuclei (Figure 1.11B). The electrons resonate back and forth (oscillation), contributing to the strong enhancement of the electric field around the surface of the spherical particle.

The light scattering spectrum of an individual metal nanoparticle in a liquid medium was explained by the Maxwell equation, which was later improved by Mie theory, [195] The extinction cross-section is given by Equation 1.1:

$$C_{ext} = \frac{24\P^2 R^3 \varepsilon_m^{3/2} N}{\lambda \ln(10)} \cdot \frac{\varepsilon_i}{(\varepsilon_r + X\varepsilon_m)^2 + \varepsilon_i^2} \qquad \textbf{(Equation 1.1)}$$

where C_{ext} is the extinction cross-section, R is the nanoparticle's radius, ε_m is the dielectric constant of the surrounding medium, N is the density of electrons, and $\varepsilon = \varepsilon_r + i\varepsilon_i$ is the complex dielectric constant of bulk metal with a real and imaginary component. Factor X is responsible for the shape of the nanoparticle, relating to the aspect ratio. For the sphere, X is assigned as 2. According to Equation 1.1, the polarisation of electrons reaches the maximum LSPR when the denominator is zero ($\varepsilon_r = -2\varepsilon_m$). In the case of the AuNSP, this condition is usually met in the visible range of the light spectrum.

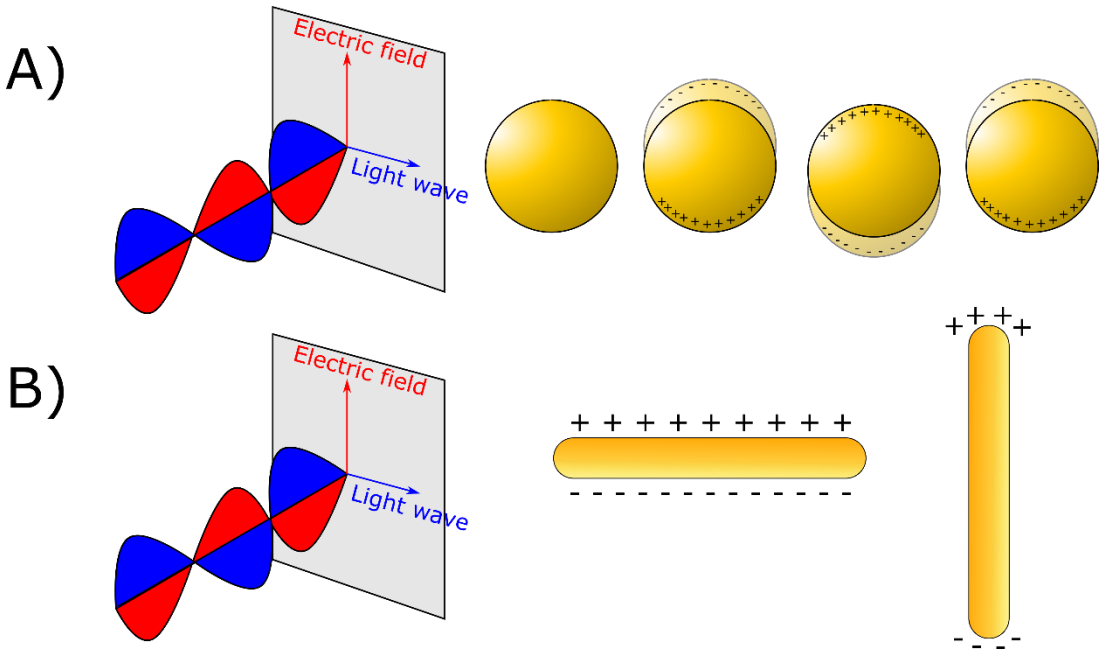

Figure 1.12 The schematic of the interaction of a nanoparticle and electromagnetic radiation of A) nanosphere and B) nanorod.

In a non-spherical nanoparticle, the optical absorption spectrum is altered and depends on the orientation of the electric field. For example, in a rod-shaped nanoparticle, the polarisation is split independently along and across the rod, unlike the poralisation of a spherical nanoparticle (Figure 1.12). In this case, the polarisation

is divided into two plasmon bands: the longitudinal plasmon resonance along the long axis, which is responsible for the peak appearing at a higher wavelength, and the transverse plasmon resonance along the shorter axis, which contributes to the smaller peak at the shorter wavelength (Figure 1.13). [193] Moreover, it can be seen that the absorption spectra is altered when the shape of plasmonic nanoparticles changes.

To predict the optical properties of rod-like particles, Mie's theory was modified by Gans to find the LSPR by assuming that the particles are ellipsoidal, due to the curvature of the rod. The equation for the extinction coefficient is given in Equation 1.2.

$$\mathbf{C_{ext}} = \frac{2\P V N \varepsilon_m^{3/2}}{3\lambda} \sum_j \frac{(\frac{1}{P_j^2})\varepsilon_1}{(\varepsilon_r + \left(\frac{1-P_j}{P_j}\right)\varepsilon_m)^2 + \varepsilon_i^2} \quad \textbf{(Equation 1.2)}$$

$$\mathbf{P_{length}} = \frac{1-e^2}{e^2}\left[\frac{1}{2e}\ln\left(\frac{1+e}{1-e}\right) - 1\right] \quad \textbf{(Equation 1.3)}$$

$$\mathbf{P_{width}} = \frac{1-P_{length}}{2} \quad \textbf{(Equation 1.4)}$$

$$\mathbf{e^2} = 1 - (\frac{\mathbf{width}}{\mathbf{length}})^2 \quad \textbf{(Equation 1.5)}$$

where V is the volume of the nanoparticle and P_j is the factor of depolarisation for an elongated nanoparticle, regarding the mode of polarisation (Equations 1.3 and 1.4), and e is ellipticity (Equation 1.5).

Ellipsoidal particles express a strong LSPR but a small change in the aspect ratio can significantly influent the absorption and scattering. The LSPR of the longitudinal axis is found to be sensitive to the aspect ratio and reflective index, but the transverse plasmon band is not. Increasing the aspect ratio results in a redshift of the optical absorption. Therefore, the absorption wavelength can be tuned from the ultraviolet to the NIR range of the electromagnetic spectrum by changing the aspect ratio.

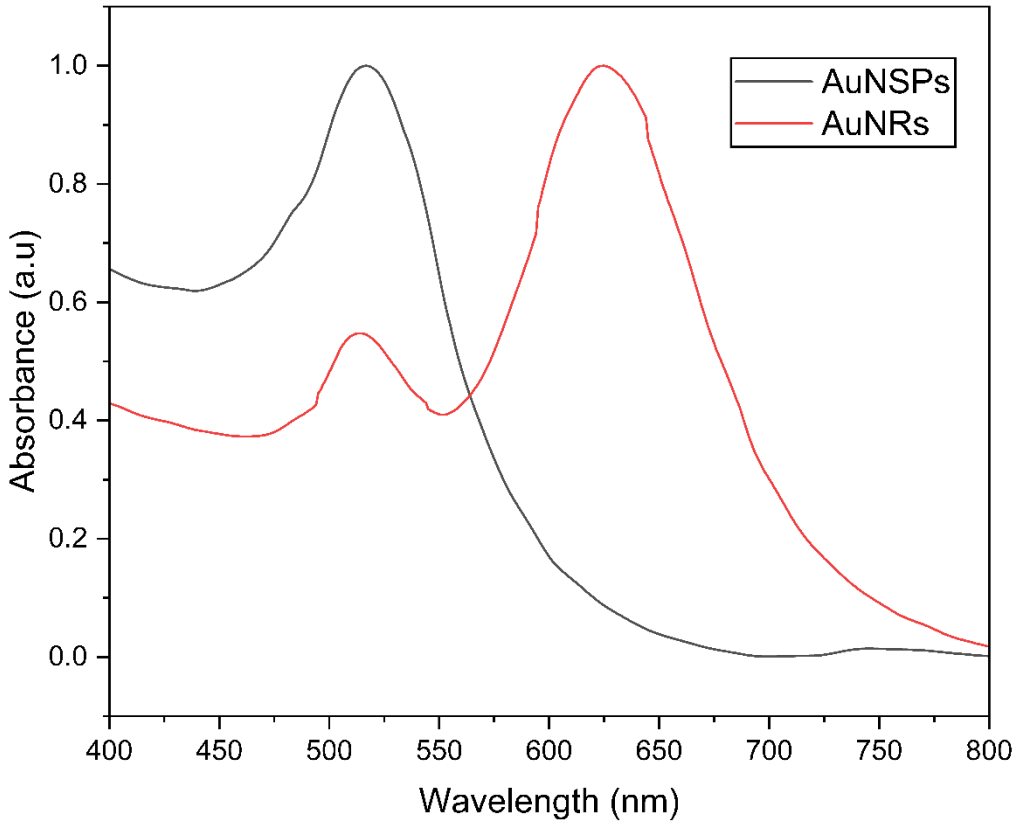

Figure 1.13 The absorption spectrums of AuNSPs and AuNRs.

The LSPR property of plasmonic nanoparticles makes them strongly absorb and scatter incident light at the resonance frequency. It depends on the size and shape of the particles, as well as the reflective index of the medium. Changes in the reflective index leads to a shift in the extinction spectrum. [195] In general, the polariszation (α) of a nanoparticle is defined as:

$$\boldsymbol{\alpha(\lambda) = 4\P\varepsilon_m(\lambda)R^3 \frac{\varepsilon(\lambda)-\varepsilon_m(\lambda)}{\varepsilon(\lambda)+2\varepsilon_m(\lambda)}} \qquad \textbf{(Equation 1.6)}$$

When a nanoparticle is coated with a thin layer of dielectric, the polariszation (α) is given as:

$$\boldsymbol{\alpha(\lambda) = 4\P\varepsilon_m(\lambda)(R+d)^3 \frac{\varepsilon(\lambda)\varepsilon_A(\lambda)-\varepsilon_m(\lambda)\varepsilon_B(\lambda)}{\varepsilon_d(\lambda)\varepsilon_A(\lambda)+2\varepsilon_m(\lambda)\varepsilon_B(\lambda)}} \qquad \textbf{(Equation 1.7)}$$

$$\boldsymbol{\varepsilon_A(\lambda) = \varepsilon(\lambda)(3-2P) + 2\varepsilon_d(\lambda)P} \qquad \textbf{(Equation 1.8)}$$

$$\boldsymbol{\varepsilon_B(\lambda) = \varepsilon(\lambda)P + \varepsilon_d(\lambda)(3-P)} \qquad \textbf{(Equation 1.9)}$$

$$\boldsymbol{P = 1 - (\frac{R}{R+d})^3} \qquad \textbf{(Equation 1.10)}$$

where d is the thickness of the dielectric layer, $\varepsilon_d(\lambda)$ is the dielectric constant, and R is the radius of a nanoparticle. When the dielectric constant of the coating increases, it red-shifts the spectral absorption. This allows the tunability of the LSPR band of the nanoparticles by changing these dominating parameters to achieve the requirements of desired applications.

1.5.2 Heat production

When LSPR is optically induced, it energizes superficial electrons, generating heat between the surface of the nanoparticle and the environment. [28] Plasmonic nanoparticles have been exploited in photothermal applications because of their distinct absorption at plasmon resonance, which yields significant heat. In principle, when the incident light is delivered to the outer surface of nanoparticles, the LSPR of the nanoparticles resonate with the electromagnetic wave, causing the electrons to heat up. [28] The hot electrons then release their kinetic energy as heat, subsequently increasing the temperature of the nanoparticles and the local environment. Since the local heat production is contributed by the LSPR effect, maximum heat production can be achieved by tuning the absorbance peak of the nanoparticles.

The photothermal conversion efficiency (η) of gold nanoparticles can be calculated as: [28, 43]

$$\eta = \frac{hS(T_{max} - T_{amb}) - Q_s}{I(1 - 10^{-A_\lambda})} \qquad \textbf{(Equation 1.11)}$$

where h is the heat transfer coefficient, S is the surface area of the container, T_{max} is the maximum temperature production, T_{amb} is the ambient temperature, Q_s is the heat related to the absorption of the solvent, I is the power of the light source, and A_λ is the absorbance of the sample at the wavelength of λ nm.

According to Equation 1.11, the light-to-heat conversion capability is related to the optical absorption of the nanoparticle. It implies that the maximum efficiency can be reached when the nanoparticles are irradiated with the light at LSPR wavelength. However, it is importnat to note that, according to Maxwell's theory, the cross-

section of nanoparticles relates to their optical properties, which affects the heat production when they are optically stimulated. [196, 197] However, the Maxwell's equation only explains the optical effects of a single nanoparticle which is not applicable to nanoparticle ensemble. [198]

1.6 Research aim and objectives

1.6.1 Research aim

This thesis aims to develop a novel thermochromic-based LFA that is cost-effective, easy-to-use, and highly sensitivie for the detection of *Salmonella typhimurium* and DENV2-NS1.

1.6.2 Research obejctives

- Prepare and characterise photothermal nanoparticles, including IONPs, ZFNPs, AuNSPs, AuNRs, and AuNSTs.
- Investigate the photothermal effets of these nanoparticles under white-light LED illumination.
- Demonstrate the feasibility of using a thermochromic-based technique to improve the analytical performance of LFAs and compare its effectiveness with conventional and thermal-sensing LFAs.
- Prepare and characterise the immobilisation of nanoparticles with biorecognisition molecules for detecting *Salmonella typhimurium* and DENV2-NS1.
- Evaluate and optimise the capture efficiencies of biorecognition molecule-conjugated nanoparticles for LFA applications using half-strip assays against *Salmonella typhimurium* and DENV2-NS1.
- Fabricate full-strip LFAs for the detection of *Salmonella typhimurium* and DENV2-NS1.

- Assess the analytical performance of the developed thermochromic LFAs for *Salmonella typhimurium* and DENV2-NS1 detection compared to conventional LFAs.

Chapter 2 : Fabrication of magnetic nanoparticles and gold nanoparticles

2.1 Introduction

This chapter aims to prepare and characterise various types and shapes of photothermal nanoparticles, namely iron oxide nanoparticles (IONPs) and zinc ferrite nanoparticles (ZFNPs), AuNSPs, AuNRs, and gold nanostars (AuNSTs).

MNPs have been involved in cancer threatment for many decades due to their magnetic and photothermal properties. In biosensors, MNPs provide magnetisation that can be monitored by a magnetic reader. They also bring purification and concentration to the detection assay to enhance the sensitivity, especially in complex matrix samples. Despite these advantages, the use of MNPs in the thermal-based LFA has never been reported. Since MNPs are promising candidates to be used in thermochromic LFA, they were produced and characterised in this chapter. There are many methods to fabricate MNPs, such as thermal decomposition, [199] solvothermal, [200] and polyol methods. [201-203] IONPs and ZFNPs were produced in this chapter by the polyol-mediated synthesis due to its controllable diameter, reproducibility, and ease of further modification. [204]

Apart from the MNPs, plasmonic nanoparticles were also prepared because of their excellent optical properties. Isotropic and anisotropic AuNPs, including AuNSPs, AuNRs, and AuNSTs, were synthesised and characterised. The synthesis of AuNSPs has been widely published. The classic protocol of AuNSP production is known as Turkevich's method, [205-208] which was later improved by Frens. [209] Simplicity and reproducibility are the reasons that the synthesis of AuNSP has gained high attention.

Anisotropic AuNPs, including AuNRs and AuNSTs, were produced based on the seed-mediated method. By reducing gold salt in the presence of surfactant, it can vary the

shapes of the obtained gold-based nanoparticles, resulting in anisotropic shapes. [56, 57, 210-213] The effect of the reducing agents, gold precursor, and salt additive on the morphology and optical properties was investigated.

2.2 Synthesis and characterisation

2.2.1 Materials

Chemicals were reagent grades and used as received. For the production of MNPs, iron(III) acetylacetonate ($Fe(acac)_3$, ≥99.9% trace metals basis), zinc acetylacetonate hydrate ($Zn(acac)_2$, 99.995% trace metals basis), triethylene glycol (TREG, ReagentPlus®, 99%), trisodium citrate dihydrate, hydroxylamine hydrochloride (ReagentPlus®, 99%), 1,10-phenanthroline monohydrate (ACS reagent, 99%), 70% nitric acid (70% HNO_3 for ICP, 99.999% trace metal basis), and Fe standard and Zn standard for ICP (TraceCERT®) were purchased from Sigma-Aldrich (UK). Acetone (technical grade) and iron (II) chloride tetrahydrate ($FeCl_2{\cdot}4H_2O$, 99.0%) were received from VWR (UK) and Honeywell (UK), respectively. Hydrochloric acid (37% HCl) was supplied by Acros Organics (UK). Sodium acetate anhydrous (ReagentPlus®99.0%) was bought from Sigma Life Science (UK). Water was purified by Purelab Ultra Elga (UK) in the lab to yield deionised (DI) water.

For the synthesis of gold-based nanoparticles, gold (III) chloride solution ($HAuCl_4$, 99.99% trace metals basis), trisodium citrate dihydrate, hexadecyl trimethylammonium bromide (CTAB, for molecular biology, ≥ 99%), silver nitrate ($AgNO_3$, ACS reagent, ≥ 99.0%), sodium borohydride ($NaBH_4$, ReagentPlus®, 99%), L-Ascorbic acid, sodium bromide (NaBr, ACS reagent, ≥ 99.0%), sodium nitrate ($NaNO_3$, ReagentPlus®, ≥ 99.0%) were purchased from Sigma Aldrich (UK). HCl (37%) was supplied from Acros Organics (UK). DI water was used for all synthesises and redispersion of AuNPs. All glass wares and magnetic stir bars were cleaned with Aqua regia to remove any residual gold traces and dried in the oven before each use.

2.2.2 Synthesis of nanoparticles

2.2.2.1 Iron oxide and zinc ferrite nanoparticles

Polyol-based synthesis has been previously described in the literature. [201] This method yields polyol-capped IONPs. The synthesis of the ZFNPs in this thesis is based on the same method with slight modifications.

Briefly, the precursor for the IONP synthesis was prepared by blending 4 mmol of $Fe(acac)_3$ in 20 mL of TREG, followed by vigorous vortexing and 2 h of sonication to homogenise. To prepare the precursor for the ZFNPs, 174 mM of $Fe(acac)_3$ and 26 mM of $Zn(acac)_2$ were added to a tube containing 20 mL of TREG solution, followed by vortex and sonication for 2 h.

Both metal precursor solutions were transferred to 45 mL-capacity Teflon liners and loaded into alloy-steel autoclave jackets. Their tops were closed with PTFE gaskets and sealed with screw caps before placing them in an oven (Memmert, model UFP400). To investigate the effect of the reaction duration, the program was pre-set to immediately increase the temperature to 250 °C and remain at this point for 8, 24, or 48 h. Then, the temperature was ramped down to 20 °C and held for 2 h. The excess solvent and by-products were eliminated by magnetic separation in acetone and DI water. The washing process was performed twice. Black pellets were retrieved and redispersed in DI water. At this step, the IONPs@TREG and ZFNPs@TREG were received.

2.2.2.1.1 Ligand exchange reaction

A ligand exchange reaction was carried out to improve the water dispersibility of the MNPs by replacing the original coating ligands with citrate. The experiments were designed to optimise the exchange reaction under different conditions, including the mechanical mixing force, the reaction duration, the concentration of citrate, and the reaction temperature.

The IONPs@TREG and ZFNPs@TREG were produced as described in section 2.2.2.1, where the precursors of IONPs and ZFNPs were placed in the oven for 8 h. Different parameters were varied to explore the optimum conditions for citrate absorption. The ligand exchange was performed using two mixing devices: a magnetic stirrer and a rotary mixer, which provide different mechanical forces. The impact of the citrate concentration, reaction temperature, and reaction duration was investigated. All samples were prepared in triplicate and their hydrodynamic diameters were measured using dynamic light scattering (DLS).

2.2.2.1.1.1 Magnetic stirrer

To determine the effect of the citrate concentration, colloidal IONPs@TREG and ZFNPs@TREG were mixed with different molarities of trisodium citrate (25, 100, 500, and 1000 mM) by continuous stirring (1300 rpm) at 70°C for 2 h in DI water. The resulting citrate-coated nanoparticles were washed by magnetic separation and rinsed with acetone and DI water to remove residual TREG and citrate. DI water was then added to redisperse them, followed by brief sonication to aid the dispersion of MNPs@citrate.

To optimise the reaction temperature, 1000 mM trisodium citrate was mixed with TREG-coated MNPs. The reaction was heated to 70 °C and 90 °C in an oil bath with continuous stirring at 1300 rpm for 2 h. One of the samples was subjected to ligand exchange at room temperature (RT) with continuous stirring at 1300 rpm for 2 h. Residual citrate and dissociated TREG were discarded by magnetic decantation. The retrieved MNPs were dispersed in DI water for further analysis.

2.2.2.1.1.2 Rotary mixer

All ligand exchange reactions under a rotary mixer were operated at RT. First, the concentration of the citrate was optimised. The solutions containing MNPs@TREG and trisodium citrate (25, 100, 500, and 1000 mM) were gently shaken on a rotary mixer for 24 h. Unbound TREG and citrate in the aqueous solution were removed by a permanent magnet and rinsed several times with acetone and DI water. The final products were dispersed in DI water.

Next, an experiment was designed to examine the effect of the reaction length on the hydrodynamic size of the nanoparticles. MNPs@TREG were suspended in 1000 mM of citrate solutions and left under continuous and gentle rotation for 24, 48, and 72 h. Finally, they were washed by magnetic decantation with acetone and DI water and resuspended in DI water.

2.2.2.2 Gold nanospheres

Spherical AuNPs were prepared according to the well-established Turkevich's method. [158, 206] To study the relevant factors to the morphology of the AuNSPs, the amount of gold precursor and reducing agent (trisodium citrate) were altered in the experiments. Firstly, to study the influence of gold salt, 0.01 and 0.03 wt% of chloroauric acid ($HAuCl_4$) solutions were prepared in 50 mL of DI water and brought to the boiling point. Then, 5 mL of the trisodium citrate (1 wt%) were added to the gold solution. The colour changed from light yellow to red wine within 3 min, indicating the reduction reaction and the growth of nanocrystals. The reaction was continued with vigorous mechanical stirring at the boiling point for another 10 min before removing the heat source and was left for 20 min.

The influence of the reducing agent in the AuNP synthesis was examined as follows. First, 50 mL of 0.03 wt% $HAuCL_4$ were boiled, and then 0.4, 1.25, 2.5, and 5.0 mL of 1 wt% citrate were added. The colour change must be observed; otherwise, the sample was discarded. The reaction was kept under mechanical stirring at the boiling pointing for 10 min and then left to cool down at RT for 20 min.

2.2.2.3 Gold nanorods

Rod-like gold nanoparticles were reproduced from previous reports. [56, 57, 210] These reports demonstrated the seed-mediated growth strategy to produce AuNRs. Since AuNRs will be used in the photothermal test in the next chaper, the synthesis aimed to explore the recipe that yields AuNRs with LSPR peaks aligning with the wavelength provided by the LED (see Figure 1 in Appendix A).

This section will describe the production of AuNRs using two different salt additives: NaBr and $NaNO_3$. In addition, the amount of $AgNO_3$ was varied in the experiments, as it affects the aspect ratio of AuNRs. The morphologies and optical spectra of AuNRs were assessed by TEM and UV-vis spectrophotometry. The preparation steps are described below.

2.2.2.3.1 Method 1: Synthesis of gold nanorods using NaBr additive

The protocol was reproduced from the literature. [210] To make the seed solution, 10 mL of the mixture containing 0.25 mM $HAuCl_4$ and 0.1 M CTAB was prepared, followed by an injection of fresh ice-cold 10 mM $NaBH_4$ (0.6 mL). The mixture was vigorously stirred and left undisturbed for 1 h to age the growth of the gold seeds. This solution was labelled as a seed solution.

Secondly, to prepare the growth solution, 5 mL of 1.4 mM $HAuCl_4$ was mixed with 5 mL of 0.2 M CTAB. Then, different volumes of 10 mM $AgNO_3$ were added to the solutions: 75, 100, and 125 µL. This was followed by additions of 1.25 M NaBr (0.25 mL) and 37% HCl (10 µL). Next, 79 mM of L-ascorbic acid (105 µL) was injected quickly and stirred for 30 s until it became colourless. At this step, the growth solution was received.

Finally, the freshly prepared growth solution was mixed with 60 µL of the seed solution. The mixture was incubated at 30 °C overnight to grow the rods. The particles were purified by centrifugation (8500 rpm) for 20 min. The supernatant was discarded and the pellets were redispersed in water.

2.2.2.3.2 Method 2: Synthesis of gold nanorods using $NaNO_3$ additive

The procedure is similar to the method described in Section 2.3.2.2.1, except that $NaNO_3$ was used as an additive instead of NaBr. The seed solution was prepared by mixing 0.25 mM $HauCl_4$ and 0.1 M CTAB (10 mL), followed by the addition of 0.6 mL of fresh and cold $NaBH_4$ (10 mM). The mixture was vigorously stirred and then left undisturbed for 1 h for seed ageing process.

To make the growth solution, 50 µL of 10 mM $AgNO_3$ was added to a vial containing 5 mL of 0.1 M CTAB, followed by 5 mL of 0.5 mM $HAuCl_4$. The mixture was injected with 75 µL of 2.78 M $NaNO_3$ and 12 µL of 37 wt% HCl. Finally, 75 µL of 790 mM L-ascorbic acid was pipetted into the mixture and stirred for 30 s until the solution became transparent.

The growth of rod-shaped nanoparticles was initiated by the adding 60 µL of the seed solution to the growth solution. The mixture was incubated at 30 °C overnight to promote the elongation of the particles. Finally, the colloidal AuNRs were collected by centrifugation (8500 rpm for 10 min) to remove impurities and residual surfactant.

2.2.2.4 Gold nanostars

The synthesis of AuNSTs is also based on the seed-mediated assay from the previous study with slight modifications. [56] The seeds were prepared using the classical citrate-stabilized AuNSP preparation as described in Section 2.2.2.2. Two different sizes of the gold seeds were prepared in this section. Briefly, 0.03 wt% $HAuCl_4$ in 50 mL of DI water was boiled and then 2 or 5 mL of 1 wt% trisodium citrate was added. The mixtures were stirred at the boiling point for 10 min before being cooled down at RT for 20 min.

To form the spikes from the gold seeds, 10 mL of 0.25 mM $HauCl_4$ was mixed with 10 µL of 1 M HCl. The prepared seed solution (100 µL), 3 mM $AgNO_3$ (100 µL), and 100 mM ascorbic acid (50 µL) were then added. The mixture was mechanically stirred for 30 s. After that, the particles were stabilized with 1.74 mL of 7 mM CTAB. The unbound surfactant was removed by centrifugation (8500 rpm) and the particles were resuspended in DI water.

2.2.3 Characterisation of nanoparticles

2.2.3.1 Transmission electron microscope

The shape and diameter of nanoparticles were analyzed using a Transmission electron microscope (TEM) (JEOL-1200 EX microscope) with an accelerating voltage

of 120 kV. To prepare the sample for imaging, nanoparticle suspension was diluted in water and 10 µL was pipetted to a carbon-coated copper grid, which was then left to air-dry overnight. A total of 500 random particles were measured using ImageJ software to determine the average diameter and size distribution. The TEM images were recorded using Gatan DigitalMicrograph software.

2.2.3.2 Hydrodynamic size and zeta potential

The electrical surface properties and hydrodynamic size of the nanoparticles were determined using a dynamic size scattering (DLS) and zeta potential analyser (Malvern Nanosizer ZS instrument) operating with a He-Ne laser with the wavelength of 633 nm (Malvern Instruments Ltd, Worcestershire, UK). The colloidal sample was diluted and sonicated for 10 min to reduce the aggregation effect before DLS measurement.

To study the colloidal stability, the pH of the sample was manually adjusted to various values from 3 to 9. The zeta potential measurements were carried out at 25 °C in a disposable capillary cell (DTS1070). The DLS and zeta potential data were analysed on Malvern Software ver. 7.11 (Malvern, UK).

2.2.3.3 Fourier transform infrared spectroscopy

Fourier transform infrared (FTIR) spectroscopy was used to investigate the presence of molecules on the outer surface of nanoparticles. Solid samples of nanoparticles were obtained using freeze-drying method. Sample suspensions were initially frozen in nitrogen liquid. The frozen samples were immediately placed under negative temperature and vacuum overnight to remove water and solvents. PerkinElmer Spectrum 100 was utilised to measure the IR transmission of each sample in the range of 4000 to 800 cm^{-1}.

2.2.3.4 X-ray powder diffraction

X-ray powder diffraction (XRD) technique was utilised to characterise the crystallinity and purity of the obtained nanoparticles. Powder samples of nanoparticles were prepared by freeze drying method, as described in Section 2.2.3.3, and then

submitted for XRD measurement. The elemental composition of nanoparticles was scanned using a PANalytical X'Pert equipped with a Co Kα (λ = 1.789 Å) between 20-90°. The X'Pert HighScore Plus software was used for data analysis. The crystalline size of nanoparticles was estimated using the Scherrer equation: [214]

$$\boldsymbol{L = \frac{K\,\lambda}{\beta\,cos\theta}} \qquad \textbf{(Equation 2.1)}$$

where L is the mean size of nanocrystalline, K is the shape factor corresponding to the shape of crystalline which is typically 0.89, β is the line broadening at full width half maximum, and θ is the Bragg angle.

2.2.3.5 Inductive coupled plasma atomic emission spectroscopy

Inductive coupled plasma atomic emission spectroscopy (ICP-AES) is an emission spectroscopy that measures the electromagnetic radiation emitted from samples excited by plasma to find the elemental fingerprint of a sample. It was carried out in this thesis to measure the concentration of the elements of interest in the samples.

Powder samples of nanoparticles (1 to 5 mg) were digested in 1 mL of 70% nitric acid (HNO_3) at RT until the metallic particles were completely dissolved. If the metallic particulates remained, heat was applied at 65 °C for an hour to accelerate the dissolution. This was done to avoid blocking the nebulizer of the machine. Then, the aqueous dissolute samples in 70% HNO_3 were diluted to 2% with water to reach a final volume of 10 mL. The standard calibration curves were created from known-concentration standard solutions. The plasma measurement was carried out using an Agilent Varian-720ES ICP-AES instrument. The optical intensities emitted from the elements were converted to the concentration using ICP Expert II software.

2.2.3.6 Ultraviolet-visible spectroscopy

The absorption spectra of colloidal nanoparticles were measured using an ultraviolet-visible (UV-Vis) spectrophotometer (SpectraMax M2, Molecular device). Colliodal nanoparticles were transferred to cuvettes and their absorbance was measured either over a range of wavelengths (400-800 nm) or at a specific wavelength.

2.3 Statistical analysis

To compare the obtained data, statistical analysis was performed using SPSS software. The mean difference is significant at the 0.05 level ($\alpha = 0.05$). A two-tailed paired-samples t-test was applied to determine significant differences between two groups of samples. For multiple groups, a one-way Anova test was applied to determine significant differences between samples. Homogeneity of variance was tested to assess the variance across samples (equal or unequal variances). Following this, the appropriate post-hoc test was applied: Bonferroni test for samples with equal variance and Dunnett's T3 test for samples with unequal variance.

2.4 Results and discussion

2.4.1 Synthesis and Characterisation of magnetic nanoparticles

2.4.1.1 Morphology of magnetic nanoparticles

Polyol-mediated synthesis is a method that relies on the thermal decomposition of metal-salt precursors at high temperatures in an organic solution phase. [199, 201, 215] The hydrate contained in the precursors serves as a source of oxide. [204] This method has previously been used to fabricate IONPs, [201] and can be slightly modified to dope other materials into the nanoparticles. [204, 216] Hence, $Zn(acac)_2$ was added to the mixture of the precursor to form ZFNPs@TREG .

In the polyol-based approach, the precursors are subjected to high temperature resulting in the decomposition into metal ions. The formation of the nanocrystals in high-pressure and -temperature environment leads to the generation of MNPs with a narrow size distribution and reproducibility. [201] As shown in Table 2.1, the diameter of the MNPs can be tailored by customising relevant parameters, such as the reaction duration and temperature, the concentration and types of precursors,

and the types of polyol-solvents. [201, 204] In this thesis, only the impact of reaction duration on the size of the resulting MNPs was examined.

Table 2.1 Impact of various parameters tested on MNPs using modified-polyol method. [201] Top panel shows the influence of reaction time and precursor mass on MNP size. Bottom panel shows the effect of solvents on MNP size and polydispersity.

	Parameters			
	Reaction time		Mass of precursors	
	Increase	Decrease	Increase	Decrease
MNP size	**Increase ↑**	**Decrease ↓**	**Increase ↑**	**Decrease ↓**

Solvent used					
Diethylene glycol		Triethylene glycol		Tetraethylene glycol	
MNP size	Polydispersity	MNP size	Polydispersity	MNP size	Polydispersity
Smallest	**Medium**	**Medium**	**Smallest**	**Largest**	**Largest**

Based on the TEM images shown in Figure 2.1, spherical IONPs and ZFNPs were obtained, being similar to the previous finding. [201] The average diameter was dependent on the duration of the reaction, with a longer reaction time resulting in a larger diameter of the MNPs. The size of the IONPs@TREG increased from 10.63 nm to 15.43 nm with the increase of the reaction time from 8 to 48 h. The size of the ZFNPs@TREG was slightly larger than the IONPs@TREG, increasing from 11.97 nm to 17.32 nm with the increase of the reaction duration. It was also found that a longer reaction time in the oven improved the uniformity of the obtained MNPs. This suggests that free iron atoms continued to absorb and stack on the surface of the MNPs.

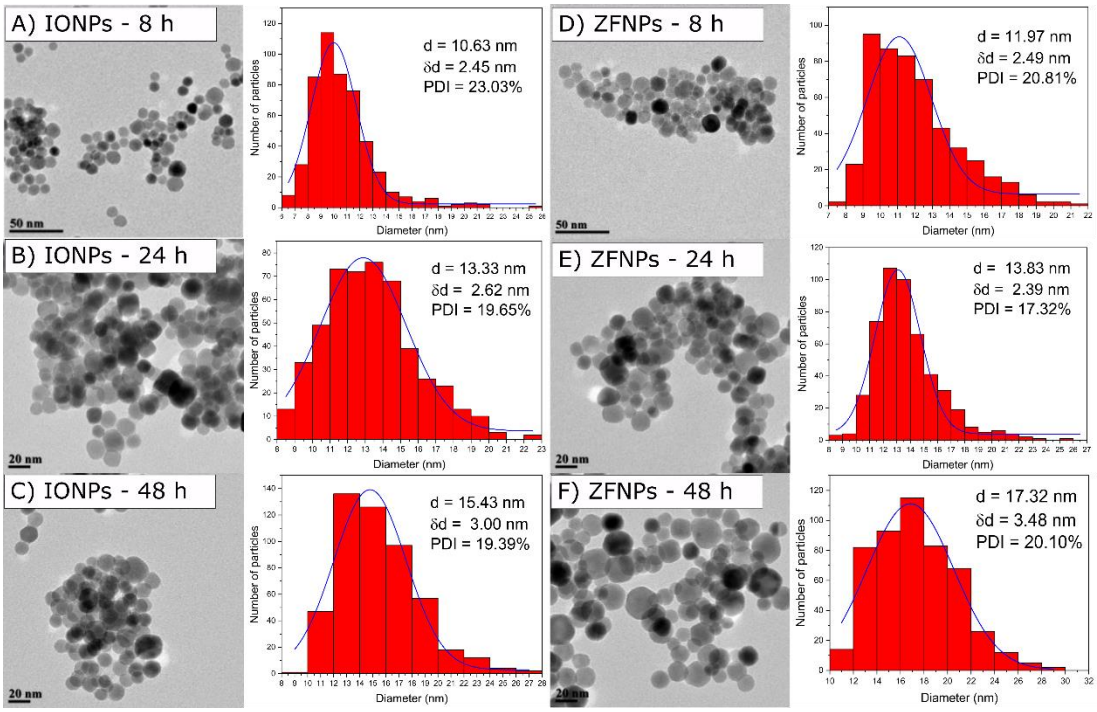

Figure 2.1 TEM images at 50000X magnification and size distribution of the IONPs@TREG and the ZFNPs@TREG yielded from the polyol synthesis. They represent the structural detail of IONPs@TREG that were incubated in an autoclave for A) 8 h, B) 24 h, and C) 48 h, and ZFNPs@TREG that were incubated for D) 8 h, E) 24 h, and F) 48 h (n = 500). d = mean diameter, δd = standard deviation, PDI = polydispersity index.

There are many related factors that could affect the size of the obtained MNPs, such as the types of polyol ligands used, the reaction temperature, and the concentration of the precursors. However, this thesis only assesses the impact of the reaction duration. The effects of the other factors on the size of the MNPs have already been thoroughly investigated elsewhere. [201] They investigated the synthesis of IONPs using three different polyol ligands: diethylene glycol, TREG, and tetraethylene glycol. They found that the solvent affected the diameter of the final products as the use of longer-length glycol resultd in larger IONPs. According to their report, adding TREG as a capping agent offered reproducibility of IONP production with good crystallinity. Hence, TREG was chosen to be the original coating ligand in the polyol synthesis in this work.

The presence of ethylene glycol in the synthesis is highly beneficial to the fabrication of metal oxide nanoparticles. It serves as both a reducer and a stabilizer, [199, 200, 203]

and the hydroxyl ions of the polyol provide nucleation sites for nanocrystal growth. [202, 203] Moreover, polyols have excellent chelating features, facilitating the anchoring of the polyol itself and the cation of the metal atom, particularly an oxide. [199, 204] The absorption of TREG on the surface of the MNPs promotes steric repulsion forces for stabilisation, making the as-synthesized IONPs@TREG and ZFNPs@TREG water-soluble.

2.4.1.2 Elemental analysis

The XRD pattern of the IONP was consistent with the reference pattern of the magnetite (Fe_3O_4) phase, as shown in Figure 2.2. [199, 201] The IONP sample exhibited major peaks corresponding to the angles of the crystalline phase of magnetite. The solid sample of zinc ferrite, on the other hand, showed a slight angle shift of the peaks, implying a change in the crystalline structure compared to that of magnetite. This is possibly due to the integration of zinc into the iron lattice.

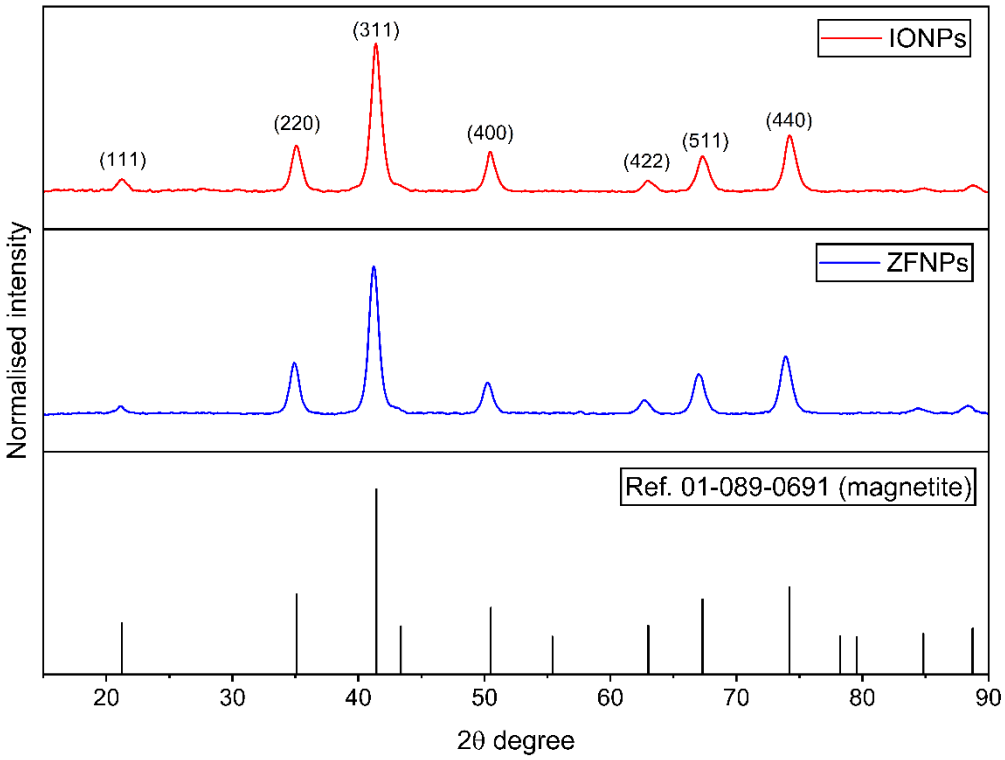

Figure 2.2 The XRD patterns of IONPs (red) and ZFNPs (blue). The bottom panel (black) represents the diffraction patterns of magnetite according to PDF No. 01-089-0691.

In addition, the details of the XRD diffraction allow for the estimation of the crystalline size. [214] According to the Scherrer formula in Equation 2.1, the average crystalline size of IONPs was 10.30 nm and that of ZFNPs was 10.42 nm. These sizes were in agreement with the sizes determined by TEM measurement. Therefore, the MNPs obtained from the polyol method in this study had highly crystalline structures.

Further confirmation of the incorporation of zinc into the particles was performed by ICP-AES measurement. The emission of electromagnetic radiation from the IONP and ZFNP samples can be used to determine the concentration of iron and zinc in these samples. In Figure 2.3, the sample of IONPs was treated as a control of the experiment. Only iron was present in the sample and the ICP result found that iron accounted for merely 100% of the total metal content. On the other hand, the ZFNPs were composed of 86±0.85% iron and 13.36±0.84% zinc. This is also in accordance with the ratio of the starting materials: $(Fe(acac)_3$: $Zn(acac)_2$ = 174 mM: 26 mM), which is equivalent to the ratio of 87:13.

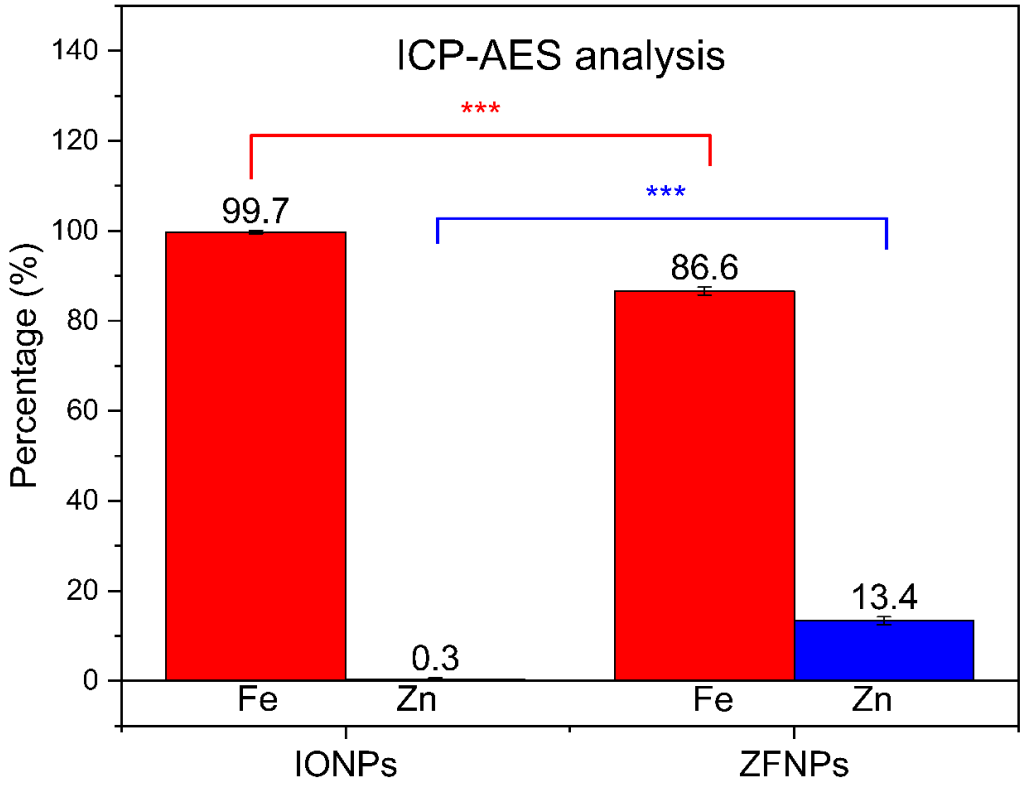

Figure 2.3 Percentage of metallic contents of IONPs and ZFNPs determined by ICP-AES measurement. Data are presented as the mean ± standard deviation (n = 3). P-values were obtained using a two-tailed paired-samples t-test. *p < 0.05, **p < 0.01, ***p < 0.001, and ****p < 0.0001.

2.4.1.3 Ligand exchange reaction

The polyol-assisted synthesis method yields MNPs that are coated with polyols. Due to the low polarity of the TREG, the MNPs are not stable when dispersed in DI water. As observed, the MNPs@TREG sediment in a short time. The steric repulsion force alone is not sufficient to maintain the stability of the MNPs in water, inducing the attraction between neighboring MNPs by the van der Waals force and subsequent aggregation. [217] Hence, electrostatic repulsion is essential.

The substation of the polyol coating can be simply attained in a subsequent ligand exchange reaction. Citrate, a strong binder with high affinity, was introduced to the MNPs@TREG to replace the TREG molecules on the surface of the particles. As citrate moieties contain carboxylates, they can facilitate further functionalisation with biomolecules.

Initially, the ligand exchange reaction was carried out according to the protocol available in the previous study. [218] Nonetheless, monodisperse citrate-coated MNPs were not obtained. The as-synthesized crude MNPs@TREG were directly proceeded to the ligand exchange reaction. Although the obtained MNPs were well-dispersed in water, the DLS results showed that the MNPs were aggregated. It was assumed that free polyols were abundant in the solution and hindered the citrate molecules from approaching the surface of the MNPs by steric interaction. [219] Thus, it is essential to remove TREG from the solution before conducting the ligand exchange. The citrate exchange process was optimized in this study to encourage the binding efficiency of the citrate.

2.4.1.3.1 Magnetic stirrer

For the size comparison study, the hydrodynamic diameters of IONPs@TREG and ZFNPs@TREG were measured by DLS. They were negative controls in this study to compare with the MNPs obtained from the ligand exchange. The hydrodynamic diameter of the IONPs@TREG in water was 291.13 nm and that of the ZFNPs@TREG was 225.93 nm (Figure 2.4), which were relatively high compared to the core size of the IONPs (10.63 nm) and the ZFNPs (11.97 nm) determined by TEM measurement

(Figure 2.1). Similar observations were reported by Hachani *et al*. [201] The results indicate the poor water dispersibility of the MNPs@TREG. Nonetheless, the results are controversial to those reported by Maithy *et al*. [199] The IONPs@TREG were fabricated by thermal decomposition under an inert atmosphere, expressing excellent water sobility. They reported that the hydrodynamic diameter of the IONPs@TREG was 13 nm whereas the core size was 11 nm. The zeta potential was +40 mV, showing great stabilisation by electrostatic force in water. They explained that the H^+ ions polarized from TREG molecules during elevated temperature (R-OH → $R\text{-}O^-$ + H^+) were responsible for the highly positive charge of the particles. Hence, an individual nanoparticle is protected by both steric and electrostatic hindrances, resulting in excellent water stability.

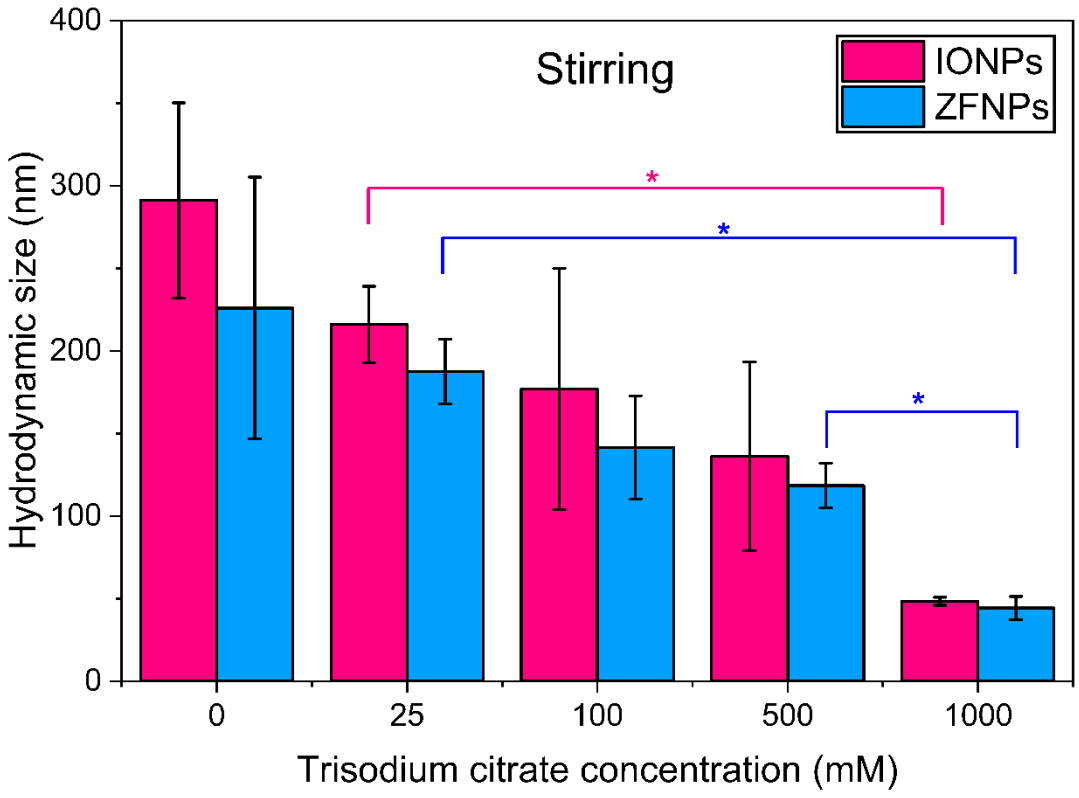

Figure 2.4 Hydrodynamic sizes of IONPs@citrate and ZFNPs@citrate after ligand exchange reaction performed at 70 °C for 2 h under mechanic stirring. The citrate concentration was varied from 25 mM to 1000 mM and 0 mM of trisodium citrate coating was used as a negative control (IONPs@TREG and ZFNPs@TREG). Data represented as the mean ± standard deviation of three independent samples (n = 3). P-values obtained by one-way ANOVA, followed by Dunnett's T3 t-test (unequal variances t-test). *p < 0.05, **p < 0.01, ***p < 0.001, and ****p < 0.0001.

Hachani *et al*. reported similar problems with the stability of IONPs@TREG when dispersed in water. [201] This is assumed to be due to the low polarity and long carbon chain of polyethylene glycol. [204] Aggregation and sedimentation occurred and increased over time. Moreover, the binding affinity of the polyols on the particle surface may be weak, leading to the dissociation of TREG molecules. It is important to emphasize the difference in synthesis methods and experimental conditions. Maity *et al.* demonstrated the fabrication of IONPs@TREG using thermal decomposition under intert environment. The method represented by Hachini *et al.* and this study are based on the polyol method in an autoclave condition and normal atmosphere. The fundamental interactions between polyethene glycol and metal nanoparticles in the autoclave-assisted polyol method need further investigation to reaveal a robust binding mechanism.

Turning back to the replacement of the ligand, the first method carried out the ligand exchange under mechanical stirring at 70 °C. After the reaction, the hydrodynamic sizes of both MNPs were inversely correlated with the concentration of added citrate (Figure 2.4). Increasing the concentration of the citrate resulted in a decrease in their hydrodynamic diameters. The optimum concentration of citrate for the ligand exchange using mechanical stirring was 1000 mM. The hydrodynamic diameters of IONPs@citrate and ZFNPs@citrate were 48.39 nm and 44.31 nm, respectively, which were close to their core sizes.

Then, the coating temperature under stirring force was optimized. The MNPs@TREG were reacted with 1000 mM citrate at RT, 70 °C, and 90 °C. The hydrodynamic size of the IONPs@citrate ranged from 52.98 nm to 19.15 nm and that of the ZFNPs@citrate varied from 45.55 nm to 25.28 (Figure 2.5). The coating temperature at 90 °C resulted in a significant decrease in the hydrodynamic sizes of the MNPs@citrate compared to those coated at RT and 70 °C. It reveals that heat affects the rate of citrate absorption. [219] However, at 90 °C, the colour of the MNPs@citrate turned from its original dark brown to a light yellowish brown. It suggests that an oxidation reaction occured during the ligand exchange when the MNPs@citrate were exposed to heat. [6, 215, 217, 220] Citrate molecules covering the surface of the nanoparticles can prevent oxidation. Citrate is known as a reducing agent. Upon heat stimuli, it may decompose

from the surface of the metal oxide nanoparticles and the particles become oxidised. This repercussion subsequently impairs magnetization negatively. Hence, the reaction at 90 °C was discarded. According to Figure 2.5, there was no significant difference in the hydrodynamic diameters between the RT and 70 °C samples. Therefore, the ligand exchange reaction under mechanical stirrer was found to be optimized when the concentration of citrate was 1000 mM and the reaction was operated at RT.

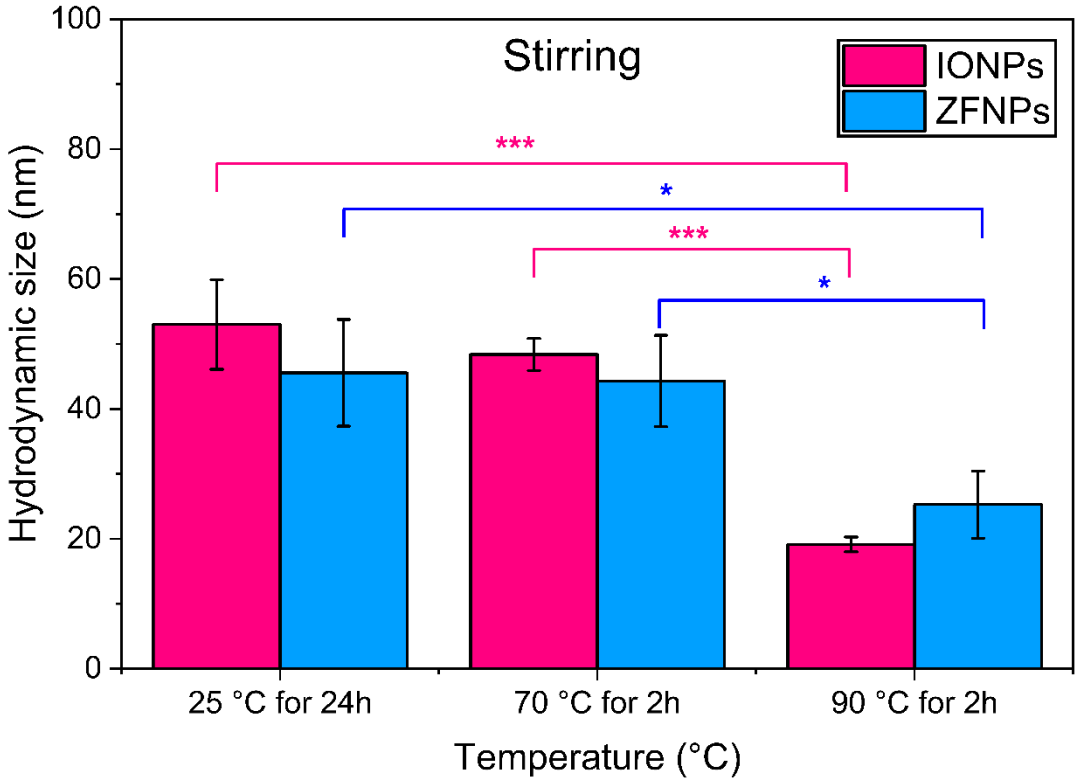

Figure 2.5 Hydrodynamic sizes of IONPs@citrate and ZFNPs@citrate after ligand exchange reaction performed at different reaction temperatures under mechanic stirring. The citrate concentration was 1000 mM. Data represented as the mean ± standard deviation of three independent samples (n = 3). P-values obtained by one-way ANOVA, followed by Bonferroni t-test (equal variances t-test). *p < 0.05, **p < 0.01, ***p < 0.001, and ****p < 0.0001.

2.4.1.3.2 Rotary mixer

Due to the limitations of using a magnetic stirrer, the mass production of the citrate-coated nanoparticles is hindered. It is also of interest to investigate whether the mechanical stirring force affects the efficiency of the ligand replacement reaction.

The reaction was conducted under a rotary mixer which provided gentle force to continuously mix the MNPs@TREG and the citrate. The optimum concentration of the citrate was determined and the results are shown in Figure 2.6. Similar to the stir-based method, the optimum citrate concentration was found to be 1000 mM. The hydrodynamic diameter significantly decreased with the increasing concentration of the added citrate. At 1000 mM citrate addition, the hydrodynamic size of IONPs@citrate was 41.23 nm and that of ZFNPs@citrate was 38.49 nm.

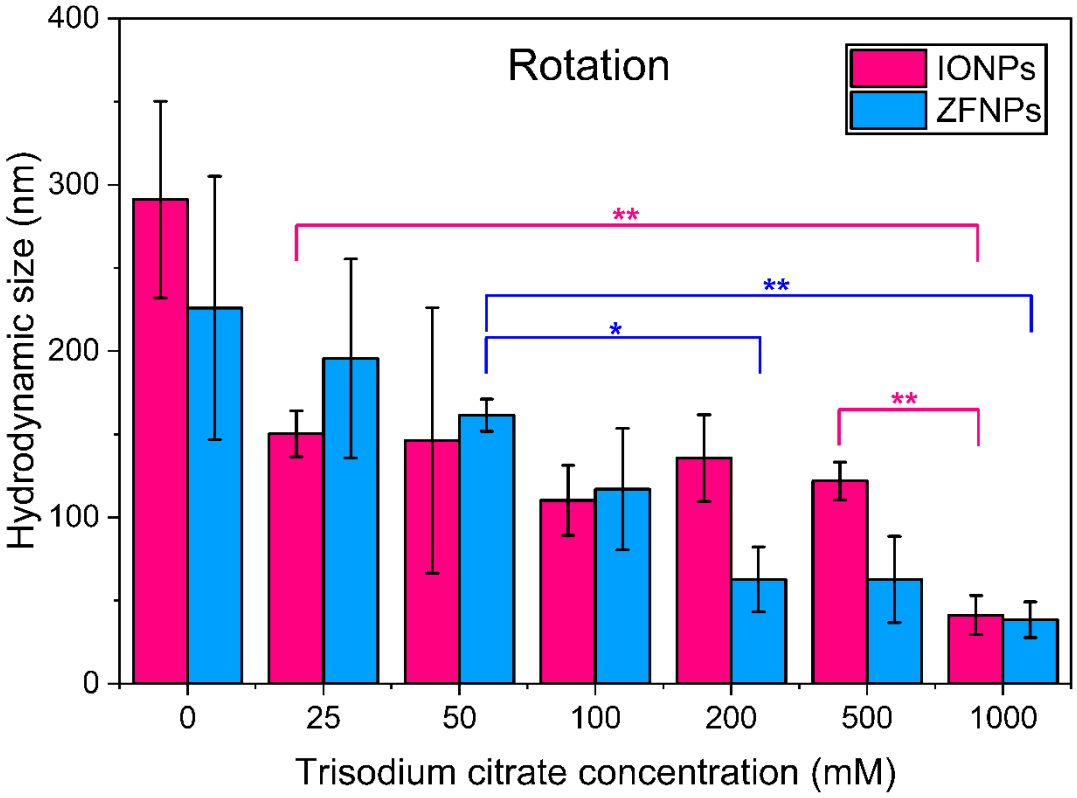

Figure 2.6 Hydrodynamic sizes of IONPs@citrate and ZFNPs@citrate after ligand exchange reaction performed at RT under gentle rotation. The citrate concentration was varied from 25 mM to 1000 mM and 0 mM of trisodium citrate coating was used as a negative control (IONPs@TREG and ZFNPs@TREG). Data represented as the mean ± standard deviation of three independent samples (n = 3). P-values obtained by one-way ANOVA, followed by Dunnett's T3 t-test (unequal variances t-test). *p < 0.05, **p < 0.01, ***p < 0.001, and ****p < 0.0001.

The solutions of IONPs@TREG and ZFNPs@TREG were mixed with 1000 mM citrate and the ligand exchange reactions were held at RT for 24 h, 48 h, and 72 h. The DLS results showed that increasing the duration of MNPs@TREG in the citrate solution

did not result in significant change in the hydrodynamic diameter (Figure 2.7). Therefore, the MNPs@TREG were incubated with 1000 mM citrate using the rotary mixer for 24 h. The hydrodynamic sizes of IONPs@citrate and ZFNPs@citrate were 41.23 nm and 38.49 nm, respectively.

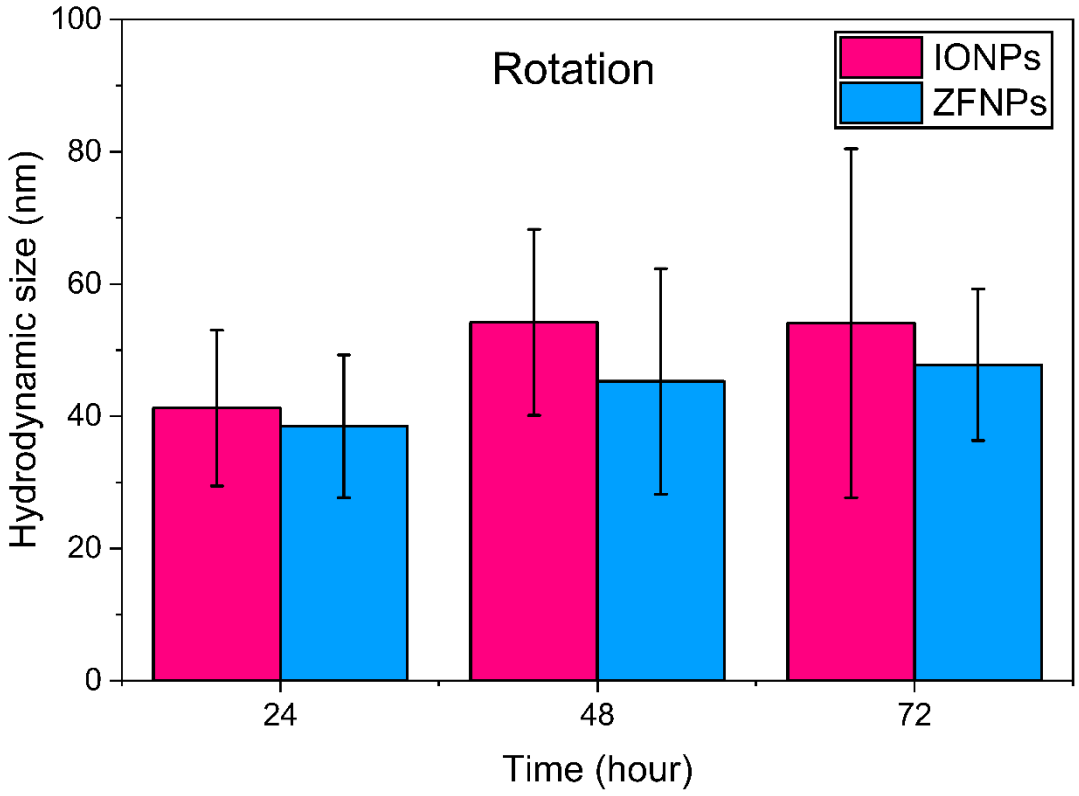

Figure 2.7 Hydrodynamic sizes of IONPs@citrate and ZFNPs@citrate after ligand exchange reaction performed under gentle rotation with different reaction times: 24 h, 48 h, and 72 h, at a citrate concentration of 1000 mM. Data are represented as the mean ± standard deviation of three independent samples (n = 3). P-value obtained by one-way ANOVA indicates no significant differences between samples.

After the ligand exchange reaction, the MNPs@citrate suspended in water were responsive to a permanent magnet (Figure 2 in Appendix A). Citrate moieties are the derivative of citric acid which chemically coordinate their carboxylates to the Fe-OH sites of metal oxide particles. [219] The remaining carboxylate groups are exposed to water, resulting in the hydrophilicity of the MNPs@citrate and high stability in water. The citrate coating prevents aggregation by electrostatic repulsion.

The protocol for citrate coating using a magnetic stirrer was optimised showing that the citrate was added at 1000 mM and the reaction could be performed at RT. This method yieled IONPs@citrate and ZFNPs@citrate with hydrodynamic diameters of 52.98 nm and 45.55 nm, respectively. The rotary mixer was also used for the ligand exchange at RT, with the citrate concentration kept at 1000 mM. It yielded the IONPs@citrate with hydrodynamic size of 41.23 nm and the ZFNPs@citrate with a diameter of 38.49 nm.

In comparison, both the stirrer and the rotator required 1000 mM citrate and operation at RT. However, gentle rotation to continuous activate the ligand replacement reaction resulted in slightly smaller hydrodynamic sizes of the MNPs@citrate. Moreover, the rotary mixer does not require setup like the magnetic stirrer and several samples can be added to the rotator at a single time. Therefore, the rotary mixer was used to produce the carboxylate-containing MNPs in this thesis.

To confirm that citrate molecules had replaced TREG, FTIR measurement was carried out. This technique is based on the energy absorbed by the the surface chemistry coating of solid samples and the optical transmission is measured. According to Figure 2.8, IONPs@TREG and ZFNPs@TREG obtained from the polyol-based fabrication showed peaks in the region of 1586 cm^{-1} (O-H stretching), 1418 cm^{-1} (C-H bending), 1388 cm^{-1} (O-H bending). [199, 221] A broad range of the spectrum between 3600 and 3000 cm^{-1} with a centre at around 3407 cm^{-1} indicated the –OH groups of the TREG and residual water. [199, 222] These absorption peaks confirmed the presence of TREG molecules on the surface of IONPs@TREG and ZFNPs@TREG.

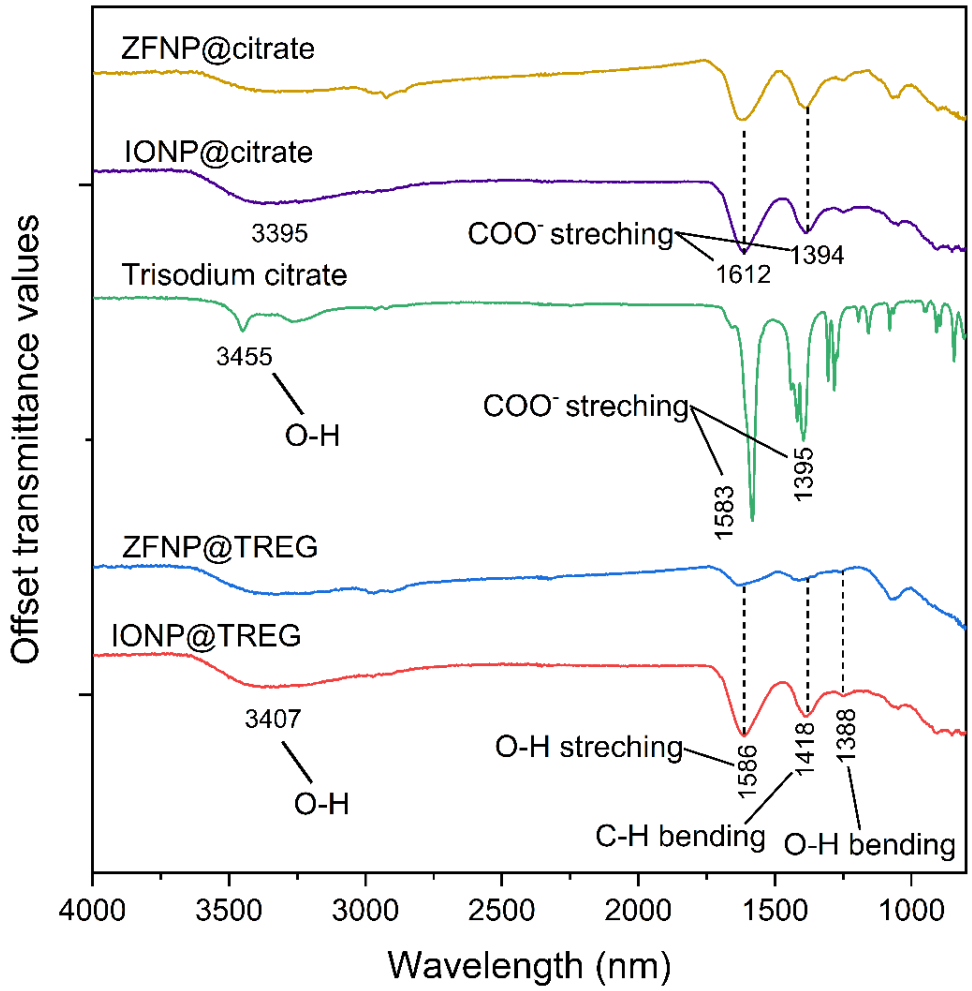

Figure 2.8 The IR spectrums of IONPs@TREG, ZFNPs@TREG, trisodium citrate, IONPs@citrate, and ZFNPs@citrate

A change in spectral absorption was found after replacing TREG with citrate. The IR absorption of trisodium citrate powder exhibited asymmetric stretching (1583 cm^{-1}) and symmetric stretching vibration (1395 cm^{-1}) of carboxylate, suggesting the deprotonation of free acids. [223, 224] Both IONPs@citrate and ZFNPs@citrate showed distinct peaks at 1612 cm^{-1} and 1394 cm^{-1},correspondind to the carboxylate, which were slightly shifted due to the chelation effect as the oxygen atoms of the carboxylate bind to the surface of the MNPs. [200, 217, 224, 225] The FTIR results confirmed the absorption of citrate on the nanoparticles.

Confirmation of citrate coating was also performed using zeta potential measurement. The pH of the IONPs@citrate and ZFNPs@citrate suspensions was altered from 3 to 9. As shown in Figure 2.9, the isoelectric points of both

IONPs@citrate and ZFNPs@citrate were not observed in this pH range. IONPs@citrate and ZFNPs@citrate were highly negatively charged in water and their zeta potentials became more negative as the pH increased. The maximum zeta potential values were found at pH 6.0 for IONPs@citrate (-44.3 mV) and pH 8.0 for ZFNPs@citrate (-40.7 mV). The carboxylate groups of the citrate contributed to the negative charge of the MNPs@citrate, confirming the coating of citrate molecules on the nanoparticles. In theory, nanoparticles with an absolute zeta potential value greater than 20 are considered to be colloidal stable due to electrostatic repulsion. [226] Therefore, the MNPs@citrate were very stable in water after the ligand exchange reaction.

The long-term stability of MNPs@citrate has not been investigated in this study but it has been demonstrated in previous works. Citrate-coated IONPs remained stable in water for up to 21 days [227] and 36 days. [220] Another study demonstrated the stability of citric acid-coated IONPs in different pH conditions, revealing that the IONP dispersions maintained a stable hydrodynamic size for 30 days at pH 5, 7 and 9.

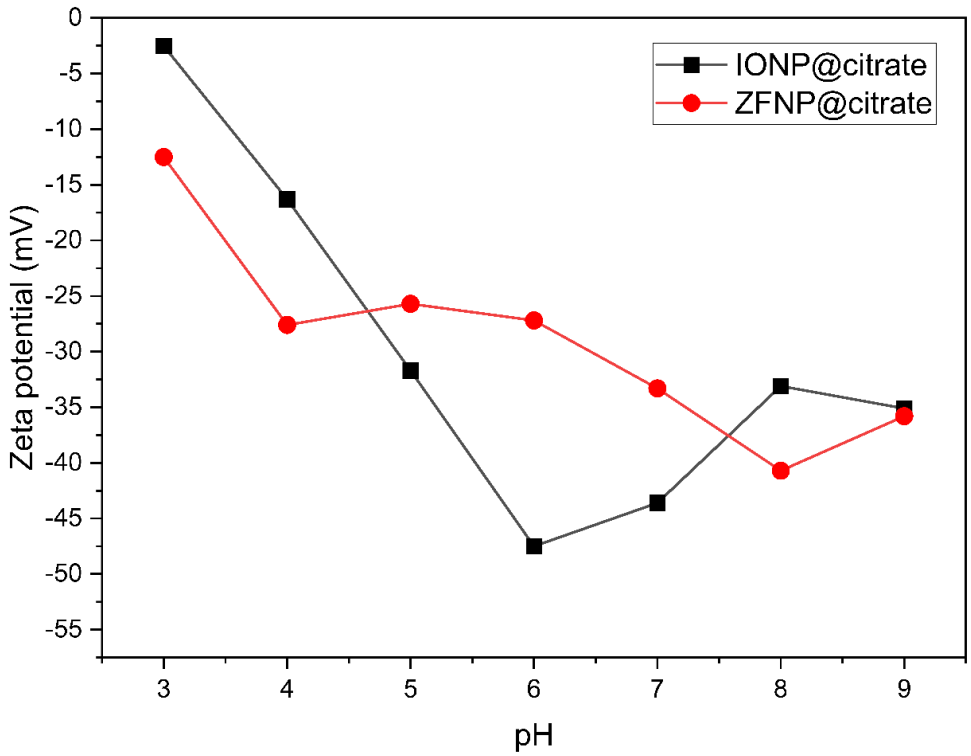

Figure 2.9 Zeta potential of IONPs@citrate and ZFNPs@citrate in water with pH ranging from 3 to 9.

2.4.2 The synthesis and characterisation of gold nanospheres

In the synthesis of AuNSPs, the concentrations of gold precursor and the reducing agent were altered to assess the kinetic growth of spherical gold formation and reveal the size tunability. Figure 2.10 presents the effect of the amount of gold precursor when the amount of the reducing agent was held constant. At 0.01 wt% chloric acid, AuNSPs with an average size of 20.87 nm were obtained. The size distribution was relatively high due to a ceratin amount of non-spherical and large particles (Figure 2.10A). Increasing the concentration of the gold salt (0.03 wt%) reduced the diameter of the AuNSPs to 11.02 nm and improved the uniformity of the nanoparticles (Figure 2.10B). It was found that elevating the concentration of the gold salt decreased the number of large and non-spherical particles.

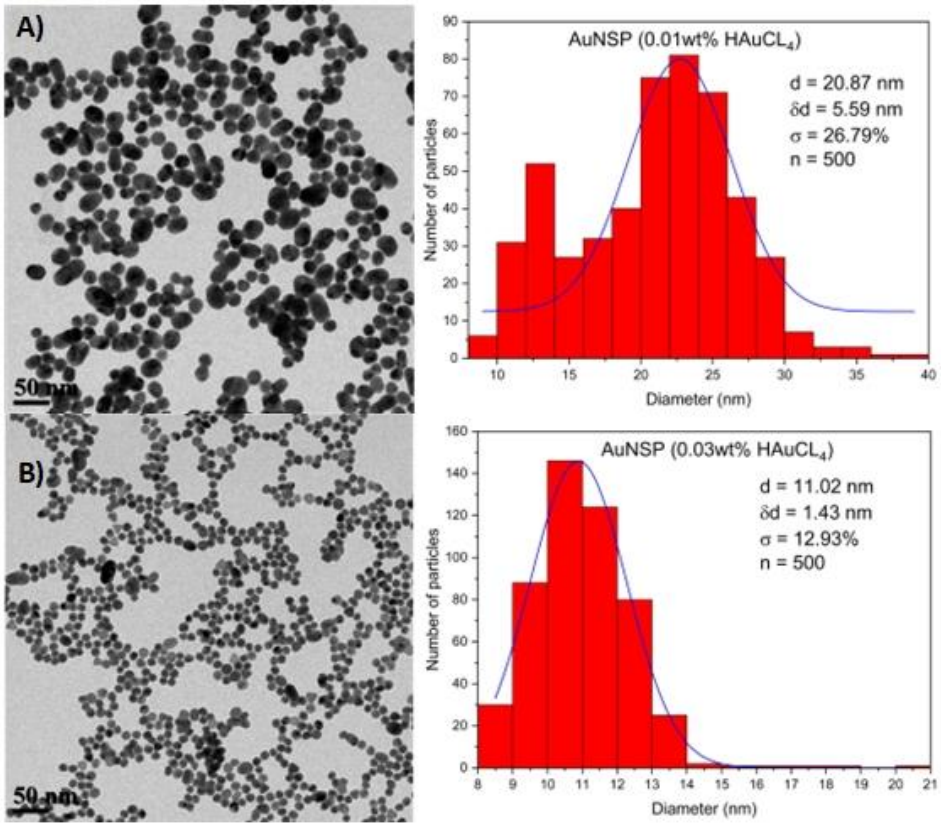

Figure 2.10 TEM images (on the left) and size distributions (on the right) of AuNSPs produced with A) 0.01 wt% $HAuCL_4$ and B) 0.03 wt% $HAuCL_4$ (n = 500). d = mean diameter, δd = standard deviation, σ = polydispersity index.

To further understand the growth mechanism of AuNSPs, the amount of citrate added was varied. As shown in Figure 2.11, the average diameter of AuNSPs was inversely proportional to the amount of trisodium citrate. The diameter and size distribution of the resulting AuNSPs were affected by an increase in the reducing agent. When 5mL of 1 wt% trisodium citrate was added, 12.03 nm AuNSPs with a negligible amount of non-spherical particles were produced. The largest AuNSPs, which were 33.54 nm in diameter, were received by adding 1.25 mL of the reducer. However, the polydispersity index (σ) was relatively high (41.10%) and the yield of the synthesis was low. This suggests that an insufficient amount of the reducer cannot produce monodispersed AuNSPs with a high yield.

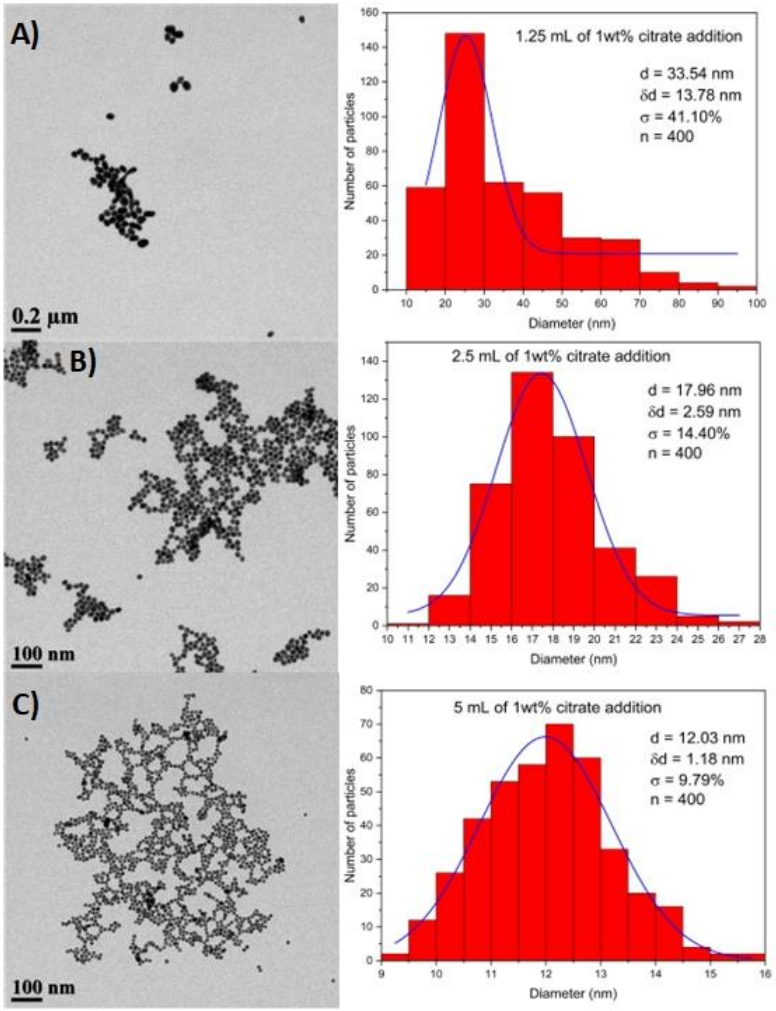

Figure 2.11 TEM images (on the left) and size distributions (on the right) of AuNSPs produced with different volumes of 1 wt% trisodium citrate: A) 1.25 mL, B) 2.5 mL, and C) 5 mL (n = 400). d = mean diameter, δd = standard deviation, σ = polydispersity index.

The AuNSPs with diameters ranging from 12.03 to 33.54 nm were subjected to UV-vis measurement and the results are presented in Figure 2.12. The LSPR wavelengths of the AuNSPs, from the smallest to the largest, are 517 nm, 522 nm, and 534 nm. The maximum absorption peaks were red-shifted due to the change in their optical extinctions, which typically depends on the size of the plasmonic nanoparticles. [42, 228] This size-dependence enables the potential to tune the LSPR of the AuNSPs by modifying the amount of gold salt and citrate. However, this study cannot produce AuNSPs with an LSPR at 600 nm, which is the maximum wavelength provided by the LED (see Figure 1 in Appendix A).

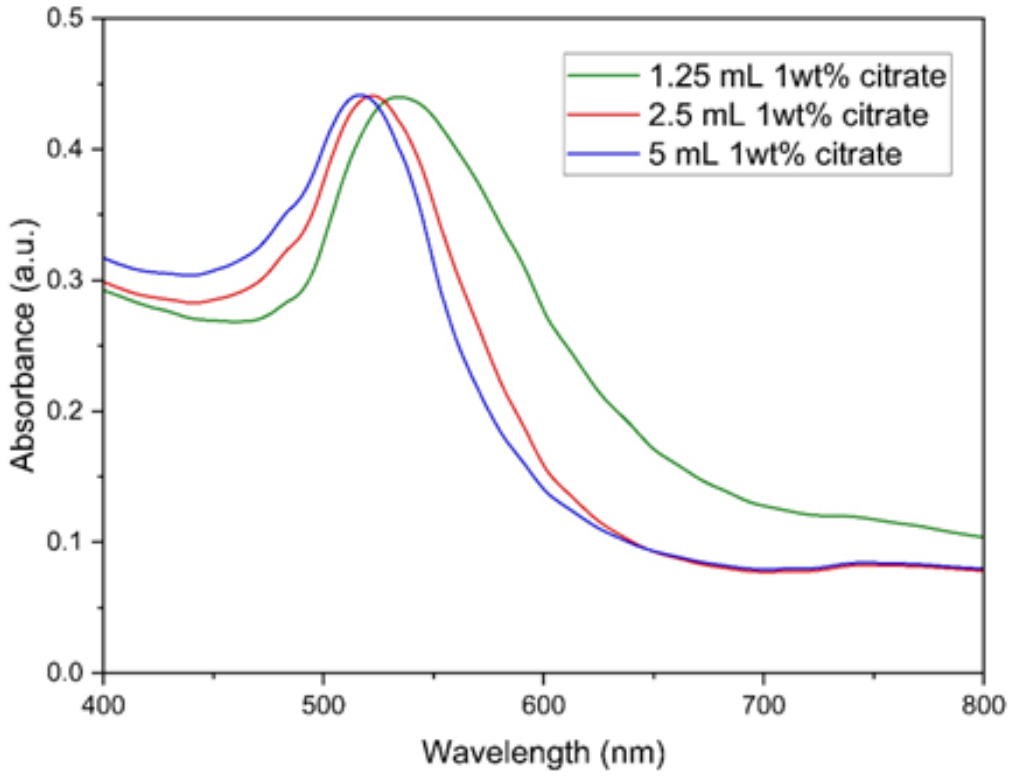

Figure 2.12 Absorption spectra of AuNSPs produced by the addition of different volumes of trisodium citrate, in the wavelength range of 400-700 nm.

The well-established Turkevich method was carried out in this study to produce AuNSPs due to its simplicity and reproducibility. The synthesis is based on the reduction of gold chloride by a reducer, typically trisodium citrate. [209] The nucleation and gold nanoparticle formation can be identified by the colour change during the synthesis. After pouring the trisodium citrate into the boiled solution of the gold salt, a sudden colour change from light yellow to dark purple to red wine was observed.

This phenomenon was caused by the reduction of Au^{3+} to Au atoms and the subsequent isotropic growth of nanocrystals. The colour of the solution became red wine indicating the successful formation of AuNSPs in the solution. [209] After this point, extra addition of trisodium citrate or extending the heating duration does not affect the size and shape of the resulting particles.

In this study, the diameter of the AuNSPs can be tailored between 12.03 to 33.54 nm by modifying the concentration of the gold salt and trisodium citrate. The larger the diameter the AuNSPs, the lower the monodispersity, which is in consistent with previous studies. [205, 206, 209] It is worth noting that the synthesis was also done with the addition of 0.4 mL trisodium citrate to the gold salt solution. According to the TEM image in Figure 2.13, the AuNSPs were large and many non-spherical shapes appeared in the sample. The optical absorption showed an LSPR peak at 529 nm. The contamination of various shapes broadened the absorption peak of the sample. In the experiment, it was observed that the solution did not change to red but instead changed to a faint purple-blue at the end of synthesis, pointing out that the mixture of gold salt and trisodium citrate may have failed to sufficiently convert Au^{3+} into atoms in the nucleation process. Due to the shortage of gold atoms, it led to adverse effects of agglomeration, large size distribution, broad-spectrum absorption, and instability of the nanoparticles. It is reasonable because 1.25 mL of trisodium citrate addition showed a sign of insufficient reduction to provide uniformity of the final product.

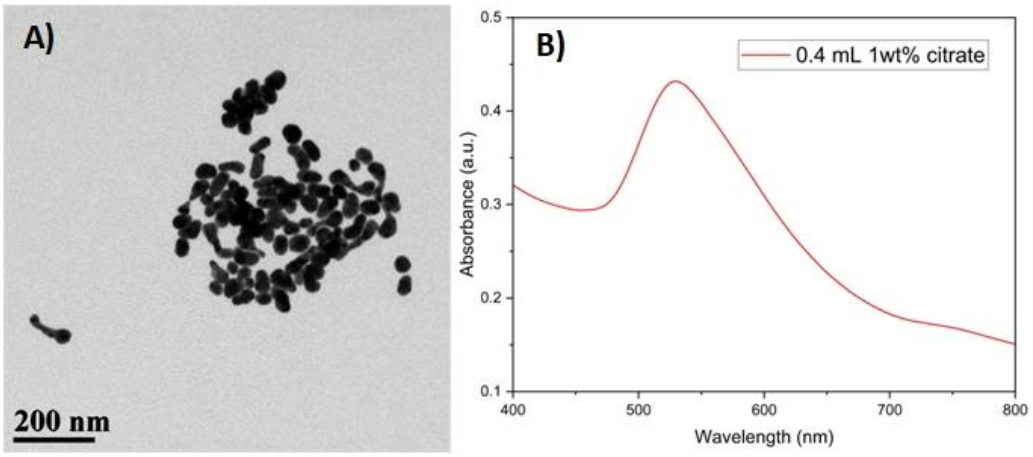

Figure 2.13 A) TEM image and B) optical absorption of AuNSPs with 0.4 mL trisodium citrate added.

Empirically, AuNSPs were observed to remain stable in dispersion after synthesis. However, a comprehensive stability study was not conducted in this work. Nevertheless, the literature reports the colloidal stability of citrate-stabilised gold-coated IONPs for up to 21 days. [227] Additionally, another previous study demonstrated that citrate-stabilised AuNSPs can maintain their stability without any significant changes in hydrodynamic size for up to 20 days when stored in the dark at 4 °C. [229] Since all AuNSPs were consistently stored at 4 °C in a refrigerator until use, it is reasonable to assume that aggregation of the particles was minimal.

2.4.3 The synthesis and characterisation of gold nanorods

AuNRs were produced using a silver-assisted seed-mediated growth method. To tune the longitudinal LSPR absorption peak to aligh with the wavelength provided by the LED (400-700 nm), the amounts of additive salts and reactants were altered to examine the impact on the dimensions and optical spectra of the AuNRs. A variety of characterisations was performed to reveal the physical properties of the resulting nanoparticles.

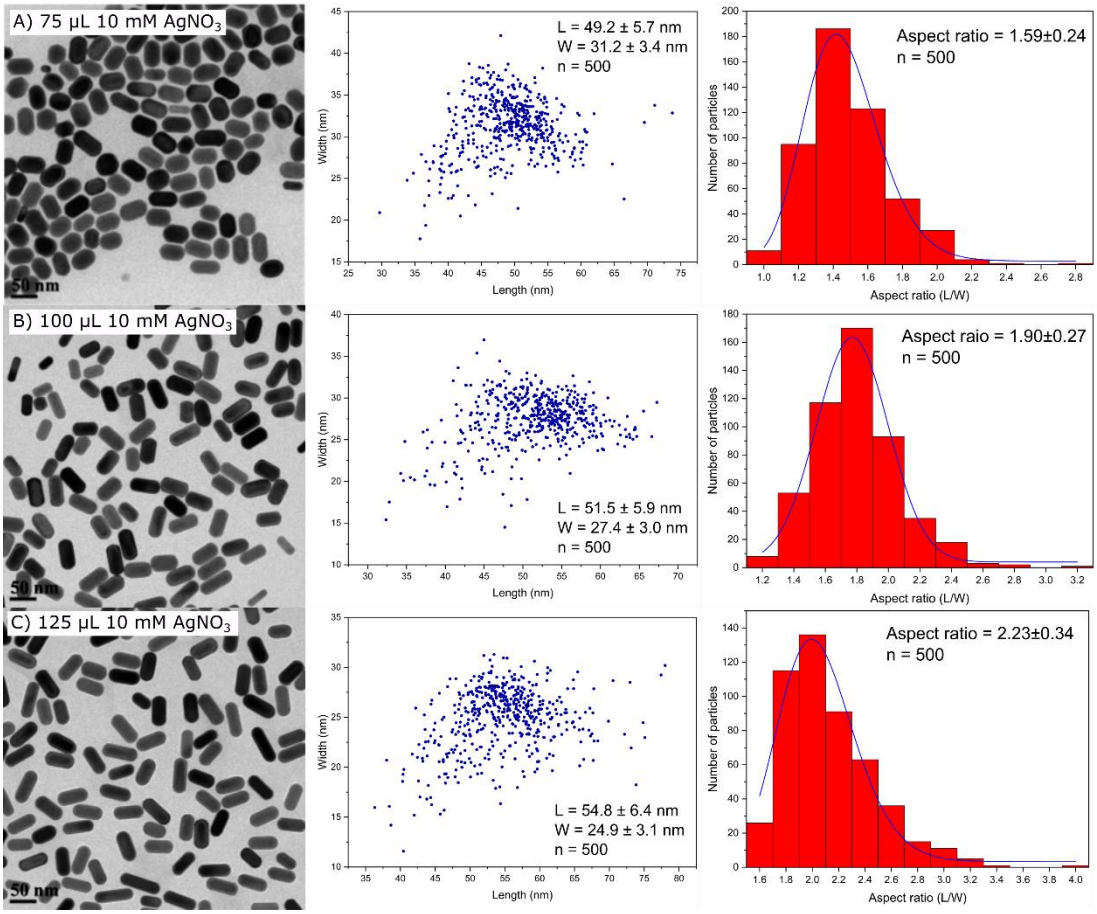

Figure 2.14 TEM images and aspect ratios of the NaBr-assissted AuNRs synthesized with different amounts of 10 mM $AgNO_3$: A) 75, B) 100, and C) 125 µL (n = 500). L = average length of AuNRs, W = average width of AuNRs.

A set of AuNR synthesis experiments aimed to explore the role of the additive salts (NaBr and $NaNO_3$) in tuning the shape and LSPR of the nanorods. The TEM images of the AuNRs synthesized with the addition of the NaBr are presented in Figure 2.14. A small number of spheroid impurities were observed when 75 µL of silver nitrate was added (Figure 2.14A). Increasing the silver content reduced the formation of non-rod particles (Figure 2.14B and Figure 2.14C). It is clear that the amount of silver nitrate is associated with the aspect ratio of the AuNRs. The minimum volume of silver nitrate was found to be 75 µL, below which only spheroids were obtained. The higher the level of silver ions, the longer the length and the smaller the width of the rods. Therefore, increasing the amount of the silver resulted in a higher aspect ratio of the nanorod.

In contrast, the presence of $NaNO_3$ in the growth solution resulted in longer rod-like nanoparticles. In Figure 2.15, the aspect ratio of the rods was 4.91 which was much higher than those of the AuNRs synthesized with NaBr additive. Moreover, fewer impurities were observed. The aspect ratio of the NaBr-assisted AuNRs ranged from 1.59 and 2.23 while the $NaNO_3$-assisted AuNRs had an aspect ratio of 4.91. The length of the AuNRs obtained by NaBr and $NaNO_3$ syntheses was similar (~50 nm). However, the thickness of the rods in the $NaNO_3$-assisted method (~10 nm) was less than that of the NaBr-assisted method (~25-30 nm).

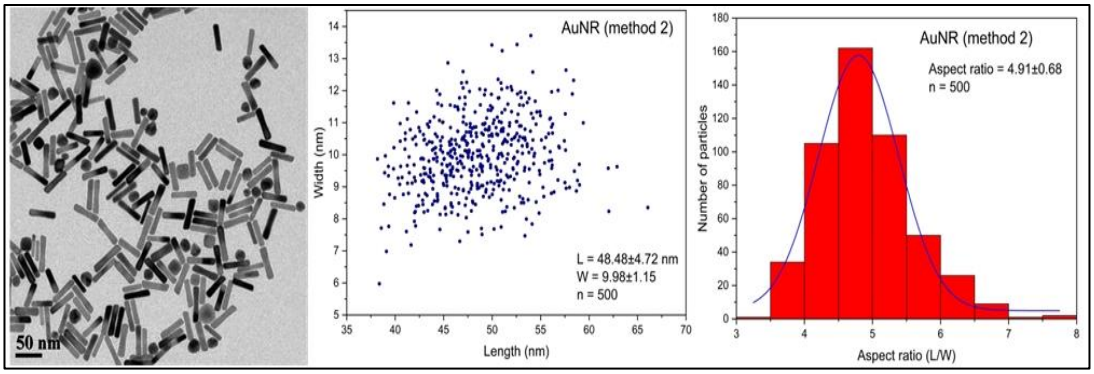

Figure 2.15 TEM image and aspect ratio of the $NaNO_3$-assissted AuNRs (n = 500). L = average length of AuNRs and W = average width of AuNRs.

Unlike isotropic plasmonic AuNSPs, AuNRs exhibited two peaks in their spectra, corresponding to the transverse LSPR (weaker intensity) and the longitudinal LSPR (stronger intensity) plasmon bands of the nanorods (Figure 2.16). In accordance with the aspect ratio, the LSPR bands of the AuNRs produced with NaBr addition were at shorter wavelengths than those synthesized with the addition of $NaNO_3$.

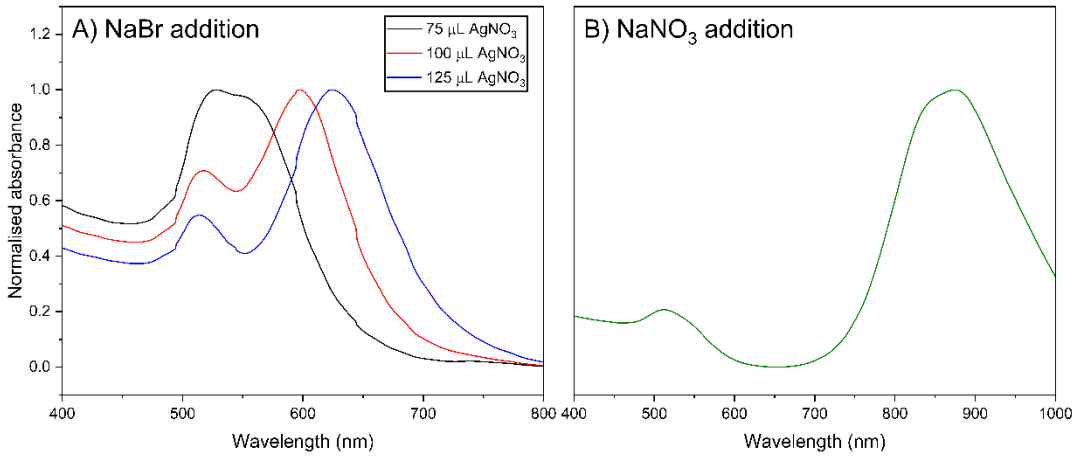

Figure 2.16 Absorption spectra of AuNRs produced with the A) NaBr additive with the diversity of the added amount of $AgNO_3$ and B) $NaNO_3$ additive.

The LSPR peaks of the AuNRs were observed at 560, 600, and 625 nm when 75, 100, and 125 µL of silver nitrate were added, respectively (Figure 2.16A). Increasing the amount of silver nitrate caused a redshift corresponding to the aspect ratio. [210, 213] With the addition of 75 uL of silver nitrate, it was difficult to distinguish between longitudinal and transverse LSPR because the peaks were merely merged due to low aspect ratio (1.59) of the rods. The electrons that travel along the x and y axes had almost the same distance, and hence, the longtitudinal and transvere LSPR peaks were close in the spectrum. On the other hand, in Figure 2.16B, the rods grown in the presence of $NaNO_3$ had an LSPR band at 870 nm, showing the maximum absorption in the NIR spectrum.

Typically, the aspect ratio of AuNRs is related to the maximum absorption wavelength of the LSPR. [210] Adding NaBr additive yielded AuNRs with the LSPR in the visible region of the electromagnetic spectrum, whereas the addition of $NaNO_3$ redshifted the LSPR to the NIR region. The maximum absorption wavelength of the $NaNO_3$-assissted AuNRs fell into the NIR region, which was not the region of interest. Because the study was interested in the LSPR in the visible range, the NaBr-assisted method was chosen to prepare the AuNRs for photothermal testing in the next chapter.

The finding is in agreement with an earlier study which reports that the use of NaBr yields AuNRs with a lower aspect ratio than the use of $NaNO_3$. [210] NaBr and $NaNO_3$ have counterions to the cation CTAB. Modifying their concentrations leads to the change of micelle morphology due to the screening effect of the electrostatic repulsion of the CTAB polar heads. [210] In turn, this triggers a shape transition and affects the surfactant arrangement of micelles. Furthermore, bromide causes the passivation of the gold but induces silver underpotential attachment on the gold surface which inhibits the formation of gold in a certain direction.

Silver nitrate plays an essential role in the formation of AuNRs, as its mechanism has been elucidated. [213, 230] The presence of CTAB micelles in the growth solution leads to the formation of "Ag-Br-surfactant" complexes having higher binding affinity than CTAB. This complex competitively binds to specific facets of the gold seed, reinforcing the micelle bilayers of the complex. [226] Subsequently, the surfactant hinders the absorption of gold ions on these facets, forcing them to diffuse to the tip end and elongate in a certain direction, where the growth of rod-shaped nanoparticle begins. Moreover, the remaining ions in the growth solution including Ag^+, $AuCl_4^-$, and ascorbate are consumed over time until depletion, ensuring the continuous growth of the nanorods. It emphasizes the vital role of the precursors and the reducers in controlling the aspect ratio of the rods. [210]

To produce gold seed, gold salt was firstly reacted with the strong reducing agent $NaBH_4$, leading to the rapid reduction of Au^{3+} to Au^0. [211] This was followed by the formation of small CTAB-capped seeds. The ascorbic acid in the growth solution reduced Au^{3+} to Au^+ and successful reaction was indicated by a colour change of the solution from brownish to colourless. However, the reduction of Au^+ to Au^0 did not occur because the ascorbic acid is a weak reducer. [210, 231] Once the seeds were brought to the growth solution, further reduction (Au^+ to Au^0) was executed on the surface of the gold seeds, which served as nucleation sites for the elongation of nanorods. [231] The colour of the mixture slowly changed indicating the formation of the nanorods. Different aspect ratios result in the different colour expression due to the optical extinction of the rods corresponding to the aspect ration. [213]

The advantage of using CTAB as the surfactant in the synthesis is the monodispersity of the final products, with negligible non-cylindrical shapes that could otherwise lead to a broad plasmonic absorption band. [213] The existence of the CTAB surfactant in the seed solution is responsible for the generation of isotropic nanoparticles. [210] Because of the ampliphilic nature of CTAB molecules, they self-assembled into spherical micelles in water, resulting in the formation of tiny CTAB-capped AuNSPs.

An important aspect to consider is the long-term stability of AuNRs. A previous study demonstrated the colloidal stability of CTAB-coated AuNRS using a seed-medaited method, similar to the one used in this thesis. [232] They revealed that storing AuNRs in 0.01 M CTAB solution at RT would maintained the rods' stability for up to 9 months. However, it is important to note that AuNRs in this thesis were stored in water at RT, which could affect their short-term stability. As a consequence, CTAB potentially detached and must be addressed in future works.

2.4.4 The synthesis and characterisation of gold nanostars

In addition to AuNRs, this study attempted to produce another type of asymmetric gold nanoparticles: AuNSTs. These star-like nanoparticles were produced using a seed-mediated method, following the previous protocol with slight modifications. [56] AuNSPs with two different diameters (12 and 20 nm) were used as core seeds. Several spikes grew from the cores of the AuNSTs, as shown in the TEM images in Figure 2.17. The AuNSTs had diameters of 65.37±12.45 nm and 243.69±36.10 nm for the 12 nm and 20 nm gold seeds, respectively. As expected, the synthesis using the larger AuNSPs produced larger AuNSTs than the synthesis using the smaller AuNSPs. However, the yield of the synthesis was low and the CTAB surfactant was not sufficient to stabilise the AuNSTs in water, resulting in rapid aggregation. It is hypothesized that the CTAB surfactant cannot overcome the electrical attraction of the small AuNSTs due to high surface charge density. [233, 234] The protocol needs to be optimised to improve the yield and stability of the AuNSTs. Ligand exchange is a promising approach to improving the stability of the AuNSTs. Other parameters that need to be investigated include the volume of the gold seed solution, reducing

agents, gold salt concentration, duration of growth time, temperature, and type of surfactant. Changing the morpholoygy of the stars such as the length of their tips, can also alter the working wavelength of the plasmonic resposnse. This study only varied the size of gold seed particles. Overall, the AuNSTs were not optimised in this thesis and discarded.

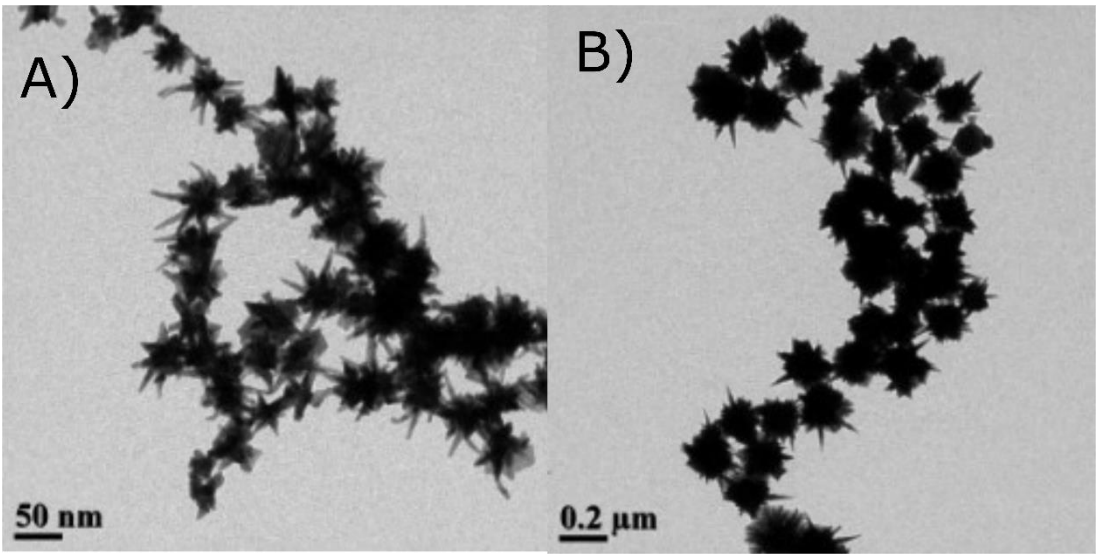

Figure 2.17 TEM images of AuNSTs produced with A) 12 nm and B) 20 nm AuNSPs.

2.5 Conclusion

This chapter explains the preparation and the characterisation of promising nanoparticles to be used in the thermochromic LFA: MNPs (IONPs and ZFNPs) and plasmonic nanoparticles (AuNSPs, AuNRs, and AuNSTs).

The spherical TREG-coated IONPs and ZFNPs were fabricated using a pressurized polyol-based method. The reaction time was found to have an impact on the morphological structure of the resulting MNPs. The longer reaction times lead to larger MNP diameter. XRD analysis confirmed the crystalline phase of IONPs and ZFNPs, and ICP-AES measurement conclusively ensured the integration of zinc into iron lattice.

Although the polyol synthesis is beneficial for reproducibility and low polydispersity, TREG ligand is not well-dispersed in water due to its low polarity and is difficult to functionalise further. Therefore, the TREG moleucles were replaced with citrate moieties in a subsequent ligand exchange process. The protocol was optimised in this study and found that mixing 1000 mM trisodium citrate with the MNPs@TREG under rotation for 24 h yielded the highest citrate coating efficiency. Heating during the ligand replacement process may cause oxidation of the MNPs. After the exchange reaction under the optimised conditions, the hydrodynamic diameters of IONPs@citrate and ZFNPs@citrate were significantly reduced to 41.23 and 38.49 nm**,** respectively, compared to the diameters of IONPs@TREG (291.13 nm) and ZFNPs@TREG (225.93 nm). The suspensions of IONPs@citrate and ZFNPs@citrate exhibited high negative zeta potentials of -44.3 mV and -40.7 mV, respectively, indicating considerable stability in the water due to electrostatic repulsion. FTIR measurement confirmed the anchoring of citrate moieties on the MNPs. The attachment of citrates provides carboxylates, which not only stabilise the MNPs but are also highly beneficial for biological functionalisation.

However, this study did not identify the number of ligands on the MNP surfaces. Thermogravimetric analysis can be included in future works to measure the mass of remaining TREG and the citrate on the surface of the MNPs after the ligand exchange reaction. With this method, the underlying mechanism of ligand exchange can be understood, which in turn allows for the improvement of the ligand exchange method.

Various shapes of plasmonic nanoparticles were produced in this study: spheres, rods, and stars. The synthesis of AuNSPs was performed by the reduction of the gold salt with trisodium citrate, known as the Turkevic method. Modification of the precursor and the reducer can tune the diameter of AuNSPs from 11.02 and 20.87 nm, with acceptable size variation. The wavelength of maximum absorption was found to be related to the size of the nanoparticles as increasing diameter redshifted the LSPR peaks of the AuNSPs from 517 to 534 nm.

The minimum volume of 1wt% trisodium citrate added was 1.25 mL, below which the final product had high polydispersity. Adding trisodium citrate below the critical level resulted in the presence of non-spheical and large gold nanoparticles, thus poor size distribution.

Asymmetric growth of the gold nanoparticles is associated with the further growth of gold seeds assisted by complex surfactants and salt additives. For the fabrication of AuNRs, adding either $NaNO_3$ or NaBr to the growth solution disrupts isotropic growth, thereby producing fine rod-like gold nanoparticles. This work found that the addition of $NaNO_3$ yielded AuNRs with a higher aspect ratio and their LSPR peaks were shifted to the NIR range. Therefore, $NaNO_3$ was not of interest in this work because the maximum absorption does not aligh with the LED spectrum, which will be used in the photothermal test. On the other hand, the addition of NaBr allows tunability of the LSPR peaks in the visible spectrum. Hence, the synthesis of the AuNRs was assisted by the addition of NaBr. In addition to salt additives, $AgNO_3$ also play an essential role in the aspect ratio of the nanorods. In this study, the LSPR peaks of the AuNRs were tunable with size-dependence in the range between 560 nm and 625 nm.

Lastly, AuNSTs were prepared from gold seeds and 63 nm and 243 nm AuNSTs were obtained. They were coated with CTAB molecules but aggregation was a problem, especially with the 63 nm AuNSTs, which sedimented quickly. In addition, the yield of the synthesis was low, indicating the need to optimise the synthesis. Therefore, AuNSTs were not included in the photothermal test in the next chapter.

The sizes and shapes of all nanoparticles were characterised using TEM measurement. Scanning electron microscopy was not employed in this study as it is primarily characterises surface morphology, whereas this study focuses on nanoparticle shapes and dimensions. For IONPs and ZFNPs, their surface coating was investigated by FTIR to confirm the success of the ligand exchange. Additionally, XRD and ICP-AES were used to ensure the incorporation of zinc into the lattice of the nanoparticles. On the other hand, these methods (FTIR, XRD, and ICP-AES) were not necessary for the characterisation of gold-based nanomaterials because their

synthesis did not involve doping or ligand exchange. Their optical properties were of importance and revealed using UV-vis measurement to determine the LSPR wavelength.

In conclusion, the production of MNPs and AuNPs has been successfully completed with proper characterisations performed. The nanomaterials that will be introduced to the initial photothermal test include IONPs, ZFNPs, AuNSPs, and AuNRs. These materials are monodisperse, reproducible, and sufficiently stable in solution. They will be used in the photothermal test, which will be discussed in the next chapter.

Chapter 3 : Light-to-heat conversion capability of photothermal nanoparticles

3.1 Introduction

A proof-of-concept study was conducted earlier (see Appendix B) to investigate the use of a thermochromic sheet as a thermal detector to improve the sensitivity of LFA detection. Various types of light sources were included in photothermal experiments to heat the MNPs (see Table 1 of Appendix B). In the pilot study, IONPs@citrate and ZFNPs@citrate suspensions (25 and 200 μg/mL) were spotted on nitrocellulose membranes and illuminated by a green laser (532 nm), an LED with the spectrum of 400-700 nm, and the same LED equipped with a 605 nm cut-on filter (final spectrum was 605-700 nm). The nitrocellulose membrane and the thermochromic sheet absorbed a certain amount of photons, leading to a slight increase in temperature, but there was no significant difference between blank and positive samples. Using the 605-700 nm LED yielded the least temperature gradient. This was reasonable becasue the use of the filter resulted in the loss of a certain amount of photons to interact with the nanoparticles and the membranes. The temperature created by the green laser was comparable to that of the full-spectrum LED. Nonetheless, the use of a laser with a radiant power between 5 and 500 mW is classified as a dangerous tool that has potential to cause serious biological damage. [235] On the other hand, using an LED is much safer and easier to install and setup. Therefore, the LED was definitively chosen to act as the light source in this project.

Colloidal IONPs@citrate and ZFNPs@citrate were manually spotted on a ntirocelluloes membrane using a pipette. after the membrane was dried, the “coffee ring” effect was observed, which hindered the determination of the correlation between concentration and temperature gradient (see Figure 1 in Appendix B). However, the results still pointed out the potential of using photothermal

nanoparticles in conjunction with the thermochromic sheet to improve the sensitivity of the LFA.

This chapter demonstrates the initial development of the thermochromic LFA, with the aim of finding the most suitable nanoparticles for heat generation and investigating the potential of using the liquid crystal thermochromic sheet to provide strong visual signals. The photothermal nanoparticles fabricated in Chapter 2 (IONPs, ZFNPs, AuNSPs, and AuNRs) were placed on nitrocellulose membranes by a reagent dispenser to simulate LFA result. Actual antibody-antigen interaction was avoided. A broad-spectrum LED (400-700 nm) was utilised to activate the photothermal effects of the nanoparticles. Subsequently, the selected nanoparticles were introduced to the comparison study to compare the signals between the typical visual signal, the thermal signal, and the theromochromic signal. An IR camera was used to track the temperature gradient for thermal signal measurement. A mobile phone (Samsung S9+, UK) was used to take photos of the nanoparticle-deposited membranes and the colour of the thermochromic sheets to measure the intensity of the coloured visual signals. Image processing using Bayer filter technology was then performed to determine the intensity of primary colours (red, blue, and green). [152, 165]

3.2 Materials and methods

3.2.1 Materials

All chemicals were of reagent grade and used as received. Hydroxylamine hydrochloride (ReagentPlus®, 99%) and 1,10-phenanthroline monohydrate (ACS reagent, 99%) were purchased from Sigma-Aldrich (UK). Hydrochloric acid (37% HCl) was delivered by Acros Organics (UK). Sodium acetate anhydrous (ReagentPlus®99.0%) was bought from Sigma Life Science (UK). Iron (II) chloride tetrahydrate ($FeCl_2 \cdot 4H_2O$, 99.0%) was purchased from Honeywell (UK). Purified water was pbtained using a Purelab Ultra Elga (UK) system and used in all reactions and nanoparticle suspension.

Whatman FF170HP nitrocellulose membranes were received from GE Healthcare Life Sciences (UK). Liquid crystal thermochromic sheets (30-35 °C) were supplied by SFXC (UK). A white warm light LED (400-700 nm) (product code: MWWHLP1) and a digital meter thermal sensor (product code: PM125D) were purchased from Thorlabs (UK). The thermal imager was the Testo 875-2i model from Testo (UK). The Testo IRsoft software was used for thermal analysis. A reagent dispenser was purchased from ClaremontBio. The photothermal nanoparticles, including IONPs, ZFNPs, AuNSPs (12 and 18 nm), and AuNRs (LSPR = 560, 600, and 625 nm) were prepared as described in Section 2.2.2.3.

All photos of samples were taken by a mobile phone (Samsung S9+, UK) to obtain .RAW files for quantitative measurement using MATLAB software. Camera settings (focal length, shutter speed, flash, and ISO) were kept constant for all images to minimise ambient interference.

3.2.2 Determination of nanoparticle concentration

3.2.2.1 Concentration of iron oxide and zinc ferrite nanoparticles

The quantification of iron mass in the IONP and ZFNP suspensions was based on a colourimetric method. [217] The calibration curve of iron mass was created to determine the iron concentration of the samples.

First, a stock of iron solution was prepared by dissolving 0.0712 g of $FeCl_2 \cdot 4H_2O$ in 500 mL of 4 M hydrochloric acid in a volumetric flask. Then, stocks of sodium acetate anhydrous (125 mg/ml), hydroxylamine hydrochloride (10 mg/mL), and 1,10-phenanthroline monohydrate (10 mg/mL) were prepared in 0.04 M HCl.

Once the iron salt was completely dissolved, two-fold dilutions of the iron salt were prepared from 0.00625 to 0.2 mg/mL. Then, 200 µL of each dilution were mixed with 450 µL of sodium acetate, 50 µL of hydroxylamine hydrochloride, and 300 µL of 1,10-phenanthroline monohydrate. They were incubated in the dark at RT for 30 min and 200 µL of each sample were transferred to a 96-well plate for absorbance

measurement at 510 nm. The absorbance values were plotted against concentration to establish the calibration curve.

The iron concentrations of the unknown-concentration samples were determined using the calibration curve. The unknown samples were diluted by a factor of ten in 4 M HCl, and 200 µL of the samples were then mixed with 450 µL of sodium acetate, 50 µL of hydroxylamine hydrochloride, and 300 µL of 1,10-phenanthroline monohydrate. They were incubated in the dark at RT for 30 min and their absorbance was measured at 510 nm.

All UV-Vis measurements were performed using a SpectraMax Me^2 microplate reader (Molecular Devices).

3.2.1.2 Concentration of gold nanoparticles

The quantification of the gold mass of gold nanoparticles was carried out using a simple method based on optical extinction coefficient. [228, 236, 237] The Lambert-Beer law, a well-known formula, is the key of this optical measurement for quantifying the mass of gold content in the nanoparticles. The formula is shown in Equation 3.1:

$$A = \varepsilon * b * C \qquad \textbf{(Equation 3.1)}$$

where A is the absorption of gold colloid, b is the standard path length of 1 cm, ε is the extinction coefficient, which was obtained elsewhere, [228, 237] and C is the concentration of gold in the solution (Molar).

The degree of polydispersity must be considered for the colourimetric-based measurement to be valid. This is because it estimates the concentration, and a broad size distribution will lead to unreliable results. The shape and size of gold nanoparticles were assumed to be ideally monodispersed. The other necessary formulas, such as the volume calculation, can be found in Appendix C.

3.2.3 Nanoparticle alignment on nitrocellulose membranes

To simulate the LFA result, nanoparticles were aligned on the nitrocellulose membrane, similar to the test line found in a common LFA strip. Only IONPs were used in this experiment.

First, the concentrations of IONP suspension was determined by the colourimetric assay (see Section 3.2.2.1) and was adjusted to 0.5 mg/mL. The dispenser was pre-programmed to feed IONPs on a nitrocellulose membrane. According to the datasheet provided by the manufacturer, synchronizing the flow rate of a syringe pump and the moving speed of the printing is necessary to achieve the desirable dispensing rate. These factors affect the width of the printed line. [124] The equation is provided as follows:

$$\frac{\textbf{Desired volume } (\mu\textbf{L})}{\textbf{Distance } (\textbf{mm})} = \frac{\textbf{Flow rate } (\mu\textbf{L/sec})}{\textbf{Head speed } (\textbf{mm/sec})} \qquad \textbf{(Equation 3.2)}$$

In this experiment, the dispensing rates were adjusted to 0.1, 0.2, and 0.3 µL/mm to investigate the variation in the width of the printed lines. The measurement was performed using ImageJ software.

3.2.4 Visual signal measurement

The colour measurement allows the determination of the intensities of red, green, and blue (RGB) colours that are composed in the image pixels. The mathematical software MATLAB was utiliesd in this work and the code was kindly provided by Dr Terrence Leung (UCL). This experiment was designed to find the most sensitive channel of the Bayer filter for optical measurement.

In the preparation step, colloidal ZFNPs in water were prepared at four different concentrations: 0.5, 1.0, 1.5, and 2.0 mg/mL. They were printed on nitrocellulose membranes using the dispenser with a dispensing rate of 0.1 and 0.2 µL/mm. The photos of the nanoparticle-deposited strips were recorded. The area of the printed line was cropped and processed in MATLAB.

Regarding the visualisation of the printied lines, the results are shown in the form of the intensity ratio between the visual signal of the line and the background. The diagram of the principle is displayed in Figure 3.1. The calculation of the signal ratio is given by Equation 3.3:

$$\textbf{Typical visual signal ratio} = \frac{I(b)}{I(t)} \qquad \textbf{(Equation 3.3)}$$

where I(b) is the average colour intensity of the background and I(t) is the average intensity of the test line.

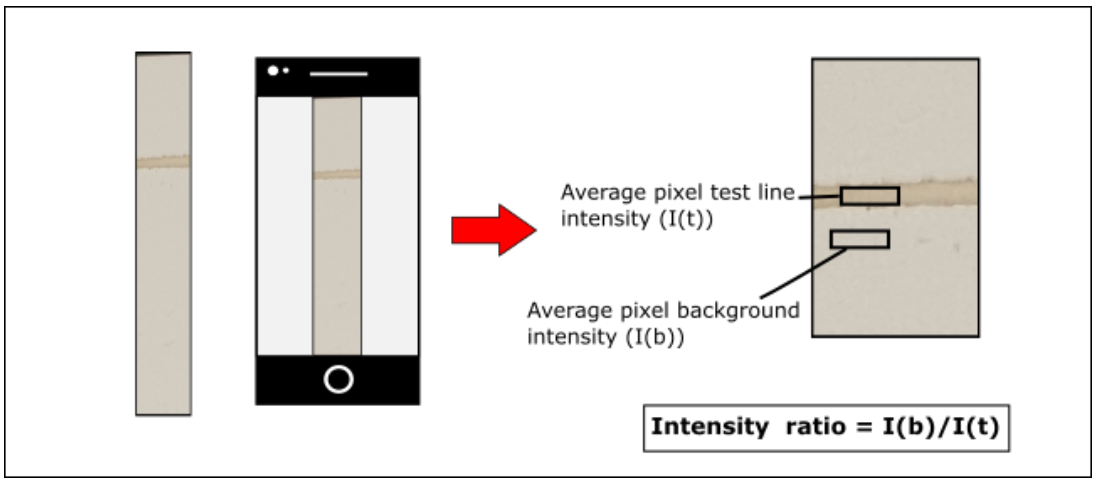

Figure 3.1 The principle of image recording and determination of the colour intensity ratio. A .RAW image of the strip containing the region of nanoparticle alignment is taken and then analysed in MATLAB to find the average RGB intensities of printed nanoparticles and the background of the membrane.

3.2.5 Thermal signal measurement

Photothermal nanoparticles were prepared in Chapter 2, including IONPs, ZFNPs, AuNSPs (12 and 18 nm), and AuNRs (LSPR = 560, 600, and 625 nm). The experiment was designed to find nanoparticles that optically respond to the illumination of the LED by showing a significant temperature gradient.

Nanoparticle-deposited nitrocellulose membranes were prepared as described in Section 3.2.3. The concentrations of nanoparticle suspensions were determined by colourimetric assays (see Section 3.2.2) and were adjusted to the concentrations

ranging from 0.0625 to 2.0 mg/mL. Then, each concentration of nanoparticles was dispensed onto the membrane at 0.1 and 0.2 µL/mm. The nanoparticle-deposited membranes were illuminated by the LED at the maximum power of 6.5 W/cm^2 for 3 min. The temperature of the area of the printed nanoparticles was measured by an IR camera with 60-s intervals: 0, 60, 120, and 180 s. The experimental setup for the heat test is displayed in Figure 3.2. A bare nitrocellulose membrane was a negative control in the experiment. Each sample was done in triplicate. The temperature gradient is determined as follows:

$$\Delta T = T_{average} - T_{initial} \quad \textbf{(Equation 3.4)}$$

where ΔT is the temperature gradient, $T_{average}$ is the average temperature of the test line, and $T_{initial}$ is the initial temperature before turning on the LED.

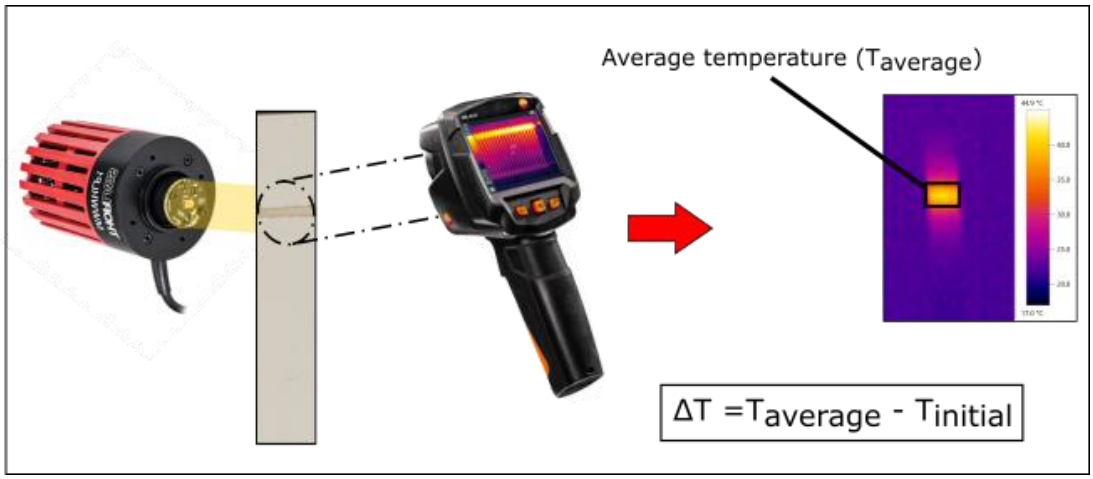

Figure 3.2 Principle of thermal signal measurement. The nanoparticles on the nitrocellulose membrane are illuminated by the LED and the thermal recording is performed by an IR camera.

3.2.6 Thermochromic signal measurement

The concentration of ZFNPs in water was adjusted to 0.0625, 0.125, 0.25, 0.5, 1.0, 1.5 and 2.0 mg/mL (see Section 3.2.2.1) and they were printed on nitrocellulose membranes by the dispenser at 0.1 µL/mm. A thermo-responsive sheet was adhered to the other side of the membrane to transform heat energy into a coloured signal

(Figure 3.3). The optimal channel of the Bayer filter to measure the colour intensity of the thermochromic signal was determined in this study.

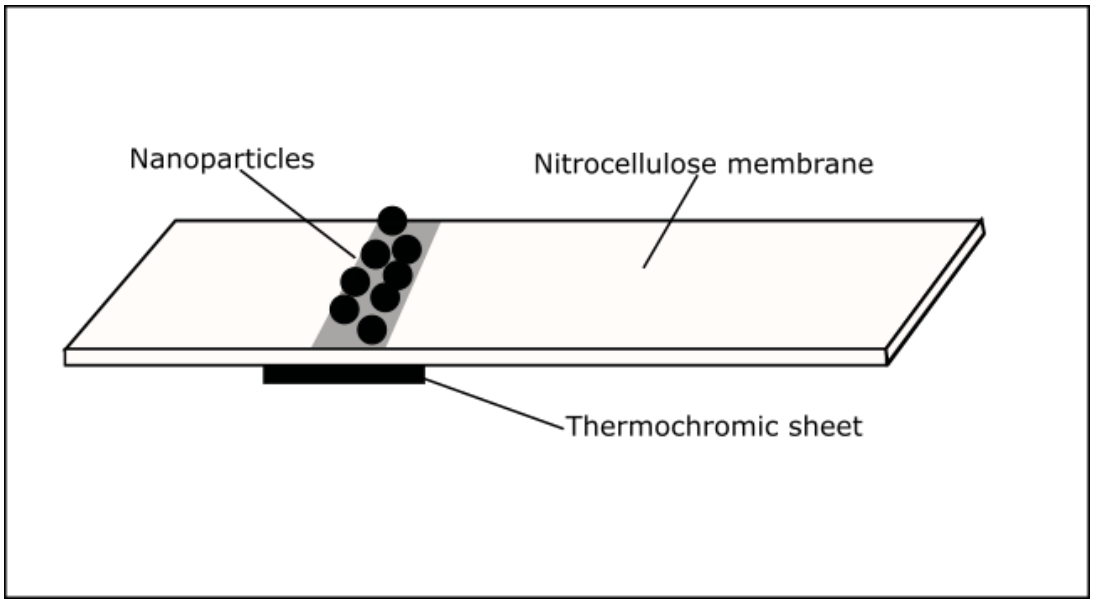

Figure 3.3 The ZFNP-deposited nitrocellulose membrane. A piece of a thermochromic sheet is attached underneath the area of ZFNPs.

The ZFNPs-deposited membranes were irradiated with 6.5 W/cm^2 of LED light for 20 s. Immediately after turning off the LED, images of the thermochromic sheets were recorded using a smartphone (Figure 3.4). The taken photos were processed in MATLAB software to extract RGB values and calculate the inntensity ratio in the corresponding channels (Equation 3.5):

$$\textbf{Thermochromic signal ratio} = \frac{\mathbf{I(t)}}{\mathbf{I(b)}} \qquad \textbf{(Equation 3.5)}$$

where I(t) is the average intensity of the nanoparticle area and I(b) is the average intensity of the thermochromic background. A non-deposited nitrocellulose membrane was used as a negative control. All samples were done in triplicate. The experiments were carried out at 25 °C.

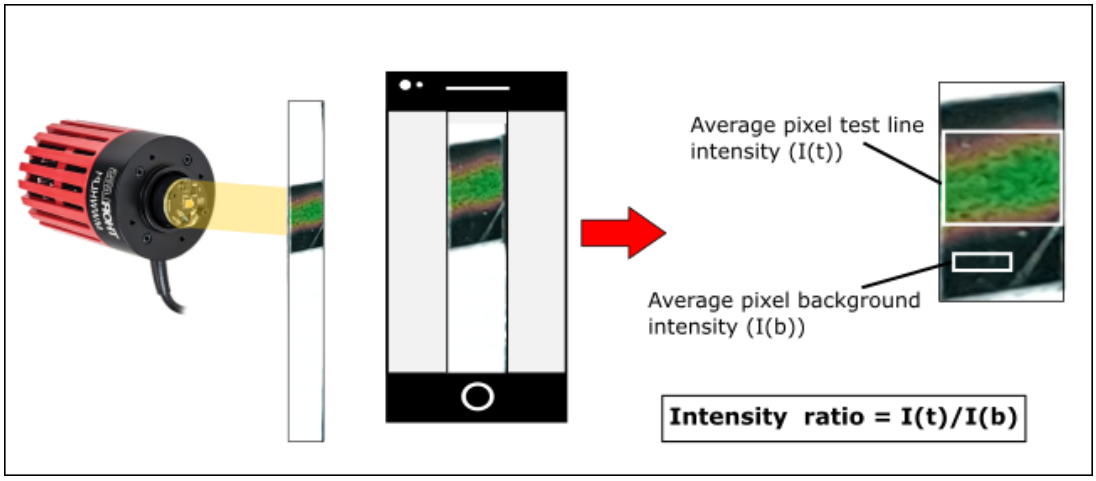

Figure 3.4 Diagram of the thermochromic signal measurement. The LED generates light to illuminate a membrane sample. A mobile phone camera records the colour change of the thermochromic sheet, which is then analysed in MATLAB.

3.2.7 Comparison between different types of signals

This section investigates the signal intensities of the typical visual signal, the thermal signal, and the thermochromic signal. ZFNPs were chosen as the model nanoparticles in this study to provide visual colouration on the strip and raise the temperature upon illumination. ZFNP colutions were prepared at the following concentrations: 0.0625, 0.125, 0.25, 0.5, 1.0, 1.5, and 2.0 mg/mL. They were printed on the membranes at a dispensing rate of 0.1 µL/mm using the reagent dispenser. The bare nitrocellulose membranes were negative controls in the experiment.

The prepared ZFNP-deposited membranes underwent three different types of measurements. To determine the colour intensity ratio, photos of the ZFNPs aligned on the nitrocellulose membranes were taken. The visual signal intensity was measured on the blue channel of Bayer filter using MATLAB to determine the intensity ratio. The protocol is demonstrated in Figure 3.1.

The temperature measurement of the ZFNP-deposited nitrocellulose membranes was carried out as shown in Figure 3.2. Thermal images were recorded before turning on the LED. Then, the ZFNP-depostied membranes were illuminated by the LED at 6.5 W/cm^2 for 20 s before the thermal images were recorded. The temperatures of

the ZFNPs at before and after illumination were compared to calculate the temperature gradient.

The determination of the thermochromic signal was performed according to the procedure in Figure 3.4. The ZFNP-printed membranes were exposed to the LED light at the power intensity of 6.5 W/cm^2 for 20 s. The LED was then turned off and images of the thermochromic sheets were immediately recorded using the smart phone camera.

3.2.8 Statistical analysis

For the experiment in Section 3.2.3, the alignment of nanoparticles on the membranes, the IONPs were printed on the membranes and the thickness of the printed lines were measured. The significant difference of the thickness was identified by the paired-samples t-test at a significance level of 0.05.

To determine the significant difference between a positive signal (ZFNP-deposited nitrocellulose membrane) and a negative signal (bare nitrocellulose membrane), the IUPAC method for limit of detection (LOD) was applied. [129, 177, 178, 238] It is a widely used technique in analytical chemistry to identify the LOD, which is the least signal of measurement that can be discriminated from the average signal of the blamk sample. The IUPAC equation is provided as follows:

$$S_{LOD} > S_B + 3 * \sigma_B \quad \textbf{(Equation 3.6)}$$

where S_{LOD} is the LOD, S_B is the average signal of the blank sample, and σ_B is the standard deviation of the blank signal.

3.3 Results and discussion

3.3.1 Determination of nanoparticle concentration

The concentrations of the IONPs and ZFNPs in mass per volume were quantified by the colourimetric assay. In the spectrophotometric measurement, the ferric ions (Fe^{3+}) were reduced to ferrous ions (Fe^{2+}) by hydroxylamine hydrochloride. It is important to ensure that all Fe^{3+} ions are chemically reduced to Fe^{2+} to maintain the accuracy of the measurement. The chemical reaction for the reduction is as follows: [217, 239]

$$4Fe^{3+} + 2NH_2OH{\cdot}HCl \leftrightarrow 4Fe^{2+} + N_2O + 4H^+ + H_2O$$

Ferric Iron Hydroxylamine Hydrochloride Ferrous Iron Nitrous Oxide Proton Water

This was followed by the addition of 1,10 – phenanthroline to react with ferrous ions. A subsequent colour change to orange indicated the formation of $[Fe(phen)_3]^{2+}$ complex. By reducing a series of known-concentration standard solutions, a linear relationship between the absorbance and the concentration of the iron was eatablished as a calibration curve (see Figure 1 in Appendix D). Afterwards, the absorbance of the unknown-concentration samples of IONPs and ZFNPs was compared to the calibration curve to determine the iron mass.

The concentration of gold mass was calculated using the Lampert-Beer's law (Equation 3.1). The extinaction coefficients at a specific wavelength of the AuNSPs and AuNRs were drawn from previous studies. [228, 237] It is important to note that the colourimetric assay is only applicable for the mass of metallic content. The weights of other compounds, such as citrates, an oxide layer, and CTAB molecules, were not taken into account.

3.3.2 Nanoparticle alignment on nitrocellulose membranes

To deposite nanoparticles on nitrocellulose membranes, the solutions of the nanoparticles were fed to the dispenser by a syring pump and drawn on the membranes as a single line. However, several parameters affect the shape of the printed line. Hence, the first experiment in this chapter was designed to examine the impact of the dispensing rate and the movement speed of the dispenser head. It was expected that the printed line of nanoparticles would be approximately 1 mm in thickness, similar to that of the test and control lines typically found in acutaul LFAs. [153]

In fact, the width of the liquid that contacts to the nitrocellose membrane during the fabrication process affects the sensitivity of the LFA test. [124] It determines the density of the biological molecules in a specific area of the membrane. This is also the case with the deposition of the nanoparticles on the membrane. The arrangement of the nanoparticles affects the heat production. [240] Given that they locate closer to the adjacent nanoparticles, they produce more heat than those that are loosely packed in the membrane. Therefore, the effect of the dispensing rate and the speed of the dispenser on the thinkness of the printed line of nanoparticles was investigated.

Table 3.1 Appearance of the IONPs absorbed on the nitrocellulose membranes. The dispensing rates ranged from 0.1 to 0.3 µL/mm and the head speed was varied to 32.5 and 50 mm/sec.

Dispensing rate	Head speed of the dispenser	
	32.5 mm/sec	50 mm/sec
0.1 µL/mm		
0.2 µL/mm		
0.3 µL/mm		

Table 3.1 displays the nitrocellulose membranes on which the IONPs were printed using the dispenser at various dispensing rates and head speeds. It is seen that the increase in the dispensing rate resulted in the formation of a thicker printed line. The average thicknesses of the printed lines of IONPs are shown in Figure 3.5. The printing of IONPs at the dispensing rates of 0.1 and 0.2 µL/mm resulted in the thickness of 1 and 1.7 mm, respectively. At a dispensing rate of 0.3 µL/mm, the thichkness of the lines was 3 nm which was larger than the thickness of typical LFA results. The speed of the nozzle did not have a significant effect on the thickness of the printed lines when the dispensing rates were adjusted to 0.2 and 0.3 µL/mm. However, it was found that at 0.1 µL/mm, faster movement of the nozzle resulted in significantly smaller printed lines of IONPs on the membranes.

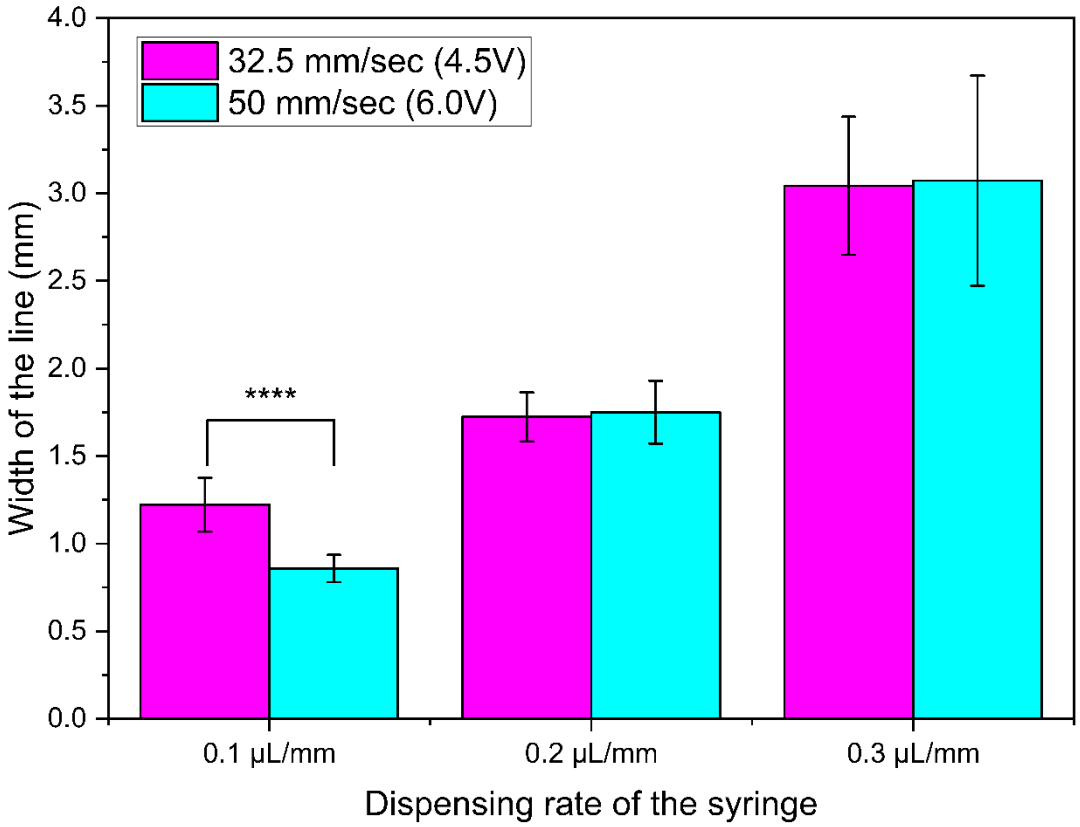

Figure 3.5 The thickness of the IONP line created from various dispensing rates (0.1, 0.2, and 0.3 µL/mm) and head speeds (32.5 and 50 mm/sec). Data are presented as the mean ± standard deviation (n = 50). P-values were obtained using a two-tailed paired-samples t-test. *p < 0.05, **p < 0.01, ***p < 0.001, and ****p < 0.0001.

3.3.3 Visual signal measurement

After identifying the effect of the dispensing rate, the IONP solutions with concentrations scaling from 0.5 to 2 mg/mL were printed on the membranes at 0.1 and 0.2 µL/mm. The "coffee ring" effect was noticed after the solutions were left to dry at RT (Figure 3.6). This phenomenon generally occurs during the evaporation of a droplet. [152, 241] Solid nanoparticles are dragged to accumulate around the edge of the droplet by a capillary force, resulting in an uneven distribution of the IONPs. This is undesirable, as it is difficult to measure the colour intensity using MATLAB. Previous studies have suggested that the coffee ring formation can be minimised by increasing the evaporation rate. It can be done by adding a solvent to the solution of nanoparticles [242] or by applying heat to accelerate the evaporation rate. [241, 243]

However, the coffee ring is not usually found in actual LFAs because the nitrocellulose membrane is designed to promote the fixation of biological molecules. [124] Proteins, such as antibodies, can immediately bind to the porous membrane.

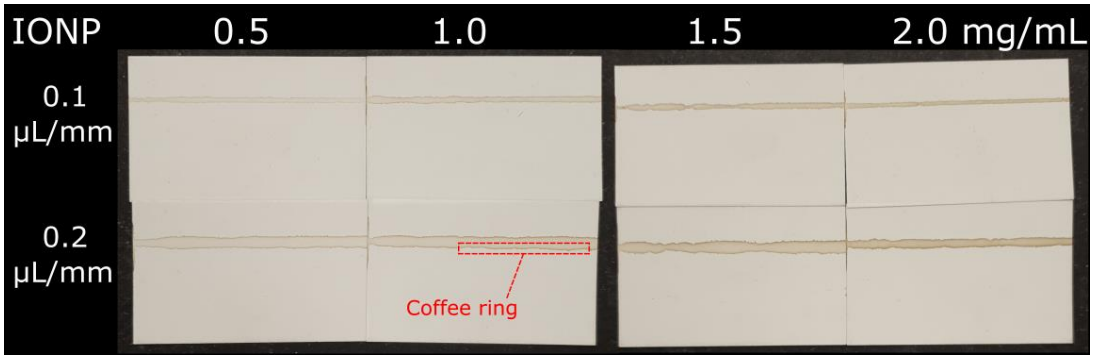

Figure 3.6 Appearance of the membranes deposited with various concentrations of IONPs (0.5, 1, 1.5, and 2 mg/mL) and dispensing rates (0.1 and 0.2 µL/mm). The coffee ring effect is highlighted in red.

In this study, to minimise the negative impact of the coffee ring effect, the average colour intensity was measured across the middle area of the printed lines, avoiding the area around the edges where the particles were more densely packed than usual. Each pixel of an image stores digital values that represent the colour intensity in RGB coordinates of which the MATLAB software was used in conjunction with the Bayer filter to identify the intensity. In general, the highest value (the brightest colour or white) is 255 whereas the lowest value (no colour or black) is 0. In the visual signal measurement, the results were represented in the intensity ratio to identify the colour contrast between the IONPs and the nitrocellulose membrane. An accumulation of IONPs appeared as a dark brown colour which decreased the value of I(t). Given that the intensity of the background, I(b), was constant, the more IONPs on the membrane, the higher the intensity signal ratio, I(b)/I(t).

Determining the ratio of the signal intensity of IONPs to that of the membrane is highly beneficial. Typially, many parameters must be controlled, such as ambient light, the distance between the object and the camera, and shadows. Images should be recorded in a black box to minimised external intereferences. Finding the ratio between the signal of the printed IONPs and the nitrocellulose membrane can compensate for the drift of the output because the degree of the drift caused by

ambient light is similar. [152, 165] Therefore, the interference of external light was subtracted from the images.

The correlartion between the colour intensity ratios and the concentrations of IONPs is shown in Figure 3.7. Linear relationships were found in all colour channels as increasing the concentration of the IONPs led to an increase in the colour intensity ratio. Among these, the blue channel showed the largest sensitivity compared to the other channels. From a physics perspective, the white colour of the nitrocellulose membrane scatters most of the incident light (near-zero absorption), while the maximum absorption of the IONPs is found in the "blue" region of the electromagnetic wavelength (Figure 3.8). As a result, the difference between the colour intensity of the IONPs and the nitrocellulose membrane falsl into the blue channel of the Bayer filter. The result is consistent with the finding in a previous report. [152] The red channel showed the least sensitivity, possibly because the IONPs do not effectively absorb electromagnetic radiation in the red region of the visible spectrum. The blue channel was selected as the optimum channel for measuring the colour intensity of the IONPs.

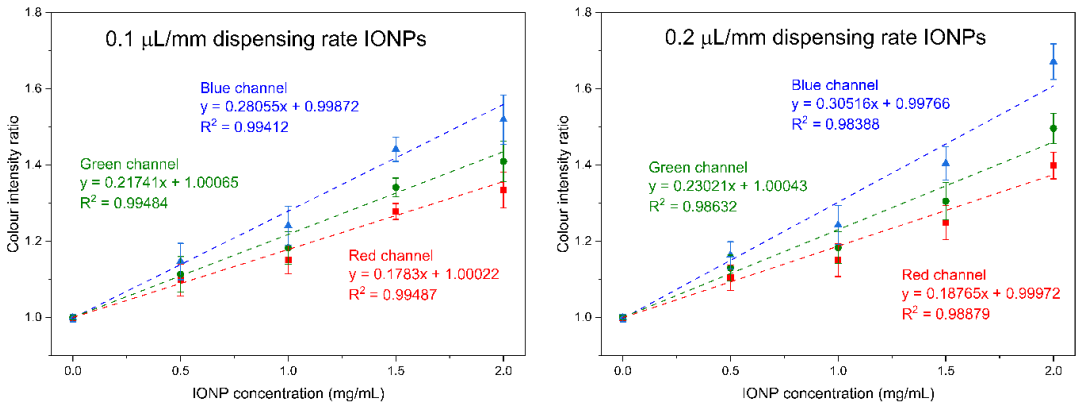

Figure 3.7 Correlation between the colour intensity ratios and the concentrations of IONPs on nitrocellulose membranes. The colour intensity ratios are shown in red, green, and blue channels. The dash lines represent the linear trend lines. The linear equations and the R^2 values are labelled alongside the graph. Data are presented as the mean ± standard deviation (n = 3).

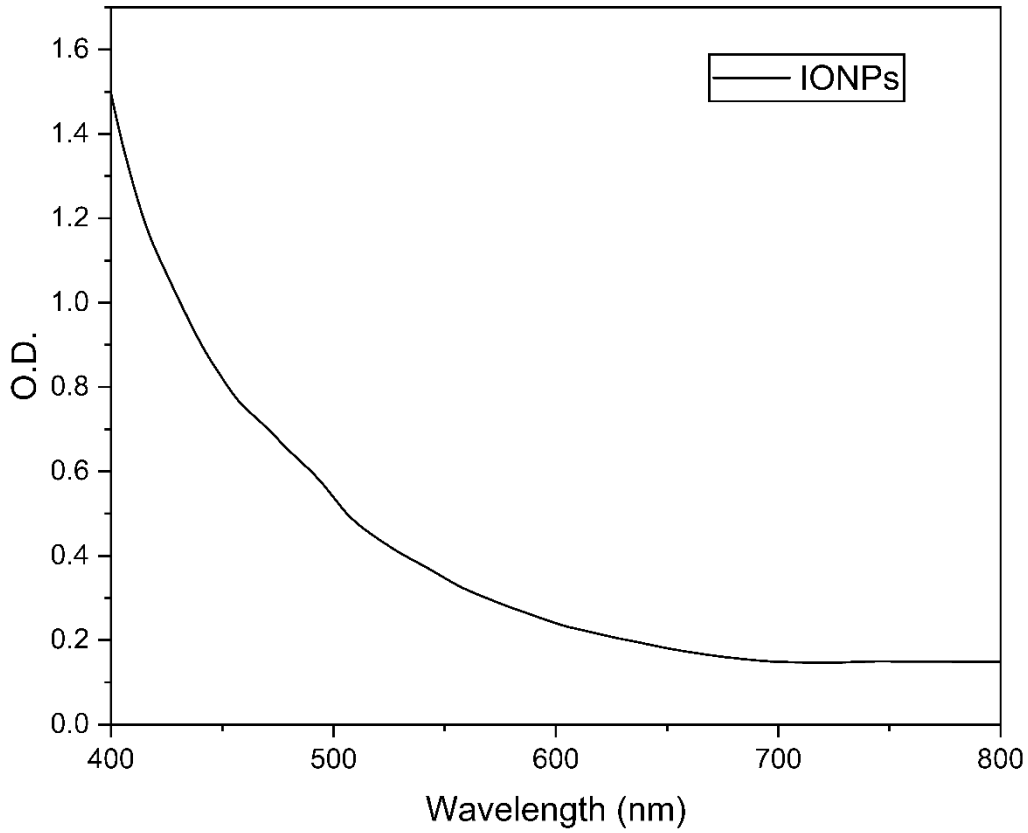

Figure 3.8 Absorption spectrum of IONPs in water

3.3.4 Thermal signal measurement

In the previous chapter, several photothermal nanoparticles were fabricated and prepared for testing with the LED. To select the most effective nanoparticles, the light-to-heat conversion efficiency on nitrocellulose membranes was investigated.

In this thermal study, the nanoparticles were illuminated by white light for 3 min. It was empirically found that the temperature reached a steady state within 1 min (data not shown). The temperature sharply increased after 10 s of exposure, but did not significantly change after 1 min. Therefore, in this comparative study, the nanomaterials were deposited on the nitrocellulose membranes and irradiated for 3 min before thermal recording. The concentrations of the colloidal nanoparticles ranged from 0.5 to 2.0 mg/mL and they were printed at dispensing rates of 0.1 and 0.2 µL/mm. Bare nitrocellulose membranes were used as the null signal.

In Figure 3.9, the highest temperature gradient of ZFNPs was 25 °C whilst the maximum temperature change of IONP was 18 °C. Even at the most diluted concentrations, IONPs and ZFNPs exhibited distinct temperature gradients compared to the temperature gradient of the nanoparticle-free nitrocellulose membranes. These results emphasize the excellent photothermal conversion performance of the MNPs toward white light LED.

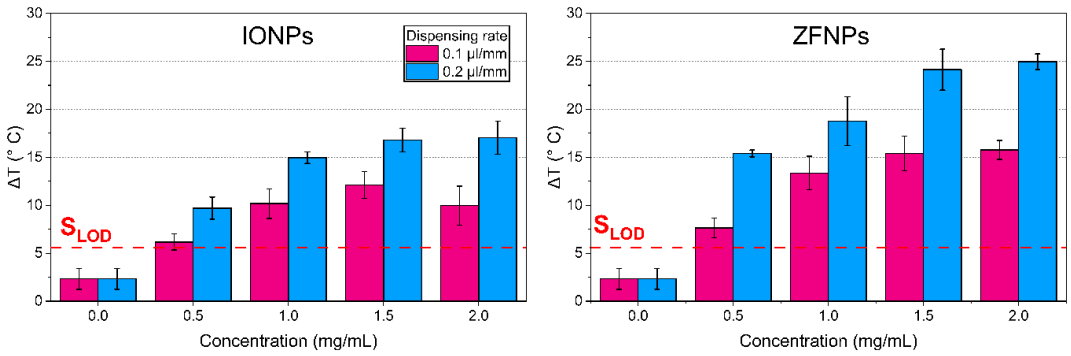

Figure 3.9 Temperature gradients of IONPs and ZFNPs after 3 min of light irradiation. The concentrations of IONPs and ZFNPs ranged from 0.5 to 2 mg/mL and the dispensing rates were adjusted to 0.1 and 0.2 µL/mm. Data are presented as the mean ± standard deviation (n = 3). * indicates the LOD and S_{LOD} indicates the signal of detection limit determined by IUPAC.

The second group of samples consisted of the AuNSPs with diameters of 12 and 18 nm. The results are presented in Figure 3.10, which suggests that the capability of AuNSPs to convert incident light into heat energy was lower than that of the MNPs. However, the photothermal effect of the 12-nm diameter AuNSP at 2 mg/mL was comparable to that of the IONPs as they could raise the temperature up to 18 °C. On the other hand, the 18-nm AuNSPs did not raise the temperature above the detection limit, indicating their poor photothermal effect toward the LED.

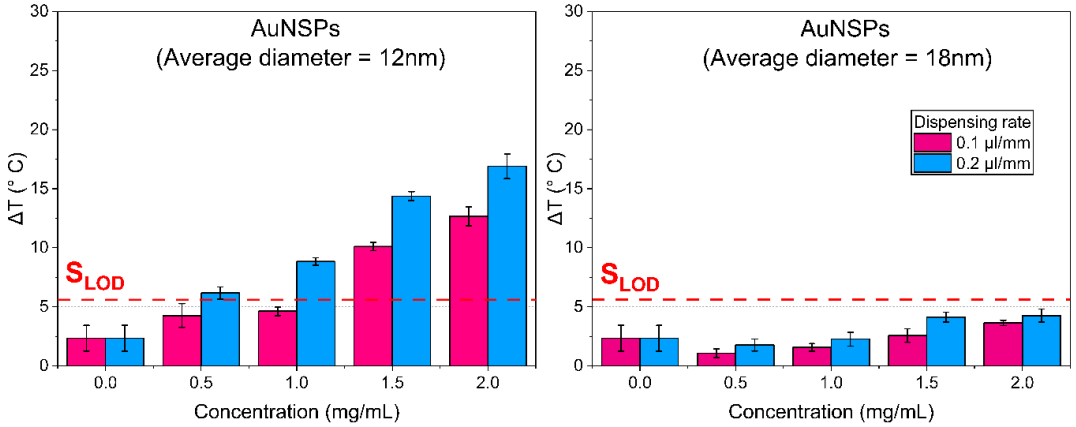

Figure 3.10 Temperature gradients of 12-nm and 18-nm AuNSPs after 3 min of light irradiation. The concentrations ranged from 0.5 to 2 mg/mL and the dispensing rates were adjusted to 0.1 and 0.2 µL/mm. Data are presented as the mean ± standard deviation (n = 3). * indicates the LOD and S_{LOD} indicates the signal of detection limit determined by IUPAC.

In Figure 3.11, the AuNRs with a resonance of surface plasmon of 560 nm were unable to raise the temperature to a level distinguishable from that of the null samples. To maximise the optical properties of the nanorods, the aspect ratios were tuned to centralise the LSPR peaks around 600 and 625 nm, which are near the maximum emission of the LED. Their photothermal conversion efficiencies were greater than that of the AuNRs with the LSPR at 560 nm. Yet they were still less effective than the MNPs and the 12-nm AuNSPs. At the highest concentration, the medium nanorods (maximum absorption at 600 nm) raised the temperature by 14 °C while the longest rods (maximum absorption at 625nm) produced a temperature of about 13 °C.

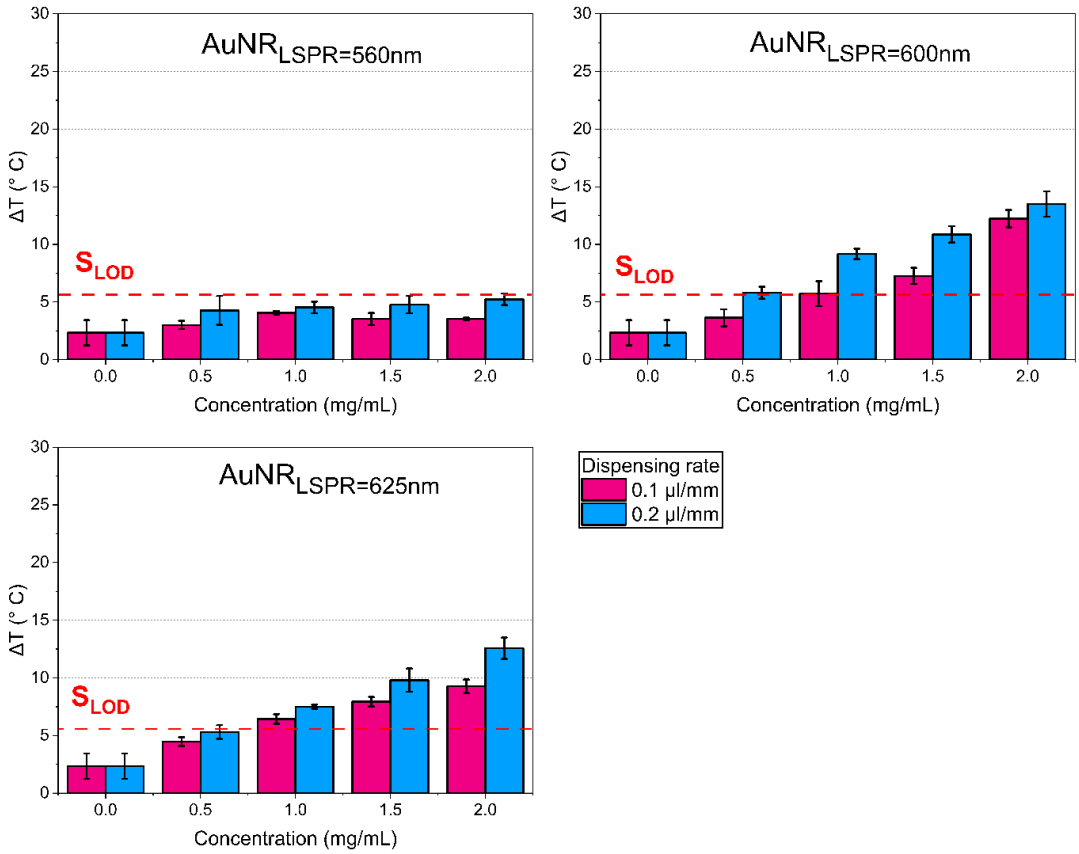

Figure 3.11 Temperature gradients of AuNRs with LSPRs of 560, 600, and 625 nm after 3 min of light irradiation. The concentrations ranged from 0.5 to 2 mg/mL and the dispensing rates were adjusted to 0.1 and 0.2 µL/mm. Data are presented as the mean ± standard deviation (n = 3). * indicates the LOD and S_{LOD} indicates the signal of detection limit determined by IUPAC.

Plasmonic nanoparticles are well-known for their ability to convert light into heat, especially at their LSPR frequency. It was hypotised that the AuNRs with an LSPR peak at 600 nm would yield the strongest response to the electromagnetic radition of the white-light LED, which has a maximum emission at 600 nm (see Figure 1 in Appendix A). Nonetheless, it was found that the IONPs and the ZFNPs showed the highest photothermal effect toward the illumination by the white-light LED.

In physics, optical extinction is the sum of absorption and scattering. It defines how strong the light can interact with nanoparticles. [198] Scattering of incident light is essential for imaging applications, and light absorption plays a vital role in heat production. [153, 197, 198] Therefore, all nanoparticle solutions were diluted to 0.05 mg/mL and subjected to a spectrophotometer to measure spectral absorbance from 400 to 800 nm. The UV-vis spectrum absorption is displayed in Figure 3.12. The IONPs

and ZFNPs absorbed a broad spectrum of the light, with a maximum absorption in the blue region. As the wavelength increases, the optical absorption of the MNPs decreased. The absorption of the MNPs covered the broad emission of the LED, resulting in excellent photothermal efficiency.

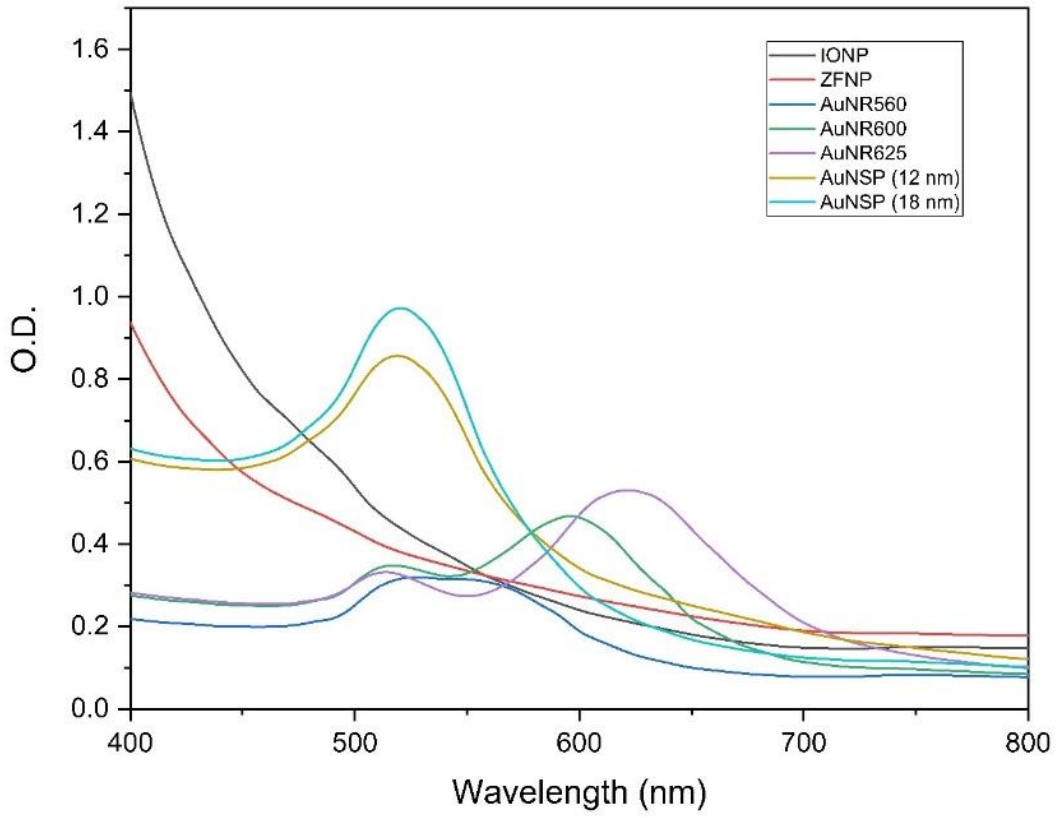

Figure 3.12 Absorption spectra of nanoparticles (0.05 mg/mL) in the wavelength range of 400 to 800 nm

In the case of the gold-based nanoparticles, 18-nm AuNSPs showed larger optical absorption than the smaller AuNSPs at the same mass and should be able to generate significant heat. Nonetheless, the 12 nm AuNSPs exhibited a stronger light-to-heat convertion efficiency than the 18 nm AuNSPs, creating a conflict between the results obtained from the UV measurement and the photothermal test.

In plasmonic thermalization, the efficiency of thermal radiation depends on the generation of the heat within gold lattice and the ability to dissipitate heat to the surrounding. This study found that the 12 nm AuNSPs unexpectedly outperformed the AuNRs, despite the large cross-sectional absorption of the rods. It is possibly

attibuted to the “shielding” effect. The main hot region of plasmonic nanoparticles is at the outer surface which interacts with the incident light. [197] The core is prevented from engaging in optical activity. Moreover, increasing the size of nanoparticles leads to an increase in heat capacity. [244] So, smaller plasmonic nanoparticles have less heat capacity and can release heat in a shorter time than larger plasmonic nanoparticles due to a higher surface-to-volume ratio. Moreover, when incident light comes into contact with nanoparticles with high optical absorption, they absorb most of the incident light, with a small amount being scattered, and *vice versa*. [196-198, 245]. Recent research demonstrates that the photothermal conversion efficiency of nanoparticles is size-dependent. [198] Upon laser irradiation, it is reduced as the size of nanoparticles increases because the scattering effect becomes dominant in the optical extinction. Hence, the 12 nm AuNSPs exhibited greater light-to-heat conversion efficienc than the 18 nm AuNSPs and the AuNRs.

The environment is also a related factors contributing to the heat generation of nanoparticles as it affects the heat capacity, dielectric constant, and heat diffusion of the medium. [198, 240] The medium interacts with the radiative transport events and can induce re-scattering of incident light, followed by re-absorption of the light by the nanparticles. The re-absorption causes extra thermal amplification of the nanoparticles resulting in a higher ttemperature than the expection in the theory. [196, 198] This is especially applicable when the nanoparticles are dispersed in water which encourages re-sacttering of light to be re-absorbed by the nanoparticles. However, it is important to note that the nanoparticles in this study were surrounded by air while most previous works have demonstrated the photothermal properties of colloidal nanoparticles in solution.

In addition, the concentration of nanoparticles plays a crucial role in heat production, as given by the following equation: [129, 175, 196, 245]

$$\mathbf{Q = N * C_{abs} * I} \qquad \textbf{(Equation 3.7)}$$

where Q is the total heat production (W/m^3), N is the concentration of nanoparticles (number of particles/m^3), C_{abs} is the cross-sectional absorption area (m^2), and I is the power intensity of the light (W/m^2). In this study, the mass of nanoparticles was kept

constant to minimise the impact of cross-sectional area absorption. However, from Equation 3.7, it can be seen that given the incident intensity and the cross-sectional absorption area are constant, the number of nanoparticles plays a major role in thermalization.

Therefore, the number of the nanoparticles per volume was converted from the mass concentration (see Table 1 in Appendix E). In Figure 3.13, at the same mass concentration (0.5 mg/mL), the number of IONPs and ZFNPs were higher than the other nanoparticles due to their smaller diameter. According to Equation 3.7, the higher particle number of the IONPs and ZFNPs leads to a greater amount of heat generation than the other nanoparticles. As the MNPs have a higher particle number, the collective "Coulomb" effect plays a role in the heat generation. [240] In this study, the nanoparticles were located in the porous membrane. Therefore, the density of the IONPs and ZFNPs were greater than the gold-based nanoparticles, as there were more particles in a single volume unit. This shortens the distance between individual nanoparticles and then an electric field enhancement effect. Moreover, a high concentration of the nanoparticles increases the chance of the re-sacttering events and hence the chance of optical re-absorption. [198] A high number of nanoparticles in the pores of the membrane increases the likelihood of the indicent light to be scattered by the nitrocellulose membrane and the nanoparticles. This multiple light scattering affects thermal generation. Therefore, the MNPs and the 12 nm AuNSPs exhibited higher photothermal efficiency toward the LED than the 18 nm AuNSPs and AuNRs.

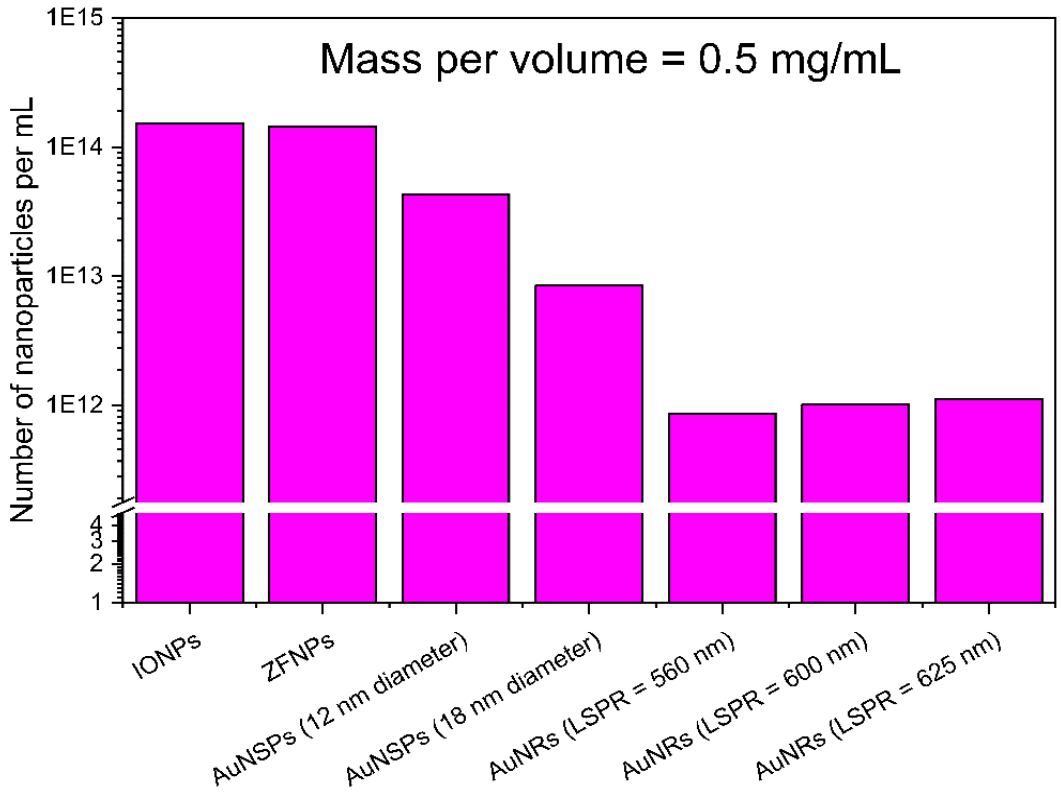

Figure 3.13 Particle number of nanoparticles in 1 mL of water, calculated based a the mass of 0.5 mg.

3.3.5 Thermochromic signal measurement

Since the ZFNPs exhibited the greatest light-to-heat conversion efficiency, they were chosen to be utilised as thermal generators. According to Figure 3.14, a red-pink circle appeared on the thermochromic sheet at a concentration of 0.0625 mg/mL ZFNPs as after LED illumination. The colour of the thermochromic sheet changed to green as the concentration of the ZFNPs increased and the number of red pixels on the sheet decreased. The colour change of the thermochromic sheet was obvious, even at a low concentration of the nanoparticles, once the activation temperature was reached.

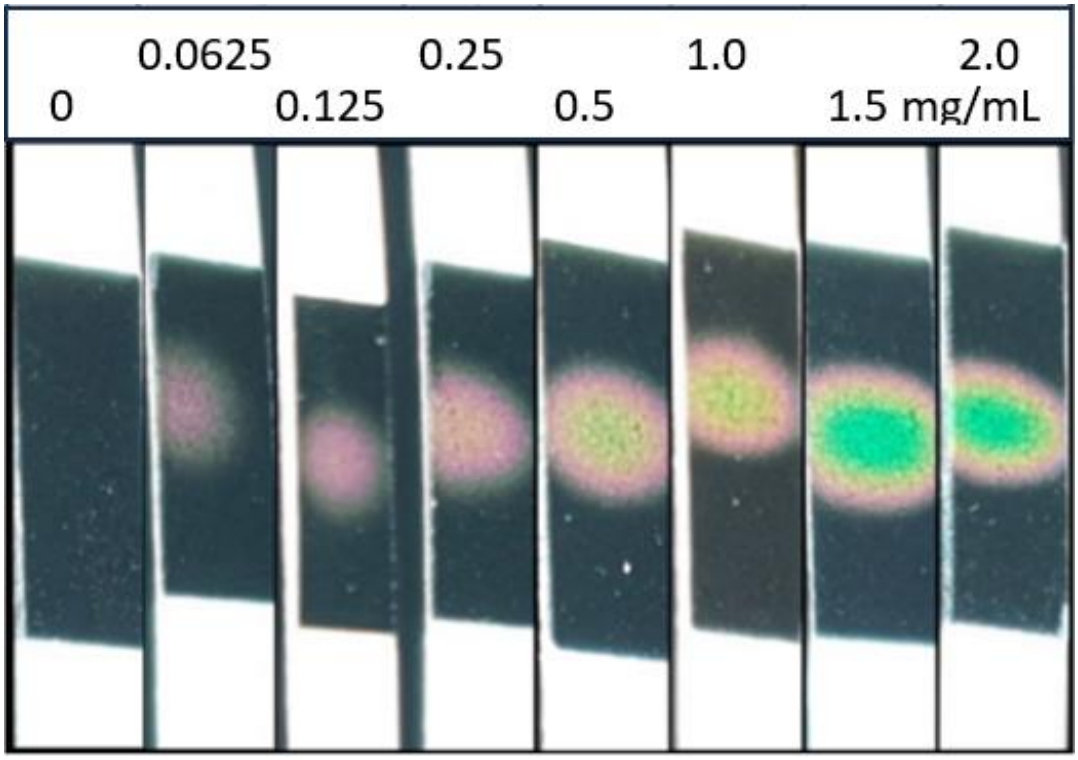

Figure 3.14 Display of the thermochromic sheets at different concentrations of ZFNPs (0.0625 to 2 mg/mL) and a bare nitrocellulose membrane (negative control). The images of the thermochromic sheets were taken after LED illumination.

The thermochromic signal was determined by MATLAB to measure the intensities of RGB coordianates. The intensity ratio of the thermochromic signal is reversed to the ratio calculation of the typical signal. The thermochromic sheet is black in the initial stage and during the colour transition phase, the test line intensity I(t) increases. Assuming that the intensity of the thermochromic sheet is similar at every concentration, the value of I(t)/I(b) will increase, cancelling out the ambient light intensity. In Figure 3.15, the red channel of the Bayer filter showed the greatest sensitivity of detection when the concentration of ZFNPs was at 0.00625 mg/mL. However, the thermochromic intensity ratio of the red channel suddenly dropped as the concentration increased beyond 0.25 mg/mL. The analysis of the green channel presented greater sensitivity than that of the blue channel. The intensity ratios of the green and blue colours were found to increase with the concentration before reaching a platue. The reverse trend was not observed. However, the green and blue channels were less sensitive than the signal ratio of the red channel.

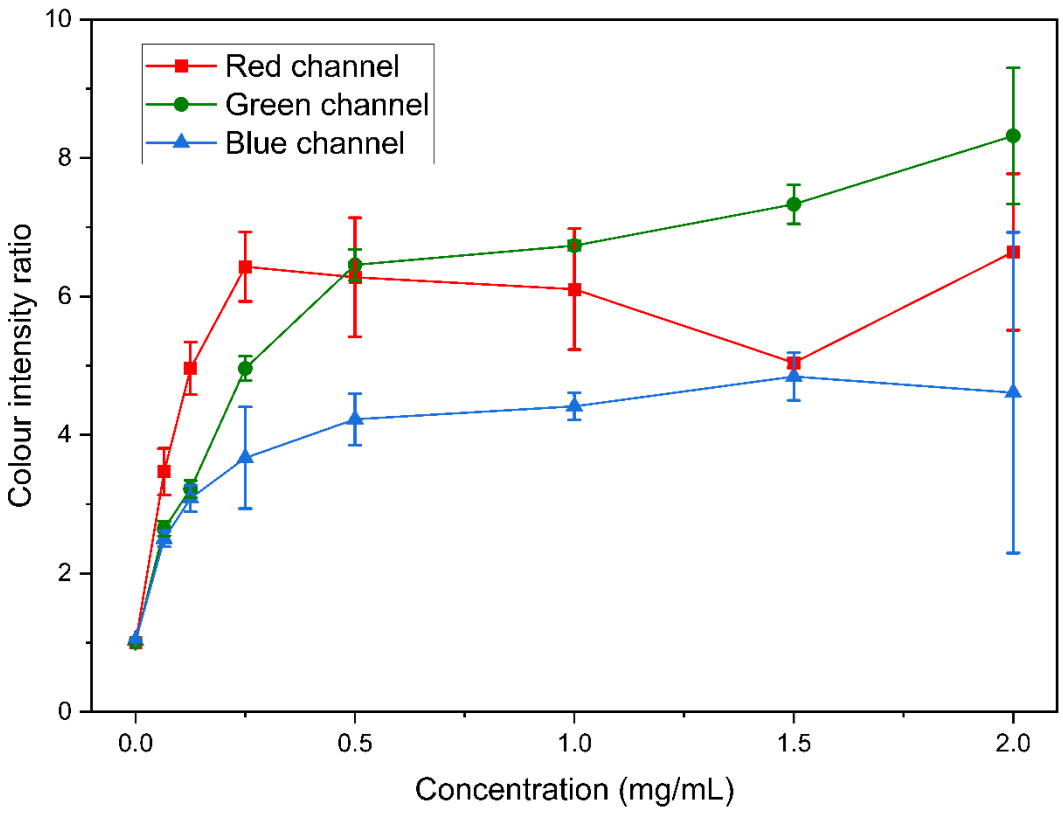

Figure 3.15 Colour intensity signal ratios of RGB of the thermochromic sheet. The ZFNP concentrations ranged from 0 and 2 mg/mL. Data are presented as the mean ± standard deviation (n = 3).

At low concentration of ZFNPs, the thermochromic sheet did not express green or blue pixels. Only the red colour was detected on the thermochromic sheet which mainly contributed to the colour analysis of the Bayer filter in the red channel. As the ZFNP concentration increased, the red colour became less dominant on the sheet and was replaced by green pixels. Bacaue the overlab between green and blue colours, the intensity ratio in the green and blue channels increased.

This study found the channel that is most sensitive to thermochromic-based detection. Therefore, the red channel was selected as the optimum channel for the measurement of the thermochromic signal.

3.3.6 Comparison between different types of signals

The ZFNPs were used in the experiment to provide a typical visual signal similar to that of the common LFA. Furthermore, the ZFNPs acted as heat providers in the thermal sensing and the thermochromic assays. Herein, three different types of the signals were compared.

The displays of the ZFNPs at different concentrations on the nitrocellulose membrane, the thermal images of them upon the exposure to the LED, and the thermochromic sheets that responsed to the heat generated by the ZFNPs were shown in Figure 3.16. It can be seen that the ZFNPs became visible on the nitrocellulose membrane at 0.125 mg/mL (Figure 3.16A). Nonetheless, the colour of the ZFNPs was very faded which may cause misinterpretation. It was clearly observed with confidence at 0.5 mg/mL.

In Figure 3.16B, the thermal image of the blank sample (0 mg/mL) showed that the membrane itself absorbed the broad-spectrum emission of the LED resulted in temperature increase. At 0.5 mg/mL. It was seen that the ZFNPs could interact with the indicdent light raising a small degrees of temperature. Furthermore, the membrane had less interaction with the light, so the ZFNPs mainly contributed to the heat production. Increasing the concentration to 2.0 mg/mL resulted in a considerable temperature production as the bright spot was seen in the thermal image. However, the interpreatation of the result strongly requires the thermal analysis software as the temperature may differ in a small fraction and is impossible to analyse by naked-eyes.

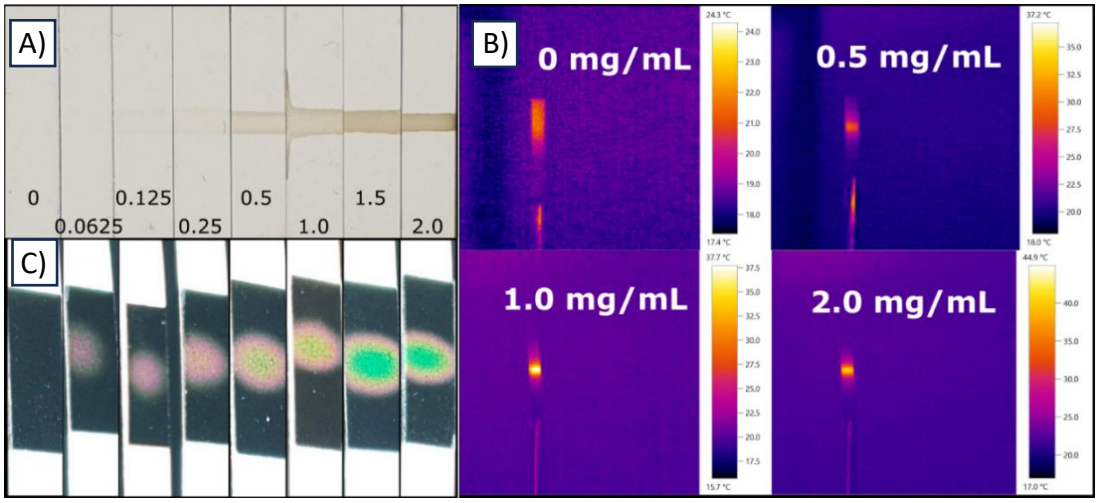

Figure 3.16 Appereances of the signals of A) typical membrane strips B) thermal images and C) thermochromic sheets with various concentrations of ZFNPs.

The colour expression of the thermochromic sheets in response to the heat of the ZFNPs is shown in Figure 3.16C. A visual signal was seen on the thermochromic sheet at a concentration as low as 0.0625 mg/mL. It shows that the thermochromic signal can enhance the sensitivity of detection by multiple degrees compared to the conventional visual signal in Figure 3.16A.

The typical visual signal, temperature gradient, and the thermochromic signal were quantified and are presented in Figure 3.17. The analytical performance of each measurement is summarised in Table 3.2. The colour intensity ratio of the ZFNPs was measured via the blue channel of the Bayer filter. The relationship between the concentration and the blue intensity ratio was linear in a broad range, covering concentrations from 0 to 2 mg/mL (Figure 3.17A). The LOD of the typical visual signal was 0.5 mg/mL.

The thermal contrast of the ZFNPs provided a linear correlation between the temperature gradient versus the ZFNP concentration in the range of 0 to 1.5 mg/mL (Figure 3.17B). Although the working range of the temperature-based method is narrower than that of the typical signal, the LOD is lower (0.125 mg/mL), as the thermal signal can be detected at a lower concentration.

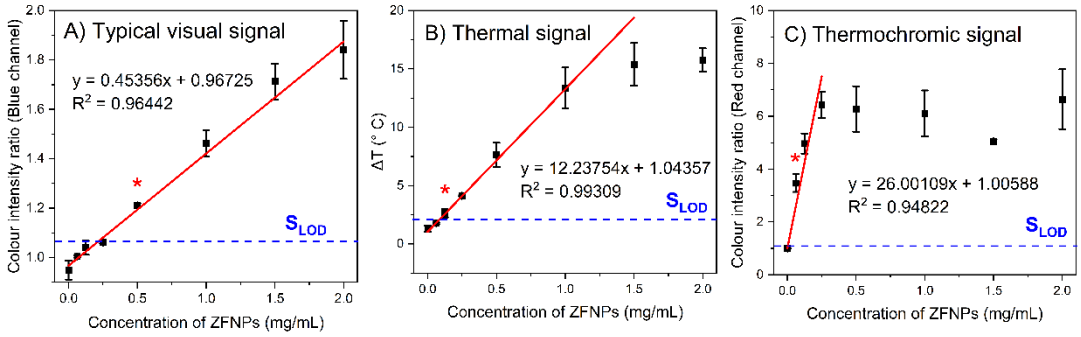

Figure 3.17 Correlations between ZFNP concentration and the intensities of various types of signals: A) typical visual signal ratio, B) thermal gradient signal, and C) thermochromic signal ratio. The red lines in each panel represent the linear trendlines. Data are presented as the mean ± standard deviation (n = 3). * indicates the LOD and S_{LOD} indicates the signal of detection limit determined by IUPAC.

For the thermochromic assay, the red channel was investigated as it offers the most sensitivity. The working range of this method is shorter than the other methods. The correlation between the red intensity ratio and the ZFNP concentration is linear from 0 to 0.25 mg/mL. However, the LOD of the thermochromic method is 0.0625 mg/mL, which is lower than the LOD of the typical and thermal methods.

Table 3.2 Analytical performances of typical visual, thermal contrast, and thermochromic measurements, determined by IUPAC.

Types of signals	Fitting formula	Linear working range (mg/mL)	R^2	Sensitivity	S_{LOD}	LOD (mg/mL)
Typical visual signal	y = 0.45356x + 0.96725	0 – 2.0	0.96442	0.45356	1.0636	0.5
Thermal signal	y = 12.23754x + 1.04357	0 – 1.5	0.99309	12.23754	2.093725	0.125
Thermochromic signal	y = 26.00109x + 1.00588	0 – 0.25	0.94822	26.00109	1.08004	0.0625

Each measurement provided different working ranges of the linear relationship between the signal and the ZFNP concentration. Each method have both advantages and disadvantages. The typical visual measurement are the least sensitive method but it offers the broadest working range of detection. The temperature measurement based approach is effective and has been widely used in the LFA application. However, the thermal analysis software and the IR camera are essentially needed. For the thermochromic based assay developed in this thesis, it offers the most sensitivity and the lowest LOD compared to the other methods. The result can be read by observation. However, it has the narrowest linear working range.

According to the results obtained in this section, integrating the thermo-responsive sheet to the nitrocellulose membrane can considerably enhance the visual signal, making it much stronger than the tyical visual signal. The key of the thermochromic sensing method is that once the working temperature of the thermochromic sheet is reached, its colour-changing behaviour is triggered resulting in a strong appearance of colouration on the sheet. Whilst the colour intensity of the ZFNPs on the membrane gradually increases with increasing ZFNP concentration, the thermochromic signal sharply surges when the working temperature is activated.

Despite the strong visual signal of the thermochromic sheet, there are several factors that need to be taken into account when operating the thermochromic-based method. The thermochromic sheet is highly sensitive to temperature and therefore the incident LED power, duration of illumination, and the activation temperature of the thermochromic sheet must be optimised to operate at a certain ambient temperature. Otherwise, false results may occur. For example, if the ambient temperature is 25 °C, a thermochromic sheet with a colour transition point of 30 °C should be selected for optimal performance. The 5 °C difference between the ambient and transition temperature prevents undesired temperature generated by the nitrocellulose membrane (approximately 3 °C). Additionally, the LED power intensity and illumination duration must be carefully controlled to avoid overheating the nitrocellulose membrane and the thermochromic sheet, which could lead to a false positive signal. Alternatively, if the surrounding temperature is not controllable, thermochromic sheets with higher working temperature windows, such as 40-45 °C

and 45-50 °C, can be used. Increasing the LED intensity and exposure duration can compensate for the required temperature.

3.4 Conclusion

This chapter aims to determine the potential of the thermochromic-based approach to improve the sensitivity of the LFA. A proof-of-concept study was carried out using several types and shapes of photothermal nanoparticles, including IONPs, ZFNPs, 12 nm AuNSPs, 18 nm AuNSPs, and AuNRs with LSPR peaks of 560, 600, and 625 nm. The nanoparticles were prepared on nitrocellulose membranes as seen in actual LFA results. A 400-700 nm LED was used to optically stimulate the nanoparticles. The typical visual signal, thermal signal, and the thermochromic signal were then compared.

First, the nanoparticles were aligned on the nitrocellulose membrane using IONPs as a model system. The flow rate of the solution ejection and the head speed of the dispenser affected the shape of the printed lines. Printing at the volume of 0.3 µL per mm overload the nanoparticles, resulting in the formation of a thick line. The speed of the nozzle significantly affected the size of the printed line at a dispensing rate of 0.1 µL/mm. The coffee ring effect was observed after drying the membranes which caused variation in colour and thermal measurements.

Then, the IONP-deposited membranes were brought to the measurement of the coulour intensity using a Bayer filter on MATLAB. The dark-brown coulour of the IONPs was the most sensitive to the blue channel of the filter. It indicates that the optimum colour channel needs to be determined to maximise the analytical efficiency.

The results revealed from the photothermal experiment show that the MNPs had the greatest optical response toward the broad emission LED. IONPs and ZFNPs increased temperature at a higher magtitude than gold-based nanoaprticles. The maximum temperatures raised by the IONPs and the ZFNPs were 18 °C and 25 °C, respectively. The 12 nm AuNSPs also expressed a strong photothermal effect, increasing the

temperature up to 18 °C, which was comparable to the IONPs. On the other hand, the 18 nm AuNSPs were inactive against white-light exposure as they could not increase the temperature to a level distinguishable from the temperature of the bare membrane. The AuNRs with different LSPR frequencies (560, 600, and 625 nm) were illuminated with the white-light LED. It was fond that the AuNRs with the LSPR at 600 nm could increase the temperature by 14 °C, being higher than the other AuNRs as their LSPR aligned with the maximum emission of the LED. The ZFNPs were selected to be used in the thermochromic platform study due to the strongest photothermal performance.

A liquid crystal thermo-responsive sheet was used with ZFNPs to assess the potential of being a new sensitivity enhancement technique. Upon LED exposure, the ZFNPs as low as 0.0625 mg/mL could induce a sufficient temperature increase to activate the colour transition of the thermochromic sheet. The red channel provided the most sensitive result in this study.

Comparing the signals, the thermochromic measurement at the optimum condition had the highest sensitivity, while the typical visual signal analysis had the lowest sensitivity. It indicates that the thermochromic-based method is a promising colourimetric technique for increasing the the sensitivity of LFA detection.

It is crucial to acknowledge that this study has not yet considered the impact of MNP shape on photothermal effects. While the investigation focused on varying the shapes of plasmonic nanoparticles and examining their photothermal effets due to their remarkable optical properties, particularly LSPR, which plays a significant role in heat generation, it would be valuable to extend this exploration to MNPs as well. Different MNP geometries may exhibit distinct light absorption and scattering characteristics, potentially influencing the way light interacts with electrons and consequently affecting photothermal performance. Thereforem a comprehensive evaluation of photothermal effects across various MNP shapes is neccessar to gain a more insight of theses materials and their potential applications.

Chapter 4 : Bioconjugation of nanoparticles and lateral flow assay detection

4.1 Introduction

This chapter demonstrates the preparation of conjugated nanoparticles to be ustilised in the detection of *Salmonella typhimurium* and DENV2-NS1. Firstly, the growth curve of *Salmonella typhimurium* was graphed based on the correlation between the number of bacteria and the absorbance. Then, ZFNPs@citrate were covalently immobilised with amine-modified aptamers using the EDC/sulfo-NHS coupling technique. The chemical modification was characterised by gel electrophoresis, DLS, and zeta potential measurements. ZFNPs@aptamer were introduced to a microbiological experiment to examine capture activity upon exposure to *Salmonella typhimurium*.

Next, the conjugates were prepared for use in the LFA platforms for the detection of *Salmonella typhimurium* and DENV2-NS1. The 12 nm AuNSPs were conjugated with antibodies accordingly via the physical absorption technique. The conjugation procedures were optimised using flocculation studies.

Lastly, the functionality of the AuNSPs@antibody was assessed by a half-strip test. Two systems were investigated separately for the detection of *Salmonella typhimurium* and DENV2-NS1. The colouration of the test results was measured by the Bayer filter technique.

4.2 Materials and methods

4.2.1 Materials

Colloidal ZFNPs@citrate and AuNSPs with diameters of 12 nm and 11 nm, respectively, were fabricated as described in Chapter 2. For covalent crosslinking, 2-(N-morpholino) ethanesulfonic acid (MES), EDC, potassium carbonate (K_2CO_3), and Tween 20 were received from Sigma-Aldrich (UK). Sulfo-NHS was purchased from Bioscience (UK). The Amicon centrifugal filter (30K NMWL) was obtained from Merck Life Science (UK). SYBR™ Safe DNA gel stain and tris-borate-EDTA buffer were received from Thermofisher (UK).

Amine-terminated aptamers for *Salmonella typhimurium* detection (H_2N-C_6H_{12}-5'-TA TGG CGG CGT CAC CCG ACG GGG ACT TGA CAT TAT GAC AG-3') (MW = 12541.2 Da) were produced by Integrated DNA Technologies (UK). The sequence of the *Salmonella typhimurium* specific aptamer was selected from the literatures. [123, 246] The aptamer was redispersed in autoclaved DI water to achieve the concentration of 1 M and stored at 4 °C. Note that before use, aptamers were reconstituted by heating in a thermoblock at 95 °C for 10 min in PBS buffer and cooling down at RT for 15 min.

For the microbiological experiment, Luria Bertani (LB) broth was purchased from Sigma-Aldrich (Gillingham, UK). LB agar was bought from Invitrogen (Paisley, UK). The strain of *Salmonella typhimurium* in this study was ATCC 14028. The phosphate buffer saline (PBS) was bought from Gibco (UK). Borate buffer was received from Thermofisher (UK).

Biological products including mouse anti-dengue virus Pan-Serotype NS1 antibody "EA1" (product code: MAB12295), mouse anti-dengue virus pan-serotype NS1 antibody "DA034" (product code: AbDENVNS1-DA034), mouse anti-dengue virus NS1 serotype 2 antibody "LH5" (product code: MAB12133), rabbit anti-dengue virus pan serotype NS1 polyclonal antibody (pAB) (product code: PAB21481), and recombinant dengue virus serotype 2 NS1 protein (HEK293) (product code: DENV2-NS1) were

produced by The Native Antigen Company (UK). Mouse anti-IgG *Salmonella typhimurium* LPS monoclonal antibody (product code: MA1-83451) was received from Thermofisher (UK). Bovine serum albumin (BSA) was obtained from Merck Life Science (UK).

To assembling the LFA, Whatman FF170HP nitrocellulose membranes (for DENV2-NS1 detection), Prima 40 nitrocellulose membranes (for bacteria detection) and backing cards were obtained from GE Healthcare Life Sciences (UK). An absorbent pad was bought from Merck (UK).

4.2.2 *Salmonella typhimurium* growth curve

4.2.2.1 Bacteria culture

A single colony of *Salmonella typhimurium* was collected from a petri dish by an inoculation loop and transferred to 30 mL of LB broth. The bacteria suspension was incubated at 37 °C with 250 rpm shaking speed.

4.2.2.2 Correlation between optical density and incubation time

The growth curve of *Salmonella typhimurium* was established by measuring the turbidity of the bacteria suspension at a specific wavelength. The bacteria suspension was prepared as explained in Section 4.2.2.1 and incubated at 37 °C for 4 h. Then, 1 mL of the suspension was collected every 30 min for the optical measurement. The absorbance of the *Salmonella typhimurium* suspension was measured at the optical density (OD) of 600 nm (OD_{600}) using a spectrophotometer with UV-vis Analyst software. All samples were conducted in triplicate.

4.2.2.3 Correlation between colony forming unit and optical density

A *Salmonella typhimurium* suspension was prepared as stated in Section 4.2.2.1. The bacteria suspension was kept in an incuabtor at 37 °C for 3 h. The bacteria cells were washed by centrifugation at 4000 rpm for 10 min. The pellets of *Salmonella typhimurium* were re-suspended in PBS buffer and mixed vigorously using a vortex.

The OD_{600} of the bacteria suspension was adjusted to 0.5, 1.0, 1.5, and 2.0, using UV-Vis spectrophotometry. Following that, 20 µL of each sample was streaked onto LB agar plates and incubated overnight at 37 °C. The CFU of *Salmonella typhimurium* was counted using a traditional colony counting approach. All samples were done in triplicate.

4.2.3 Aptamer-immobilised zinc ferrite nanoparticles

4.2.3.1 EDC/sulfo-NHS ratio optimisation

ZFNPs@citrate (0.1 mg/mL) were suspended in MES buffer (pH 5.0). Different amounts of EDC, ranging from 3.5 mM to 28 mM, were added to the solutions of ZFNPs@citrate. The hydrodynamic diameter and surface charge was characterised by the DLS and zeta potential measurements.

Next, ZFNPs@citrate were chemically reacted with various concentrations of EDC ranging from 1.25 mM to 14 mM. The molarity of sulfo-NHS was kept twice higher than the concentration of EDC. The hydrodynamic diameter and surface charge were analysed by DLS and zeta potential measurements.

4.2.3.2 Volume of aptamer optimisation

A solution of MES (pH 5.0) containing ZFNPs@citrate (0.1 mg/mL) was mixed with EDC and sulfo-NHS to reach a final concentration of 7 and 14 mM, respectively. The reaction was mixed on a rotator mixer for 20 min. Different volumes of 100 mM aptamers (10, 20, 30, 40, and 50 µL) were added to the solution of activated ZFNPs@citrate. Unreacted EDC and sulfo-NHS, unbound aptamers and byproducts were removed using a centrifugal filter in the centrifuge at 8500 rpm for 20 min. The washing step was repeated three times. The supernatant from the first round of centrifugation was collected for gel electrophoresis analysis (see Section 4.2.3.3). Then, ZFNPs@aptamer were re-dispersed in MES buffer (pH 5.0) to be characterised by DLS and zeta potential measurements and were dried using a freeze dryer for FTIR measurement (see Section 2.2.3.3).

4.2.3.3 Gel electrophoresis measurement

Agarose gel (1%wt) was prepared by dissolving 0.5 g of agarose powder in 50 mL of tris-borate-EDTA buffer, then microwaving for 2 min. Then, it was cooled down for 5 min, followed by the addition of 5 µL of SYBR™ Safe DNA gel stain. The gel mixture was solidified in a tray equipped with a gel comb. Finally, the solid agarose gel was flooded with tris-borate-EDTA buffer in the electrophoresis tank.

The samples of ZFNPs@citrate and ZFNPs@aptamer were stained with ethidium bromide and pipetted into the sample wells of the agarose gel. Electrodes were connected to the electrophoresis tank to supply an electric potential at 60 volts for 30 min. The result was visualised with a UV lamp at a wavelength of 280 nm in a transilluminator box. The intensity of fluorescent bands was measured using the built-in gel analysis function in ImageJ software.

4.2.3.4 *Salmonella typhimurium* detection

4.2.3.4.1 Preparation of aptamer-immobilised zinc ferrite nanoparticles

EDC and sulfo-NHS powders were added to the solution of MES buffer (pH 5.0) containing 0.1 mg/mL ZFNPs@citrate, to reach a final concentration of 7 mM of EDC and 14 mM of sulfo-NHS. The mixture was rotated at ambient temperature for 20 min to form the intermediated crosslinker. Following this, 30 µL of the aptamer (100mM) was added to the mixture of the activated ZFNPs@citrate followed by continuously rotation at RT for 2 h. The immobilisation of aptamers to the ZFNPs@citrate using EDC/sulfo-NHS coupling assay is displayed in Figure 4.1.

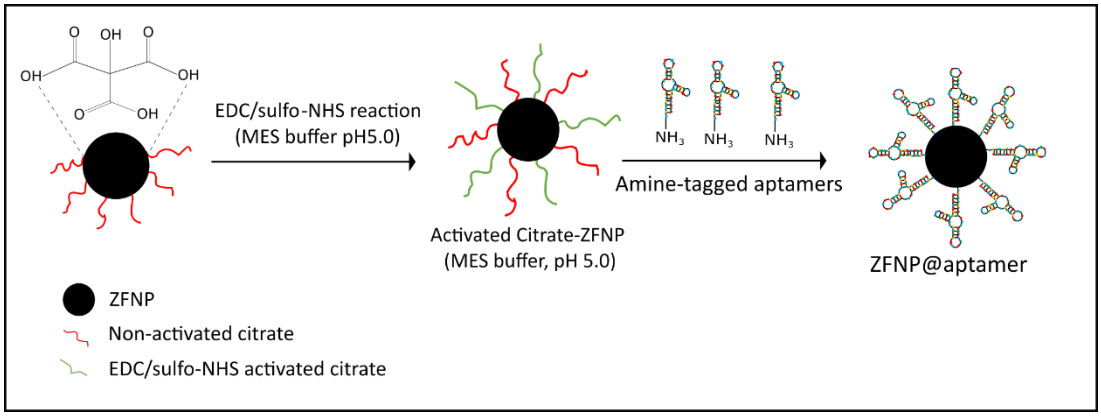

Figure 4.1 Schematic showing covalent immobilisation between amine-containing aptamers and ZFNPs@citrate using EDC and sulfo-NHS. ZFNPs@citrate are activated by EDC and sulfo-NHS in MES buffer. Amine-tagged aptamers are then added to mix wih the particles.

4.2.3.4.2 Bacteria capture efficiency

The capture efficiency of ZFNPs@aptamer was assessed using a magnetic separation technique. This study also investigated the effect of BSA as a blocking agent.

Four samples were included in the bacteria capture efficiency test: bare ZFNPs@citrate, ZFNPs@citrate/BSA, ZFNPs@aptamer, and ZFNPs@aptamer/BSA. To block nanoparticles with BSA, the ZFNPs@citrate and the ZFNPs@aptamer were purified by the centrifugation at 8500 rpm for 20 min using centrifugal filters. The ZFNPs@citrate and the ZFNPs@aptamer were subsequently redispersed in 10 mM PBS buffer containing 1% BSA for 30 min. They were washed again and dispersed in PBS buffer containing 0.5% BSA and 0.1% Tween 20.

In microbiological experiment, S*almonella typhimurium* was spiked into 1 mL of the ZFNPs@citrate, ZFNPs@citrate/BSA, ZFNPs@aptamer, and ZFNPs@aptamer/BSA samples. The concentration of the nanoparticles was 0.1 mg/mL while *Salmonella typhimurium* was 10^5 CFU/mL. The interaction between the nanoparticles and the bacteria was held for 20 min. Captured bacteria were isolated by a permanent magnet. The supernatant discarded after magnetic decantation was collected and grown on agar plates. The operation of the magnetic immunoseparation assay is displayed in Figure 4.2.

Capture efficiency was calculated from the number of unbound *Salmonella typhimurium* that was found in the supernatant after magnetic decantation. The total number of bacteria was 10^5 CFU. The capture efficiency was identified by the following equation:

$$\textbf{Capture efficiency (\%)} = \left(1 - \left(\frac{\textbf{Unbound bacteria}}{\textbf{Total bacteria}}\right)\right) \textbf{x } 100\% \qquad \textbf{(Equation 4.1)}$$

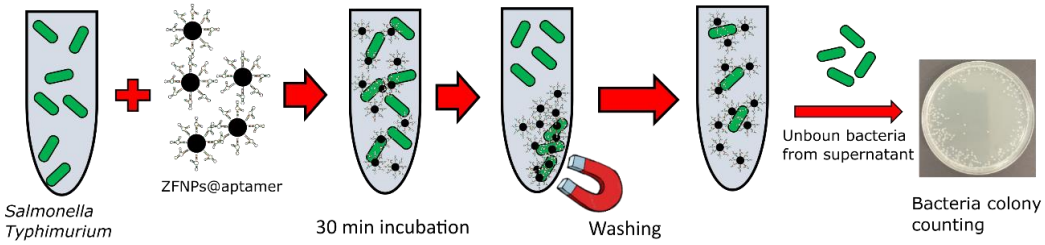

Figure 4.2 Diagram of the immunoseparation technique. The aptamer-conjugated ZFNPs were incubated with bacteria to allow for antigen-aptamer interaction. A permanent magnet was held aside the mixture to attract the ZFNP-bound bacteria cells. Unbound bacteria were transferred to an LB agar plate for colony counting.

4.2.4 Antibody-conjugated gold nanospheres

4.2.4.1 Optimisation of conjugation reaction

Determining the ideal condition for the absorption of antibodies on to the surface of AuNSPs was carried out by a flocculation study. A half-strip assay was applied in this section to optimise the preparation of the conjugate to be used in the LFA.

The gold conjugates were prepared for the detection of two analytes: *Salmonella typhimurium* and DENV2-NS1. The first part of the section explains the optimisation of anti-*Salmonella typhimurium* monoclonal antibody conjugation for the LFA system. Various conditions were investigated to maximise the LFA visual signal.

The second part shows the exploration of the optimum condition to conjugate anti-DENV2-NS1 DA034 mAb (DA034-mAb). Then, the optimised condition was applied to other DENV2-NS1 specific antibodies and the conjugates were investigated to find

the pair of antibodies (capture and detection antibody) that expresses the strongest visual signal on the half-strip LFA.

UV-vis spectrometer (SpectraMax M2, Molecular device) was utilised for optical measurement. Determining the colour intensity ratio of lateral flow strips follows the protocol provided in Section 3.2.4.

4.2.4.1.1 Conjugation of anti-*Salmonella typhimurium* mAb

To determine the optimal pH for antibody adsorption onto AuNSPs, the pH of as-synthesized AuNSPs (OD_{517} = 1.0) was adjusted to between 6.5 and 9.5 with 0.5 pH unit interval using 0.1 M K_2CO_3. 200 µL of each pH were transferred to a 96-well plate. Then, 10 µL of anti-*Salmonella typhimurium* mAb were added to each sample to obtain a final concentration of 14 µg/mL. The absorption of antibodies was proceeded for 30 min at RT under vigorous mixing. Following that, 20 µL of 10% NaCl were pipetted to the mixtures, then continuously mixing for another 10 min. The absorption spectrum was measured from 400 and 800 nm.

To determine the optimal amount of added antibody, the pH of the colloidal AuNSPs was modified to 9.0 using 0.1 M K_2CO_3 and 200 µL of the AuNSPs were transferred to a 96-well plate. Then, 10 µL of anti-*Salmonella typhimurium* mAb were added to each well to reach final concentrations scaling from 5 to 20 µg/mL. The mixtures were left at RT for 30 min with continuous mixing. Then, 20 µL of 10% NaCl were added to disturb the stability of the conjugates for 10 min. The absorption spectrum was measured from 400 and 800 nm.

4.2.4.1.2 Conjugation of anti-DENV2-NS1 mAb

To identify the optimum pH for antibody absorption onto AuNSPs, 0.1 M K_2CO_3 was added to modify the pH of the AuNSP solution from 6.5 and 9.5. 200 µL of each pH were transferred to a 96-well plate. 10 µL of anti-NS1 DA034 mAb were added to each well to achieve a final concentration of 20 µg/mL. The reaction was kept for 30 min. Colloidal stability was disturbed by adding 20 µL of 10% NaCl, followed by

vigorous mixing for another 10 min. The absorption spectrum was recorded from 400 and 800 nm.

Next, to determine the optimal concentration of the added antibody, the AuNSPs were adjusted to a pH of 9.0 and transferred to a 96-well plate. 200 µL of AuNSPs were added to each well. Then, anti-DENV2-NS1 DA034 mAb was added to each well to reach final concentrations ranging from 5 to 20 µg/mL. The conjugation reaction was kept under continuous rotation for 30 min at RT. Subsequently 20 µL of 10% NaCl were added and the mixtures were mixed for another 10 min. The absorption spectra of the conjugates were measured from 400 to 800 nm.

4.2.4.2 Half-strip assays

4.2.4.2.1 *Salmonella typhimurium* detection

To prepare the gold conjugate for *Salmonella typhimurium* detection, 1 mL of AuNSPs (OD_{517} = 1.0) at pH 7.5 was mixed with the corresponding antibody (14 µg/mL) and rotated for 30 min. BSA was then added to the mixture to reach a concentration of 1% and mixed for another 30 min. The conjugate was washed by the centrifugation at 14000 rpm for 20 min at 4 ˚C. The pellets were redispersed in PBS buffer containing 0.5% BSA and 0.1% Tween 20 and kept at 4 ˚C until use.

A nitrocellulose membrane (Prima 40) was spotted by 0.2 µL of anti-*Salmonella* pAb (1 mg/mL) and dried at 37 °C. The suspension of *Salmonella typhimurium* was prepared in a series of 10-fold dilutions from 10^1 to 10^8 CFU/mL in 100 µL of PBS buffer added with 0.5% BSA and 0.1% Tween 20 in a 96-well-plate. Then, 20 µL of the conjugates were pipetted into the wells of the plate. The strips were immediately dipped into each well and left for 20 min to complete antigen-antibody interaction and migration of the conjugates. The membranes were washed by adding PBS buffer with 1% tween 20. The protocol is displayed in Figure 4.3.

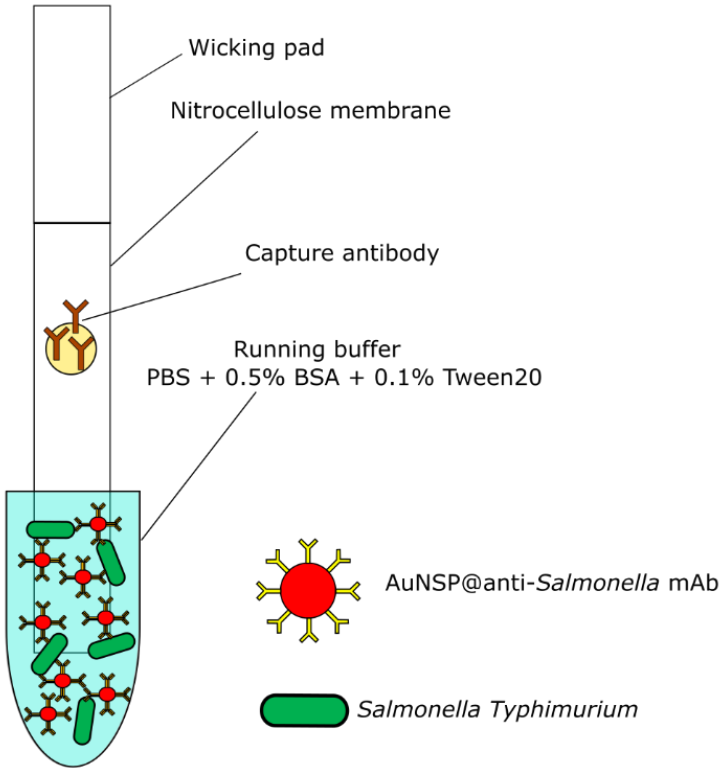

Figure 4.3 Diagram of a half-strip LFA for *Salmonella typhimurium* detection. Capture antibody is coated on the membrane.The strip is dipped into the mixture of gold conjugates and the bacteria in running buffer.

4.2.4.2.2 DENV2-NS1 detection

Four different antibodies were introduced into the experiment to find the most compatible pair of antibodies that generated the highest signal intensity on the nitrocellulose membrane. The antibodies were used as the detection antibody (being conjugated to the AuNSPs) and the capture antibody (being coated on the nitrocellulose membrane), as illustrated in Figure 4.4. The antibodies, namely anti-DENV-NS1 pAb, anti-DENV2-NS1 “DA034” mAb, anti-DENV2-NS1 “EA1” mAb, and anti-DENV2-NS1 “LH5” mAb, were used as a detection antibody and a capture antibody to determine the most suitable pair for LFA providing the highest visual signal.

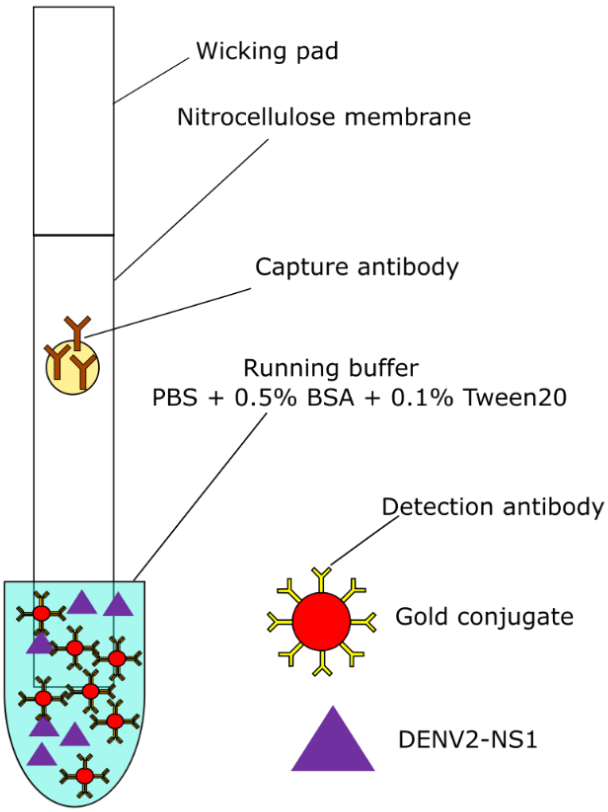

Figure 4.4 Diagram of a half-strip LFA for DENV2-NS1 detection. Capture antibody is coated on the membrane.The strip is dipped into the mixture of gold conjugates and DENV2-NS1 in running buffer.

The suspension of AuNSPs was adjusted to pH 9.0, and vigorously mixed with one of the antibodies (10 µg/mL) for 30 min. Following that, their non-specific binding sites of the AuNSPs were blocked with 1% BSA for 30 min. Unbound antibodies and BSA were removed by centrifugation at 14,000 rpm for 20 min at 4 ˚C. The pellets were redispersed in a storage buffer (20 mM borate buffer (pH 9.0) with the addition of 1% BSA, 0.5% Tween 20) and store at 4 ˚C until use.

To prepare the strips, 2 µL of one of the antibodies (0.5 mg/mL) were pipetted onto the membranes and dried at 37 °C for 2 h. Then, the strips were kept at 4 °C with desiccant until use. Each well of a 96-well plate was filled with 100 µL of DENV2-NS1 (100 ng/mL) in the sample buffer (PBS with 0.5% BSA and 0.1% Tween 20), followed by the addition of 20 µL of the conjugates. The strips were dipped into each well for 20 min and washed with the PBS buffer containing 0.5% Tween 20. The strips were

photographed for image analysis and the results were presented in the format of intensity ratio via the green channel of the Bayer filter (Section 3.2.4).

4.3 Results and discussion

4.3.1 *Salmonella typhimurium* growth curve

The calibration growth curve of *Salmonella typhimurium* is essentially needed to identify the CFU of the bacteria in the solution. It can be established by monitoring the turbidity of bacteria culture media. [247, 248] The suspension of *Salmonella typhimurium* was subjected the wavelength of 600 nm and the optical absorption of the incident light was measured. In Figure 4.5A, the graph of the OD versus the duration of incubation is plotted. It is seen that the OD value increased slightly in the first 2 h followed by an exponential increase. This suggests that the number of pathogens doubled over time. The period of this rapid growth is known as the "exponential phase" which provides fresh and viable bacteria. [247]

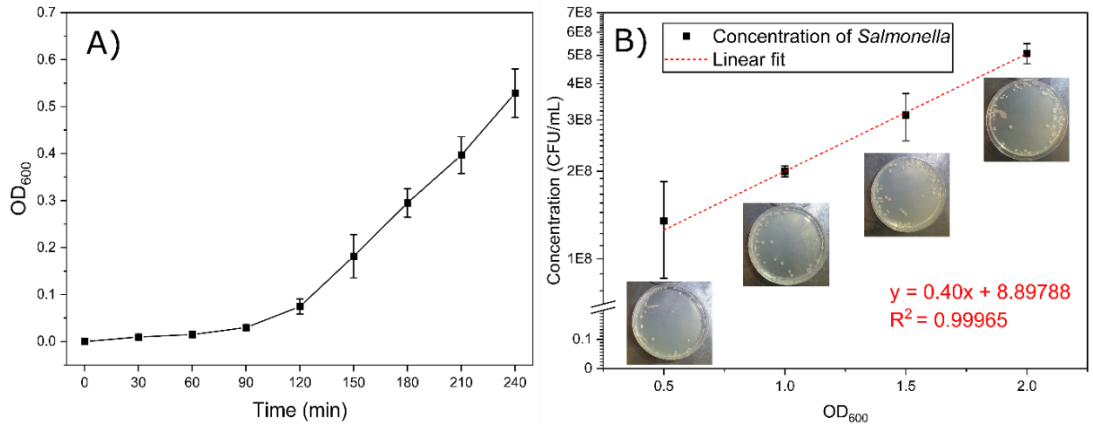

Figure 4.5 Optical characteristic of *Salmonella typhimurium*. A) Calibration growth curve of *Salmonella typhimurium*, showing OD_{600} as a function of incubation time. B) The concentration of *Salmonella typhimurium* versus OD_{600} identified by the colony counting method. Insets display bacteria culture plates. Data are presented as the mean ± standard deviation (n = 3).

Viable bacteria cells were collected from the exponential growth stage and suspended in PBS buffer. The turbidity was adjusted and cultured on agar plates for

colony counting. The graph is plotted in Figure 4.5B shows the relationship between CFU per mL and the OD value on a semi-logarithmic scale. The concentration of *Salmonella typhimurium* scaled up linearly and was proportion to the OD value with a good linear fit (R^2 = 0.99965). The result shows that the number of bacteria colonies can be adjusted from ~1 x 10^8 CFU/mL to ~5 x10^8 CFU/mL by modifying the OD of the suspension.

A previous report mentions the issue of cell geometry on optical measurement. [248] In general, the optical measurement of bacterial turbidity is the detection of incident light that is scattered by bacterial cells and non-reacted incident light. The photons are received by the optical detector and converted into an OD value. The Beer-Lambert law is applied to determine the relationship between OD and cell concentration. However, a major concern is the change in the size of bacteria during the measurement of bacteria turbidity, which leads to a diversity of incident light scattering. Under optimal conditions, such as rich nutrient and proper temperature, bacteria cells continuously grow and become larger, which changes their optical properties. Therefore, at a certain point, the OD value is no longer proportional to the cell number.

To address the problem, dilution of the bacteria suspension is required. At low OD values, the correspondence between OD and cell number remains valid. The linear dependency of the growth curve is applicable when OD ≤ 0.4 [247] or ≤ 0.2. [248] At low bacteria concentrations, the pure event of single light scattering can be assumed as the light is only scattered once before reaching the detector. In this regime, the OD value is proportional to the concentration of bacteria, as defined by the Beer-Lambert law. On the other hand, at high density of bacteria, the incident light is likely to scatter multiple times, significantly decreasing the number of photons approaching the detector and resulting in a parabolic growth.

In this work, nutrients were removed from the suspension of *Salmonella typhimurium* to minimise the effect of morphological change. The shortage of nutrient also hinders the bacteria from dividing, thereby keeping the number of the bacteria constant. Moreover, it can be assumed that the size of *Salmonella*

typhimurium remained constant during the measurement. The graph showing the correlation between the CFU of *Salmonella typhimurium* and OD value was used to adjust the concentration of the bacteria in this thesis.

4.3.2 Aptamer-immobilised zinc ferrite nanoparticles

4.3.2.1 EDC/sulfo-NHS ratio optimization

A layer of citrates on the surface of ZFNPs provides electrostatic hindrance to keep themselves stable in aqueous solution. The citrates contain carboxylate groups allowing further functionalisation with proteins via amide bonds. Carbodiimide crosslinking assay was applied to immobilise amine-modified aptamers to ZFNPs.

Firstly, ZFNPs@citrate were activated by EDC treatment, without succinimide ester, to monitor the pure impact of the EDC on the physical properties. Carbodiimide reaction was performed in MES buffer (pH 5.0) to provide the most coupling efficiency. [147, 148] Before EDC treatment, the initial hydrodynamic diameter and zeta potential of ZFNPs@citrate were 44 nm and -27 mV, respectively. Figure 4.6 shows that the size and the surface charge of the ZFNPs@citrate increased with the amount of EDC. The negative charge of the citrates is responsible for the stability of ZFNPs. Nonetheless, the EDC activation turned the carboxylates of the citrates into a neutral-charged o-Acylisourea active ester. Since the electrical surface charge increased, the hydrodynamic size increased due to the disruption of the electrostatic barrier.

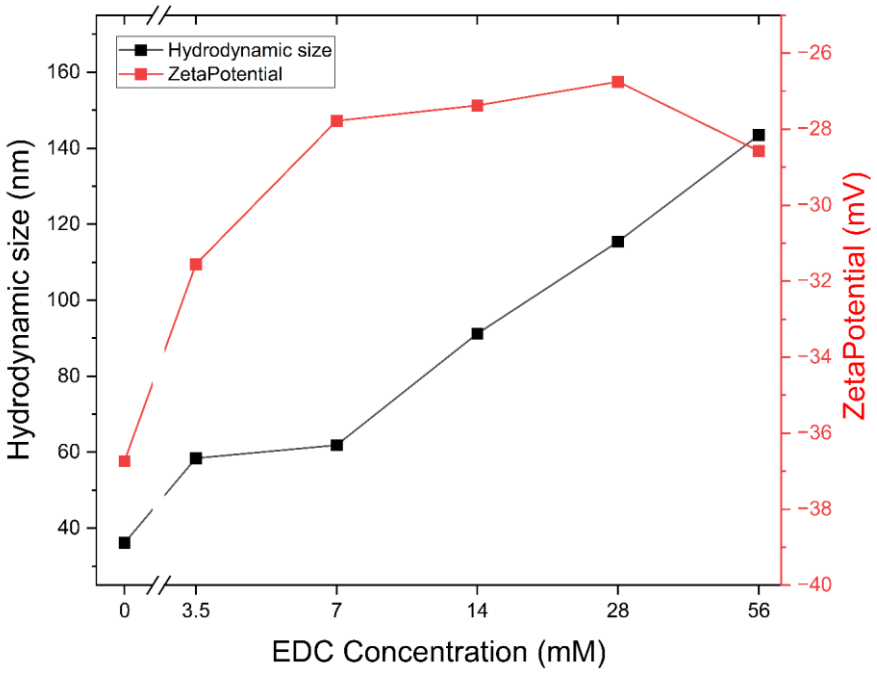

Figure 4.6 Results of DLS and zeta potential measurements of ZFNPs@citrate after adding various concentrations of EDC: 3.5, 7, 14, 28, and 56 mM.

In the steady state, ZFNPs@citrate were stabilised by electrostatic repulsion from citrates. However, when the repulsive force is insufficient, the stability is collapsed and the individual nanoparticle are overwhelmed by the van der Waals force. [31, 134, 148, 249] This results in the attraction between adjacent nanoparticles and the formation of clustered nanoparticles. It is reported that the EDC intermediates that do not interact with primary amines will revert to original citrates. [147] However, it was empirically observed that the use of EDC caused irreversible aggregation and subsequent precipitation. This suggests that the electrostatic repulsion of citrates cannot overcome the strong attraction of the van der Waals force. It points out the need to balance the number of EDC-treated and untreated citrates to maintain monodispersity of ZFNPs@citrate and improve coupling efficiency.

Because of the rapid hydrolysis rate of EDC intermediates and water solubility concerns, sulfo-NHS was added to improve the effectiveness of immobilisation. In the coupling reaction, colloidal ZFNPs@citrate were treated with various ratios of EDC and sulfo-NHS (1.25:1.5, 2.5:5, 5:10, 7:14, and 14:28). In Figure 4.7A, the hydrodynamic diameter and zeta potential of ZFNPs@citrate changed after

EDC/sulfo-NHS reaction, compared to the inactivated ZFNPs@citrate. Decreasing the concentration of EDC and sulfo-NHS (1.25 mM: 2.5 mM and 2.5 mM: 5mM) led to the increase in the hydrodynamic diameter, probably because of the aggregation of ZFNPs@citrate during carbodiimide treatment.

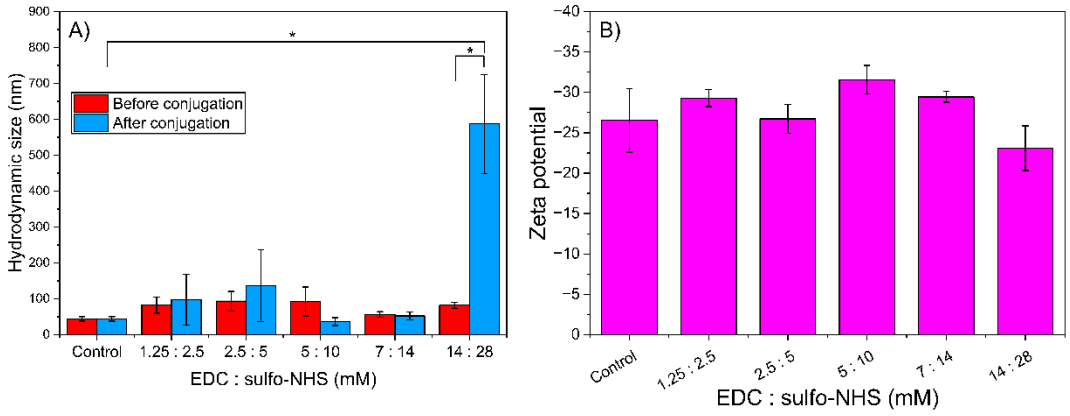

Figure 4.7 Hydrodynamic sizes and electrical surface properties of ZFNPs before and after conjugation. A) The hydrodynamic diameter of ZFNPs before and after aptamer immobilisation with various concentrations of EDC and sulfo-NHS. P-values were obtained using a two-tailed paired-samples t-test. *p < 0.05, **p < 0.01, ***p < 0.001, and ****p < 0.0001. B) The hydrodynamic diameter and zeta potential of the aptamer immobilised ZFNPs with various concentrations of EDC and sulfo-NHS (p > 0.05). P-values obtained by one-way ANOVA. Data are represented as the mean ± standard deviation of three independent samples (n = 3).

After the addition of amine-modified aptamers to the EDC-treated ZFNPs@citrate, a significant increase in the hydrodynamic size was found only in the sample that was treated by 14 mM EDC and 28 mM sulfo-NHS. However, the large change in the hydrodynamic diameter is possibly contributed by the aggregation of the nanoparticles during the EDC and sulfo-NHS treatment. In addition, the aptamer is a small oligonucleotide (MW ~8-25 kDa) having the length of *ca.* 2 nm. [250] Therefore, DLS measurement may not be able to confirm the successful conjugation of the aptamers but is more likely to be associated with the aggregation of the nanoparticles.

The surface charge of the nanoparticles was measured after the functionalisation of the aptamers (Figure 4.7B). However, a significant difference in the zeta potential of ZFNPs@citrate and ZFNPs@aptamers could not be detected by one-way ANOVA,

indicating no significant difference between the samples. The non-immobilised ZFNPs@citrate had a zeta potential of -27.7 mV, due to the profuse coverage of negatively charged citrate molecules. None of the immobilised samples showed significant change in the electrical surface charge. This is likely becasaue the aptamer is negatively charged due to the presence of the phosphodiester backbone, [251] as are the citrate and the succinimide. Therefore, no significant change in the surface charge was observed in the ZFNPs@aptamer.

The ratio of 7 mM EDC to 14 mM sulfo-NHS showed the least variation in hydrodynamic diameter after carbodiimide reation indicating the most stability. Therefore, this ratio was chosen to be used to prepare the immobilisation of aptamers to ZFNPs@citrate.

The formation of the amide bond was investigated by FTIR measurement (Figure 4.8). The IR absorption of ZFNPs@citrate showed peaks at 1397 cm^{-1} and 1613 cm^{-1}, contributing to the stretching of COO^- of the carboxylates in the citrates. The absorption at 1063 cm^{-1} is associated with the hydroxyl group. [252] For ZFNPs@aptamer, the shape of the IR spectrum changed indicating an alteration in surface chemistry after the aptamer immobilisation process. The intensity of peak at 1613 cm^{-1} of COO^- was weaker than that of ZFNPs@citrate, indicating a decrease in the number of carboxylates on the surface. The evidence of secondary amide bond formation was the observation of peaks at 1647 cm^{-1} and 1687 cm^{-1} due to the C=O stretching vibration of amide I. The absorption at 1539 cm^{-1} was associated with the bending of NH_2 of amide II. [46, 253, 254] The chemical structure of the aptamers was also seen from the IR absorption at 969 cm^{-1} and 1011 cm^{-1} associating with the stretching of the phosphates in nucleotides. [255, 256] The change in the IR spectrum after immobilisation with the aptamers confirms the formation of a covalent peptide bond.

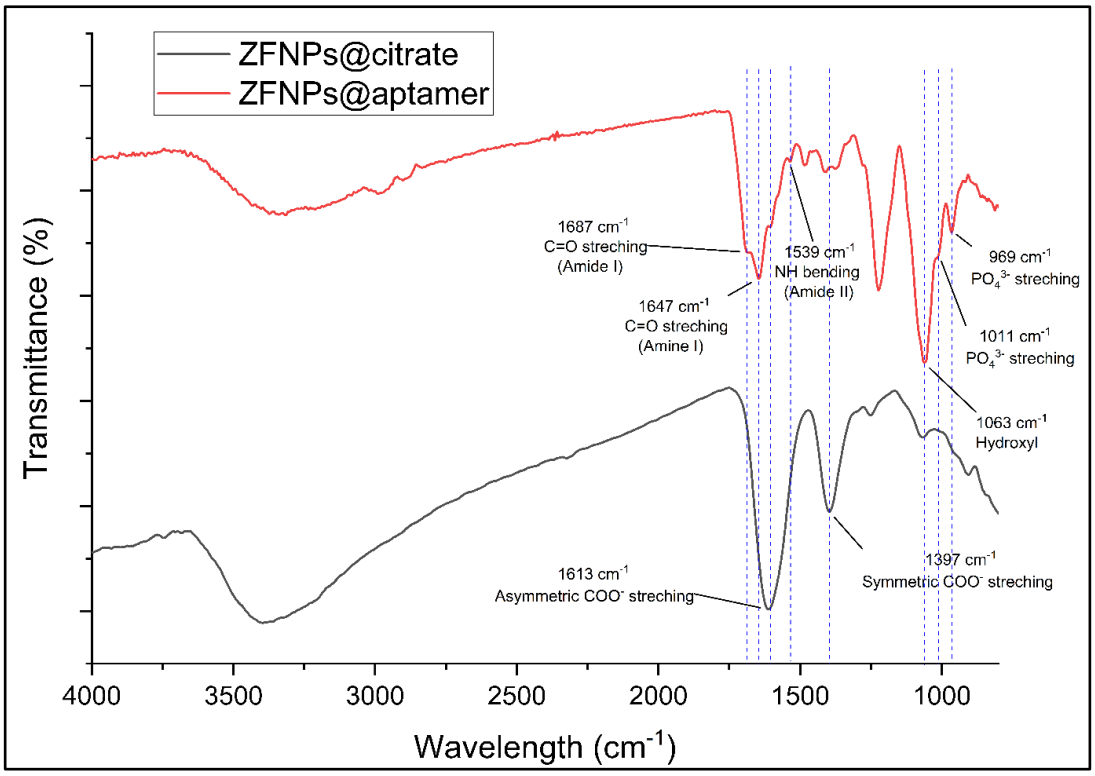

Figure 4.8 FTIR spectra of ZFNPs@citrate and ZFNPs@aptamer.

4.3.2.2 Addition of aptamer optimisation

Following the carbodiimide reaction, ZFNPs@citrate interacted with the amine groups of the aptamers to form amide bonds. However, the optimum amount of aptamers to be added needs to be determined to reduce the cost of fabrication and increase the capturing efficiency.

To visualise the presence of the aptamers on the surface of the nanoparticles, gel electrophoresis technique was carried out. The aptamers were stained with fluorescent dye and the visuallisation of the result under UV excitation is shown in Figure 4.9. In the principle of gel electrophroresis, the distance of nanoparticle migration is dependent on the potential difference and the mass of the nanoparticles. [47] In this case, the negatively charaged nucleic acids moved to the counter pole through the porous gel by electrical force. The lighter the sample, the longer the distance it migrated.

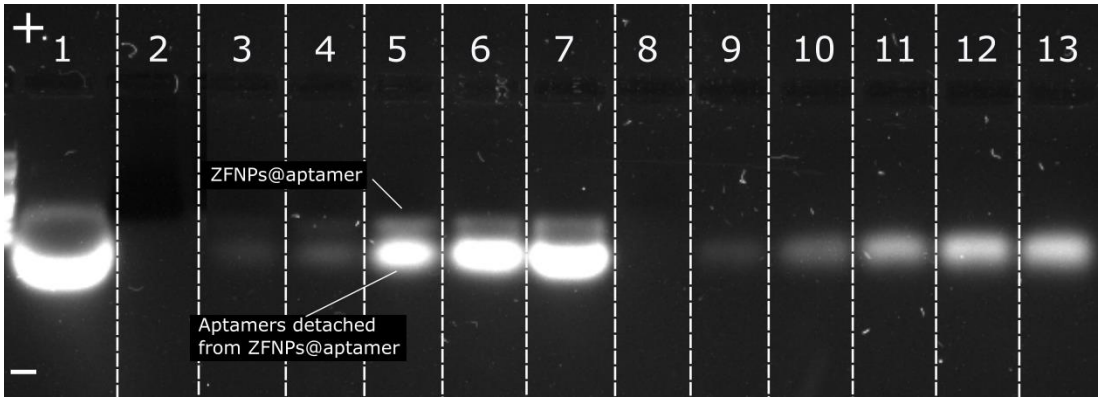

Figure 4.9 Visualisation of the stained aptamers under UV illumination: lane 1) free aptamer; lane 2) ZFNPs@citrate; lane 3) – lane 7) ZFNPs@aptamer with the addition of 10 to 50 µL of 100 mM aptamers; lane 8) blank; lane 9) – lane 13) supernatant collected after centrifuged of after conjugation of ZFNPs@aptamer with the addition of 10 to 50 µL of 100 mM aptamers.

The first and second lanes served as the controls of the experiment showing the fluorescence of the pure aptamers and the ZFNPs@citrate, respectively. The stained aptamers (lane 1) expressed strong fluorescent emission whilst the ZFNPs@citrate (lane 2) did not show any observable fluorescent signal on the agarose gel. Lanes 3 to 7 represent the fluorescence of the aptamer-immobilised ZFNPs with the addition of 10 to 50 µL of aptamers. Unexpectedly, two fluorescent bands were observed in all samples, indicating that two populations were presented: detached aptamers and ZFNPs@aptamer. The bands with a longer migration distance aligned with the band of the pure aptamers in lane 1, indicating the elution of the aptamers from the surface of ZFNPs. The other bands migrated a shorter distance due to their higher mass and were therefore possibly the aptamer-conjguated ZFNPs. The signals from lanes 9 to 13 were the fluorescence of the supernatant solution collected from the first wash during the immobilisation step. These fluorescent signals were proportional to the amount of aptamers added, suggesting that an excess amount of aptamers were added to react with the ZFNPs@citrate.

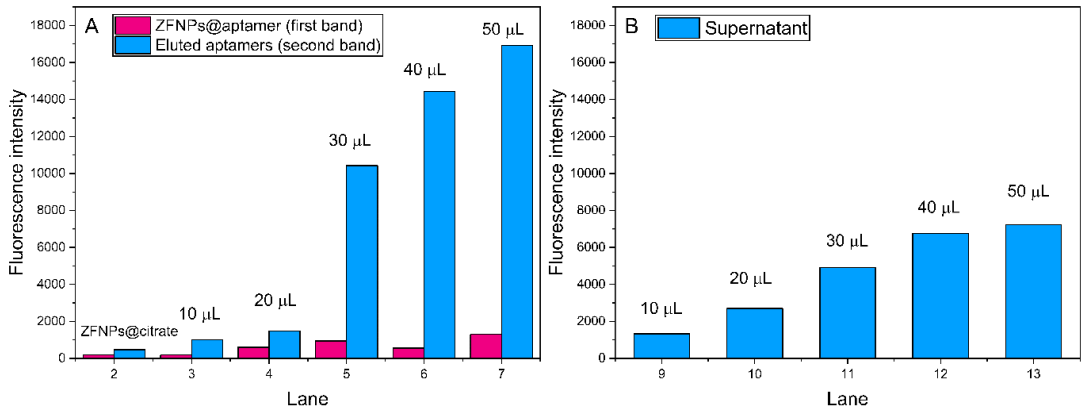

Figure 4.10 Fluorescene intensities of aptamers on an agarose gel. A) The fluorescence intensities of ZFNPs@aptamer (top bands) and the aptamers that eluted from ZFNPs@aptamer (bottom bands) from lanes 2 to 7. B) The intensities of the supernatant after conjugation from lanes 9 to 13.

The fluorescent bands on the agarose gel were quantified using the built-in gel analysis function in ImageJ to determine fluorescent intensities. Figure 4.10 shows that the fluorescent intensity of the stained aptamers depends on the amount of aptamers added. More aptamers reacting with ZFNPs@citrate resulted in more aptamers being covalently immobilised, as well as more aptamers being detached (Figure 4.10A). The aptamers that did not bind to ZFNPs@citrate were separated by centrifugation and released in the supernatant. The amount of unbound aptamers was proportional to the amount of aptamers added (Figure 4.10B).

A significant amount of aptamers were not covalently adhere to the surface of ZFNPs. These aptamers were probably absorbed by electrostatic attraction between the negatively charged citrates and positively charged amine groups [134, 135, 147]. Hence, they were desorbed when introduced to Tris-borate-EDTA buffer during the electrophoresis measurement. The remaining aptamers may be anchored by stronger peptide bonds.

The FTIR and gel electrophoresis results imply that the aptamers were covalently bound to the surface of the ZFNPs. Nonetheless, most of the aptamers were loosely bound to the nanoparticles by weak physical absorption. Therefore, they easily detached in high-ionic solutions. Despite low immobilisation efficiency, some aptamers were covalently bound with ZFNPs@citrate.

4.3.2.3 Capture efficiency of aptamer-immobilised zinc ferrite nanoparticles

The capture efficiency of the ZFNPs@aptamer against *Salmonella typhimurium* was assessed using a magnetic immunoseparation assay. To determine the efficiency of the conjugates in binding to *Salmonella typhimurium*, it is important to calculate the efficiency based on the number of unbound bacteria in the supernatant after magnetic decantation. On the other hand, calculating the efficiency based on the number of the bacteria captured by the nanoparticles is likely to underestimate the actual number of bacteria colonies due to the aggregation of the nanoparticle-bacteria complexes during magnetic separation. [257, 258] After magnetic decantation, the MNPs are expected to bind to the bacteria and are transferred to the LB agar plates to grow the bacteria into visible colonies. However, the MNPs may capture more than a single bacteria cell or form a cluster. As a result, the grown colonies on the agar plates may appear as one colony, thereby low accuracy. Therefore, this study determined the number of viable *Salmonella typhimurium* using a traditional colony counting method which counts the number of colonies that appears on LB agar plates.

According to Figure 4.11, the capture efficiency of ZFNPs@citrate was 29.56% which is high considering the absence of aptamers. The number of captured bacteria was reduced to 17.43% after BSA was attached to the surface of the ZFNPs@citrate. This suggests that *Salmonellay typhimurium* were captured by non-specific interactions. A similar finding was observed in the samples with aptamer immobilisation. The ZFNPs@aptamer without BSA could extract 30.35% of *Salmonella typhimurium* from PBS buffer while ZFNPs@aptamer/BSA only capture 17.19% of the bacteria in the sample. These results points out that the aptamers used in this study lack binding activity toward *Salmonella typhimurium* as there is no significant difference between the ZFNPs@citrate and the ZFNPs@aptamer.

Salmonella typhimurium is a gram-negative bacterium which generally carries a negative charge due to the presence of teichoic acid and lipopolysaccharides on its the membrane. [259] The negatively charged ZFNPs@citrate and the ZFNPs@aptamer should create an electrostatic barrier to prevent the absorption of the bateria. Hence,

the nanoparticles likely bound with *Salmonella typhimurium* by non-specific absorption. Therefore, the attachment of the BSA blocked the free space on the their surface of the nanoparticles and reduced the capture efficiency of *Salmonella typhimurium*.

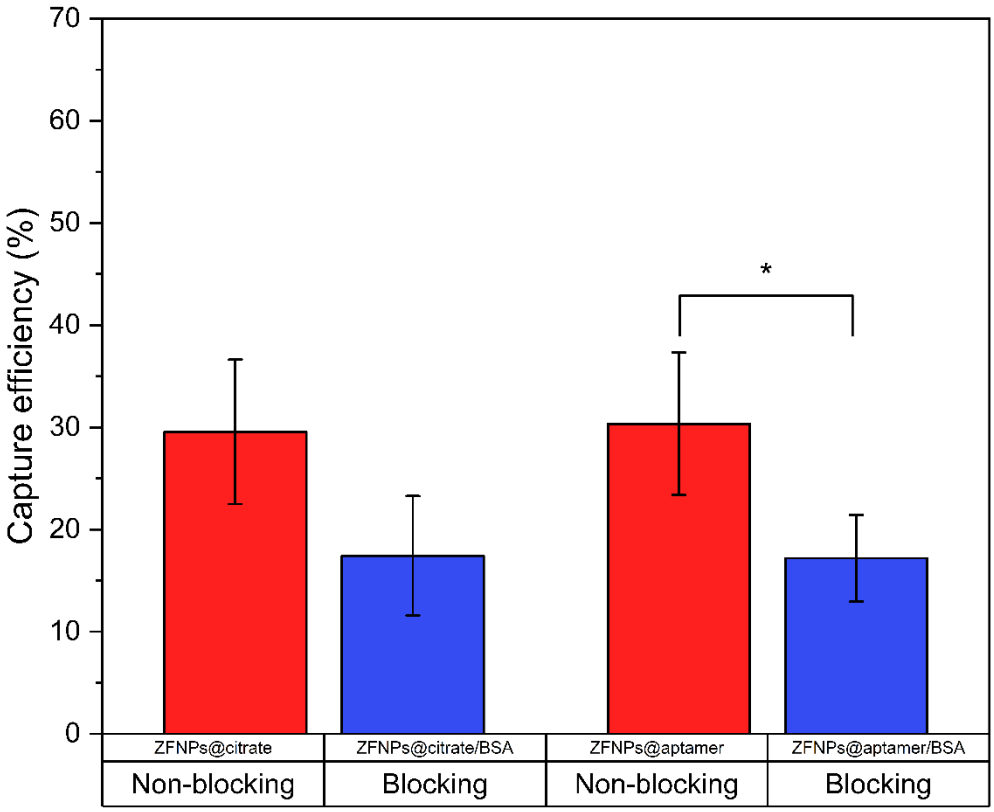

Figure 4.11 Capture efficiencies of ZFNPs@citrate and ZFNPs@aptamer with and without BSA blocking. Data are presented as the mean ± standard deviation (n = 3). P-values were obtained using a two-tailed paired-samples t-test. *p < 0.05, **p < 0.01, ***p < 0.001, and ****p < 0.0001.

The sequence of the aptamer used in this study has been reported to be specific to *Salmonella typhimurium* in the literature and it was therefore selected for immobilisation on the ZFNPs. [123, 246] However, the ZFNPs@aptamer did not effectively bind to *Salmonella typhimurium* in the sample as expected. There are several possible reasons for the poor binding activity of the ZFNPs@aptamer. Firstly, the steric barrier of BSA. Considering the geometries of BSA and the aptamer, the protein BSA (*ca.* 14 nm, MW ~ 66.5 kDa) is considerably larger than the nucleic acid (*ca.* 2-3 nm, MW ~ 12 kDa), which may generate a shielding effect. [148, 250] The presence of BSA may block the binding site of the aptamer, thus reducing its binding

activity. However, eliminating non-specific binding sites on the nanoparticles is necessary to prevent false positive results. [146] So, other blocking components, *e.g.* Tris-HCl buffer [141] and sucrose, [146] may be more suitable.

Another possibility is that the aptamer sequence was not properly folded on the surface of the ZFNPs. Aptamers are three-dimensional structures and their binding activity depends on their correct folding. If the aptamers are not folded properly, they will not able to bind to *Salmonella typhimurium*.

It is also possible that the aptamer sequence itself is not specific to *Salmonella typhimurium* in the conditions used in this study. In general, aptamers are selected for their binding affinity to a specific target molecule in a particular set of conditions. If the conditions used in this study were different from the conditions in which the aptamer was developed, it is possible that the aptamer did not bind to *Salmonella typhimurium*.

The efficiency of carbodiimide coupling could lead to failure. Generally, EDC crosslinker is used for the biological immobilisation of the MNPs. [134, 140, 141] However, carbodiimide coupling is complex and difficult as it can cause irreversible aggregation of the MNPs during the coupling reaction. The is due to imbalance between the charges of the EDC-treated carboxylates and the untreated carboxylates, which disrupts the electrostatic repulsion and allows the van der Waal force to overwhelm the stability of the MNPs causing aggregation.

Changing the chemical agent to stabilise the EDC intermediates to NHS should be considered. Sulfo-NHS was deployed in this study to promote water solubility of the ZFNPs@citrate and stabilise the EDC intermediates. However, the sulphonate groups (SO^{3-}) of sulfo-NHS provided a negative charge which may raise electrostatic repulsion and prevent the aptamers from interacting with the nanoparticles. [148] In this case, NHS ester is likely to be more suitable than sulfo-NHS, as it is a neutral species and does not cause electrostatic repulsion with the aptamers. This would encourage them to access to the EDC-treated carboxylates of the nanoparticles.

Otherwise, new ligands may need to be introduced into the ligand exchange reaction. Citrate is a small ligand whose the repusion is mainly contributed by electrostatic force. Other long-chain carboxylate-containing ligands, such as poly(ethylene glycol) [249] and poly(methyl methacrylate), [148] may be required to substitute the former glycol ligands of the ZFNPs. As the carbodiimide reaction alters the surface charge of the nanoparticles, the steric repulsion force of the long-chain ligands can be keep the nanoparticles monodisperse during the coupling reaction.

In addition, many studies mention the importance of the pH of the buffer. [135, 140-142] The pH can control the surface charge of the nanoparticles and biomolecules, which affects the electrostatic interaction. Maintaining the pH of the buffer below the isoelectric point of the aptamer can ensure the absorption of the aptamer to the ZFNPs@citrate via electrostatic attraction. [135, 140-142]. In an acidic solution where the pH is below the isoelectric point of the aptamer, NH_2 is protonated to NH_3^+ which encourages the aptamers to localise to the ZFNPs@citrate, hence the increasing the rate of carbodiimide crosslinking. The isoelectric pH of the aptamers has not yet been investigated in this study, and further investigation is essentially required. The isoelectric point can be determined by an electrophoresis-based assay, called "isoelectric focusing". [135]

In conclusion, the aptamer was covalently immobilised to the ZFNPs@citrate using EDC/sulfo-NHS method. However, the findings suggest the poor coupling efficiency and a lack of the binding activity of the ZFNPs@aptamer toward *Salmonella typhimurium*. The coupling assay needs to be revisited and optimised. The ZFNPs@aptamer were not used further in this thesis.

4.3.3 Antibody-conjugated gold nanospheres

Due to low efficiency of aptamer immobilisation on ZFNPs@citrate, they were replaced with 12 nm AuNSPs. As demonstrated in Chapter 3, 12 nm AuNSPs exhibit excellent photothermal effect under LED stimulation, comparable to those of the MNPs. The conjugation of antibodies to AuNSPs was achieved through physical

absorption, a non-directional and non-covalent attachment method. This approach was chosen because of its simplicity and speed process than covalent bonding. Moreover, it has been shown to provide robust attachment in certain environments, as explored in this section. Regarding stability, antibody-conjugated gold nanoparticles have been shown to retain their effectiveness in LFAs for up to 21 days when stored at 4 °C or RT. [260] Therefore, physical absorption is a suitable method for rapid optimisation of conjugate preparation for application in LFAs.

The physical absorption of antibodies is mainly contributed by hydrophobic interaction, thiol group, and the Coulomb interaction between the NH_2 groups of lysine and citrate ions on the surface of AuNSPs [135, 142, 261]. Antibody coverage provides the gold particles stability in high electrolytes solution.

The flocculation study was introduced to identify the optimal condition for antibody absorption. [135, 145, 146] This technique is based on the displacement of the charge on the AuNSPs surface. A surplus amount of salt is added to disturb the stability of the nanoparticles. However, the salt addition cannot displace the charge if the antibodies are linked via Au-S bond. The aggregation of the AuNSPs induces a shift and decrease in the LSPR absorption whereas the absorption at 650 nm increases. Hence, the difference between the absorption intensity at 520 and 650 nm is assigned as an indicator of the stability.

While Bradford assay is a widely used technique for quantifying protein concentrations in samples and has been used in optimising nanoparticle-protein conjugates, it was not included in this study. Instead, the flocculation test was performed to determine the minimum amount of antibodies required for absorption while ensuring sufficient stability in high electrolyte solutions. The Bradford assay, on the other hand, is more commonly used to determine immobilised antibodies. [131, 134, 135, 262] However, the Bradford assay does not provide a direct measure of the stability of conjugates in high-ionic solutions. Given the objectives of this study, the flocculation test is a more straightforward and generally a preferred method. However,the Bradford assay could be also used in conjunction with flocculation test to confirm the results.

4.3.3.1 *Salmonella typhimurium* detection

4.3.3.1.1 Anti-*Salmonella typhimurium* mAb conjugation

Firstly, the coupling buffer pH and the number of anti-*Salmonella typhimurium* mAb were varied. The turbidity of colloidal conjugates was triggered by the addition of salt and monitored on the UV-Vis spectrophotometer (Figure 4.12). The antibodies were added in excess to ensure full coverage of antibodies and sufficient protection. The variation of the pH did not significantly change the shape of the spectral absorption but the LSPR absorption at 520 nm and 650 nm slightly shifted (Figure 4.12A), probably becasue the isoelectric pH of the anti-*Salmonella typhimurium* is below 6.5. The difference between the absorption at 520 and 650 nm (Figure 4.12B) indicates that the most suitable conjugation pH is 7.5 at which the conjugates are the most stable when exposed to high-electrolyte solutions.

The pH of the buffer solution was kept at 7.5 and the concentration of the antibody was altered. The result in Figure 4.12C shows that the coverage of antibodies is vital for the stabilisation of the conjugates. The spectral absorptions at 520 and 650 nm significantly shifted and a colour change was observed in the experiment, from red ruby to violet to colourless, indicating aggregation. When the antibody concentration was beyond the stabilisation point, the AuNSPs were fully covered by the antibodies which protected them from the ionic strength. Hence, the gold solution was red even after the salt addition, implying the high stability of the conjugates. The difference between 520 and 650 nm (Figure 4.12D) shows that the stability increased with the amount of antibody and became plateaued at 14 µg/mL which was the stabilising concentration. Therferefore, the gold conjugates were prepared in PBS buffer at pH 7.5 with the addition of 14 µg/mL of the anti-*Salmonella typhimurium* mAb to be used in the microbiological test.

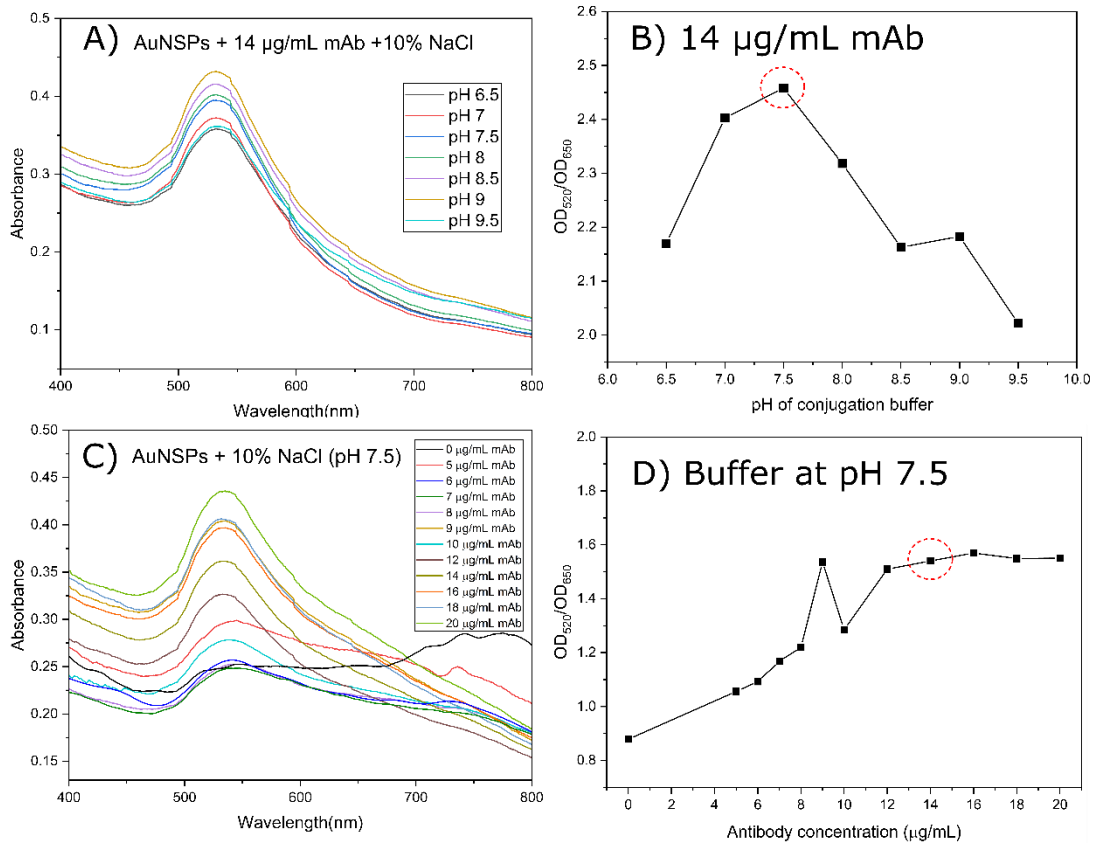

Figure 4.12 Results of the flocculation tests to identify optimal conjugation conditions of anti-*Salmonella typhimurium* mAb. A) UV spectrum absorption of the conjugation at different pH values. B) The stability index at different pH values while keeping the number of antibodies. C) The spectral absorption of the conjugate at various antibody concentrations. D) The stability index at different antibody concentrations while keeping the pH constant.

4.3.3.1.2 Half-strip assay for *Salmonella typhimurium* detection

Colloidal gold conjugates were prepared according to the optimal procedure described in Section 4.3.3.1.1 and dispersed in the storage buffer solution (PBS with the addition of 0.5% BSA and 0.1% Tween 20). The conjugates were then introduced into the half-strip LFA to assess whether the conjugates could detect *Salmonella typhimurium* and provide a visual signal. The bacteria were prepared in PBS buffer by serial dilution to concentrations ranging from 10^1 to 10^8 CFU/mL.

In Figure 4.13, a red stain was observed in the detection area at the highest concentration of pathogens (10^8 CFU/mL). The colouration was drastically decreased at 10^7 CFU/mL, likely due to the severe aggregation of the conjugates at the entry of the strips. This circumstance is unfavourable and commonly found in the

development of LFA for bacteria detection, [160] leading to a deficient sensitivity of detection as the LOD was at 10^7 CFU/mL.

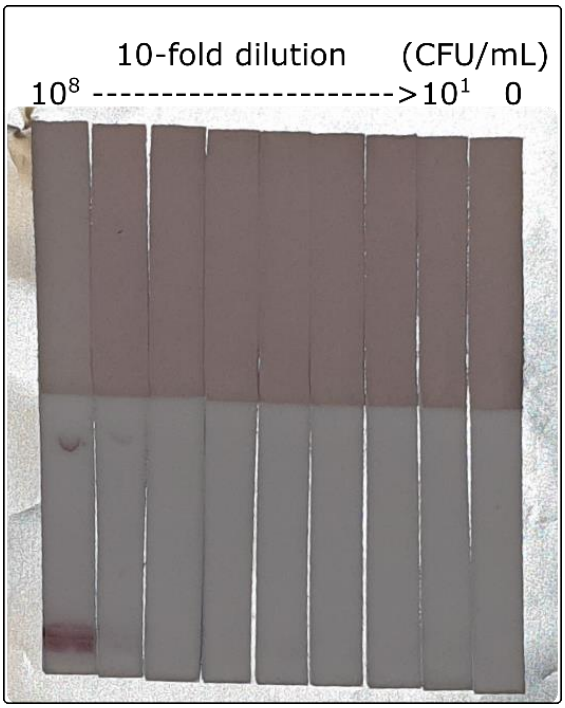

Figure 4.13 The membranes strips after interaction with blank sample and Salmonella Typhimurium at the concentrations between 10^1 and 10^8 CFU/mL.

It was hypothesized that the issue was caused by non-specific binding effect at the interface of the nitrocellulose membrane and PBS buffer, trapping the conjugates and *Salmonella typhimurium* in the pores of the membranes. [177] The first attempt to solve the issue was carried out to investigate the impact of the running buffer (see Figure 1 in Appendix F). The concentrations of the blocking protein additive (BSA) and the surfactant (Tween 20) was altered to determine the optimum amount that could minimise the non-specific binding of the nitrocellulose membrane and improve the stability of the conjugates. The absence of both BSA and Tween 20 in the running buffer resulted in a high background signal due to non-specific interaction between the nanoparticles and the membrane. Furthermore, the anti-*Salmonella* pAb in the detection zone blocked the migration of the conjugates, resulting in a "ghost spot" where the interaction between the conjugate-bacteria complexes and the anti-*Salmonella* pAb did not occur. Increasging the concentration of Tween 20 above 0.1% did not show any significant effects. Even at a concentration of 10% of Tween 20, the

nanoparticle-bacteria complexes were still stuck at the entry. The combination of the BSA and Tween 20 reduced the background signal caused by non-specific binding. The results suggest that at least 0.1% Tween 20 and 0.5% BSA are required in the running buffer to produce a clean background. Nonetheless, severe aggregation was still observed.

Clearly, most of the conjugates could not migrate through the membrane because of the formation of the nanoparticle-bacteria complexes which are larger than the pores of the membrane. To prove that, bare AuNSPs and AuNSPs@anti-*Salmonella typhimurium* mAb were prepared with and without BSA coating and incubated with *Salmonella typhimurium* (10^6-10^8 CFU/mL). According to the results in Figure 4.14A, the bare AuNSPs (without BSA coating) were captured by anti-*Salmonella* pAb in the detection zone regardless of the existence of bacteria. On the other hand, the visual signal was completely absent in the case of the BSA-blocking conjugates. Hence, the coloured signals in Figure 4.14A were caused by non-specific binding. [146] Notably, aggregation was not found when the antibody was not coated on the surface of the AuNSPs.

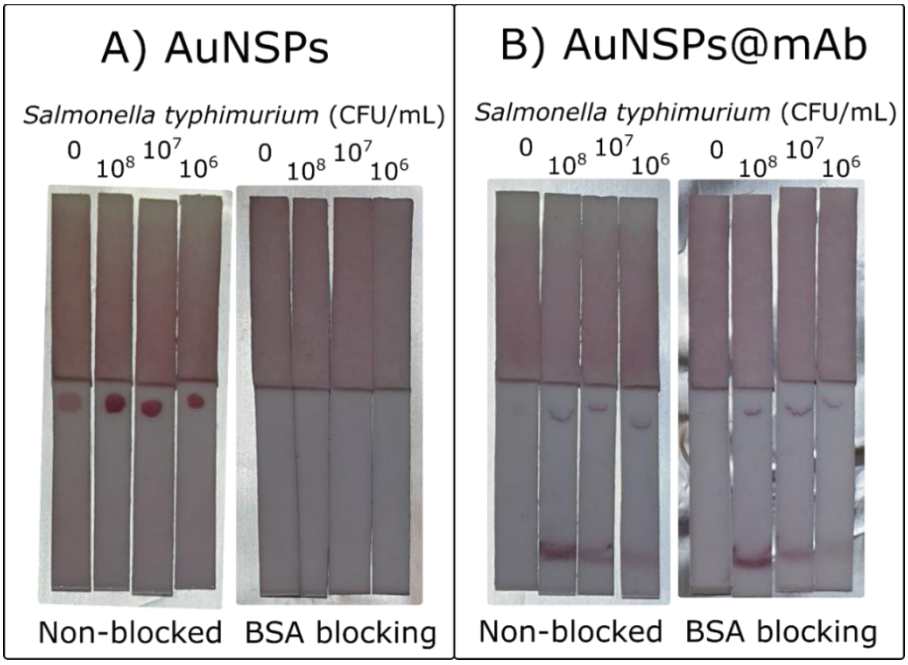

Figure 4.14 Appearance of the strips after migration of A) bare AuNSPs and B) AuNSPs@anti-*Salmonella typhimurium* mAb, with and without BSA blocking. Theses strips were incubated with *Salmonella typhimurium* (10^6 – 10^8 CFU/mL) and blank samples (negative controls).

AuNSPs@anti-*Salmonella typhimurium* mAb with and without BSA coating were added to react with the bacteria. In Figure 4.14B, when *Salmonella typhimurium* was absent in the sample, the conjugates could move through the membranes, reaching the wicking pads and a positive signal was not observed. However, the presence of *Salmonella typhimurium* in the samples caused the aggregation of the conjugates and most of them could not migrate through the membranes. The degree of blockage was dependent on the concentration of the bacteria. Moreover, the coloured spots in the detection zone appeared in a meniscus-like shape. This incidence occurred when the early-arrival nanoparticle-bacteria complexes were captured by the anti-*Salmonella* pAb in the detection zone and blocked the migration of the late-arriving nanoparticle-bacteria complexes. It is possibly caused by the crosslinking effect which occurrs when the single anti-*Salmonella typhimurium* mAb of the conjugates binds more than one epitope of the bacteria, as the antibody naturally has two antigen binding sites. [263, 264] As a result, induvial nanoparticle-bacteria complexes could bind to each other to form large clusters.

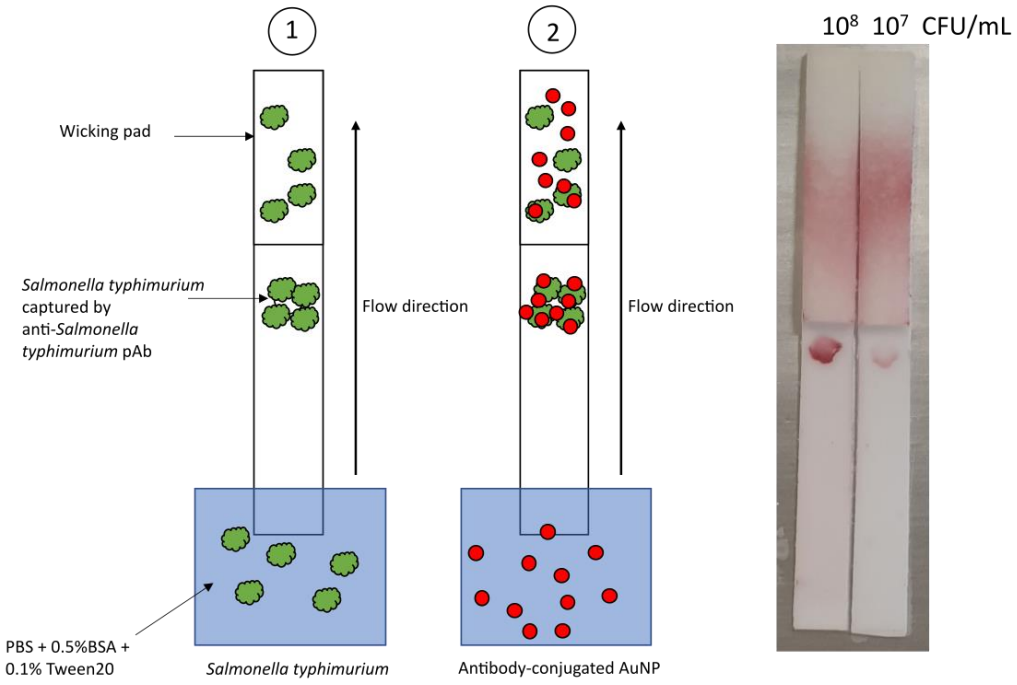

Figure 4.15 Diagram of the sample loading strategy. The strips were incubated with different concentrations of *Salmonella typhimurium* (10^8 and 10^7 CFU/mL), followed by the addition of conjugates. The displays of the strips after the assays were completed are shown on the right.

To identify whether the crosslinking effect of the antibody contributes to the aggregation of the conjugates and pathogens, the operation procedure was changed. In the original half-strip method, *Salmonella typhimurium* and the conjugates were mixed before being added to the test strips. This allows adequate time for the conjugates and bacteria to interact, which induces the nanoparticle-bacteria complexes to crosslink. In Figure 4.15, the strip was dipped into the bacteria suspension and the bacteria were captured by the antibodies in the membrane. Following that, the conjugates were added and bound to the captured bacteria in the membrane. Interestingly, the accumulation of conjugates at the entry disappeared and the coloured signal was visible at a concentratrion of 10^7 CFU/mL. In this scenario, the conjugates could not crosslink with each other, which is why there was no aggregation in the membrane. It suggests that the crosslinking effect was responsible for poor detection sensitivity.

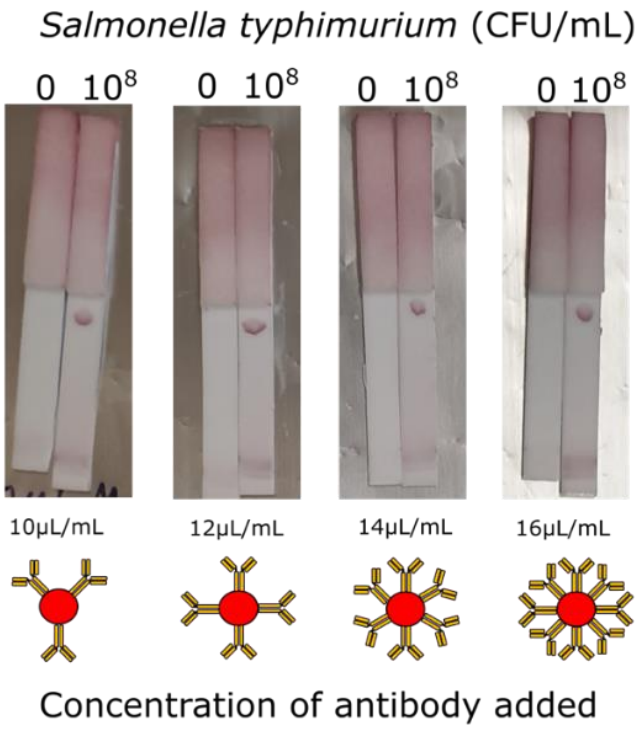

Figure 4.16 Images of the stips after incubating with *Salmonella typhimurium* and AuNSPs@anti-*Salmonella typhimurium* mAb with various concentrations of antibody coating.

Reducing the number of coating antibodies would result in a decrease in the available binding sites. Hence, the contration of anti-*Salmonella typhimurium* mAb was varied

from 10 to 16 µg/mL and conjugated to the AuNSPs. However, the result shows that altering the amount of the coated antibodies did not affect the colour intensity and did not reduce the crosslinking effect as severe aggregation was still existed (Figure 4.16).

The impact of the number of conjugats and *Salmonella typhimurium* on the crosslinking effect is illustrated in Figure 4.17. When the concentration of both conjugates and bacteria is high in the solution, there are abundant antigens and antibodies, which considerably increases the likelihood of aggregation due to crosskinking of nanoparticle-bacteria complexes Decreasing the concentration of the conjugates reduces the opportunity of cross-binding events by limiting the number of antibodies available to interact with the bacteria.

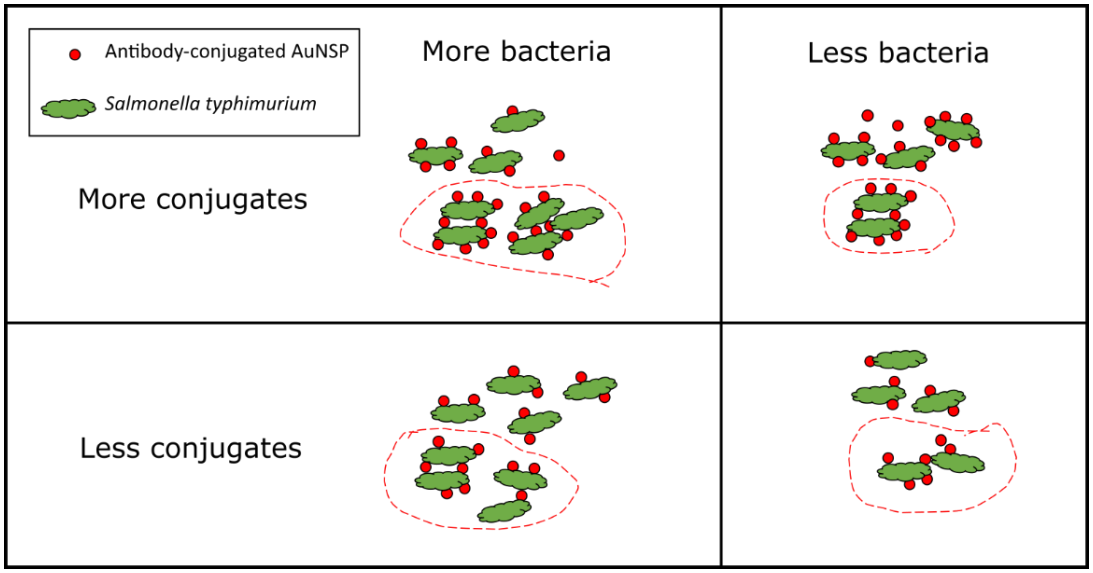

Figure 4.17 Diagram illustrating the interaction between various concentrations of *Salmonella typhimurium* and AuNSPs@anti-*Salmonella typhimurium* mAb.

Therefore, the conjugates were diluted by half before adding them to the suspension of *Salmonella typhimurium*. Figure 4.18 shows that the severity of aggregation was mitigated. The LOD was lowered to 10^4 CFU/mL since the complexes could move to the detection area to interact with the anti-*Salmonella* pAb. It points out the elimination of the large clumps of the complexes caused by crosslinking. Therefore, the concentration of the conjugates is very important and needs to be optimised.

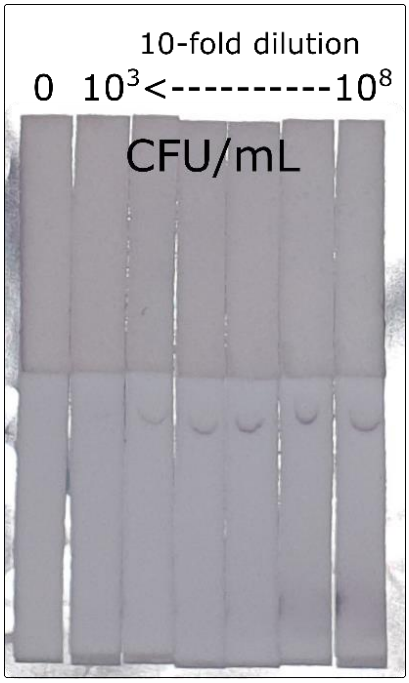

Figure 4.18 Images of the strips after incubating with the diluted conjugates and *Salmonella typhimurium* (10^3 – 10^8 CFU/mL).

4.3.3.2 DENV2-NS1 detection

4.3.3.2.1 Anti-DENV2-NS1 antibody conjugation

The agglutination tests were implemented to explore the optimal buffer pH and to determine the minimum amount of anti-DENV2-NS1 DA034 mAb required for the conjugation. The effect of pH was more pronounced than that demonstrated in the conjugation of anti-*Salmonella typhimurium* mAb. Varying the pH of the buffer resulted in significant change in the spectrum, as seen in Figure 4.19A. The attachment of the anti-DENV2-NS1 DA034 mAb preferred the pH of 9.0 as the flocculation index was highest (Figure 4.19B).

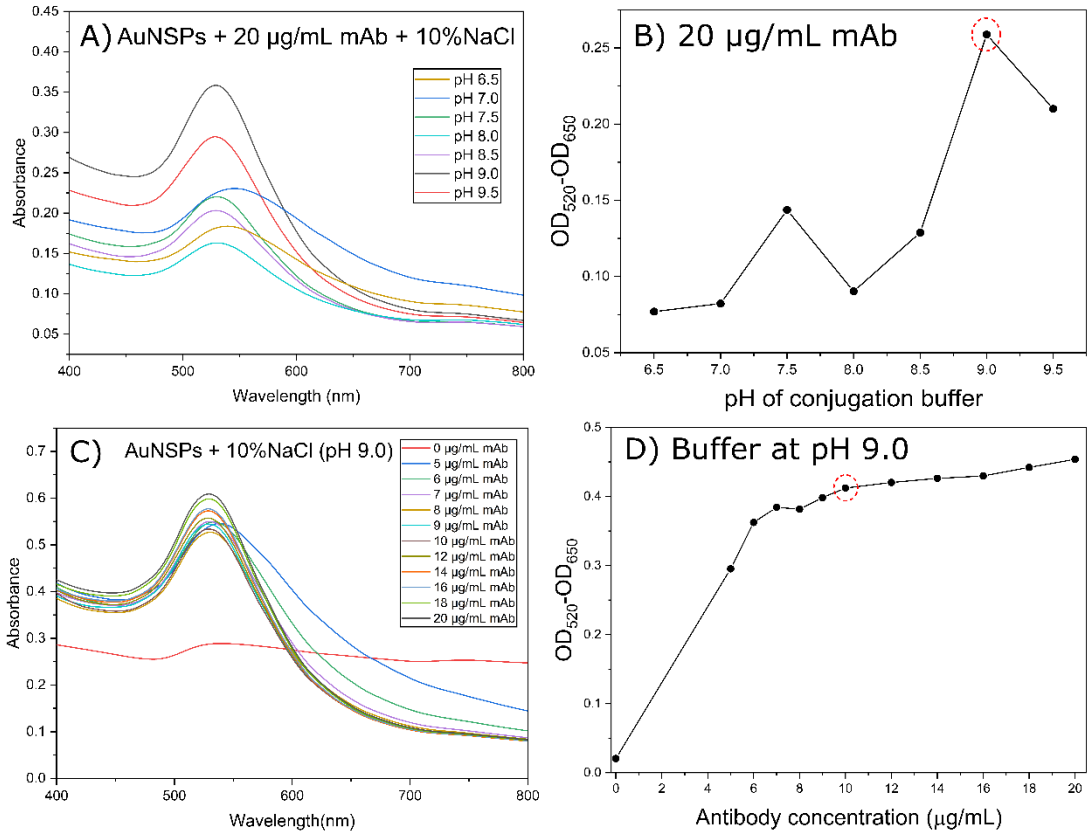

Figure 4.19 Results of the flocculation tests to identify optimal conjugation conditions of anti-DENV-NS1 DA034 mAb. A) UV spectrum absorption of the conjugation at different pH values. B) The stability index at different pH values while keeping the number of antibodies. C) The spectral absorption of the conjugate at various antibody concentrations. D) The stability index at different antibody concentrations while keeping the pH constant.

To determine the minimum coating antibody, various concentrations of the antibodies were added to the colloidal AuNSPs and the pH was kept constant at 9.0. Figure 4.19C shows the shift of the LSPR peaks. The stability increased with the increase of antibody concentration before becoming plateau at 10 µg/mL, which was defined as the stabilising concentration of the anti- DENV2-NS1 DA034 mAb (Figure 4.19D).

4.3.3.2.2 Half-Strip assay for DENV2-NS1 detection

The conjugates were prepared according to the optimised pH and antibody concentration (see Section 4.3.3.2.1). The capturing ability of the conjguates was examined by the half-strip LFA to detect DENV2-NS1. In the first attempt, the use of the antibody pair between the anti-DENV2-NS1 DA034 mAb (coating on the

conjugates) and anti-DENV-NS1 pAb (coating on the nitrocellulose membrane) did not produce any visual colouration on the membrane, indicating that this pair was incompatible and could not be used in the LFA.

Hence, other antibodies were introduced into the study to seek the the most effective pair that can provide the strongs visual intensity. Four antibodies were investigated and were used as a “capture antibody” in the detection area of the nitrocellulose membrane and as a “detection antibody” to be coated on the surface of the AuNSPs.

The colour intensity ratios were quantified through the green channel of the Bayer filter and the result is shown in Figure 4.20. Originally, DA034 mAb was conjugated with the AuNSPs and the anti-DENV-NS1 pAb was spotted on the membrane. This antibody pair failed to produce a visual signal strong enough to distinguish it from that of the blank sample. The highest visual signal was seen when the EA1 mAb was conjugated to the AuNSPs and the pAb was coated on the strip. Moreover, when the pAb acted as both a detection and capture antibody, it also provided a relatively high intensity signal. However, since the pAb generally recognises multiple antigen, it may induces the loss in selective binding and lead to cross-reactivity with non-target elements in the samples. Due to its superior specificity and ability to minimize cross-reactivity, the combination of anti-DENV2-NS1 EA1 mAb as the capture antibody and anti-DENV-NS1 pAb as the detection antibody was chosen for the development of the thermochromic LFA in the next chapter.

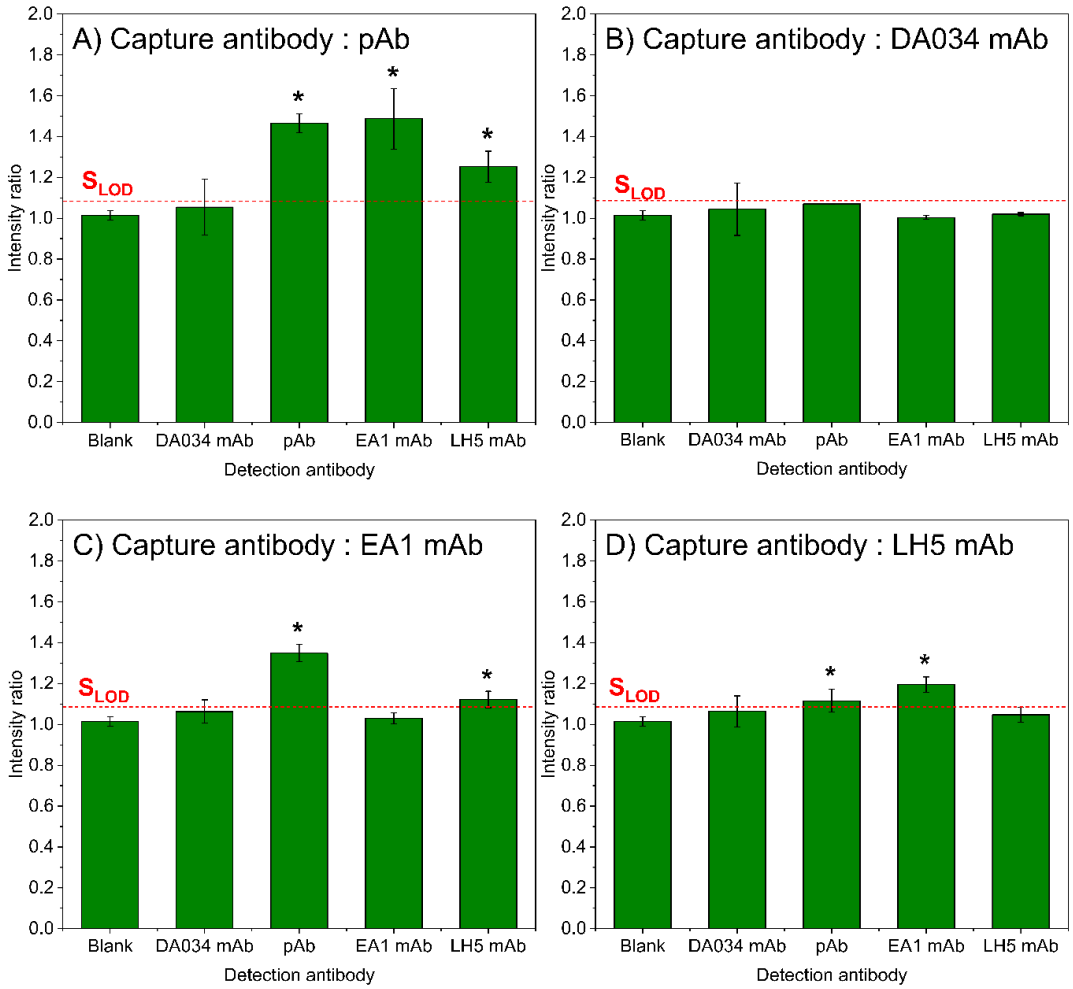

Figure 4.20 Colour intensity ratios derived from the green channel representing the visualisation of the signal. Each antibody was used as the detection antibody and capture antibody. Data are presented as the mean ± standard deviation (n = 3). * indicates the LOD and S_{LOD} indicates the signal of detection limit determined by IUPAC.

4.4 Conclusion

This chapter demonstrates the preparation of conjugated nanoparticles to be utilised in the LFA platforms to detect two analytes: *Salmonella typhimurium* and the recombinant protein NS1 of dengue virus.

For the the microbiological detection platform, the whole bacteria cells were brought to the sensing experiments. The colonies of *Salmonella typhimurium* were cultured in the lab and their turbidity was monitored to establish the calibration growth curve,

which was later used to monitor the concentration of the bacteria. The OD_{600} of *Salmonella typhimurium* was dependent on the number of colonies. The data shows that at the OD_{600} of 0.5 the bacteria suspension contained ~1 x 10^8 CFU in 1 mL and there were up to ~5 x 10^8 CFU/mL at the OD_{600} of 2.0.

In the initial plan of this thesis, ZFNPs@citrate were immobilised with biological molecules to enable the recognition ability toward the analytes of interest. Aptamers were adhered to the ZFNPs@citrate assisted by carbodiimide crosslinking method. However, it resulted in relatively low coupling yield as most of the aptamers physically absorbed on the ZFNPs. The microbiological test shows that the ZFNP@aptamer could not bind with *Salmonella typhimurium* in the sample. To address the challenge, NHS could be incorporated into the coupling reaction instead of sulfo-NHS to stabilise the carbodiimide intermediate groups. The optimal pH for the immobilisation process should be identified to facilitate aptamer attachment before introducing coupling chemistries. The covalent immobilisation of ZFNPs@citrate and aptamer selection require optimisation.

Regarding the ineffectiveness of the ZFNPs@aptamer, they were replaced by the12 nm AuNSPs which were conjugated with antibodies by physical absorption. The gold conjegates were separately prepared for detecting *Salmonella typhimurium* and DENV2-NS1. The optimum pH and the stabilising concentration of the antibody were determined based on the agglutination study. It was found that the conjugation of anti-*Salmonella typhimurium* mAb was favourable at the pH of 7.5 and the concentration of the antibody was 14 µg/mL to sufficienctly provide stability to the AuNSPs. The conjugation of anti-DENV2-NS1 DA034 mAb was conducted at pH 9.0 with the addition of the antibody at 10 µg/mL.

To evaluate the effectiveness of the conjugates in the LFA operation, the half-strip assay was carried out to quickly optimise the components, *i.e.* the type of nitrocellulose membrane, the size of nanoparticles, capture and detection antibodies, the component of running buffer, and blocking agents.

In microbiological detection, a severe clog of the conjugates at the liquid-membrane interface was initially observed. Several experiments were implemented to address the problem, which was thought to be caused by the crosslinking activity of the conjugated antibodies. Whole bacteria cells have antigenic epitopes that are prevalent on their surfaces. So, the conjguates could bind to multiple *Salmonella typhimurium* simultaneously. The crosslink with other nanoparticle-bacteria complexes led to the formation of large clusters. By diluting the added conjugates, *Salmonella typhimurium* at 10^4 CFU/mL could be detected using the half-strip method.

The aggregation of the complexes was not observed when detecting DENV2-NS1. Nonetheless, it was discovered that the antibody must be carefully selected to provide a strong signal on the nitrocellulose membrane. According to the investigation, the anti-DENV2-NS1 EA1 mAb conjugated to the AuNSPs and the anti-DENV-NS1 pAb deposited on the nitrocellulose membrane produced the highest colour intensity. Overall, gold conjugates were developed for the detection of *Salmonella typhimurium* and DENV2-NS1 in the LFA platforms.

Chapter 5 : Development of thermochromic lateral flow assay

5.1 Introduction

Recently, thermal senging LFA has received attention due to its high sensitivity of detection. The current thermal sensing technique usually requires an IR camera to measure the heat radiation. Because the thermal camera is expensive, it leads to an increase in the cost of operation and is inconvenient. A decade ago, the thermally sensitive material was harnessed in biosensor application. With this material onboard, it transforms heat into visualised colouration, resulting in the enhancement of the sensitivity of detection. The advantage of the use of thermo-sensitive material is that once the temperature threshold is triggered, it changes into an observable signal. To the best of our knowledge, the liquid crystal thermo-sensitive material has not been combined with the LFA.

The concept of the thermochromic-based assay to enhance couloured intensity for sensitive detection is stuidied in this thesis. To tackle the world's issues, the thermochrmic based assay is combined with the LFA to determine *Salmonella typhimurium* and DENV2-NS1. *Salmonella typhimurium* is a concern in food safety. Outbreaks impact the health of the population. A large number of samples to screen during outbreak require a simple, effective, and rapid method to operate the detection to stop the outbreak. Also, dengue is an endemic disease that widespread in tropical countries and easily transmitted. Dengue outbreak in remotes areas of poor countries may limit access to advanced facilities, so affordability is important. Achieving the objective in this work would have an impact on the fields of medical diagnosis, agriculture, and food safety. Therefore, these two analtyes were chosen as models to develop the thermochromic LFA as both have a significant impact on global public health and eonomy.

Herein, the fabrication of the thermochromic LFA platforms for the determination of DENV2-NS1 recombinant protein and *Salmonella typhimurium* is demonstrated. AuNSPs@mAb were the LFA labels proving both visual and thermal signals. The signal of the developed thermochromic LFA is compared with that of the conventional LFA visual intensity to evaluate the potential of using the thermochromic-based method for sensitive detection. Optimisation of the thermochromic signal by altering various factors, such as the intensity of the LED and illumination time, is shown in this chapter. The sensitivity and the LOD are determined and compared between the conventional visual singal measurement and the thermochromic signal measurement.

5.2 Materials and methods

5.2.1 Materials

Gold conjugates for *Salmonella typhimurium* detection were prepared as described in Section 4.3.3.1.1 and gold conjugates for the detection of DENV2-NS1 were described in Section 4.3.3.2.1. The antibodies for conjugation and components of LFA fabrication are described in Section 4.2.1.

To determine DENV2-NS1 recombinants, the sample buffer was prepared by adding 0.5% BSA and 0.1% Tween 20 to PBS solution. The conjugate pad buffer was 20 mM borate buffer (pH 9.0) supplemented with 1% BSA, 0.5% Tween 20, and 5% sucrose. The washing buffer was the PBS solution mixed with 1% Tween 20.

For *Salmonella typhimurium* detection, the sample buffer was prepared by adding 0.5% BSA and 0.1% Tween 20 to the PBS buffer. The conjugate pad buffer was the PBS solution added with 0.1% Tween 20 and 5% sucrose. The washing buffer was the PBS solution mixed with 1% Tween 20.

5.2.2 Fabrication of thermochromic lateral flow strips

Structurally, the newly developed thermochromic LFA resembles a typical LFA strip with the addition of a liquid crystal thermochromic sheet to enable heat-to-visualisation transformation. A depiction of the thermochromic-integrated strip device can be found in Figure 5.1. The nitrocellulose membrane was trimmed to 25 x 300 mm using a guillotine.

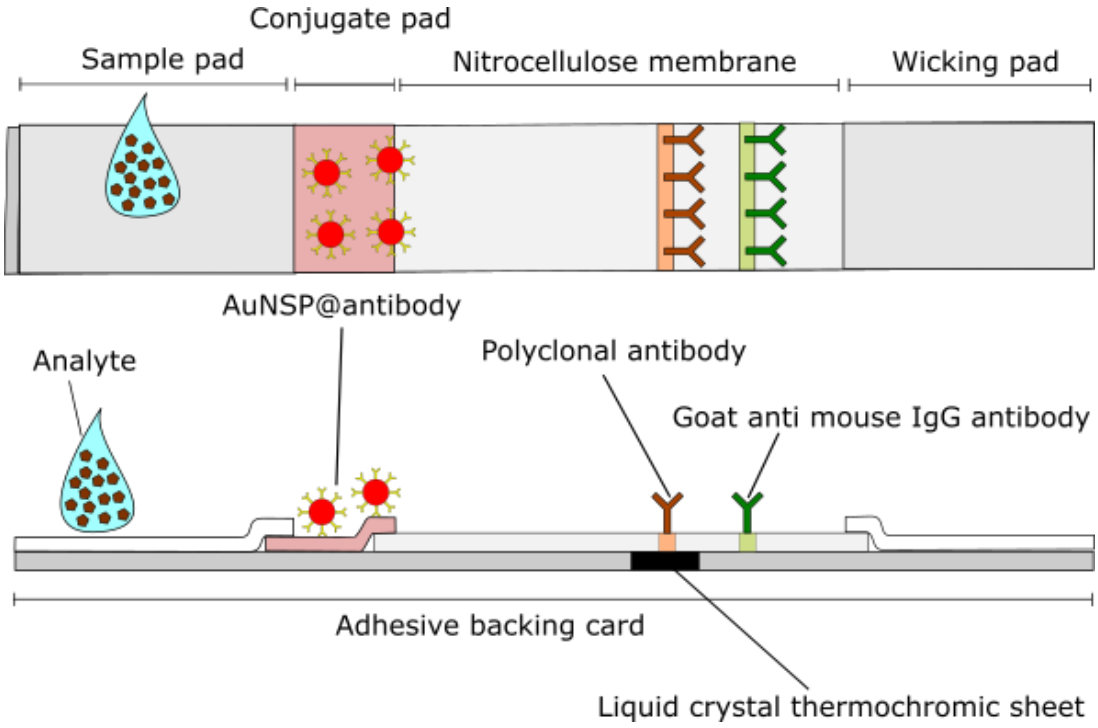

Figure 5.1 Illustration of the thermochromic LFA architecture comprising of a sample pad for loading an aqueous sample containing biological analytes of interest, a conjugate pad to release conjugated nanoparticles and maintain optimal conditions for the reaction, a nitrocellulose membrane containing test line and control line antibodies, and a wicking pad at the terminal end. All components are attached on a backing card. A piece of a thermochromic sheet is attached to the backside of the nitrocellulose membrane.

Following that, antibodies were printed on the membranes. The LFA strips for *Salmonella typhimurium* detection were produced by dispensing anti-*Salmonella* pAb (0.5 mg/mL) and goat anti-mouse IgG (0.3 mg/mL) onto the membrane as the test and control lines, respectively.

For DENV2-NS1 detection, 0.5 mg/mL rabbit anti-dengue virus pan serotype NS1 pAb (test line) and 0.3 mg/mL goat anti-mouse IgG (control line) were printed onto the mebrane. All antibodies were prepared in PBS buffer with 5% methanol to assist the fixation of the antibodies on the nitrocellulose membrane. The dispensing rate was kept at 0.1 µL/mm. After antibody coating, all nitrocellulose membranes were dried at 37 °C for 2 h.

The conjugate glass fibre pad was cut into 6 x 300 mm using a guillotine and soaked in the solution of the conjugates before drying. The sample pad and the wicking pad were cut into 25 x 300 mm using a guillotine. All components were assembled on the adhesive backing card with a 2-mm overlap between adjacent parts. The liquid crystal thermochromic sheet (5 x 300 mm) was adhesively adhered underneath the strip to cover the region of the test line. The LFA assembly was cut into a 4-mm width and stored at 4 °C with desiccant until use. The display of the thermochromic assembly can be found in Figure 1 of Appendix G.

5.2.3 The operation of lateral flow assay

To identfify the presence of *Salmonella typhimurium* in samples using LFA, the concentration of the bacteria in the sample buffer was modified. Then, 100 µL of the bacteria suspension were added to the sample pad of the strip. The solution was allowed to migrate via capillary action for 30 min. After that, 50 µL of the washing buffer were added to the strips.

For dengue detection, the sample buffer was spiked with DENV2-NS1 to achieve the desired concentration. Then, 100 µL of the sample solution was pipetted onto the sample pad of the strip. It was left for 30 min to complete the migration. Following that, 50 µL of the washing buffer were added to the test strips.

5.2.4 Conjugate pad preparation and optimisation

To prepare the conjugate pad for *Salmonella typhimurium* detection, the AuNSPs@anti-*salmonella typhimurium* mAb were prepared as described in Section 4.3.3.1.1. The ODs of the gold conjugates were adjusted to 2.0 and 4.0 in the conjgute pad buffer. The conjugate pads were soaked in the conjugate solutions and left to dry overnight at RT. The assembly of the LFA strips is described in Section 5.2.2. The strips were testsed with *Salmonella typhimurium* at concentrations of 10^7 and 10^8 CFU/mL.

To prepare the conjugate pad for the DENV2-NS1 detection, AuNSPs@anti-DENV2-NS1 EA1 mAb were adjusted to ODs of 2.0 and 5.0 in the conjugate pad buffer. The conjugate pads were soaked in these solutions and left overnight at RT. The assembly was carried out as stated in Section 5.2.2.The concentrations of the DENV2-NS1 in the sample buffers were adjusted to range from 0.78 to 200 ng/mL.

The operation of the LFA is provided in section 5.2.3 and the image analysis is described in Section 3.2.4.

5.2.5 Optimisation of the thermochromic signal

The thermochromic signal of the assay for the detection of *Salmonella typhimurium* was optimized at an ambient temperature of 23 °C. The bacteria suspensions were adjusted to concentrations of 10^6, 10^7, and 10^8 CFU/mL in the sample buffer. The LFA operation is explained in Section 5.2.3. Then, the strips were subjected to the illumination of the LED with power intensities of 3.69, 5.2, and 6.5 W/cm^2. The colour changing of the thermochromic sheets were recorded at 20, 30, and 40 s to determine the intensity ratio (see Section 3.2.6).

The thermochromic LFA strips were prepared for DENV2-NS1 detection and the thermochromic signal was optimized at 22 °C. Various concentrations of DENV2-NS1 (0.78, 1.5, 12.5, and 100 ng/mL) were applied to the sample pads of the the strips to

run the assay (see Section 5.2.3). The LED illuminated the test lines of these strips with the incident light intensities of 5.2, 6.5, and 8.16 W/cm^2. The colour measurement of the thermochromic sheet was performed as explained in Section 3.2.6. The images of the thermochromic sheets were taken after 10, 20, 30, and 60 s of illumination.

5.2.6 Comparison between typical signal and thermochromic signal

Once the optimal power intensity and illumination duration were determined, various concentrations of *Salmonella typhimurium* were adjusted from 10^5 to 10^8 CFU/mL in the running buffers. The tests were conducted as explained in Section 5.2.3. The LFA strips were exposed to the LED light at 5.2 W/cm^2 for 30 s to activate the colour changing of the thermochromic sheets.

For the detection of DENV2-NS1, the viral dengue recombinants were spiked into the running buffer at two-fold dilutions, ranging from 0.78 to 400 ng/mL. The LFA detection was operated following the procedure in Section 5.2.3. The strips were then illuminated by the LED at 6.5 W/cm^2 for 30 s.

To investigate whether the newly developed thermochromic LFA can enhance the sensitivity of detection, the measurement of the typical visual signal follows the protocols in Section 3.2.4. and the measurement of the thermochromic signal follows the protocol in Section 3.2.6. The IUPAC method was applied to evaluate the performance of the the typical and thermochromic LFA (see Section 3.2.8).

5.3 Results and discussion

5.3.1 Development of the thermochromic lateral flow assay for *Salmonella typhimurium* detection

5.3.1.1 Conjugate pad preparation and optimisation

The conjugate pad was prepared by soaking the glass fiber in the solution of gold conjugates. The amount of gold conjugates affects the sensitivity of the LFA result as seen in Section 4.3.3.1.2. A low concentration of conjugates results in a lack of sensitivity while overloading the assay with the conjugates leads to aggregation of the nanoparticles and the bacteria, thus decreasing the sensitivity of detection. Both scenarios lead to a decrease in the number of AuNSPs accumulating in the test line which affects the visual and thermal signals. Therefore, the concentration of AuNSPs@anti-*Salmonella typhimurium* mA was optimized.

Glass fibres were immersed in the solutions AuNSPs@anti-*Salmonella typhimurium* mAb with ODs of 2.0 and 4.0 before assembly. As shown in Figure 5.2, the visual intensity ratios were not significantly different between using the conjugate pad prepared from the OD 2.0 and 4.0 of the conjugate pad solutions. Hence, the solution of the conjugates was adjusted to an OD of 2.0 for the preparation of the conjugate pad as an extra addition of gold conjugates did not affect the number of nanoaprticels accumulating in the membrane.

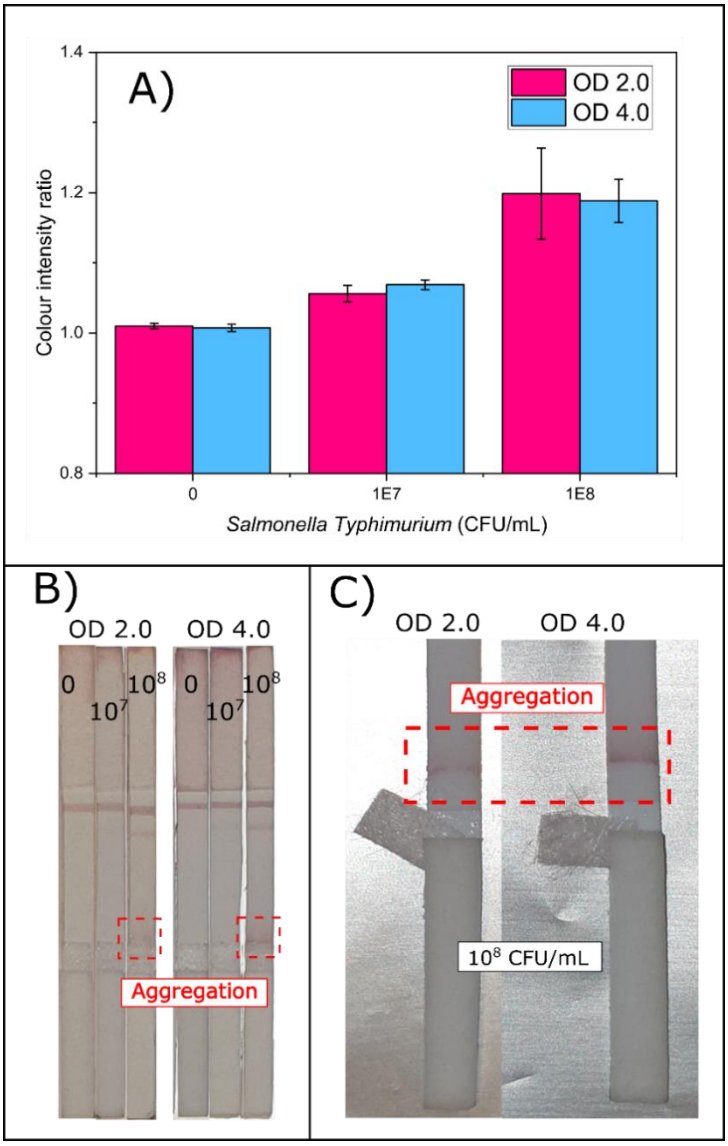

Figure 5.2 Impact of the gold conjugate concentration (OD 2.0 and OD 4.0) on visaulisation of test and control lines. A) The intensity ratio of the test line. Data are presented as the mean ± standard deviation (n = 3). P-values were obtained using a two-tailed paired-samples t-test ($p > 0.05$). B) Images of the LFA results. C) Images of the LFA strips showing the aggregation of the particles.

At the bacteria concentration of 10^8 CFU/mL, the aggregation of the gold conjugates at the interface between the nitrocellulose membrane and the conjugate pad was observed. (Figure 5.2B and Figure 5.2C). The gold conjugates and *Salmonella typhimurium* formed clusters and induced severe aggregation as seen in the half-strip assay (Section 4.3.3.1.2).

5.3.1.2 Optimisation of the thermochromic signal

The newly developed thermochromic LFA was used to detect *Salmonella typhimurium* at an ambient temperature of 23 °C. To maximise photo-induced thermochromic signal, the power and duration of the incident light were varied. Table 5.1 shows the thermochromic sheets response to LED exposure at different power intensities and durartion. At the high power intensity of 6.5 W/cm^2, the colour transformation of the blank sample was triggered after 20 s of illumination, indicating a false positive signal. On the other hand, the thermochromic sheet corresponding to the null sample changed its coulour after 40 s of the exposure of 3.69 W/cm^2, at which the detection limit was 10^7 CFU/mL. The colour transtion was observed after 30 s.

The optimal LED power intensity and duration for operating the thermochromica LFA for *Salmonella typhimurium* detection at 23 °C were 5.2 W/cm^2 and 30 s of illumination. Prolonging the exposure to 40 s caused a false positive signal of the thermochromic sheet. The detection limit of *Salmonella typhimurium* was as low as 10^6 CFU/mL. This was applicable when the surrounding temperature was 23 °C and the colour changing temperature of the liquid crystal thermochromic sheet was 30-35 °C.

Table 5.1 Response of the 30-35 °C thermochromic sheet under different conditions of illumination. The power intensities are 3.69, 5.2, and 6.5 W/cm^2 and the lengths of exposure are 20, 30, and 40 s. The concentrations of *Salmonella typhimurium* range from 0 to 10^8 CFU/mL.

Salmonella typhimurium concentration	Power intensity (W/cm^2)								
	3.69 W/cm^2			5.2 W/cm^2			6.5 W/cm^2		
	20	30	40 s	20	30	40 s	20	30	40 s
0 CFU/mL	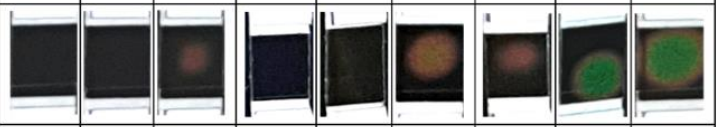								
10^6 CFU/mL	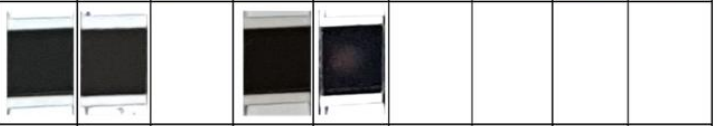								
10^7 CFU/mL	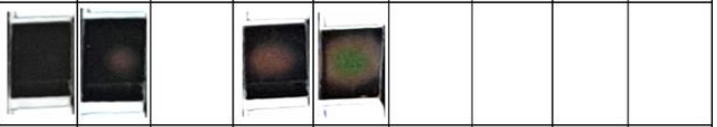								
10^8 CFU/mL	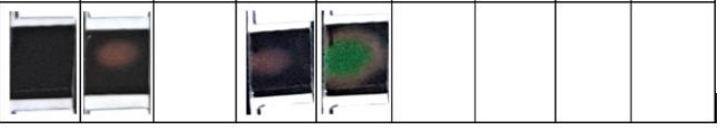								

5.3.1.3 Comparison of typical and thermochromic lateral flow assays for *Salmonella typhimurium* detection

The concentrations of *Salmonella typhimurium* were ranged from 10^5 to 10^8 CFU/mL and subjected to the comparison study to evaluate the analytical performance of the theromochromic LFA, compared to the conventional LFA. The displays of the typical LFA strips and the theromochromic sheets according to the concentration of the bacteria are shown in Figure 5.3. For the conventional method, the minimum concentration of the bacteria that the test line could be observed by naked eyes was 10^7 CFU/mL, indicating poor sensitivity.

Under optimal conditions, the thermochromic-based assay offered the detection limit of 0.5 x 10^6 CFU/mL for *Salmonella typhimurium* detection. The LOD was found to be 20 times lower than the LOD of the typical LFA. The red spot appeared on the thermochromic sheet when the concentration of the bacteria was as low as 0.5 x 10^6 CFU/mL.

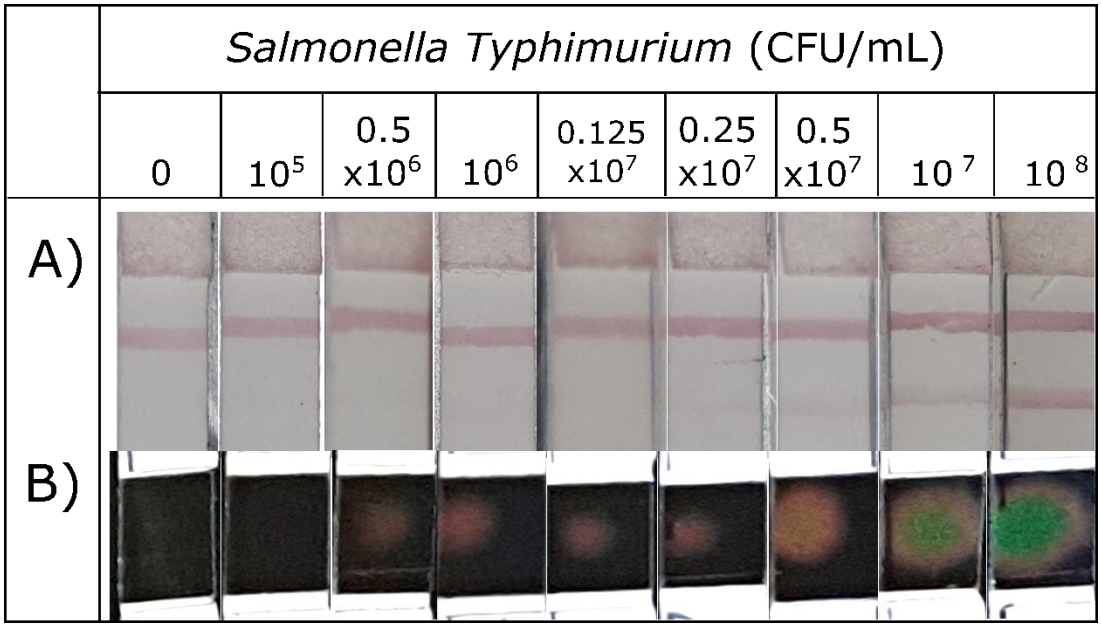

Figure 5.3 Displays of A) typical LFA strips and B) thermochromic sheets upon illumination with the incident light. They were tested with *Salmonella typhimurium* with concentrations scaling from 10^5 to 10^8 CFU/mL and the blank sample.

The RGB coordinates were extracted in MATLAB to determine the colour contrast. The correlation between the intensity ratio and the concentration of the pathogen is plotted in Figure 5.4. For the typical LFA, a linear relationship was observed from 10^6 to 10^8 CFU/mL. The coulour measurement on the red, green, and blue channels exhibited the R^2 values of 0.92981, 0.90868, and 0.92631, respectively. The red channel had the lowest sensitivity of detection, with a LOD of 10^7 CFU/mL. Quantification of *Salmonella typhimurium* using the green and blue channels allowed for the detection at 0.25 x 10^7 CFU/mL which was 4 times lower than the red channel.

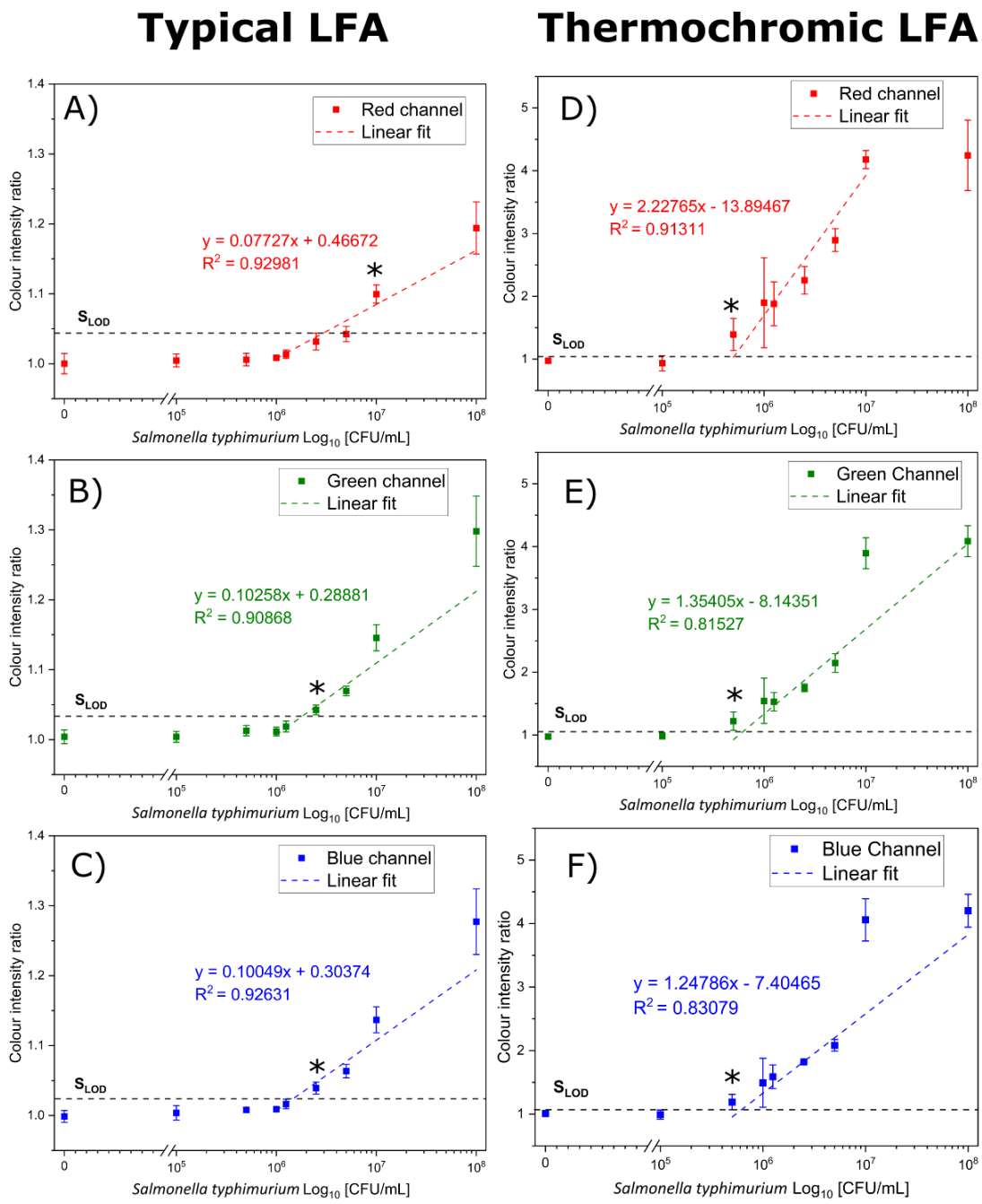

Figure 5.4 Relationships between the colour intensity ratios (red, green, blue) and *Salmonella typhimurium* concentration (0-10^8 CFU/mL). A-C) Typical LFA; D-F) thermochromic LFA. Data are presented as the mean ± standard deviation (n = 3). * indicates the LOD and S_{LOD} indicates the signal of detection limit determined by IUPAC.

However, the green channel of the Bayer filer was the most sensitive channel for analysing the accumulation of AuNSPs on the membrane. It is noteworthy that image processing technology provided a lower LOD than naked-eye interpretation of the

LFA results. The appearance of the test line staining was clearly observed at 10^7 CFU/mL, while the Bayer filter enabled the detection of bateria at 0.25 x 10^7 CFU/mL.

For comparison, the colour transition of the thermochromic sheets was quantified using the Bayer filter. The colour measurent was performed on the red channel providing a linear working range from 0.5x10^6 to 10^7 CFU/mL with an R^2 of 0.91311. Coluor quantification of the thermochromic signal on the green and blue channels showed a linear correlation between the coulour intensity ratio and the concentration from 0.5x10^6 to 10^8 CFU/mL, but with poor R^2 which were 0.81527 for the green and 0.83079 for the blue coordinates.

According to Table 5.4, the LOD determined by any channel of the Bayer filters was equivalent at 0.5 x10^6 CFU/mL. However, the sensitivity was found to be the greatest in the red channel which was the most appropriate channel for quantifying the thermochromic signal for the detection of *Salmonella typhimurium* in this study.

Table 5.2 Colour measurement of the typical and thermochromic LFA. The results are shown in red, green, and blue channels. The analytical performances of both assays are determined by IUPAC.

Type of LFA	Channel	Fitting formula	Linear working range (CFU/mL)	R^2	Sensitivity	S_{LOD}	LOD (CFU/mL)
Typical LFA	R	y = 0.07727x + 0.46672	$10^6 – 10^8$	0.92981	0.07727	1.04362	10^7
	G	y = 0.10258 + 0.28881	$10^6 – 10^8$	0.90868	0.10258	1.03358	0.25x10^7
	B	y = 0.10049x + 0.30374	$10^6 – 10^8$	0.92631	0.10049	1.02381	0.25x10^7
Thermochromic LFA	R	y = 2.22765x -13.89467	0.5x10^6-10^7	0.91311	2.22765	1.0472	0.5x10^6
	G	y = 1.35405x – 8.14351	0.5x10^6-10^8	0.81527	1.35405	1.0576	0.5x10^6
	B	y = 1.24786x -7.40465	0.5x10^6-10^8	0.83079	1.24786	1.066	0.5x10^6

5.3.2 Development of the thermochromic lateral flow assay for DENV2-NS1 detection

5.3.2.1 Conjugate pad preparation and optimisation

The coating of the conjugate pad with AuNSPs@anti-DENV2-NS1 EA1 mAb was critical to controlling the accumulation of the nanoparticles in the membrane which affects the final result of the LFA. A higher number of conjugates in the membrane results not only in a stronger visual intensity, but also in greter thermalization as more nanoparticles are irradiated. [178]

The concentration of the gold conjugates was adjtsued to 2.0 and 5.0 before the immersion of glass fibres. Figure 5.5 presents the coulour intensity ratio of the conjugate pads measured by the green channel. The signal intensity ratio of the conjugate pad immersed in the gold conjugate solution with an OD of 5.0 was higher as the lowest concentration of the DENV2-NS1 that could be observed on the strips by naked eyes was 6.25 ng/mL. For the diluted conjugate pad, a positive result was obtained at 12.5 ng/mL. The hook effect was not found even at the highest concentration of the DENV2-NS1 suggesting the sufficient addition of the gold conjugates. Therefore, in the preparation of the conjugate pad for DENV2-NS1 detection, the OD of the gold conjugates was adjusted to 5.0 for the immersion of the glass fibre.

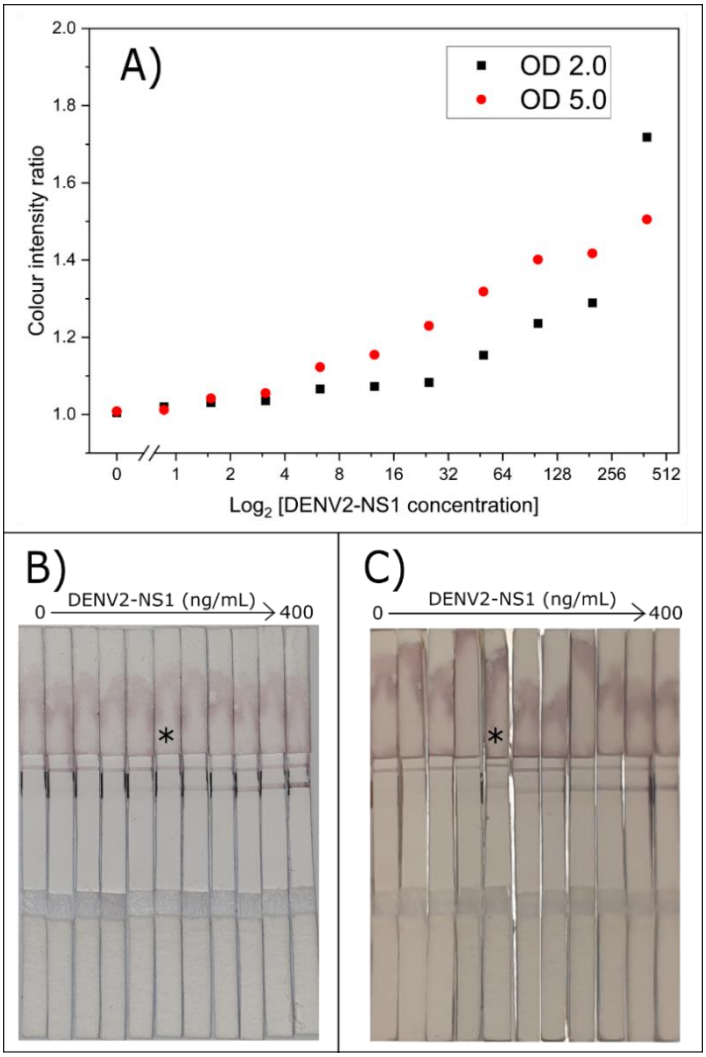

Figure 5.5 Results of the LFA strips testing with DENV2-NS1 concentration ranges from 0 to 400 ng/mL. A) Correlation between visual intensity ratio and the concentration of DENV2-NS1. B) Displays of LFA strips assembled with the conjugate pads immersed with an OD of 2.0 and C) OD 5.0. * indicates the detection limit.

5.3.2.2 Optimisation of the thermochromic signal

In general, thermochromic sheets respond quickly to temperature change. Their colour-changing characteristic is triggered when the activation temperature is reached. Hence, the thermochromic-based method is highly sensitive to the surrounding temperature. A calibration process is strongly recommended to ensure maximum analytical performance and to avoid false positive and negative results.

Table 5.3 Response of the 30-35 °C thermochromic sheet under different conditions of illumination. The power intensities are 5.2, 6.5, and 8.16 W/cm^2 and the lengths of exposure are 10, 20, 30, and 60 s. The concentrations of DENV2-NS1 ranged from 0 to 100 ng/mL.

DENV-NS1 concentration	Power intensity											
	5.2 W/cm^2				6.5 W/cm^2				8.16 W/cm^2			
	10s	20s	30s	60s	10s	20s	30s	60s	10s	20s	30s	60s
0 ng/mL					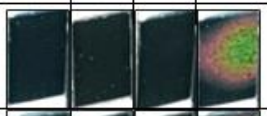				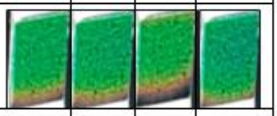			
0.78 ng/mL												
1.5 ng/mL					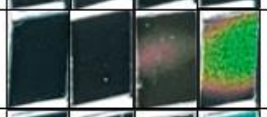							
12.5 ng/mL					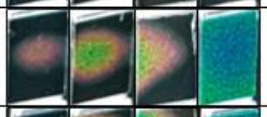							
100 ng/mL	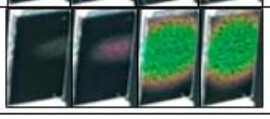				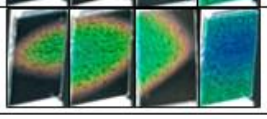							

The surrounding temperature during the experiment was set to 22 °C and the activation temperature of the liquid crystal thermochromic sheet was 30 °C. The displays of the optically stimulated thermochromic LFA strips are shown in Table 5.3. It can be seen that the incident power of 5.2 W/cm^2 was not able to trigger the colour-changing feature of the thermochromic sheet unless the DENV2-NS1 concentration was above 12.5 ng/mL and the illumination was held for 30 s. On the other hand, at a high power intensity of 8.16 W/cm^2, the thermochromic sheet relating to the blank sample turned fully green after 10 s of illumination indicating an oversupply of energy to the sheet. The medium power intensity of 5.2 W/cm^2 showed good thermal responsive behaviour. For the negative sample, it caused a false positive result after 1 min of exposure. Within 30 s of illumination, the colour transformation was not observed for the blank sample as it could not produce enough heat to activate the colour-changing trait of the thermochromic sheet. The coloured signal appeared on the sheet when the concentration was above 1.5 ng/mL. It was found that the coulor of the sheet develoed depending on the amount of DENV2-NS1. Therefore, when the

ambient temperature was 22 °C and the 30-35 °C thermochromic sheet was in use, the power of the LED was tuned to 6.5 W/cm^2 to illuminate the samples for 30 s before recording images.

5.3.2.3 Comparison of typical and thermochromic lateral flow assays for DENV2-NS1 detection

The typical LFA strips and the thermochromic sheets after completing the tests are displayed in Figure 5.6. For the typical assay, control lines appeared in all samples identifying the validity of the tests. The colour intensity of the test line was dependent on the concentration of DENV2-NS1. A positive result was observed at 3.125 ng/mL although the colour was weak. The red staining line was clearly visible at 6.25 ng/mL which was the LOD for the naked eye of the typical LFA (Figure 5.6A).

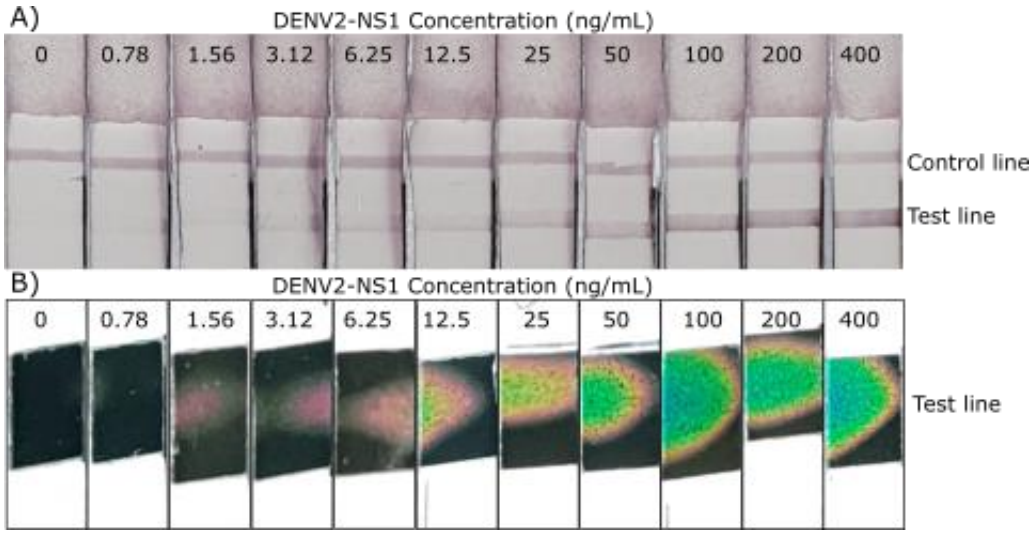

Figure 5.6 Displays of A) typical LFA strips and B) thermochromic sheets upon illumination with the incident light. They were tested with DENV2-NS1 with concentrations ranging from 0 to 400 ng/mL and the blank sample.

Interpretating the result unsing the thermochromic sheet resulted in a significant redution fo the LOD (Figure 5.6B). It could detect the dengue recombinant as low as 1.56 ng/mL, even though the test line was invisible in the typical LFA. This indicates that a certain amount of the conjugated nanoparticles was embedded in the nitrocellulose membrane. Although they were not observable, they were heated by optical stimulation and in turn activate the thermochromic sheet to exhibit visible

colouration. The utilisation of the thermochromic material could lower the LOD of DENV2-NS1 by two-fold compared to the naked-eye detection of the typical LFA format.

The RGB coordinates of the LFA strips and the thermochromic sheet were quantified using the Bayer filter. The contrast between the positive signal and the background signal was determined and compared. The relationships between the DENV2-NS1 concentration and the colour intensity ratio of the conventional and thermal sensing LFA are plotted in a semi-log scale in Figure 5.7.

For the conventional LFA readout, all colour channels exhibited good linear trend lines covering the range between 0.78 and 400 ng/mL with R^2 values of 0.99258, 0.99588, and 0.99566 for the red, green, and blue channels, respectively. The green channel of the Bayer filter offered slightly greater sensitivity than the others. The result is similar to the finding in the literature. [153, 265] The AuNSPs had the maximum absorption at 517 nm which is in the green region of the Bayer filter. As the nitrocellulose membrane scatters most of the incident light, the difference in the light reflection is found to be the largest in the green region of the Bayer filter.

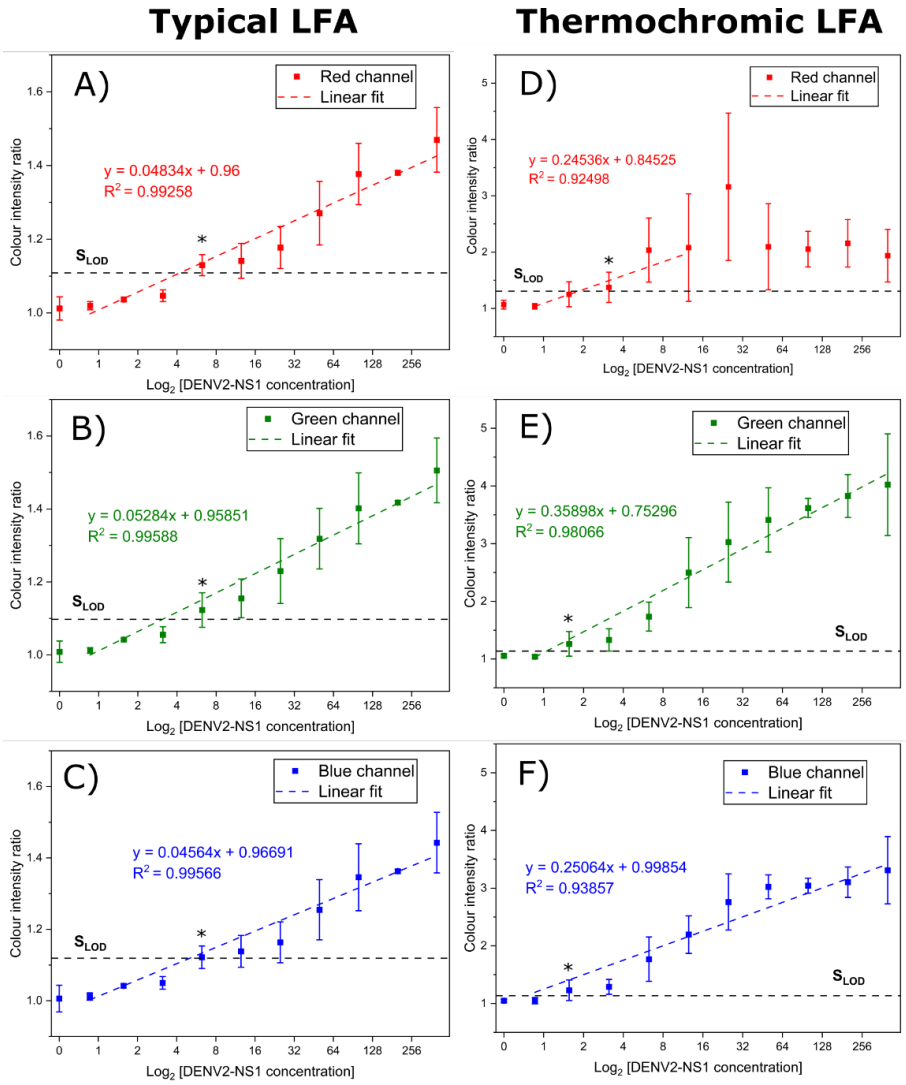

Figure 5.7 Relationships between the colour intensity ratios (red, green, blue) and DENV2-NS1 concentration (0-400 ng/mL). A-C) Typical LFA; D-F) thermochromic LFA. Data are presented as the mean ± standard deviation (n = 3). * indicates the LOD and S_{LOD} indicates the signal of detection limit determined by IUPAC.

The plots of the colour intensity ratios of the thermochromic signal in different cooulour channels showed different patterns. For the culour analysis processing through the red channel, a linear relationship was found between 0.78 ng/mL and 12.5 ng/mL (R^2 = 0.92498), followed by a sharp downturn. It is consistent with the display of the thermochromic sheet which turned red at the low concentration of DENV2-NS1 detection. At high concentrations of virus recombinants, the accumulation of conjugated AuNSPs in the membrane increased, thereby elevating the temperature upon optical stimulation. The red spots was replaced by green and

blue colours, causing a shift in the luminescence of the Bayer filter. As a result, the signal in the green and blue channels overwhelmed the visual analysis. The intensity ratios calculated from the green and blue values offered a broader linear working range from 0.78 to 400 ng/mL with R^2 coefficients of 0.98066 and 0.93857 for the green and blue channels, respectively.

In comparison, the thermochromic measurement provided a significant improvement in terms of sensitivity and detection limit compared to the typical visual measurment (Table 5.4). The quantitative detection of the visual signal assisted by image processing was found to be by 5-7 folds more sensitive than the conventional quantification by naked eye readout. Although the analysis through the red channel showed a 2-fold reduction in the LOD, the linear working range was narrow. For the green and blue channels, the LOD was lowered by 4 folds to 12.5 ng/mL compared to the LOD of the typical LFA. The linear ranges covered from 0.78 to 400 ng/mL, comparable to that of the typical LFA. Since the green channel was more sensitive than the blue channel, it was chosen for an analytical measurement to maximise the performance of the thermochromic LFA. Clearly the integration of the thermal sensing sheet improve the sensitivity and the detection limit of the LFA for dengue detection.

Table 5.4 Colour measurement of the typical and thermochromic LFA. The results are shown in red, green, and blue channels. The analytical performances of both assays are determined by IUPAC.

Type of LFA	Channel	Fitting formula	Linear working range (ng/mL)	R^2	Sensitivity	S_{LOD}	LOD (ng/mL)
Typical LFA	R	y = 0.04834x + 0.96000	0.78 – 400	0.99258	0.04834	1.1071	6.25
	G	y = 0.05284x + 0.95851	0.78 – 400	0.99588	0.05284	1.0968	6.25
	B	y = 0.04564x + 0.96691	0.78 – 400	0.99566	0.04564	1.1182	6.25
Thermochromic LFA	R	y = 0.24536x + 0.84525	0.78 – 12.5	0.92498	0.24536	1.3028	3.125
	G	y = 0.35898x + 0.75296	0.78 – 400	0.98066	0.35898	1.1332	1.5
	B	y = 0.25064x + 0.99854	0.78 – 400	0.93857	0.25064	1.1296	1.5

5.3.3 Discussion

This thesis developed thermal sensing LFA devices to separately detect *Salmonella typhimurium* and DENV2-NS1. The thermochromic readout exhibited impressive analytical performance, with a significant reduction in LOD.

The detection of *Salmonella typhimurium* using the developed thermochromic LFA improved the sensitivity by 20 times and lower the LOD by 5 times compared to the typical LFA, identifying a concentration of the bacteria as low as 0.5 x 10^6 CFU/mL. However, this does not meet the standard requirement of *Salmonella* spp. detection, which requires the identification of 1 CFU in 25 grams or 25 mL of food sample. [112, 113] Nonetheless, the thermochromic-based LFA can be an alternative method for screening a large number of samples as its improved sensitivity allows as shorter enrichment process compared to the typical LFA.

The detection limit of the typical LFA was rather high compared to other studies, which generally can detect *Salmonella* spp. at 10^4 CFU/mL with the option of bacteria enrichment or magnetic separation to even improve the sensitivity. [112, 121, 123] Additionally, the mild colouration appearance of the positive sample of *Salmonella typhimurium* detection, even at 10^8 CFU/mL, emphasizes the need for the re-development of the LFA system. Further optimisation processes should be executed with various options for LFA materials, such as changing the nitrocellulose membrane, modifying the running buffer, adjusting the concentration of test line antibodies, or changing antibodies. [97, 124]

The detection of dengue antigen using the thermochromic platform showed a good detection limit. The thermochromic signal enhancement reduced the detection limit of DENV2-NS1 to 1.56 ng/mL, increasing the sensitivity by 7 times and decreasing the LOD by 6 times. The level of circulating DENV2-NS1of infectious patient serums ranges from 3.64 to 265.7 ng/mL. [86, 88] Immunoassay-based dengue identification can antigenically detect the dengue virus at 4 and 4.9 ng/mL. [86, 96] Tran et al. developed a highly sensitive LFA using an enzyme to amplify the signal, which was capable of detecting DENV2-NS1 at 0.1 ng/mL. [97] Importantly, the median circulating

level of DENV2-NS1 in serums collected in the first two days after fever onset was 8.26 ng/mL. The thermochromic-based LFA demonstrated in this study has an LOD of 1.56 ng/mL with a dynamic range from 0.78 to 400 ng/mL which covers the range of the citculating DENV2-NS1 found in patients. This highlights the potential of using the thermochromic technique for early diagnosis of dengue infection. However, determining the progression of dengue disease depends on the condition of patients, such as whether they are experiencing a primary or secondary infection. [88] Several factors must be considered as the results here were received from the experiment with spiked samples in PBS buffer. In real human serum, many factors may interfere with the detection, such as cross-reaction, pH variation, and interfering substances that may induce competitive binding. [86, 88]

The results of the optical quantitative analysis of the thermochromic signal showed that the green filter was the most suitable for determining the visual intensity for dengue detection, while the red channel collected the most signals for *Salmonella* bacteria detection. This could be due to the nanoparticle number in the membrane which affects the temperature creation. [178] It was demonstrated that the red channel has the greatest impact on thermochromic measurement when the concentration of analytes ot he number of photothermal nanoparticles is low. In this case, the LFA for *Salmonella typhimurium* detection could not accumulate a great number of AuNSPs in the test line, thus generating less temperature. Therefore, the thermochromic signal was sensitive to the red channel. On the other hand, the dengue detection platform generated intense signal in the strips indicating a large number of AuNSPs residing in the membrane. The nanoparticles released a higher level of radiative energy. Since the thermochromic sheet turned green and blue, the largest colour reflection fell into the regions of the green and blue channels.

During the fabrication process, various nitrocellulose membranes were available for selection. The “Prima40” membrane was chosen for *Salmonella typhimurium* detection due to its large pore size, which facilitated capillary flow of the bacteria. However, this choice came with the drawback of a shorter interaction time between antigens and bioreceptors, resulting in reduced sensitivity. [124] In addition, some conjugates became trapped at the entry point and failted to travel through the

membrane due to the formation of clustered complexes. Consequently, the number of AuNSPs captured on the test line was relatively low. Conversely, the “FF170HP” membrane was selected for dengue detection. Its flow rate was slower compared to the “Prima40” membrane. This slower flow rate proved advantageous for detection as it allowed for a longer interaction time between the nanoparticle-virus complexes and test-line antibodies, thus increasing the population of conjugates available for illumination during the thermochromic measurement.

One of the key differences between DENV2-NS1 and bacteria detection was the surrounding temperature. Even a 1-degree Celsius difference had a significant impact on the colour-changing feature. In dengue detection, the surrounding temperature was set to 22 °C, allowing the LED to be used at a higher power intensity, which in turn could amplify the thermal generation to a higher degree. However, the bacterial identification was performed at a higher surrounding temperature of 23 °C. The power of the LED was limited to 5.2 W/cm^2, resulting in less heat energy than in dengue detection.

If nanoparticles accumulate in the membrane at a low number, or if the LFA has a low visual signal, there are many approaches to improve the thermochromic signal. For example, other nanoparticles with high photothermal properties, such as the gold nanocage, can be used in place of the AuNSPs. [266] Optical stimulation can generate a significant amount of heat, despite a low number of nanoparticles. They offer a great signal that can be easily distinguished from the baseline signal. [266] Additionally, using high-efficiency photothermal nanoparticles enables the utilization of the thermochromic sheet with a higher activation temperature, such as a 35-40°C liquid crystal thermochromic sheet, eliminating the chance of receiving falst-positive signals. As it requires a higher temperature for the thermochrcomic sheet to change its colour, this expands the temperature gap between negative and positive signals. It means that in the absence of targets although the thermochromic sheet temperature increases during LED illumination, its colour does not change. On the other hand, the presence of tagets would result in significant heat and thus activating colour change of the thermochromic sheet. It is imprtant to note that a calibration

step is always required to tune the LED intensity and choose a suitable thermochromic sheet to match the ambient temperature.

It is important to note that the colour of the liquid crystal thermochromic sheet used in this study reverts after the heat is removed. Therefore, the interpretation of the result must be performed immediately after turning off the LED while the thermochromic signal is still visible. This limitation could be addressed by replacing the thermochromic sheet with another thermosensitive material. For example, Polo et al. demonstrated a thermal detection biosensor using a fax paper, which turns black irreversibly when activated by high temperature. [184]

A noise signal is the main issue of thermal-based LFAs and subtraction of the baseline signal is generally required. [177, 266, 267] The nitrocellulose membrane has low light absorption as most of incident light is scattered. [151, 180, 184] In contrast, the biological molecules and thermochromic sheet can absorb light, resulting in noise background. This may hinder the analysis of certain samples, such as the patient's blood as blood components may absorb light and raise the temperature, potentially interfering with the results. The NIR region of the spectrum is known to be suitable for photothermal applications in medicine because it is not absorbed by biological substances. [184] Otherwise, an unnecessary background signal may be created leading to false positive results. An alternative approach is to incorporate purification and concentration steps into the assay to remove interfering substances before thermochromic LFA operation. Moreover, a filter can be included in the optical configuration to eliminate the absorption of unwanted wavelengths. If possible, the thermochromic sheet should be changed to white to reduce light absorption.

The thermochromic LFA developed in this study has only been evaluated using analyte-spiked buffers under controlled laboratory conditions. Its performance with real samples remains to be thoroughly investigated. The complex matrices of real samples may pose significant challenges to the applicability of this thermochromic-based LFA. The evaluation of its specificity and selectivity is strongly required in future works.

5.4 Conclusion

This chapter demonstrates the development of the colourimetric assay based on thermal detection to identify the presence of *Salmonella typhimurium* and DENV2-NS1. The liquid crystal thermochromic sheet, along with the optical properties of nanoparticles, enhanced the sensitivity and the LOD of LFA detection. The analytical performance of the thermochromic-based LFA was compared with that of the typical LFA.

Before implementing thermochromic detection method, the LED intensity and illumination duration were optimised to maximise performance and avoid misinterpretating the results. In both studies, the thermochromic sheet had an activation temperature of 30 °C. During bacteria detection, the surrounding temperature was maintained at 23 °C and the illuminating light was optimised at 5.2 W/cm^2 for 30 s. For the detection of the dengue virus, with ambient temperature of 22 °C, samples illuminated with the LED at 6.5 W/cm^2 for 30 s produced optimal results. Using AuNSP labels, the visual intensity of the typical LFA was measured on the green channel, which yielded the highest sensitivity.

In the detection of *Salmonella typhimurium*, a positive visual signal was observed when the concentration increased to 10^7 CFU/mL. Image processing allowed the detection of a mild signal down to 0.25 x 10^7 CFU/mL. Thermochromic measurement enhanced the output signal, allowing visual observation of the colour change at 0.5 x 10^6 CFU/mL upon optical stimulation. The sensitivity and LOD were improved by 20-fold and 5-fold, respectively. Optical analysis on the red channel provided the best linear range and highest sensitivity.

In dengue detection, a weak positive signal was observed by the naked eye at 3.125 ng/mL and the LOD determined by the IUPAC method was 6.25 ng/mL. The thermochromic signal was visually detectable at 1.5 ng/mL. Quantification was implemented on the green channel showing good and broad linear regression. The

IUPAC detection limit was also at 1.5 ng/mL. In the detection of DENV2-NS1, the LOD could be lowered by 4-fold using the thermochromic sheet as a sensor.

In conclusion, exploiting the heat-to-visualisation feature of the thermochromic sheet significantly improved both sensitivity and detection limit. A thermochromic assay improved *Salmonella typhimurium* detection efficiency, but the LFA design needs further development. This technique also showed a good response to DENV2-NS1 at low concentrations. Although the results in this study were performed in buffers, they showed a significant improvement in detection efficiency. Hence, this thermochromic technique is a promising strategy to enhance the performance of the LFA for sensitive detection.

Chapter 6 : Conclusions and future works

This chapter provides a summary of the whole study from the preparation of nanoparticles to the fabrication of the novel thermochromic LFA for the detection of *Salmonella typhimurium* and DENV2-NS1. The future direction and the suggestion on improvement of the thermochromic assay is also discussed at the end of this chapter.

6.1 Conclusions

This project aims to develop a novel signal enhancement technique for LFA detection using photothermal nanoparticles. The development of thermochromic LFA in this study provides several academic benefits. The kinetic growth of the magnetic and plasmonic nanoparticles were investigated. The factors related to the size and shapes of the nanoparticles were revealed, permitting morphology control. Since both magnetic and plasmonic nanoparticles have excellent photothermal properties, the response of the nanoparticles toward the white-light LED was assessed in the thesis. One of the nanoparticles was chosen to be used in the thermochromic LFA. The optimisation of the design of the typical LFA strips and the labels for the detection of DENV2-NS1 and *Salmonella typhimurium* are demonstrated.

Chapter 2 describes the synthesis and characterisations of magnetic and plasmonic nanoparticles. For the MNPs, spherical IONPs and ZFNPs with high crystallinity were obtained by the modified polyol method. The diameter of the IONPs and ZFNPs could be tuned between 10 and 17 nm by adjusting the reaction time in the autoclave. TREG ligands were initially coated on the surface of the MNPs and were subsequently replaced with carboxylate-containing citrate molecules through a ligand exchange reaction to improve water dispersibility and facilitate further functionalisation. The effects of various parameters, such as the concentration of MNPs and citrate, experimental configuration, and the duration of the ligand exchange reaction, were investigated and optimised. FTIR measurement confirmed the anchoring of citrate moieties on the surface of the MNPs and the absence of original TREG ligands. DLS

and zeta potential measurements also confirmed that the MNPs were highly stable in solution.

The plasmonic nanoparticles, including AuNSPs, AuNRs, and AuNSTs, were synthesised according to previously published protocols. [56, 57, 206, 210] The LSPRs of these gold nanoparticles were tuned to fall within the visible range of the spectrum to maximise photothermal efficiency under white-light LED irradiation (400-700 nm). Spherical gold nanoparticles were produced using the classic Turkevich method. By modifying the concentration of the reducing agent, AuNSPs with diameter ranging from 11 to 33 nm and various polydispersity indexes were obtained. Seed-mediated synthesis was used to produce AuNRs with different aspect ratios. The aspect ratio of the rod-like gold nanoparticles can be altered from 1.59 to 4.91 could be changed by adding salt additives and modifying the concentration of silver salt. Finally, seed-mediated synthesis was used to prepare AuNSTs with sizes of 65 and 243 nm. However, these AuNSTs were not stable and precipitated quickly in water, hence they were excluded from further investigation. This suggests that a ligand replacement reaction is necessary to coat AuNSTs with new ligands to improve their water dispersibility.

Chapter 3 explores the investigation inon the light-to-heat conversion capability of nanoparticles to find promising candidates for being used as LFA labels in the thermochromic LFA. To simulate the test result of a conventional LFA, colloidal nanoparticles were printed on nitrocellulose membranes as a single line and illuminated with LED light. 12 nm AuNSPs, IONPs and ZFNPs were found to produce the highest temperature. Among these, ZFNPs were selected for further experiment. In addition to excellent photothermal properties of ZFNPs, they also bring the capability of sample concentration and purification to the assay laeding to improved sensitivity, especially when dealing with complex sample matrices. Furthermore, the cost of raw material for producing ZFNPs is cheaper than that of AuNPs (see Appendix H). In the proof-of-concept study, the signals from three different methods were compared: a typical visual signal, a thermal contrast signal, and a thermochromic signal. The findings showed that the thermochromic and thermal signals were greater than the typical visual signal. Furthermore, the thermochromic signal

exhibited greater sensitivity than the thermal signal indicating the potential of this method as a signal enhancement strategy for LFA detection.

Chapter 4 focuses on the preparation of LFA for the detection of *Salmonella typhimurium* and DENV2-NS1. The chapter begins with the biofunctionalisation of ZFNPs@citrate. Initially, aptamers were aimed for being immobilized with ZFNPs@citrate due to its cost-effectiveness and high binding affinity compared to antibodies. First, ZFNPs@citrate were chemically immobilised with the amino-modified aptamer using EDC/sulfo-NHS coupling method to target *Salmonella typhimurium*. However, the immobilisation was not successful in this work. Gel electrophoresis measurement revealed that the number of covalent bonds was low, resulting in poor bacteria capture efficiency. The ongoing difficulty in this work is presumed to be caused by electrostatic repulsion between sulfo-NHS-treated ZFNPs and the negative charges of the nucleotides. Changing the chemical reagent for covalent modification to NHS, instead of sulfo-NHS, could potentially resolve the issue. NHS could activate the carboxylates of the particles, turning them to neutral charges and encouraging more aptamers to localise on the surface of ZFNPs. Furthermore, deteremining the isoelectric point of the aptamers could help identifying the optimal pH for immobilisation and to maximise the coupling efficiency. Therefore, 12 nm AuNSPs were selected to replace ZFNPs as they also exbihit great photothermal response against white-light LED producing significant heat, comparable to the MNPs. They were physically conjugated with antibodies to capture either *Salmonella typhimurium* or DENV2-NS1. Flocculation assays were conducted to optimise the antibody conjugations. A half-strip LFA was used to select the antibody pair to ensure the capture of the analytes and the formation of the test line on the membrane.

In Chapter 5, a comparison study was carried out to assess the performance of the conventional and thermochromic LFAs. Firstly, the illumination duration and LED power intensity were optimised to maximise the thermochromic signal. For the identification of *Salmonella typhimurium*, the conventional LFA could detect the bacteria at 10^7 CFU/mL by naked-eye observation and 0.25 x 10^7 CFU/mL with the assistance of image processing. The therochromic LFA allowed detection at a lower

concentration of 0.5 x 10^6 CFU/mL, significantly reducing the LOD. For the detection of DENV2-NS1, the interpretation of the LFA result by naked eye was 3.125 ng/mL of DENV2-NS1 and was reduced to 1.5 ng/mL with the use of thermochromic-based technique, offering a 4-fold reduction in LOD. These results showe that the thermochromic-based assay is an effective method for enhancing the sensitivity of LFA detection. Although the thermochromic LFA showed potential for being a rapid and sensitive detection assay, all experiments were conducted with the simulating conditions in a laboratory. The thermochromic LFA in this work has not yet been tested with real samples, which may experience difficulties.

6.2 Future works

The works presented in this thesis represent the initial stage of thermochromic LFA development. Several aspects require further investigation to transform this technology into a portable device for early detection.

A critical aspect that has not been adequately addressed in this thesis is the specificity and selectivity of the thermochromic LFAs. All experiments have employed controlled laboratory settings, which may not accurately reflect the performance of the thermochromic LFA when applied to real samples. The textures and compositions of real samples can significantly influence the test results, particularly in viscous samples. Differences between laboratory settings and real samples could lead to substantial differences in detection results. Moreover, the use of white-light LED in the thermochromic LFA potentially causes false-positive results. This is because other components may absorb the emission of the LED resulting in increased temperature that triggers the colour change of the thermochromic sheet. This non-specific activation thereby makes the interpretation of results more challenging.

For *Salmonella typhimurium* detection, required future works include testing with real samples and assessing their performance against other commonly found food pathogens, such as *Eschelichai coli,* and *Staphylococcus aureus*. To evaluate the specificity and selectivity for *Salmonella typhimurium* detection, mixtures containing

Salmonella typhimurium and other relevant pathogens should be tested. Additionally, real food samples spiked with bacteria should be incorporated into the experiment to determine the effect of food matrices on the performance of LFAs. Following this, random food samples from supermarkets should be collected and analysed using the thermochromic-based LFA alongside other confirmatory techniques, such as bacteria culture and PCR, to validate the results.

For DENV2-NS1 detection, a comprehensive evaluation of specificity and selectivity is important. This includes testing the theromochromic LFA against other dungue serotypes (DENV1-NS1, DENV3-NS1, and DENV4-NS1) in laboratory setting. Additionally, closely related flaviviruses, such as influenza, measles, Zika, chikungunya, and yellow fever, should be introduced into the testing process as they are known to cause cross-reactions with antibodies, due to similar antigenic structures, a common issue in LFA detection. Furthermore, DENV2-NS1 spiked blood samples should be analysed to evaluate the effects of blood matrices and potential interfering blood components on the detection effectiveness of the thermochromic LFA. The final step should involve testing random patients' blood samples using the thermochromic-based LFA alongside other confirmation techniques to validate the results.

Additionally, the attachment of antibodies to 12 nm AuNSPs via physical absorption presents challenges for real-world applications, as antibodies are susceptible to detachment in harsh environments. To address this limitation, future work should explore covalent coupling strategies to establish more stable covalent bonds between nanoparticle and antibodies. This approach is expected to enhance the capture efficiency of the conjugates and expand their applicability in various settings.

Despite its advantages, the colourimetric thermochromic assay has a limitation in that the thermochromic sheet is sensitive to external temperature and responds promptly once the activation point is reached. The proper temperature working range of the thermochromic sheet must be carefully selected to suit the ambient temperature. Hence, the calibration process of the LED is very essential. This disadvantage hinders on-site operation where the surrounding temperature cannot

be controlled. The device is more appropriate for use in laboratories or any other setting where the ambient temperature is stable or adjustable. This contrasts with the generic LFA that has earned popularity due to its portability and suitability for on-site operation. The sensitive thermal response characteristics of the thermochromic sheet hinders the device for being a point-of-care.

To overcome this issue, an enclosure box with a temperature controller should be fabricated. This enclosure would not only minimise the risk of unintended exposure to LED light but also regulate the ambient temperature to maintain optimal detection performance. In addition, it would reduce ambient light and provide consistent conditions for capturing images of the results for quantification. Furthermore, smartphone apps could be developed to enable portable quantification of colour intensity, eliminating the need for MATLAB software and a laptop.

It was observed that the thermochromic sheet absorbs a significant amount of light, contributing to background noise. To mitigate this issue, a filter should be installed on the LED to block unwanted wavelengths that are absorbed by the thermochromic sheet.

To enhance the performance of thermochromic LFA detection, the incorporation of highly efficient photothermal nanoparticles into the thermochromic LFA is recommended. These nanoparticles can absorb light and rapidly convert it into heat, leading to a more pronounced temperature increase. Consequently, lower light power intensity or shorter illumination durations can be employed. The substantial temperature rise generated generated by photothermal nanoparticles effectively surpasses the background noise signal, providing clear discrimination of positive signals.

Building upon the findings of this thesis, another potential area of exploration is the development of a semi-quantificative tool based on the thermochromic LFA. The liquid crytal thermochromic sheet exhibits the ability to transition through a spectrum of colours, ranging from red to green, and blue, corresponding to the degree of temperature generated. This temperature change is directly related to the

concentration of analytes present in the sample. Therefore it appears feasible to achieve semi-quantification of the assay, enabling approximation of target concentrations without the need for image analysis software.

In Figure 6.1, for instance, the results of dengue detection in Section 5.3.2.3 demonstate that the thermochromic sheet displays red colouration for DENV2-NS1 concentations ranging from 1.5 ng/mL to 6.25 ng/mL. Conversely, for concentrations exceeding 12.5 ng/mL, green and blue colours emerged on the thermochromic sheets. By leveraging this charactistics and calibrating the LED configurations, it is possible to estimate the viral biomarker concentration between 1.56 ng/mL and 12.5 ng/mL simply by observing red colour on the thermochromic sheet with the naked eye. On the other hand, the presence of green and blue pixels indicates that the DENV2-NS1 concentration surpasses 12.5 ng/mL. However, the thermochromic sheet is black when DENV2-NS1 concentration is below 1.56 ng/mL. This semi-quantitative feature holds significant promise for the thermochromic LFA and requires further investigation and development in future works.

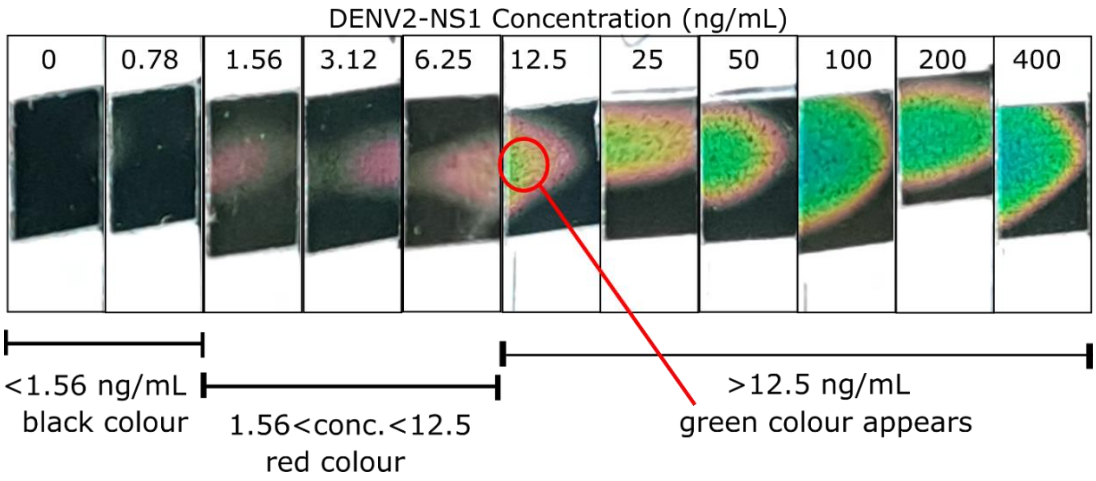

Figure 6.1 Semi-quantificative analysis of the thermochromic LFA. Thermochromic sheets were exposed to DENV2-NS1 concentrations ranging from 0 to 400 ng/mL following LED illumination.

In conclusion, the thermochromic signal was a promising colourimetric measurement to enhance the sensitivity of LFA detection. It offers simplicity, affordability, semi-quantitative results, and a greater sensitivity of detection with a prompt response, over the typical measurement and general thermal contrast method. This thermal

sensing measurement also allows the elimination of an expensive tool, such as a thermal imager for analysis. It only requires an ordinary camera, *e.g.* from a smartphone, with the software for quantification. The work presented in this thesis provides a solid foundation for further development and refinement of this technology, paving the way for its widespread adoption in point-of-care settings.

Discussing the potential for expanding the application of the thermochromic-based teachnique, it has been demonstrated in this thesis to be transferable to the detection of other anayltes. Apart from LFAs, the thermochromic-based enhancement technnique can be applied to other rapid detection methods, such as microfluidic paper-based analytical devices and thread-based analytical devices.

Recently, a phothothermal-sensing microfluidic paper-based chip was fabricated for the sensitive detection of trace amounts of diethylstilbestrol in food. [268] Black phosphorous nanosheets and gold nanoparticles were used in their work based on competitive inhibition immunochromatography. An 808-nm laser was employed to irradiate the particles and an IR camera was used to determine the temperature change. Cotton thread-based analytical device represent the most recent technoloygy employing the photothermal properties of plasmonic nanoparticles to enhance the detection sensitivity using a thermocmeter reader to determine the temperature gradient. [269] These evidence share similarities with LFAs in that they provide qualitative results to users using thermal readers. With the thermochromic sheet, multi-colour visual signals can be generated, allowing for the estimation of analyte concentrations in samples with enhanced sensitivity. This was demonstrated in Chaper 3, where the thermochromic-based sensing method exhibited greater sensitivity than the thermal-sensing method.

In addition to optical excitation, gold nanoparticles can also be heated under radio frequency excitation. [270] With this, interfering compounds in biological samples or background noise from the thermochrocmis sheet and nitrocellulose membrane can be eliminated as these substances do not absorb radio frequency energy. A previous study showed the used of superparamagnetic nanoparticels in LFAs with radio frequency excitation to measure changes in their impedance. [174] The

thermochromic-based method can be transferred to impedance paper-based sensors to eliminate complex setups and electrical reader equipment. By integrating the thermochromic sheet, the signals can be translated into visible signals.

One interesting potential of using the thermochromic-based enhancement technique lies in the application of Joule heating, a process that generates heat energy when an electrical current passes through a resistor. As is known, an electrical current is associated with heat production. [183] Thermochromic materials have been used in the field of electricity to detect temperature, as shown in a previous work. [183] Based on this evidence, the thermochromic technique holds promise for using in electrochemical sensors. A thermochromic membrane was fabricated in the literature to detect temperature-assocaited fever. [267] It may be feasible to modify the electrode of electrochemical sensors with a conductive nanoparticle-modified thermochromic membrane to convert the electrical signal into a visual signal, thereby reducing system complex. Notably, electrochemical LFAs have been demonstrated in the literature and may be suitable for applying this thermochromic technique. [271, 272]

Bibliography

1. Byakodi, M., N.S. Shrikrishna, R. Sharma, et al., *Emerging 0D, 1D, 2D, and 3D nanostructures for efficient point-of-care biosensing.* Biosensors and Bioelectronics: X, 2022. **12**: p. 100284.

2. Abid, N., A.M. Khan, S. Shujait, et al., *Synthesis of nanomaterials using various top-down and bottom-up approaches, influencing factors, advantages, and disadvantages: A review.* Advances in Colloid and Interface Science, 2022. **300**: p. 102597.

3. Saha, S., S. Bansal, and M. Khanuja, *Chapter 2 - Classification of nanomaterials and their physical and chemical nature*, in *Nano-enabled Agrochemicals in Agriculture*, M. Ghorbanpour and M.A. Shahid, Editors. 2022, Academic Press. p. 7-34.

4. Sudha, P.N., K. Sangeetha, K. Vijayalakshmi, et al., *Chapter 12 - Nanomaterials history, classification, unique properties, production and market*, in *Emerging Applications of Nanoparticles and Architecture Nanostructures*, A. Barhoum and A.S.H. Makhlouf, Editors. 2018, Elsevier. p. 341-384.

5. Abbas, M., K. Yan, J. Li, et al., *Agri-Nanotechnology and Tree Nanobionics: Augmentation in Crop Yield, Biosafety, and Biomass Accumulation.* Frontiers in Bioengineering and Biotechnology, 2022. **10**.

6. Patil, S.P. and V.V. Burungale, *2 - Physical and chemical properties of nanomaterials*, in *Nanomedicines for Breast Cancer Theranostics*, N.D. Thorat and J. Bauer, Editors. 2020, Elsevier. p. 17-31.

7. Sharifi, S., S. Behzadi, S. Laurent, et al., *Toxicity of nanomaterials.* Chemical Society Reviews, 2012. **41**(6): p. 2323-2343.

8. Karakoti, A.S., L.L. Hench, and S. Seal, *The potential toxicity of nanomaterials—The role of surfaces.* JOM, 2006. **58**(7): p. 77-82.

9. Zhang, N., G. Xiong, and Z. Liu, *Toxicity of metal-based nanoparticles: Challenges in the nano era.* Frontiers in Bioengineering and Biotechnology, 2022. **10**.

10. Mancuso, L. and G. Cao, *Acute toxicity test of CuO nanoparticles using human mesenchymal stem cells.* Toxicol Mech Methods, 2014. **24**(7): p. 449-54.

11. Kumah, E.A., R.D. Fopa, S. Harati, et al., *Human and environmental impacts of nanoparticles: a scoping review of the current literature.* BMC Public Health, 2023. **23**(1): p. 1059.

12. Sohaebuddin, S.K., P.T. Thevenot, D. Baker, et al., *Nanomaterial cytotoxicity is composition, size, and cell type dependent.* Particle and Fibre Toxicology, 2010. **7**(1): p. 22.

13. Sukhanova, A., S. Bozrova, P. Sokolov, et al., *Dependence of Nanoparticle Toxicity on Their Physical and Chemical Properties.* Nanoscale Res Lett, 2018. **13**(1): p. 44.

14. Huang, Y.W., M. Cambre, and H.J. Lee, *The Toxicity of Nanoparticles Depends on Multiple Molecular and Physicochemical Mechanisms.* Int J Mol Sci, 2017. **18**(12).

15. Dong, L., S. Tang, F. Deng, et al., *Shape-dependent toxicity of alumina nanoparticles in rat astrocytes.* Science of The Total Environment, 2019. **690**: p. 158-166.

16. Lee, J.H., J.E. Ju, B.I. Kim, et al., *Rod-shaped iron oxide nanoparticles are more toxic than sphere-shaped nanoparticles to murine macrophage cells.* Environ Toxicol Chem, 2014. **33**(12): p. 2759-66.

17. Wang, S., W. Lu, O. Tovmachenko, et al., *Challenge in Understanding Size and Shape Dependent Toxicity of Gold Nanomaterials in Human Skin Keratinocytes.* Chem Phys Lett, 2008. **463**(1-3): p. 145-149.

18. Nel, A., T. Xia, L. Mädler, et al., *Toxic potential of materials at the nanolevel.* Science, 2006. **311**(5761): p. 622-7.

19. Auclair, J. and F. Gagné, *Shape-Dependent Toxicity of Silver Nanoparticles on Freshwater Cnidarians.* Nanomaterials (Basel), 2022. **12**(18).

20. Liu, Y., Q. Zhou, J. Li, et al., *Selective and sensitive chemosensor for lead ions using fluorescent carbon dots prepared from chocolate by one-step hydrothermal method.* Sensors and Actuators B: Chemical, 2016. **237**: p. 597-604.

21. Gokul Eswaran, S., D. Thiruppathi, and N. Vasimalai, *Synthesis of highly fluorescent carbon dots from bread waste and their nanomolar lead ions sensor application.* Environmental Nanotechnology, Monitoring & Management, 2022. **18**: p. 100748.

22. Wu, L., X. Cai, K. Nelson, et al., *A Green Synthesis of Carbon Nanoparticle from Honey for Real-Time Photoacoustic Imaging.* Nano Res, 2013. **6**(5): p. 312-325.

23. Kumar, V., D.K. Singh, S. Mohan, et al., *Green synthesis of silver nanoparticle for the selective and sensitive colorimetric detection of mercury (II) ion.* Journal of Photochemistry and Photobiology B: Biology, 2017. **168**: p. 67-77.

24. Bharadwaj, K.K., B. Rabha, S. Pati, et al., *Green Synthesis of Gold Nanoparticles Using Plant Extracts as Beneficial Prospect for Cancer Theranostics.* Molecules, 2021. **26**(21).

25. Liaqat, N., N. Jahan, Khalil-ur-Rahman, et al., *Green synthesized silver nanoparticles: Optimization, characterization, antimicrobial activity, and cytotoxicity study by hemolysis assay.* Frontiers in Chemistry, 2022. **10**.

26. Alhalili, Z., *Green synthesis of copper oxide nanoparticles CuO NPs from Eucalyptus Globoulus leaf extract: Adsorption and design of experiments.* Arabian Journal of Chemistry, 2022. **15**(5): p. 103739.

27. Santhosh, P.B., J. Genova, and H. Chamati, *Green Synthesis of Gold Nanoparticles: An Eco-Friendly Approach.* Chemistry, 2022. **4**(2): p. 345-369.

28. Yang, W., B. Xia, L. Wang, et al., *Shape effects of gold nanoparticles in photothermal cancer therapy.* Materials Today Sustainability, 2021. **13**: p. 100078.

29. Mitchell, M.J., M.M. Billingsley, R.M. Haley, et al., *Engineering precision nanoparticles for drug delivery.* Nature Reviews Drug Discovery, 2021. **20**(2): p. 101-124.

30. Liu, R., C. Luo, Z. Pang, et al., *Advances of nanoparticles as drug delivery systems for disease diagnosis and treatment.* Chinese Chemical Letters, 2023. **34**(2): p. 107518.

31. Aldewachi, H., T. Chalati, M.N. Woodroofe, et al., *Gold nanoparticle-based colorimetric biosensors.* Nanoscale, 2018. **10**(1): p. 18-33.

32. Šišoláková, I., J. Hovancová, R. Oriňaková, et al., *Electrochemical determination of insulin at CuNPs/chitosan-MWCNTs and CoNPs/chitosan-MWCNTs modified screen printed carbon electrodes.* Journal of Electroanalytical Chemistry, 2020. **860**: p. 113881.

33. Zhu, W., L. Xu, C. Zhu, et al., *Magnetically controlled electrochemical sensing membrane based on multifunctional molecularly imprinted polymers for detection of insulin.* Electrochimica Acta, 2016. **218**: p. 91-100.

34. DeRosa, M.C., C. Monreal, M. Schnitzer, et al., *Nanotechnology in fertilizers.* Nature Nanotechnology, 2010. **5**(2): p. 91-91.

35. Ashfaq, A., N. Khursheed, S. Fatima, et al., *Application of nanotechnology in food packaging: Pros and Cons.* Journal of Agriculture and Food Research, 2022. **7**: p. 100270.

36. Biswas, R., M. Alam, A. Sarkar, et al., *Application of nanotechnology in food: processing, preservation, packaging and safety assessment.* Heliyon, 2022. **8**(11): p. e11795.

37. Giraldo, J.P. and S. Kruss, *Nanosensors for monitoring plant health.* Nature Nanotechnology, 2023. **18**(2): p. 107-108.

38. Hoang, V.C., K. Dave, and V.G. Gomes, *Carbon quantum dot-based composites for energy storage and electrocatalysis: Mechanism, applications and future prospects.* Nano Energy, 2019. **66**: p. 104093.

39. Sun, M., H. Dong, A.W. Dougherty, et al., *Nanophotonic energy storage in upconversion nanoparticles.* Nano Energy, 2019. **56**: p. 473-481.

40. Wang, Z., W. Xu, F. Jie, et al., *The selective adsorption performance and mechanism of multiwall magnetic carbon nanotubes for heavy metals in wastewater.* Scientific Reports, 2021. **11**(1): p. 16878.

41. Mohamed, A., R.R. Atta, A.A. Kotp, et al., *Green synthesis and characterization of iron oxide nanoparticles for the removal of heavy metals (Cd2+ and Ni2+) from aqueous solutions with Antimicrobial Investigation.* Scientific Reports, 2023. **13**(1): p. 7227.

42. Huang, X. and M.A. El-Sayed, *Gold nanoparticles: Optical properties and implementations in cancer diagnosis and photothermal therapy.* Journal of Advanced Research, 2010. **1**(1): p. 13-28.

43. Liu, Y., K. Ai, J. Liu, et al., *Dopamine-melanin colloidal nanospheres: an efficient near-infrared photothermal therapeutic agent for in vivo cancer therapy.* Adv Mater, 2013. **25**(9): p. 1353-9.

44. Thong, P.Q., L.T. Thu Huong, N.D. Tu, et al., *Multifunctional nanocarriers of Fe(3)O(4)@PLA-PEG/curcumin for MRI, magnetic hyperthermia and drug delivery.* Nanomedicine (Lond), 2022. **17**(22): p. 1677-1693.

45. Loizou, K., S. Mourdikoudis, A. Sergides, et al., *Rapid Millifluidic Synthesis of Stable High Magnetic Moment FexCy Nanoparticles for Hyperthermia.* ACS Applied Materials & Interfaces, 2020. **12**(25): p. 28520-28531.

46. Sahoo, S.L., C.-H. Liu, and W.-C. Wu, *Lymphoma cell isolation using multifunctional magnetic nanoparticles: antibody conjugation and characterization.* RSC Advances, 2017. **7**(36): p. 22468-22478.

47. Xu, H., Z.P. Aguilar, L. Yang, et al., *Antibody conjugated magnetic iron oxide nanoparticles for cancer cell separation in fresh whole blood.* Biomaterials, 2011. **32**(36): p. 9758-9765.

48. Liu, S., Z. Shen, L. Deng, et al., *Smartphone assisted portable biochip for non-invasive simultaneous monitoring of glucose and insulin towards precise diagnosis of prediabetes/diabetes.* Biosensors and Bioelectronics, 2022. **209**: p. 114251.

49. Kouchakinejad, S., S. Babaee, F. Roshani, et al., *The performance of the new modified pencil graphite electrode in quantifying of insulin.* Chemical Physics Letters, 2020. **759**: p. 137987.

50. Wardani, N.I., T. Kangkamano, R. Wannapob, et al., *Electrochemical sensor based on molecularly imprinted polymer cryogel and multiwalled carbon nanotubes for direct insulin detection.* Talanta, 2023. **254**: p. 124137.

51. Abazar, F., E. Sharifi, and A. Noorbakhsh, *Antifouling properties of carbon quantum dots-based electrochemical sensor as a promising platform for highly sensitive detection of insulin.* Microchemical Journal, 2022. **180**: p. 107560.

52. Priyadarshini, E. and N. Pradhan, *Gold nanoparticles as efficient sensors in colorimetric detection of toxic metal ions: A review.* Sensors and Actuators B: Chemical, 2017. **238**: p. 888-902.

53. Chang, C.C., C.P. Chen, T.H. Wu, et al., *Gold Nanoparticle-Based Colorimetric Strategies for Chemical and Biological Sensing Applications.* Nanomaterials (Basel), 2019. **9**(6).

54. Li, H., J. Gan, Q. Yang, et al., *Colorimetric detection of food freshness based on amine-responsive dopamine polymerization on gold nanoparticles.* Talanta, 2021. **234**: p. 122706.

55. You, Q., X. Zhang, F.-G. Wu, et al., *Colorimetric and test stripe-based assay of bacteria by using vancomycin-modified gold nanoparticles.* Sensors and Actuators B: Chemical, 2019. **281**: p. 408-414.

56. Rossi, F., E.H. Khoo, X. Su, et al., *Study of the Effect of Anisotropic Gold Nanoparticles on Plasmonic Coupling with a Photosensitizer for Antimicrobial Film.* ACS Applied Bio Materials, 2020. **3**(1): p. 315-326.

57. Rossi, F., N.T.K. Thanh, and X.D. Su, *Gold Nanorods Embedded in Polymeric Film for Killing Bacteria by Generating Reactive Oxygen Species with Light.* ACS Applied Bio Materials, 2019. **2**(7): p. 3059-3067.

58. Yao, Y., Y. Zhou, L. Liu, et al., *Nanoparticle-Based Drug Delivery in Cancer Therapy and Its Role in Overcoming Drug Resistance.* Frontiers in Molecular Biosciences, 2020. **7**.

59. Yan, L., J. Shen, J. Wang, et al., *Nanoparticle-Based Drug Delivery System: A Patient-Friendly Chemotherapy for Oncology.* Dose Response, 2020. **18**(3): p. 1559325820936161.

60. Baliyarsingh, B. and C.K. Pradhan, *Prospects of plant-derived metallic nanopesticides against storage pests - A review.* Journal of Agriculture and Food Research, 2023. **14**: p. 100687.

61. Li, Z., Y. Liu, O. Hossain, et al., *Real-time monitoring of plant stresses via chemiresistive profiling of leaf volatiles by a wearable sensor.* Matter, 2021. **4**(7): p. 2553-2570.

62. Lew, T.T.S., V.B. Koman, K.S. Silmore, et al., *Real-time detection of wound-induced H2O2 signalling waves in plants with optical nanosensors.* Nature Plants, 2020. **6**(4): p. 404-415.

63. Wu, H., R. Nißler, V. Morris, et al., *Monitoring Plant Health with Near-Infrared Fluorescent H2O2 Nanosensors.* Nano Letters, 2020. **20**(4): p. 2432-2442.

64. Son, W.K., Y.S. Choi, Y.W. Han, et al., *In vivo surface-enhanced Raman scattering nanosensor for the real-time monitoring of multiple stress signalling molecules in plants.* Nature Nanotechnology, 2023. **18**(2): p. 205-216.

65. Gupta, S., C.H. Huang, G.P. Singh, et al., *Portable Raman leaf-clip sensor for rapid detection of plant stress.* Scientific Reports, 2020. **10**(1): p. 20206.

66. Giraldo, J.P., M.P. Landry, S.Y. Kwak, et al., *A Ratiometric Sensor Using Single Chirality Near-Infrared Fluorescent Carbon Nanotubes: Application to In Vivo Monitoring.* Small, 2015. **11**(32): p. 3973-84.

67. Nißler, R., A.T. Müller, F. Dohrman, et al., *Detection and Imaging of the Plant Pathogen Response by Near-Infrared Fluorescent Polyphenol Sensors.* Angewandte Chemie International Edition, 2022. **61**(2): p. e202108373.

68. Boonyaves, K., M.C.-Y. Ang, M. Park, et al., *Near-Infrared Fluorescent Carbon Nanotube Sensors for the Plant Hormone Family Gibberellins.* Nano Letters, 2023. **23**(3): p. 916-924.

69. Nißler, R., J. Ackermann, C. Ma, et al., *Prospects of Fluorescent Single-Chirality Carbon Nanotube-Based Biosensors.* Analytical Chemistry, 2022. **94**(28): p. 9941-9951.

70. Ackermann, J., J.T. Metternich, S. Herbertz, et al., *Biosensing with Fluorescent Carbon Nanotubes.* Angewandte Chemie International Edition, 2022. **61**(18): p. e202112372.

71. Son, W.K., Y.S. Choi, Y.W. Han, et al., *In vivo surface-enhanced Raman scattering nanosensor for the real-time monitoring of multiple stress signalling molecules in plants.* Nat Nanotechnol, 2023. **18**(2): p. 205-216.

72. Maria-Hormigos, R., C.C. Mayorga-Martinez, T. Kinčl, et al., *Nanostructured Hybrid BioBots for Beer Brewing.* ACS Nano, 2023. **17**(8): p. 7595-7603.

73. Hortelão, A.C., T. Patiño, A. Perez-Jiménez, et al., *Enzyme-Powered Nanobots Enhance Anticancer Drug Delivery.* Advanced Functional Materials, 2018. **28**(25): p. 1705086.

74. Giri, G., Y. Maddahi, and K. Zareinia, *A Brief Review on Challenges in Design and Development of Nanorobots for Medical Applications.* Applied Sciences, 2021. **11**(21): p. 10385.

75. Clyde, K., J.L. Kyle, and E. Harris, *Recent advances in deciphering viral and host determinants of dengue virus replication and pathogenesis.* J Virol, 2006. **80**(23): p. 11418-31.

76. Halstead, S.B., *Dengue.* Lancet, 2007. **370**(9599): p. 1644-52.

77. de la Cruz-Hernández, S.I., H. Flores-Aguilar, S. González-Mateos, et al., *Determination of viremia and concentration of circulating nonstructural protein 1 in patients infected with dengue virus in Mexico.* Am J Trop Med Hyg, 2013. **88**(3): p. 446-54.

78. Paranavitane, S.A., L. Gomes, A. Kamaladasa, et al., *Dengue NS1 antigen as a marker of severe clinical disease.* BMC Infect Dis, 2014. **14**: p. 570.

79. Bhatt, S., P.W. Gething, O.J. Brady, et al., *The global distribution and burden of dengue.* Nature, 2013. **496**(7446): p. 504-7.

80. DESK, N., *Thailand dengue cases top 60,000; Mae Hong Son province reports highest prevalence*, in *Outbreak News Today*. 2020.

81. DESK, N., *Thailand reports 71,000 dengue cases in 2020*, in *Outbreak News Today*. 2021.

82. Gubler, D.J., *Dengue and dengue hemorrhagic fever.* Clin Microbiol Rev, 1998. **11**(3): p. 480-96.

83. Yung, C.F., K.S. Lee, T.L. Thein, et al., *Dengue serotype-specific differences in clinical manifestation, laboratory parameters and risk of severe disease in adults, singapore.* Am J Trop Med Hyg, 2015. **92**(5): p. 999-1005.

84. Muller, D.A., A.C. Depelsenaire, and P.R. Young, *Clinical and Laboratory Diagnosis of Dengue Virus Infection.* J Infect Dis, 2017. **215**(suppl_2): p. S89-s95.

85. Libraty, D.H., P.R. Young, D. Pickering, et al., *High circulating levels of the dengue virus nonstructural protein NS1 early in dengue illness correlate with the development of dengue hemorrhagic fever.* J Infect Dis, 2002. **186**(8): p. 1165-8.

86. Young, P.R., P.A. Hilditch, C. Bletchly, et al., *An antigen capture enzyme-linked immunosorbent assay reveals high levels of the dengue virus protein NS1 in the sera of infected patients.* J Clin Microbiol, 2000. **38**(3): p. 1053-7.

87. Pothapregada, S., B. Kamalakannan, M. Thulasingam, et al., *Is Reactive Dengue NS1Antigen Test a Warning Call for Hospital Admissions?* J Clin Diagn Res, 2016. **10**(4): p. Sc04-7.

88. Chaterji, S., J.C. Allen, Jr., A. Chow, et al., *Evaluation of the NS1 rapid test and the WHO dengue classification schemes for use as bedside diagnosis of acute dengue fever in adults.* Am J Trop Med Hyg, 2011. **84**(2): p. 224-8.

89. Tezuka, K., M. Kuramitsu, K. Okuma, et al., *Development of a novel dengue virus serotype-specific multiplex real-time reverse transcription–polymerase chain reaction assay for blood screening.* Transfusion, 2016. **56**(12): p. 3094-3100.

90. Dutta, R., K. Thangapandi, S. Mondal, et al., *Polyaniline Based Electrochemical Sensor for the Detection of Dengue Virus Infection.* Avicenna J Med Biotechnol, 2020. **12**(2): p. 77-84.

91. Arshad, R., A. Rhouati, A. Hayat, et al., *MIP-Based Impedimetric Sensor for Detecting Dengue Fever Biomarker.* Applied Biochemistry and Biotechnology, 2020. **191**(4): p. 1384-1394.

92. Lien, K.-Y., J.-L. Lin, C.-Y. Liu, et al., *Purification and enrichment of virus samples utilizing magnetic beads on a microfluidic system.* Lab on a Chip, 2007. **7**(7): p. 868-875.

93. Iswardy, E., T.-C. Tsai, I.F. Cheng, et al., *A bead-based immunofluorescence-assay on a microfluidic dielectrophoresis platform for rapid dengue virus detection.* Biosensors and Bioelectronics, 2017. **95**: p. 174-180.

94. Prabowo, M.H., S. Chatchen, P. Rijiravanich, et al., *Dengue NS1 detection in pediatric serum using microfluidic paper-based analytical devices.* Analytical and Bioanalytical Chemistry, 2020. **412**(12): p. 2915-2925.

95. Yrad, F.M., J.M. Castañares, and E.C. Alocilja, *Visual Detection of Dengue-1 RNA Using Gold Nanoparticle-Based Lateral Flow Biosensor.* Diagnostics (Basel), 2019. **9**(3).

96. Kumar, S., P. Bhushan, V. Krishna, et al., *Tapered lateral flow immunoassay based point-of-care diagnostic device for ultrasensitive colorimetric detection of dengue NS1.* Biomicrofluidics, 2018. **12**(3): p. 034104-034104.

97. Tran, T.V., B.V. Nguyen, T.T.P. Nguyen, et al., *Development of a highly sensitive magneto-enzyme lateral flow immunoassay for dengue NS1 detection.* PeerJ, 2019. **7**: p. e7779.

98. Bell, R.L., K.G. Jarvis, A.R. Ottesen, et al., *Recent and emerging innovations in Salmonella detection: a food and environmental perspective.* Microbial biotechnology, 2016. **9**(3): p. 279-292.

99. Saleh, S., S. Van Puyvelde, A. Staes, et al., *Salmonella Typhi, Paratyphi A, Enteritidis and Typhimurium core proteomes reveal differentially expressed proteins linked to the cell surface and pathogenicity.* PLoS Negl Trop Dis, 2019. **13**(5): p. e0007416.

100. Andino, A. and I. Hanning, *Salmonella enterica: survival, colonization, and virulence differences among serovars.* ScientificWorldJournal, 2015. **2015**: p. 520179.

101. Brenner, F.W., R.G. Villar, F.J. Angulo, et al., *Salmonella nomenclature.* J Clin Microbiol, 2000. **38**(7): p. 2465-7.

102. Tindall, B.J., P.A.D. Grimont, G.M. Garrity, et al., *Nomenclature and taxonomy of the genus Salmonella.* Int J Syst Evol Microbiol, 2005. **55**(Pt 1): p. 521-524.

103. Batz, M.B., S. Hoffmann, and J.G. Morris, Jr., *Ranking the disease burden of 14 pathogens in food sources in the United States using attribution data from outbreak investigations and expert elicitation.* J Food Prot, 2012. **75**(7): p. 1278-91.

104. Scallan, E., R.M. Hoekstra, F.J. Angulo, et al., *Foodborne illness acquired in the United States--major pathogens.* Emerg Infect Dis, 2011. **17**(1): p. 7-15.

105. Focker, M. and H.J. van der Fels-Klerx, *Economics applied to food safety.* Current Opinion in Food Science, 2020. **36**: p. 18-23.

106. Cavallaro, E., K. Date, C. Medus, et al., *Salmonella Typhimurium Infections Associated with Peanut Products.* New England Journal of Medicine, 2011. **365**(7): p. 601-610.

107. Unicomb, L.E., G. Simmons, T. Merritt, et al., *Sesame seed products contaminated with Salmonella: three outbreaks associated with tahini.* Epidemiol Infect, 2005. **133**(6): p. 1065-72.

108. Morton, V.K., A. Kearney, S. Coleman, et al., *Outbreaks of Salmonella illness associated with frozen raw breaded chicken products in Canada, 2015-2019.* Epidemiol Infect, 2019. **147**: p. e254.

109. *Update: recall of dry dog and cat food products associated with human Salmonella Schwarzengrund infections--United States, 2008.* MMWR Morb Mortal Wkly Rep, 2008. **57**(44): p. 1200-2.

110. Soon, J.M., A.K.M. Brazier, and C.A. Wallace, *Determining common contributory factors in food safety incidents – A review of global outbreaks and recalls 2008–2018.* Trends in Food Science & Technology, 2020. **97**: p. 76-87.

111. SCHARFF, R.L., *Food Attribution and Economic Cost Estimates for Meat- and Poultry-Related Illnesses.* Journal of Food Protection, 2020. **83**(6): p. 959-967.

112. Lee, K.-M., M. Runyon, T.J. Herrman, et al., *Review of Salmonella detection and identification methods: Aspects of rapid emergency response and food safety.* Food Control, 2015. **47**: p. 264-276.

113. Mooijman, K.A., A. Pielaat, and A.F.A. Kuijpers, *Validation of EN ISO 6579-1 - Microbiology of the food chain - Horizontal method for the detection, enumeration and serotyping of Salmonella - Part 1 detection of Salmonella spp.* Int J Food Microbiol, 2019. **288**: p. 3-12.

114. Eijkelkamp, J.M., H.J.M. Aarts, and H.J. van der Fels-Klerx, *Suitability of Rapid Detection Methods for Salmonella in Poultry Slaughterhouses.* Food Analytical Methods, 2009. **2**(1): p. 1-13.

115. Gorski, L., *Selective enrichment media bias the types of Salmonella enterica strains isolated from mixed strain cultures and complex enrichment broths.* PLoS One, 2012. **7**(4): p. e34722.

116. Wang, W., L. Liu, S. Song, et al., *A highly sensitive ELISA and immunochromatographic strip for the detection of Salmonella typhimurium in milk samples.* Sensors (Basel), 2015. **15**(3): p. 5281-92.

117. Prusak-Sochaczewski, E. and J.H. Luong, *An improved ELISA method for the detection of Salmonella typhimurium.* J Appl Bacteriol, 1989. **66**(2): p. 127-35.

118. Thorns, C.J., I.M. McLaren, and M.G. Sojka, *The use of latex particle agglutination to specifically detect Salmonella enteritidis.* International Journal of Food Microbiology, 1994. **21**(1): p. 47-53.

119. Xu, Z., X. Bi, Y. Huang, et al., *Sensitive colorimetric detection of Salmonella enteric serovar typhimurium based on a gold nanoparticle conjugated bifunctional oligonucleotide probe and aptamer.* Journal of Food Safety, 2018. **38**(5): p. e12482.

120. Fang, Z., W. Wu, X. Lu, et al., *Lateral flow biosensor for DNA extraction-free detection of Salmonella based on aptamer mediated strand displacement amplification.* Biosens Bioelectron, 2014. **56**: p. 192-7.

121. Bu, T., X. Yao, L. Huang, et al., *Dual recognition strategy and magnetic enrichment based lateral flow assay toward Salmonella enteritidis detection.* Talanta, 2020. **206**: p. 120204.

122. Paião, F.G., L.G. Arisitides, L.S. Murate, et al., *Detection of Salmonella spp, Salmonella Enteritidis and Typhimurium in naturally infected broiler chickens by a multiplex PCR-based assay.* Braz J Microbiol, 2013. **44**(1): p. 37-41.

123. Oh, S.Y., N.S. Heo, S. Shukla, et al., *Development of gold nanoparticle-aptamer-based LSPR sensing chips for the rapid detection of Salmonella typhimurium in pork meat.* Scientific Reports, 2017. **7**(1): p. 10130.

124. Parolo, C., A. Sena-Torralba, J.F. Bergua, et al., *Tutorial: design and fabrication of nanoparticle-based lateral-flow immunoassays.* Nature Protocols, 2020. **15**(12): p. 3788-3816.

125. Yin, H.-Y., P.-T. Chu, W.-C. Tsai, et al., *Development of a barcode-style lateral flow immunoassay for the rapid semi-quantification of gliadin in foods.* Food Chemistry, 2016. **192**: p. 934-942.

126. Panferov, V.G., I.V. Safenkova, A.V. Zherdev, et al., *Setting up the cut-off level of a sensitive barcode lateral flow assay with magnetic nanoparticles.* Talanta, 2017. **164**: p. 69-76.

127. Lu, W., K. Wang, K. Xiao, et al., *Dual Immunomagnetic Nanobeads-Based Lateral Flow Test Strip for Simultaneous Quantitative Detection of Carcinoembryonic Antigen and Neuron Specific Enolase.* Sci Rep, 2017. **7**: p. 42414.

128. Wu, J., M. Dong, C. Zhang, et al., *Magnetic Lateral Flow Strip for the Detection of Cocaine in Urine by Naked Eyes and Smart Phone Camera.* Sensors (Basel), 2017. **17**(6).

129. Wang, Y., Z. Qin, D.R. Boulware, et al., *Thermal Contrast Amplification Reader Yielding 8-Fold Analytical Improvement for Disease Detection with Lateral Flow Assays.* Analytical Chemistry, 2016. **88**(23): p. 11774-11782.

130. Koczula, K.M. and A. Gallotta, *Lateral flow assays.* Essays Biochem, 2016. **60**(1): p. 111-20.

131. Puertas, S., M. Moros, R. Fernández-Pacheco, et al., *Designing novel nano-immunoassays: antibody orientation versus sensitivity.* Journal of Physics D: Applied Physics, 2010. **43**(47): p. 474012.

132. Miguel-Sancho, N., O. Bomatí-Miguel, G. Colom, et al., *Development of Stable, Water-Dispersible, and Biofunctionalizable Superparamagnetic Iron Oxide Nanoparticles.* Chemistry of Materials, 2011. **23**(11): p. 2795-2802.

133. Arenal, R., L. De Matteis, L. Custardoy, et al., *Spatially-Resolved EELS Analysis of Antibody Distribution on Biofunctionalized Magnetic Nanoparticles.* ACS Nano, 2013. **7**(5): p. 4006-4013.

134. Puertas, S., P. Batalla, M. Moros, et al., *Taking Advantage of Unspecific Interactions to Produce Highly Active Magnetic Nanoparticle–Antibody Conjugates.* ACS Nano, 2011. **5**(6): p. 4521-4528.

135. Parolo, C., A. de la Escosura-Muñiz, E. Polo, et al., *Design, Preparation, and Evaluation of a Fixed-Orientation Antibody/Gold-Nanoparticle Conjugate as an Immunosensing Label.* ACS Applied Materials & Interfaces, 2013. **5**(21): p. 10753-10759.

136. Gallina, M.E., Y. Zhou, C.J. Johnson, et al., *Aptamer-conjugated, fluorescent gold nanorods as potential cancer theradiagnostic agents.* Materials Science and Engineering: C, 2016. **59**: p. 324-332.

137. Gong, S., H. Ren, C. Lin, et al., *Immunochromatographic strip biosensor for the rapid detection of N-glycolylneuraminic acid based on aptamer-conjugated nanoparticle.* Analytical Biochemistry, 2018. **561-562**: p. 52-58.

138. Delaviz, N., P. Gill, A. Ajami, et al., *Aptamer-conjugated magnetic nanoparticles for the efficient removal of HCV particles from human plasma samples.* RSC Advances, 2015. **5**(97): p. 79433-79439.

139. Keshtkar, M., D. Shahbazi-Gahrouei, S.M. Khoshfetrat, et al., *Aptamer-conjugated Magnetic Nanoparticles as Targeted Magnetic Resonance Imaging Contrast Agent for Breast Cancer.* Journal of medical signals and sensors, 2016. **6**(4): p. 243-247.

140. Saha, B., P. Songe, T.H. Evers, et al., *The influence of covalent immobilization conditions on antibody accessibility on nanoparticles.* Analyst, 2017. **142**(22): p. 4247-4256.

141. Saha, B., T.H. Evers, and M.W.J. Prins, *How Antibody Surface Coverage on Nanoparticles Determines the Activity and Kinetics of Antigen Capturing for Biosensing.* Analytical Chemistry, 2014. **86**(16): p. 8158-8166.

142. Welch, N.G., J.A. Scoble, B.W. Muir, et al., *Orientation and characterization of immobilized antibodies for improved immunoassays (Review).* Biointerphases, 2017. **12**(2): p. 02D301.

143. Lakhin, A.V., V.Z. Tarantul, and L.V. Gening, *Aptamers: problems, solutions and prospects.* Acta naturae, 2013. **5**(4): p. 34-43.

144. Sun, H., X. Zhu, P.Y. Lu, et al., *Oligonucleotide aptamers: new tools for targeted cancer therapy.* Molecular therapy. Nucleic acids, 2014. **3**(8): p. e182-e182.

145. Singh, J., S. Sharma, and S. Nara, *Nanogold based lateral flow assay for the detection of Salmonella typhi in environmental water samples.* Analytical Methods, 2015. **7**(21): p. 9281-9288.

146. Byzova, N.A., I.V. Safenkova, E.S. Slutskaya, et al., *Less is More: A Comparison of Antibody–Gold Nanoparticle Conjugates of Different Ratios.* Bioconjugate Chemistry, 2017. **28**(11): p. 2737-2746.

147. Walsh, M.K., X. Wang, and B.C. Weimer, *Optimizing the immobilization of single-stranded DNA onto glass beads.* J Biochem Biophys Methods, 2001. **47**(3): p. 221-31.

148. Moore, C.J., H. Montón, R. O'Kennedy, et al., *Controlling colloidal stability of silica nanoparticles during bioconjugation reactions with proteins and improving their longer-term stability, handling and storage.* Journal of Materials Chemistry B, 2015. **3**(10): p. 2043-2055.

149. Trilling, A.K., J. Beekwilder, and H. Zuilhof, *Antibody orientation on biosensor surfaces: a minireview.* Analyst, 2013. **138**(6): p. 1619-1627.

150. Ruppert, C., N. Phogat, S. Laufer, et al., *A smartphone readout system for gold nanoparticle-based lateral flow assays: application to monitoring of digoxigenin.* Microchimica Acta, 2019. **186**(2): p. 119.

151. Peng, T., X. Liu, L.G. Adams, et al., *Enhancing sensitivity of lateral flow assay with application to SARS-CoV-2.* Applied Physics Letters, 2020. **117**(12): p. 120601.

152. Park, J., *An Optimized Colorimetric Readout Method for Lateral Flow Immunoassays.* Sensors (Basel), 2018. **18**(12).

153. Khlebtsov, B.N., R.S. Tumskiy, A.M. Burov, et al., *Quantifying the Numbers of Gold Nanoparticles in the Test Zone of Lateral Flow Immunoassay Strips.* ACS Applied Nano Materials, 2019. **2**(8): p. 5020-5028.

154. Xu, H., J. Chen, J. Birrenkott, et al., *Gold-Nanoparticle-Decorated Silica Nanorods for Sensitive Visual Detection of Proteins.* Analytical Chemistry, 2014. **86**(15): p. 7351-7359.

155. Choi, D.H., S.K. Lee, Y.K. Oh, et al., *A dual gold nanoparticle conjugate-based lateral flow assay (LFA) method for the analysis of troponin I.* Biosensors and Bioelectronics, 2010. **25**(8): p. 1999-2002.

156. Chen, M., Z. Yu, D. Liu, et al., *Dual gold nanoparticle lateflow immunoassay for sensitive detection of Escherichia coli O157:H7.* Analytica Chimica Acta, 2015. **876**: p. 71-76.

157. Razo, S.C., V.G. Panferov, I.V. Safenkova, et al., *Double-enhanced lateral flow immunoassay for potato virus X based on a combination of magnetic and gold nanoparticles.* Analytica Chimica Acta, 2018. **1007**: p. 50-60.

158. Taranova, N.A., A.E. Urusov, E.G. Sadykhov, et al., *Bifunctional gold nanoparticles as an agglomeration-enhancing tool for highly sensitive lateral flow tests: a case study with procalcitonin.* Microchimica Acta, 2017. **184**(10): p. 4189-4195.

159. Hwang, J., D. Kwon, S. Lee, et al., *Detection of Salmonella bacteria in milk using gold-coated magnetic nanoparticle clusters and lateral flow filters.* RSC Advances, 2016. **6**(54): p. 48445-48448.

160. Wang, D.-B., B. Tian, Z.-P. Zhang, et al., *Detection of Bacillus anthracis spores by super-paramagnetic lateral-flow immunoassays based on "Road Closure".* Biosensors and Bioelectronics, 2015. **67**: p. 608-614.

161. Loynachan, C.N., M.R. Thomas, E.R. Gray, et al., *Platinum Nanocatalyst Amplification: Redefining the Gold Standard for Lateral Flow Immunoassays with Ultrabroad Dynamic Range.* ACS Nano, 2018. **12**(1): p. 279-288.

162. Panferov, V.G., I.V. Safenkova, N.A. Byzova, et al., *Silver-enhanced lateral flow immunoassay for highly-sensitive detection of potato leafroll virus.* Food and Agricultural Immunology, 2018. **29**(1): p. 445-457.

163. Yu, Q., H. Li, C. Li, et al., *Gold nanoparticles-based lateral flow immunoassay with silver staining for simultaneous detection of fumonisin B1 and deoxynivalenol.* Food Control, 2015. **54**: p. 347-352.

164. Rodríguez, M.O., L.B. Covián, A.C. García, et al., *Silver and gold enhancement methods for lateral flow immunoassays.* Talanta, 2016. **148**: p. 272-8.

165. Nixon, M., F. Outlaw, and T.S. Leung, *Accurate device-independent colorimetric measurements using smartphones.* PLOS ONE, 2020. **15**(3): p. e0230561.

166. Bennett, C., P. Sookwong, J. Jakmunee, et al., *Smartphone digital image colorimetric determination of the total monomeric anthocyanin content in black rice via the pH differential method.* Analytical Methods, 2021. **13**(30): p. 3348-3358.

167. Lim, J.M., M. Supianto, T.Y. Kim, et al., *Fluorescent Lateral Flow Assay with Carbon Nanodot Conjugates for Carcinoembryonic Antigen.* BioChip Journal, 2023. **17**(1): p. 93-103.

168. Singh, H., S. Singh, S.K. Bhardwaj, et al., *Development of carbon quantum dot-based lateral flow immunoassay for sensitive detection of aflatoxin M1 in milk.* Food Chemistry, 2022. **393**: p. 133374.

169. Gupta, R., P. Gupta, S. Wang, et al., *Ultrasensitive lateral-flow assays via plasmonically active antibody-conjugated fluorescent nanoparticles.* Nature Biomedical Engineering, 2023.

170. Shen, Y. and G. Shen, *Signal-Enhanced Lateral Flow Immunoassay with Dual Gold Nanoparticle Conjugates for the Detection of Hepatitis B Surface Antigen.* ACS Omega, 2019. **4**(3): p. 5083-5087.

171. Wang, J., C. Jiang, J. Jin, et al., *Ratiometric Fluorescent Lateral Flow Immunoassay for Point-of-Care Testing of Acute Myocardial Infarction.* Angewandte Chemie International Edition, 2021. **60**(23): p. 13042-13049.

172. Ju, J., X. Zhang, L. Li, et al., *Development of fluorescent lateral flow immunoassay for SARS-CoV-2-specific IgM and IgG based on aggregation-induced emission carbon dots.* Front Bioeng Biotechnol, 2022. **10**: p. 1042926.

173. Takalkar, S., K. Baryeh, and G. Liu, *Fluorescent carbon nanoparticle-based lateral flow biosensor for ultrasensitive detection of DNA.* Biosensors and Bioelectronics, 2017. **98**: p. 147-154.

174. Lago-Cachón, D., M. Rivas, J.C. Martínez-García, et al., *High frequency lateral flow affinity assay using superparamagnetic nanoparticles.* Journal of Magnetism and Magnetic Materials, 2017. **423**: p. 436-440.

175. Qin, Z., W.C.W. Chan, D.R. Boulware, et al., *Significantly improved analytical sensitivity of lateral flow immunoassays by using thermal contrast.* Angewandte Chemie (International ed. in English), 2012. **51**(18): p. 4358-4361.

176. Amendola, V., R. Pilot, M. Frasconi, et al., *Surface plasmon resonance in gold nanoparticles: a review.* Journal of Physics: Condensed Matter, 2017. **29**(20): p. 203002.

177. Zhan, L., T. Granade, Y. Liu, et al., *Development and optimization of thermal contrast amplification lateral flow immunoassays for ultrasensitive HIV p24 protein detection.* Microsystems & Nanoengineering, 2020. **6**(1): p. 54.

178. Qu, Z., K. Wang, G. Alfranca, et al., *A plasmonic thermal sensing based portable device for lateral flow assay detection and quantification.* Nanoscale Research Letters, 2020. **15**(1): p. 10.

179. Hu, X., J. Wan, X. Peng, et al., *Calorimetric lateral flow immunoassay detection platform based on the photothermal effect of gold nanocages with high sensitivity, specificity, and accuracy.* International journal of nanomedicine, 2019. **14**: p. 7695-7705.

180. Shirshahi, V., S.N. Tabatabaei, S. Hatamie, et al., *Photothermal enhancement in sensitivity of lateral flow assays for detection of E-coli O157:H7.* Colloids and Surfaces B: Biointerfaces, 2020. **186**: p. 110721.

181. Zhang, D., S. Du, S. Su, et al., *Rapid detection method and portable device based on the photothermal effect of gold nanoparticles.* Biosensors and Bioelectronics, 2019. **123**: p. 19-24.

182. Cheng, N., Y. Song, Q. Shi, et al., *Au@Pd Nanopopcorn and Aptamer Nanoflower Assisted Lateral Flow Strip for Thermal Detection of Exosomes.* Analytical Chemistry, 2019. **91**(21): p. 13986-13993.

183. Siegel, A.C., S.T. Phillips, B.J. Wiley, et al., *Thin, lightweight, foldable thermochromic displays on paper.* Lab on a Chip, 2009. **9**(19): p. 2775-2781.

184. Polo, E., P. del Pino, B. Pelaz, et al., *Plasmonic-driven thermal sensing: ultralow detection of cancer markers.* Chemical Communications, 2013. **49**(35): p. 3676-3678.

185. Bio-Tech, M., *Product description: Salmonella Rapid Test Cassette for Food and Environment*.

186. Millipore, M., *Product description: Singlepath® Salmonella (catalogue number: 104140)*. Sigma-Aldrich.

187. Labs, R., *Product description: RapidChek® SELECT™ Salmonella Test Kit*. Romer Labs Division Holding GmbH.

188. Works, B., *Product description: Salmonella Rapid Detection Kit (SKU: STLF-020)*.

189. Attogene, *Product description: Fluorescent Universal Lateral Flow Assay Kit (SKU: AU2037)*. ATTOGENE CORPORATION.

190. FlowFlex, *Product description: FlowFlex COVID-19 Rapid Test Kits*.

191. Health, A., *Product description: OraQuick® HIV Self-Test (Product Code: FG-1001-0600)*.

192. Health, A., *Product description: Check Your Drink (Product Code: FG-CYD001)*.

193. Liz-Marzán, L.M., *Tailoring Surface Plasmons through the Morphology and Assembly of Metal Nanoparticles.* Langmuir, 2006. **22**(1): p. 32-41.

194. Mayer, K.M. and J.H. Hafner, *Localized Surface Plasmon Resonance Sensors.* Chemical Reviews, 2011. **111**(6): p. 3828-3857.

195. Petryayeva, E. and U.J. Krull, *Localized surface plasmon resonance: Nanostructures, bioassays and biosensing—A review.* Analytica Chimica Acta, 2011. **706**(1): p. 8-24.

196. Qin, Z. and J.C. Bischof, *Thermophysical and biological responses of gold nanoparticle laser heating.* Chem Soc Rev, 2012. **41**(3): p. 1191-217.

197. Baffou, G., R. Quidant, and C. Girard, *Heat generation in plasmonic nanostructures: Influence of morphology.* Applied Physics Letters, 2009. **94**(15): p. 153109.

198. Meyer, S.M., J. Pettine, D.J. Nesbitt, et al., *Size Effects in Gold Nanorod Light-to-Heat Conversion under Femtosecond Illumination.* The Journal of Physical Chemistry C, 2021. **125**(29): p. 16268-16278.

199. Maity, D., S.N. Kale, R. Kaul-Ghanekar, et al., *Studies of magnetite nanoparticles synthesized by thermal decomposition of iron (III) acetylacetonate in tri(ethylene glycol).* Journal of Magnetism and Magnetic Materials, 2009. **321**(19): p. 3093-3098.

200. Liu, J., Z. Sun, Y. Deng, et al., *Highly water-dispersible biocompatible magnetite particles with low cytotoxicity stabilized by citrate groups.* Angew Chem Int Ed Engl, 2009. **48**(32): p. 5875-9.

201. Hachani, R., M. Lowdell, M. Birchall, et al., *Polyol synthesis, functionalisation, and biocompatibility studies of superparamagnetic iron oxide nanoparticles as potential MRI contrast agents.* Nanoscale, 2016. **8**(6): p. 3278-3287.

202. Kodama, D., K. Shinoda, K. Sato, et al., *Synthesis of Fe-Co Alloy Particles by Modified Polyol Process.* IEEE Transactions on Magnetics, 2006. **42**(10): p. 2796-2798.

203. Zamanpour, M., Y. Chen, B. Hu, et al., *Large-scale synthesis of high moment FeCo nanoparticles using modified polyol synthesis.* Journal of Applied Physics, 2012. **111**(7): p. 07B528.

204. Dong, H., Y.C. Chen, and C. Feldmann, *Polyol synthesis of nanoparticles: status and options regarding metals, oxides, chalcogenides, and non-metal elements.* Green Chemistry, 2015. **17**(8): p. 4107-4132.

205. Turkevich, J. and J. Hillier, *Electron Microscopy of Colloidal Systems.* Analytical Chemistry, 1949. **21**(4): p. 475-485.

206. Turkevich, J., P.C. Stevenson, and J. Hillier, *A study of the nucleation and growth processes in the synthesis of colloidal gold.* Discussions of the Faraday Society, 1951. **11**(0): p. 55-75.

207. Kimling, J., M. Maier, B. Okenve, et al., *Turkevich Method for Gold Nanoparticle Synthesis Revisited.* The Journal of Physical Chemistry B, 2006. **110**(32): p. 15700-15707.

208. Wuithschick, M., A. Birnbaum, S. Witte, et al., *Turkevich in New Robes: Key Questions Answered for the Most Common Gold Nanoparticle Synthesis.* ACS Nano, 2015. **9**(7): p. 7052-7071.

209. Frens, G., *Controlled Nucleation for the Regulation of the Particle Size in Monodisperse Gold Suspensions.* Nature Physical Science, 1973. **241**(105): p. 20-22.

210. Pallares, R.M., X. Su, S.H. Lim, et al., *Fine-tuning of gold nanorod dimensions and plasmonic properties using the Hofmeister effects.* Journal of Materials Chemistry C, 2016. **4**(1): p. 53-61.

211. Murphy, C.J., L.B. Thompson, D.J. Chernak, et al., *Gold nanorod crystal growth: From seed-mediated synthesis to nanoscale sculpting.* Current Opinion in Colloid & Interface Science, 2011. **16**(2): p. 128-134.

212. Navarro, J.R., D. Manchon, F. Lerouge, et al., *Synthesis of PEGylated gold nanostars and bipyramids for intracellular uptake.* Nanotechnology, 2012. **23**(46): p. 465602.

213. Nikoobakht, B. and M.A. El-Sayed, *Preparation and Growth Mechanism of Gold Nanorods (NRs) Using Seed-Mediated Growth Method.* Chemistry of Materials, 2003. **15**(10): p. 1957-1962.

214. Monshi, A., M.R. Foroughi, and M.R. Monshi, *Modified Scherrer equation to estimate more accurately nano-crystallite size using XRD.* World J Nano Sci Eng, 2012, 2: 154, 2012. **160**.

215. Sun, S. and H. Zeng, *Size-Controlled Synthesis of Magnetite Nanoparticles.* Journal of the American Chemical Society, 2002. **124**(28): p. 8204-8205.

216. Hildebrand, S., N. Löwa, H. Paysen, et al., *Quantification of Lipoprotein Uptake in Vivo Using Magnetic Particle Imaging and Spectroscopy.* ACS Nano, 2021. **15**(1): p. 434-446.

217. Park, Y., R.D. Whitaker, R.J. Nap, et al., *Stability of Superparamagnetic Iron Oxide Nanoparticles at Different pH Values: Experimental and Theoretical Analysis.* Langmuir, 2012. **28**(15): p. 6246-6255.

218. Kasparis, G., A.P. Sangnier, L. Wang, et al., *Zn doped iron oxide nanoparticles with high magnetization and photothermal efficiency for cancer treatment.* Journal of Materials Chemistry B, 2023. **11**(4): p. 787-801.

219. Li, L., K.Y. Mak, C.W. Leung, et al., *Effect of synthesis conditions on the properties of citric-acid coated iron oxide nanoparticles.* Microelectronic Engineering, 2013. **110**: p. 329-334.

220. Kovář, D., A. Malá, J. Mlčochová, et al., *Preparation and Characterisation of Highly Stable Iron Oxide Nanoparticles for Magnetic Resonance Imaging.* Journal of Nanomaterials, 2017. **2017**: p. 7859289.

221. Benyettou, F., I. Milosevic, J.-C. Olsen, et al., *Ultra-Small Superparamagnetic Iron Oxide Nanoparticles Made to Order.* J Bioanal Biomed, 2012.

222. ur Rahman, Z., Y.L. Dong, C. Ren, et al., *Protein adsorption on citrate modified magnetic nanoparticles.* J Nanosci Nanotechnol, 2012. **12**(3): p. 2598-606.

223. Hidber, P.C., T.J. Graule, and L.J. Gauckler, *Citric Acid—A Dispersant for Aqueous Alumina Suspensions.* Journal of the American Ceramic Society, 1996. **79**(7): p. 1857-1867.

224. Déry, J.-P., E.F. Borra, and A.M. Ritcey, *Ethylene Glycol Based Ferrofluid for the Fabrication of Magnetically Deformable Liquid Mirrors.* Chemistry of Materials, 2008. **20**(20): p. 6420-6426.

225. Gao, X., D.W. Metge, C. Ray, et al., *Surface Complexation of Carboxylate Adheres Cryptosporidium parvum Öocysts to the Hematite−Water Interface.* Environmental Science & Technology, 2009. **43**(19): p. 7423-7429.

226. Bhattacharjee, S., *DLS and zeta potential – What they are and what they are not?* Journal of Controlled Release, 2016. **235**: p. 337-351.

227. Stein, R., B. Friedrich, M. Mühlberger, et al., *Synthesis and Characterization of Citrate-Stabilized Gold-Coated Superparamagnetic Iron Oxide Nanoparticles for Biomedical Applications.* Molecules, 2020. **25**(19).

228. Haiss, W., N.T.K. Thanh, J. Aveyard, et al., *Determination of Size and Concentration of Gold Nanoparticles from UV−Vis Spectra.* Analytical Chemistry, 2007. **79**(11): p. 4215-4221.

229. Balasubramanian, S.K., L. Yang, L.-Y.L. Yung, et al., *Characterization, purification, and stability of gold nanoparticles.* Biomaterials, 2010. **31**(34): p. 9023-9030.

230. Jana, N.R., L. Gearheart, and C.J. Murphy, *Seed-Mediated Growth Approach for Shape-Controlled Synthesis of Spheroidal and Rod-like Gold Nanoparticles Using a Surfactant Template.* Advanced Materials, 2001. **13**(18): p. 1389-1393.

231. Gole, A. and C.J. Murphy, *Seed-Mediated Synthesis of Gold Nanorods: Role of the Size and Nature of the Seed.* Chemistry of Materials, 2004. **16**(19): p. 3633-3640.

232. John, C.L., S.L. Strating, K.A. Shephard, et al., *Reproducibly synthesize gold nanorods and maintain their stability.* RSC Advances, 2013. **3**(27): p. 10909-10918.

233. Munyayi, T.A., B.C. Vorster, and D.W. Mulder, *The Effect of Capping Agents on Gold Nanostar Stability, Functionalization, and Colorimetric Biosensing Capability.* Nanomaterials (Basel), 2022. **12**(14).

234. Becerril-Castro, I.B., I. Calderon, N. Pazos-Perez, et al., *Gold Nanostars: Synthesis, Optical and SERS Analytical Properties.* Analysis & Sensing, 2022. **2**(3): p. e202200022.

235. Marshall, J., *The safety of laser pointers: myths and realities.* British Journal of Ophthalmology, 1998. **82**(11): p. 1335.

236. Liu, X., M. Atwater, J. Wang, et al., *Extinction coefficient of gold nanoparticles with different sizes and different capping ligands.* Colloids and Surfaces B: Biointerfaces, 2007. **58**(1): p. 3-7.

237. Orendorff, C.J. and C.J. Murphy, *Quantitation of Metal Content in the Silver-Assisted Growth of Gold Nanorods.* The Journal of Physical Chemistry B, 2006. **110**(9): p. 3990-3994.

238. Lavín, Á., J.D. Vicente, M. Holgado, et al., *On the Determination of Uncertainty and Limit of Detection in Label-Free Biosensors.* Sensors, 2018. **18**(7): p. 2038.

239. Rao, G.G. and G. Somidevamma, *Volumetric determination of iron (III) with hydroxylamine as a reducing agent.* Fresenius' Zeitschrift für analytische Chemie, 1959. **165**(6): p. 432-436.

240. Govorov, A.O. and H.H. Richardson, *Generating heat with metal nanoparticles.* Nano Today, 2007. **2**(1): p. 30-38.

241. Li, Y., Q. Yang, M. Li, et al., *Rate-dependent interface capture beyond the coffee-ring effect.* Scientific Reports, 2016. **6**(1): p. 24628.

242. Al-Milaji, K.N., R.R. Secondo, T.N. Ng, et al., *Interfacial Self-Assembly of Colloidal Nanoparticles in Dual-Droplet Inkjet Printing.* Advanced Materials Interfaces, 2018. **5**(10): p. 1701561.

243. He, P. and B. Derby, *Controlling Coffee Ring Formation during Drying of Inkjet Printed 2D Inks.* Advanced Materials Interfaces, 2017. **4**(22): p. 1700944.

244. Kashyap, R.K., M.J. Parammal, and P.P. Pillai, *Effect of Nanoparticle Size on Plasmonic Heat-Driven Organic Transformation.* ChemNanoMat. **n/a**(n/a): p. e202200252.

245. Qin, Z., Y. Wang, J. Randrianalisoa, et al., *Quantitative Comparison of Photothermal Heat Generation between Gold Nanospheres and Nanorods.* Scientific Reports, 2016. **6**(1): p. 29836.

246. Joshi, R., H. Janagama, H.P. Dwivedi, et al., *Selection, characterization, and application of DNA aptamers for the capture and detection of Salmonella enterica serovars.* Molecular and Cellular Probes, 2009. **23**(1): p. 20-28.

247. Widdel, F., *Theory and measurement of bacterial growth.* Di dalam Grundpraktikum Mikrobiologie, 2007. **4**(11): p. 1-11.

248. Stevenson, K., A.F. McVey, I.B.N. Clark, et al., *General calibration of microbial growth in microplate readers.* Scientific Reports, 2016. **6**(1): p. 38828.

249. Shen, H., A.M. Jawaid, and P.T. Snee, *Poly(ethylene glycol) Carbodiimide Coupling Reagents for the Biological and Chemical Functionalization of Water-Soluble Nanoparticles.* ACS Nano, 2009. **3**(4): p. 915-923.

250. Zhou, J. and J. Rossi, *Aptamers as targeted therapeutics: current potential and challenges.* Nature reviews. Drug discovery, 2017. **16**(3): p. 181-202.

251. Adachi, T. and Y. Nakamura, *Aptamers: A Review of Their Chemical Properties and Modifications for Therapeutic Application.* Molecules, 2019. **24**(23): p. 4229.

252. Xu, Y., D.C. Baiu, J.A. Sherwood, et al., *Linker-free conjugation and specific cell targeting of antibody functionalized iron-oxide nanoparticles.* Journal of Materials Chemistry B, 2014. **2**(37): p. 6198-6206.

253. Parker, F.S., *Amides and Amines*, in *Applications of Infrared Spectroscopy in Biochemistry, Biology, and Medicine*, F.S. Parker, Editor. 1971, Springer US: Boston, MA. p. 165-172.

254. Ji, Y., X. Yang, Z. Ji, et al., *DFT-Calculated IR Spectrum Amide I, II, and III Band Contributions of N-Methylacetamide Fine Components.* ACS Omega, 2020. **5**(15): p. 8572-8578.

255. Graham, T.R., E.T. Nienhuis, J.G. Reynolds, et al., *Sodium site occupancy and phosphate speciation in natrophosphate are invariant to changes in NaF and Na3PO4 concentration.* Inorganic Chemistry Frontiers, 2022. **9**(19): p. 4864-4875.

256. Jastrzębski, W., M. Sitarz, M. Rokita, et al., *Infrared spectroscopy of different phosphates structures.* Spectrochimica Acta Part A: Molecular and Biomolecular Spectroscopy, 2011. **79**(4): p. 722-727.

257. Chen, J., B. Duncan, Z. Wang, et al., *Bacteriophage-based nanoprobes for rapid bacteria separation.* Nanoscale, 2015. **7**(39): p. 16230-16236.

258. VARSHNEY, M., L. YANG, X.-L. SU, et al., *Magnetic Nanoparticle-Antibody Conjugates for the Separation of Escherichia coli O157:H7 in Ground Beef.* Journal of Food Protection, 2005. **68**(9): p. 1804-1811.

259. Li, Z., J. Ma, J. Ruan, et al., *Using Positively Charged Magnetic Nanoparticles to Capture Bacteria at Ultralow Concentration.* Nanoscale Research Letters, 2019. **14**(1): p. 195.

260. Prakashan, D., N.S. Shrikrishna, M. Byakodi, et al., *Gold nanoparticle conjugate-based lateral flow immunoassay (LFIA) for rapid detection of RBD antigen of SARS-CoV-2 in clinical samples using a smartphone-based application.* J Med Virol, 2023. **95**(1): p. e28416.

261. Zhang, S., Y. Moustafa, and Q. Huo, *Different Interaction Modes of Biomolecules with Citrate-Capped Gold Nanoparticles.* ACS Applied Materials & Interfaces, 2014. **6**(23): p. 21184-21192.

262. Tripathi, K. and J.D. Driskell, *Quantifying Bound and Active Antibodies Conjugated to Gold Nanoparticles: A Comprehensive and Robust Approach To Evaluate Immobilization Chemistry.* ACS Omega, 2018. **3**(7): p. 8253-8259.

263. Yeo, E.L.L., A.J.S. Chua, K. Parthasarathy, et al., *Understanding aggregation-based assays: nature of protein corona and number of epitopes on antigen matters.* RSC Advances, 2015. **5**(20): p. 14982-14993.

264. Iarossi, M., C. Schiattarella, I. Rea, et al., *Colorimetric Immunosensor by Aggregation of Photochemically Functionalized Gold Nanoparticles.* ACS omega, 2018. **3**(4): p. 3805-3812.

265. Park, J., *An Optimized Colorimetric Readout Method for Lateral Flow Immunoassays.* Sensors, 2018. **18**(12): p. 4084.

266. Hu, X., J. Wan, X. Peng, et al., *Calorimetric lateral flow immunoassay detection platform based on the photothermal effect of gold nanocages with high sensitivity, specificity, and accuracy.* Int J Nanomedicine, 2019. **14**: p. 7695-7705.

267. Jeon, H.S., J.H. Kim, M.B.G. Jun, et al., *Fabrication of Thermochromic Membrane and Its Characteristics for Fever Detection.* Materials, 2021. **14**(13): p. 3460.

268. Wang, M., Y. Wang, X. Li, et al., *Development of a photothermal-sensing microfluidic paper-based analytical chip (PT-Chip) for sensitive quantification of diethylstilbestrol.* Food Chemistry, 2023. **402**: p. 134128.

269. Khachornsakkul, K., R. Del-Rio-Ruiz, W. Zeng, et al., *Highly Sensitive Photothermal Microfluidic Thread-Based Duplex Immunosensor for Point-of-Care Monitoring.* Analytical Chemistry, 2023. **95**(34): p. 12802-12810.

270. Moran, C.H., S.M. Wainerdi, T.K. Cherukuri, et al., *Size-dependent joule heating of gold nanoparticles using capacitively coupled radiofrequency fields.* Nano Research, 2009. **2**(5): p. 400-405.

271. Raj, N. and R.M. Crooks, *Plastic-based lateral flow immunoassay device for electrochemical detection of NT-proBNP.* Analyst, 2022. **147**(11): p. 2460-2469.

272. Cheng, J., G. Yang, J. Guo, et al., *Integrated electrochemical lateral flow immunoassays (eLFIAs): recent advances.* Analyst, 2022. **147**(4): p. 554-570.

Appendices

Appendix A

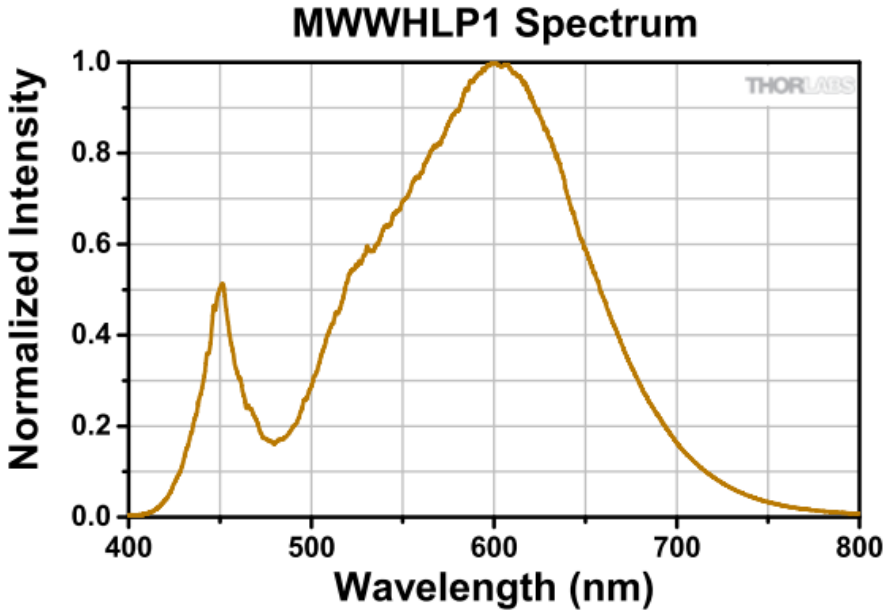

Figure 1 Emission spectrum of MWWHLP1 LED (Thorlabs, UK).

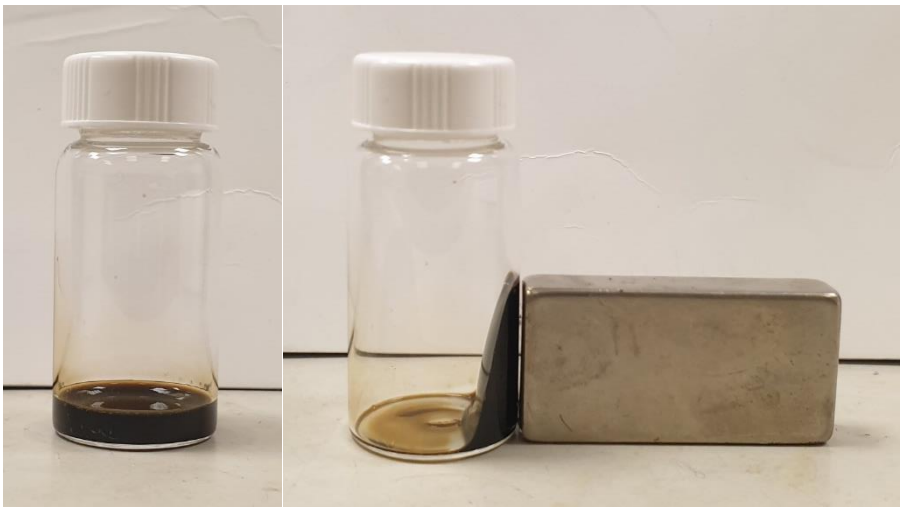

Figure 2 Response to a permanent magnet of MNPs@citrate after ligand exchange.

Appendix B

Figure 1 Coffee ring formation of MNPs@citrate on a nitrocellulose membrane.

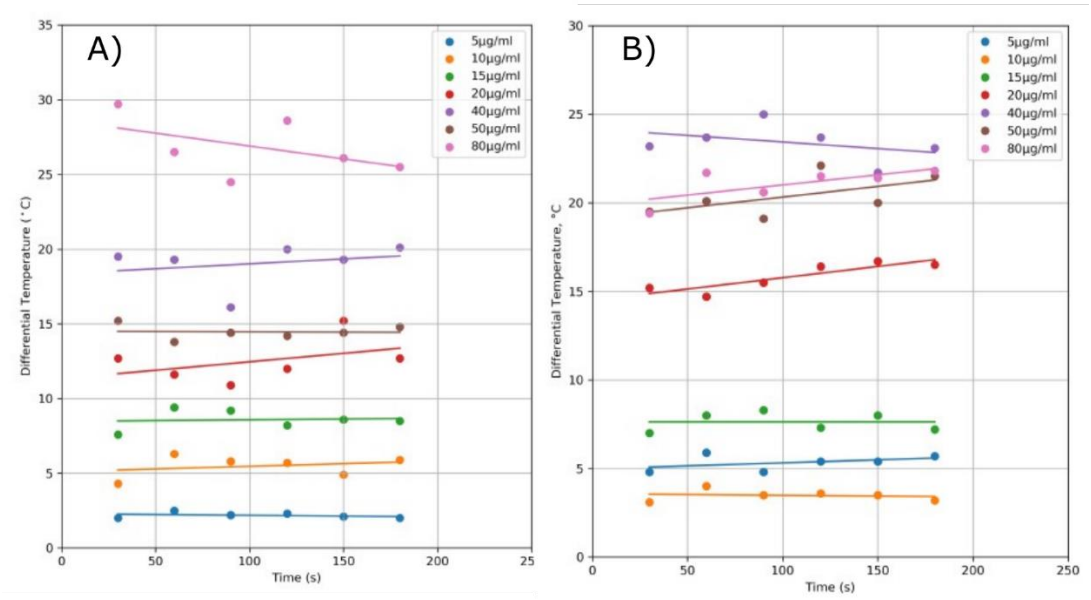

Figure 2 Differential temperature versus time for a series of concentrations of a) IONPs@citrate and b) ZFNPs@citrate exposed to a laser (780 nm, 31 mW/cm^2).

Table 1 Temperature production of IONPs@citrat, ZFNPs@citrate, nitrocellulose membrane, and thermochromic sheet upon optical stimulation by different light sources. All samples were recorded with a thermal imager after 3 min of exposure.

Samples	Light source		
	0.08 W/cm^2 532nm	0.5 W/cm^2 605-700 nm	0.5 W/cm^2 400-700 nm
Nitrocellulose membrane	3.50 °C	2.10 °C	0.80 °C
Nitrocellulose membrane + Thermochromic sheet	5.70 °C	2.60 °C	3.70 °C
25 µg/mL IONPs	9.65 °C	9.70 °C	18.40 °C
200 µg/mL IONPs	15.00 °C	10.30 °C	22.80 °C
25 µg/mL ZFNPs	15.80 °C	7.20 °C	15.80 °C
200 µg/mL ZFNPs	17.70 °C	7.10 °C	18.30 °C

Appendix C

Calculation of volume of a single nanoparticle: sphere and rod

$V_{sphere} = \frac{4}{3} * ¶ * r^3$ **(Equation 1)**

$V_{rod} = (¶ * (\frac{W}{2})^2 * L$ **(Equation 2)**

where V_{sphere} and V_{rod} are the volume of the spherical and rod nanoparticles, respectively. ¶ is a typical constant number of 3.14, while r, W, and L, the radius, width, and length, respectively, which were determined by TEM measurements.

Calculation of mass of a single nanoparticle

m = V * D **(Equation 3)**

where m is the mass per particle, V the volume calculated from the above equation depending on the shape, and D the density of material.

Calculation of molar concentration of gold nanoparticles

$N = m * 6.02 * 10^{23}$ **(Equation 4)**

where N is the molar mass (g/mol), m the mass per particle, and $6.02 * 10^{23}$ is an Avogadro constant.

Calculation of the mass per volume

Number of particles per volume = $\frac{M * N}{m}$ **(Equation 5)**

where M is the molar concentration (mol/L) [228, 237], N the mass molar (g/mol), and m the mass of a single nanoparticle.

Appendix D

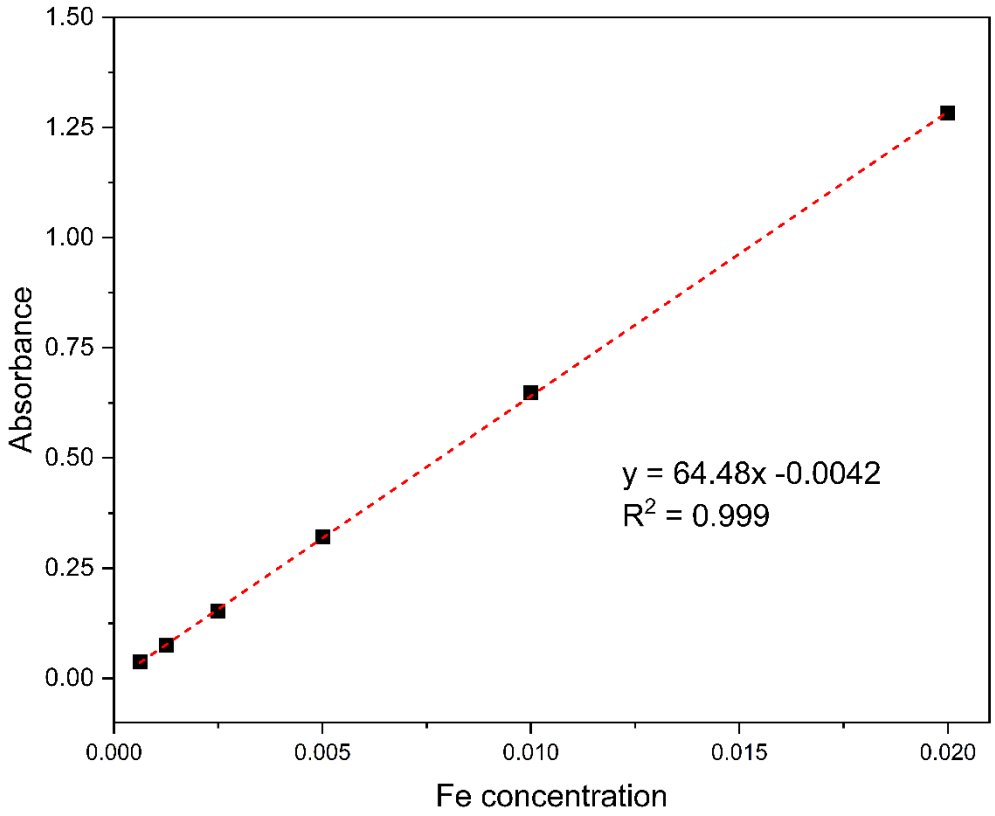

Figure 1 Calibration curve of the iron concentration (mg_{Fe}/mL) versus absorbance

Appendix E

Table 1 Number of particles per volume unit at different mass concentrations

Mass per volume (mg/mL)	Number of nanoparticles per volume (particle number/mL)						
	IONP	ZFNP	AuNSP (12 nm diameter)	AuNSP (18 nm diameter)	AuNR (LSPR = 560 nm)	AuNR (LSPR = 600 nm)	AuNR (LSPR = 625 nm)
0.5	$1.53*10^{14}$	$1.45*10^{14}$	$4.32*10^{13}$	$8.48*10^{12}$	$8.68*10^{11}$	$1.02*10^{12}$	$1.13*10^{12}$
1.0	$3.06*10^{14}$	$2.89*10^{14}$	$8.64*10^{13}$	$1.70*10^{13}$	$1.74*10^{12}$	$2.04*10^{12}$	$2.26*10^{12}$
1.5	$4.59*10^{14}$	$4.34*10^{14}$	$1.30*10^{14}$	$2.54*10^{13}$	$2.60*10^{12}$	$3.05*10^{12}$	$3.39*10^{12}$
2.0	$6.12*10^{14}$	$5.79*10^{14}$	$1.73*10^{14}$	$3.39*10^{13}$	$3.47*10^{12}$	$4.07*10^{12}$	$4.51*10^{12}$

Appendix F

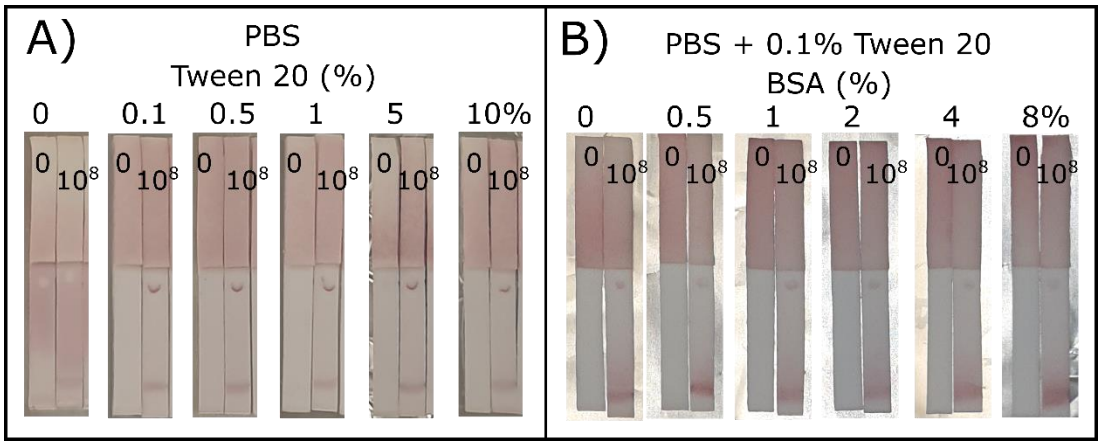

Figure 1 Impact of BSA protein and Tween 20 in a running buffer. A) Different concentrations of Tween 20 in the PBS. B) different concentrations of BSA in the PBS with 0.1% Tween20. Each sample was tested with 10^8 CFU/mL of *Salmonella typhimurium* and without bacteria.

Appendix G

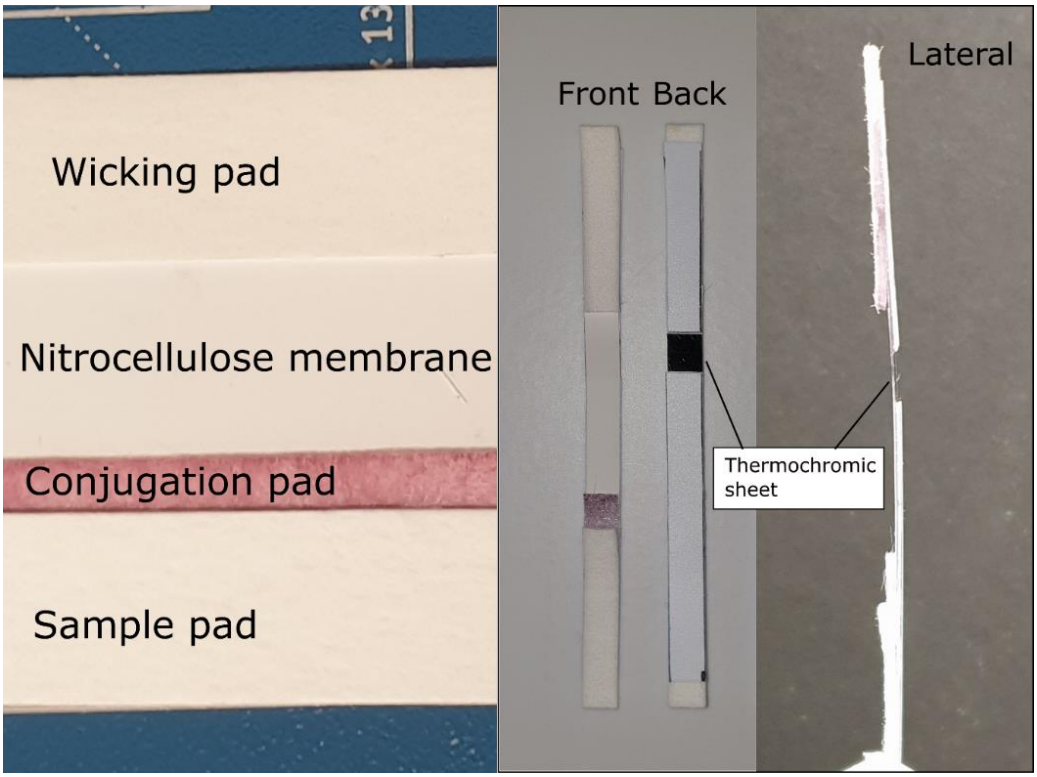

Figure 1 Assembly of LFA components on a backing card. Different views of the assembled thermochromic LFA is presented.

Appendix H

1. Cost of the synthesis of AuNSPs (12 nm diameter) per synthesis, refer to Section 2.3.2.1.

   $HAuCL_4$ (£3.48) + Trisodium citrate (£0.01) yield 0.003154 g of AuNSPs. Therefore, 1 mg AuNSPs costs ~£1.1.

2. Cost of the synthesis of ZFNPs@citrate per synthesis, refer to Section 2.2.2 and 2.2.3.

   $Fe(acac)_3$ (£3.17) + $Zn(acac)_2$ (£1.2) + TREG (£0.54) + Trisodium citrate (£0.14) yield 0.12 g of ZFNPs. Therefore, 1 mg ZFNPs costs ~£0.04.